Structural Insights from the NMR Spectroscopy of Quadrupolar Nuclei: Exploiting Electric Field Gradient and Spin-Spin Coupling Tensors

Frédéric A. Perras

A thesis submitted to the
Faculty of Graduate and Postdoctoral Studies
in partial fulfillment of the requirements
for the Doctorate in Philosophy degree in Chemistry

Ottawa-Carleton Chemistry Institute
Department of Chemistry
Faculty of Science
University of Ottawa

uOttawa

Abstract

NMR spectroscopy has evolved into one of the most important characterization techniques in chemistry with which it is possible to obtain valuable structural, dynamical, and mechanistic information. Most applications of NMR have however been limited to the use of nuclei having spin quantum numbers of 1/2. This thesis discusses the developments that have been advanced in order to extract quantitative structural information from the NMR spectroscopy of quadrupolar nuclei (spin, $I>1/2$) which account for the vast majority of the NMR-active nuclei. In a first part of the thesis, a NMR crystallographic method is developed which uses the electric field gradient tensor measured at the nuclear sites as an experimental constraint in DFT-based crystal structure refinements. This inclusion of experimental data into crystal structure refinements enables the determination of higher quality, and experimentally-relevant, structures. We apply this new methodology in order to determine higher quality crystal structures for the non-linear optical material $Na_2B_2Al_2O_7$, sodium pyrophosphates, and the near-zero thermal expansion material $ZrMgMo_3O_{12}$. In a second part of this thesis, experimental techniques are developed for the measurement of spin-spin coupling between pairs of quadrupolar nuclei; the measurement of spin-spin coupling carries with it extremely valuable distance and connectivity information. Using DOR NMR, heteronuclear residual dipolar coupling as well as homonuclear *J* coupling multiplets can be observed. Notably, the *J* coupling between quadrupolar nuclei can still be measured in A_2 spin systems, unlike in the case of pairs of spin-1/2 nuclei. The theory that was developed for the characterization of these multiplets was extended for the general simulation of exact NMR spectra of quadrupolar. This program, known as QUEST, is now

free to use by anyone in the scientific community. Pulsed *J*-resolved NMR experiments are then described which enable the facile measurement of *J* and dipolar coupling in homonuclear pairs of quadrupolar nuclei. Notably, the *J* splitting is greatly amplified in A_2 spin systems which provides strong structural information and enables the precise detection of smaller *J* coupling constants. These techniques are applied towards directly studying gallium metal-metal bonding interactions as well as boron-boron bonds in diboron compounds of importance in β-boration chemistry.

Acknowledgements

Although theses are meant to reflect on the cumulative work that an individual has performed over a given period of time, none of this work would have been possible if it wasn't for the many people I have had a chance to meet and work with during my graduate studies. I would, of course, like to firstly thank my supervisor, David Bryce, for exposing me to the beautiful technique of solid-state NMR spectroscopy. Dave's love of science and enthusiasm towards research is truly inspirational and has helped create an insatiable hunger for knowledge and science in me. I also thank you Dave for supporting all my crazy ideas that were destined to fail since, as I have learned, some 10 % of these crazy ideas end up giving good results. I am also grateful for the complicated projects he has given me as an undergraduate student, such as programming line shape simulation software (without any programming knowledge) and figuring out how to use the DOR probe. I believe that these challenges helped me become a better independent learner and researcher. Of course, the Bryce lab outings such as outings to Pub Italia, Brother's Beer Bistro, and the fabled Bryce lab ski trip truly helped create a pleasant work environment, and a lab that I will sorely miss following the end of my graduate studies.

I would also like to acknowledge, in particular, Muralee Murugesu, my honour's thesis supervisor, who has largely remained as an honorary advisor during my graduate work, pushing me to strive towards excellence. Many of the skills I have gained while working for him have been of use during my doctoral work.

I would like to thank various staff members that have helped in my experiments. Victor Terskikh and Eric Ye (who is now at the University of Ottawa) from the National

Ultrahigh Field NMR facility for Solids I thank for their impeccable support and insights; many of my nicest NMR spectra would not have been acquired without their help. Glenn Facey, your knowledge of solid-state NMR and NMR hardware has been central to the success of many of my experiments. I am also grateful for you keeping an eye on me at conferences. Tara Burchell and Ilia Korobkov I thank for your help with my humble attempts to perform diffraction experiments and your insightful discussions relating to crystallography. Lastly, I would like to thank Tom Daff and Peter Boyd for maintaining the wookie cluster and installing NMR software, such as SIMPSON, on the cluster.

My work has, of course, been greatly influenced by the fellow graduate students with which I have shared an office, most notably those which are known, to me, as Bryce lab generation alpha. The members of generation alpha, namely, Joey, Becky, Cory, and Andy have taught me much of what I know about NMR. Joey, I am grateful for you mentoring me during my undergraduate summer in the Bryce lab. I am sad to say that no one has distributed free cheese in the hallway since your graduation. I eagerly await the day when we negotiate a deal for my first NMR spectrometer over a couple of Samichlaus. Becky, I am grateful for you teaching me the basics of solid-state NMR and always finding time to answer my questions. You were also a great debate mediator, I must say that the philosophical discussions got out of hand after you left. I thank you Cory for inspiring me to follow work in large quadrupolar interactions and developing QUEST. Your attention to detail is truly inspiring; I can only strive towards producing work at your level of quality. And Andy, A.K.A. the coolest person in the lab, I thank for all your technical help.

I also would like to thank all the members of Bryce lab generation beta, namely, Kevin, Jasmine, and Rob. Kevin, the holy pope of the CGSA, our philosophical debates and

discussions have truly helped make the office an intellectually stimulating environment. I know that one day you will puzzle out the mystery that is vaterite. Jasmine, I thank for bringing a feminine presence in the lab and for all your valuable comments and corrections on my work. I hope to someday be able to master the art of poster presentations, which comes as second nature to you. Lastly Rob, the first member of generation beta to graduate, thank you for pushing Dave to purchase the amazing office chairs we now have.

The group will soon fall into the hands of Bryce lab generation gamma, i.e. Scott, Sherif, and Pat; I hope that you find your research as inspiring as I have found mine. Scott, your punctuality and rapid progress is truly motivating. Sherif, never stop thinking of crazy projects, eventually one of your ideas will lead to a great discovery. Pat, I know I will soon see an article in the newspaper talking about how you solved the climate crisis.

I would also like to acknowledge the different visiting researchers I have had the chance to work with. Dr. Oh I have greatly enjoyed your fatherly presence in the lab; your attention to detail and work ethic are rivaled by none. I hope our paths cross again in the future so that you need to tell me about the time you solved Schrodinger's equation. Igor, your knowledge of NMR was of great help of my research during the short time you spent in the lab. I thank you for modifying the DOR probe to perform ^{43}Ca NMR experiments and for all the entertaining anecdotes you have told me. Grace, your positive attitude is a nice presence in the office.

Many undergraduate students have helped me in numerous projects over the years, namely James, Ritesh, Collette, Nuiok, and Gyvenska, unfortunately many of those projects were unsuccessful. Collette, I am impressed by your drive and rapid progress, you will be a great graduate student, should you chose the Bryce lab. Nuiok, you were a great

autonomous student, and your amazing contribution with EFGShield 4.0 was of great use for myself and numerous others. I have also worked alongside many other undergraduate students, specifically Omar, Brittany, Devon, Prisca, Apurva, Calan, Aurore, Matt, Sophie, Phil, Jessica, Julia, Elisabeth, Mélanie, Yang, Mustafa, Cédric, Samuel, and Arnaud, however we had unfortunately not had the chance to work together during our time in the Bryce lab.

Interactions with many people from various labs has also had a strong impact on my doctoral work as well. I would like to, of course, thank Po-Heng, Fatemah, Justin, Carolyn, and Matt for giving me advice and lending me a hand when I was trying to perform different types of reactions. I would also like to thank Matthew Jeletic, Serge Gorelsky, Jennifer Le Roy, Muralee Murugesu, Chantelle Capicciotti, Mathieu Leclere, Robert Ben, Justin Lummiss, Deryn Fogg, Urlike Werner-Zwanziger, Carl Romao, and Mary Anne White for the fruitful collaborations we have had.

All the members of my committee are graciously thanked for reviewing my thesis.

I would lastly like to thank all the members of my family, specifically my parents for supporting me throughout my long studies. Myriam, I always appreciate your upbeat personality and your genuine interest in my research, I will one day visit your classroom.

Marie-Jo, thank you for everything you do for me and for being there whenever I needed you the most; I love you.

Statement of Originality

I certify that the work and research presented in this thesis are from my own efforts and that any references to the works of others are fully acknowledged, either explicitly or by using standard scientific referencing. My supervisor, Dr. David L. Bryce is acknowledged for guidance and support. Dr. Ilia Korobkov is acknowledged for solving the crystal structure of trisodium hydrogen pyrophosphate nonahydrate. Carl P. Romao and Mary Anne White are acknowledged for providing the diffraction data as well as the sample of $ZrMgMo_3O_{12}$. Ulrike Werner-Zwanziger is acknowledged for acquiring a ^{17}O MAS and MQMAS NMR spectrum of $ZrMgMo_3O_{12}$. Dr. Cory M. Widdifield is acknowledged for acquiring the NQR spectra presented in chapter 3.2.

Chapters 2.1 and 2.2 are based on the following publication:

Perras, F. A.; Bryce, D. L. Multinuclear Magnetic Resonance Crystallographic Structure Refinement and Cross-Validation Using Experimental and Computed Electric Field Gradients: Application to $Na_2Al_2B_2O_7$, *J. Phys. Chem. C* **2012**, *116*, 19471-19482.

Chapter 2.3 is based on the following publication:

Perras, F. A.; Korobkov, I.; Bryce, D. L. NMR Crystallography of Sodium Diphosphates: Combining Dipolar, Shielding, Quadrupolar, Diffraction, and Computational information, *CrystEngComm* **2013**, *15*, 8727-8738.

Chapter 3.1 is based on the following publications:

Perras, F. A.; Bryce, D. L. Residual Dipolar Coupling Between Quadrupolar Nuclei Under Magic-Angle Spinning and Double-Rotation Conditions, *J. Magn. Reson.* **2011**, *213*, 82-89.

Perras, F. A.; Bryce, D. L. Measuring Dipolar and J Coupling Between Quadrupolar Nuclei Using Double-Rotation NMR, *J. Chem. Phys.* **2013**, *138*, 174202.

Chapter 3.2 is based on the following publications:

Perras, F. A.; Bryce, D. L. Direct Investigation of Covalently-Bound Chlorines via ^{35}Cl Solid-State NMR and Exact Spectral Line Shape Simulations, *Angew. Chem. Int. Ed.* **2012**, *51*, 4227-4230.

Perras, F. A.; Widdifield, C. M.; Bryce, D. L. QUEST - Quadrupolar Exact Software: a Fast Graphical Program for the Exact Simulation of NMR and NQR Spectra for Quadrupolar Nuclei, *Solid State Nucl. Magn. Reson.* **2012**, *45-46*, 36-44.

Chapter 3.3 is based on the following publications:

Perras, F. A.; Bryce, D. L. Measuring Dipolar and J Coupling Between Quadrupolar Nuclei Using Double-Rotation NMR, *J. Chem. Phys.* **2013**, *138*, 174202.

Perras, F. A.; Bryce, D. L. Theoretical Study of Homonuclear *J* coupling Between Quadrupolar Spins: Single-Crystal, DOR, and *J*-Resolved NMR, *J. Magn. Reson.* **2014**, *242*, 23-32.

Chapter 3.4 is based on the following publications:

Perras, F. A.; Bryce, D. L. Symmetry-Amplified *J* Splittings for Quadrupolar Spin Pairs: A Solid-State NMR Probe of Homoatomic Covalent Bonds, *J. Am. Chem. Soc.* **2013**, *135*, 12596-12599.

Perras, F. A.; Bryce, D. L. Theoretical Study of Homonuclear *J* coupling Between Quadrupolar Spins: Single-Crystal, DOR, and *J*-Resolved NMR, *J. Magn. Reson.* **2014**, *242*, 23-32.

Perras, F. A.; Bryce, D. L. Direct Characterization of Metal-Metal Bonds Between Nuclei with Strong Quadrupolar Interactions vis NMR Spectroscopy, *J. Phys. Chem. Lett.* **2014**, *5*, 4049-4054.

Chapter 3.5 is based on the following publication:

Perras, F. A.; Bryce, D. L. Boron-Boron *J* Coupling Constants are Unique Probes of Electronic Structure: A Solid-State NMR and Molecular Orbital Study, *Chem. Sci.* **2014**, *5*, 2428-2437.

Table of Contents

List of Tables

List of Figures

List of Abbreviations

ADF	Amsterdam Density Functional
AMBASSADOR	angle modification before acquisition to suppress sidebands acquired in DOR
ASG	Alderman Solum and Grant
a.u.	atomic units
B_2cat_2	bis(catecholato)diboron
B_2cat_2·Imes	[bis(catecholato)diboron]·IMes
B_2cat_2·pic	[bis(catecholato)diboron]·picoline
B_2cat_2·pic_2	[bis(catecholato)diboron]·dipicoline
B_2pin_2	bis(pinacolato)diboron
B3LYP	Becke 3-parameter Lee Yang Parr
BcatBr	B-bromocatecholborane
BcatCl	B-chlorocatecholborane
BcatMn	manganese catecholboryl pentacarbonyl
CASTEP	Cambridge Serial Total Energy Package
CMO	canonical molecular orbital
COG	cogwheel phase cycling
COSY	correlation spectroscopy
CP	cross-polarization
CPMG	Carr Purcell Meiboom Gill

CS	chemical shift
CSA	chemical shift anisotropy
CT	central transition
dCMP	deoxycytidine monophosphate
DEPT	distortionless enhancement by polarization transfer
DFS	double frequency sweep
DFT	density functional theory
DOR	double-rotation
DQ	double quantum
DQF	double quantum filter
DSO	diamagnetic spin orbital
dUMP	deoxyuridine monophosphate
EFG	electric field gradient
FC	Fermi contact
FID	free induction decay
FOX	free objects in crystallography
GGA	generalised gradient approximation
GIAO	gauge including atomic orbitals
GIPAW	gauge including projector augmented wave
GUI	graphical user interface
HALA	heavy atom-light atom
HMQC	heteronuclear multiple quantum correlation
HOMO	highest occupied molecular orbital

IGLO	individual gauge for localized orbitals
INADEQUATE	incredible natural abundance double quantum transfer experiment
LB_2pin	pinacolato bis(2-hydroxypropyl)amino diboron
LDA	local density approximation
MAS	magic angle spinning
MO	molecular orbital
MQMAS	multiple quantum magic angle spinning
MS	magnetic shielding
NBO	natural bond orbital
NHC	N-heterocyclic carbene
NLMO	natural localised molecular orbital
NMR	nuclear magnetic resonance
NMRI	nuclear magnetic resonance imaging
NOE	nuclear Overhauser effect
NQR	nuclear quadrupole resonance
PAS	principal axis system
PAW	projector augmented wave
PBE	Perdew Burke Ernzerhof
ppm	parts per million
PSO	paramagnetic spin orbital
PXRD	powder X-ray diffraction
QCPMG	quadrupolar Carr Purcell Meiboom Gill
QUEST	quadrupolar exact software

QZ4P	quadruple-zeta quadruple-polarised
RDC	residual dipolar coupling
rf	radiofrequency
RMSD	root-mean-square deviation
SATRAS	satellite transition spectroscopy
SCF	self-consistent field
SCXRD	single crystal X-ray diffraction
SD	spin dipole
SDDOR	spin diffusion DOR
SIMPSON	a general simulation program for solid-state NMR spectroscopy
SPAM	soft-pulse added mixing
SPINAL	small phase incremental alternation
ST	satellite transition
STMAS	satellite transition magic angle spinning
THF	tetrahydrofuran
THP	tetrahydropyran
TOP	two-dimensional one-pulse
TOSS	total suppression of sidebands
TPSS	Tao Perdew Staroverov Scuseria
TQ	triple quantum
VOCS	variable-offset cumulative spectrum
WURST	wideband uniform rate smooth truncation
XRD	X-ray diffraction

ZCW	Zaremba Conroy Wolfsberg
ZORA	zeroth-order regular approximation

List of Symbols

A	universal scaling constant for spin diffusion
a, b, c	unit cell dimensions
A_2	magnetically equivalent spin pair
$\hat{A}, \hat{B}, \hat{C}, \hat{D}, \hat{E}, \hat{F}$	components of the dipolar coupling Hamiltonian
AA'	chemically equivalent spin pair
AX	non-equivalent spin pair
B_0	magnetic field strength
$\mathbf{B}_0$	magnetic field vector
B_1	radiofrequency magnetic field strength
$B_{i,j}$	asymptotic cross-peak intensity
$b_{n,m}$, $c_{n,m}$	real and imaginary coefficients of the eigenvectors
C_Q	quadrupolar coupling constant
CS-A_2	central-satellite magnetically equivalent spin pair
$\mathbf{D}$	dipolar coupling tensor
$D^l_{m,m'}$	Wigner rotation matrix
$d^l_{m',m}$	reduced Wigner rotation matrix
e	fundamental charge
$\mathbf{E}$	eigenvalue matrix
E	lattice energy
E_{NBO}	natural bond orbital energy

E^{opt}	lattice energy of the lowest energy structure
h	Planck constant
$\mathbf{H}$	general Hamiltonian matrix
$\hat{H}^{(1)}$, $\hat{H}^{(2)}$	first- and second-order perturbation Hamiltonians
$\hat{H}_{D}$	dipolar coupling Hamiltonian
$\hat{H}_{J}$	J coupling Hamiltonian
$\hat{H}_{Q}$	quadrupole Hamiltonian
$\hat{H}_{rf}$	radiofrequency Hamiltonian
$\hat{H}_{Z}$	Zeeman Hamiltonian
$\hat{H}_{Z+Q}$	Zeeman-quadrupolar Hamiltonian
$\hat{H}_{Z+S}$	Zeeman-Shielding Hamiltonian
I	spin quantum number
$\mathbf{I}$ or $\mathbf{S}$	angular momentum
$\hat{I}_x$, $\hat{I}_y$, $\hat{I}_z$, $\hat{I}^2$, $\hat{I}_+$, $\hat{I}_-$	angular momentum operators
J	indirect nuclear spin-spin coupling
$\mathbf{J}$	J coupling tensor
J_{11}, J_{22}, J_{33}	principal components of the J coupling tensor
J_{iso}	isotropic J coupling constant
J_{xx}, J_{yy}, J_{zz}	Cartesian components of the J coupling tensor
$\mathbf{K}$	rate matrix
$k_{i,j}$	rate constant for exchange of magnetization between spins i and j
m	magnetic quantum number
$\mathbf{M}$	bulk magnetization vector

$\lvert m \rangle$	a generic eigenstate
P	matrix of eigenvectors
p	stepping vector
$P_{i,j}$	cross-peak intensity
$P_{i,j}^{norm}$	normalised cross-peak intensity
P_Q	quadrupolar product
p_w	component w of the stepping vector
Q	nuclear electric quadrupole moment
$\langle Q \rangle$	expectation value of an operator, **Q**
r	internuclear distance
$\langle r^{-3} \rangle$	motional average of the inverse cube of the internuclear distance
$R(\alpha, \beta, \gamma)$	rotation matrix
R_{DD}	dipolar coupling constant
R_{eff}	effective dipolar coupling constant
$R^{\lambda}_{l,-m}$, $T^{\lambda}_{l,m'}$	space and spin part of a spherical tensor Hamiltonian
t	time
t_1, t_2	evolution periods in a 2D NMR experiment
T_1, T_2	spin-lattice and spin-spin relaxation time constants
t_{mix}	mixing time
θ, ϕ, ϑ, φ	polar angles
U	a propagator
V	EFG tensor

V_{11}, V_{22}, V_{33}	EFG tensor principal components
$V_{ii}^{(S)calc}$, $V_{ii}^{(S)expt}$	DFT-predicted and experimental EFG tensor components
V_m	EFG spherical tensor component
V_{xx}, V_{yy}, V_{zz}	Cartesian components of the EFG tensor
w	intermediate list of fractional coordinates
$\mathbf{X}$	matrix of eigenvectors of the rate matrix
$\alpha^{(S)}$	scaling factor by which PAW DFT overestimates the EFG tensor components of S
α, β, γ	Euler angles
γ	magnetogyric ratio
$\boldsymbol{\delta}$	chemical shift tensor
δ	chemical shift
δ_{11}, δ_{22}, δ_{33}	chemical shift tensor principal components
$\delta_{\alpha\beta}$	Kronecker delta
δ_{DOR}	DOR shift
ΔE	lattice energy difference from the ground state energy
δ_{iso}	isotropic chemical shift
ΔJ	anisotropy of the J coupling tensor
δ_{QIS}	second-order quadrupolar-induced shift
Δ_{rel}	relative difference in fractional coordinates
δ_{xx}, δ_{yy}, δ_{zz}	Cartesian components of the chemical shift tensor
$\Delta\delta$	difference in chemical shifts

$\Delta\Delta\nu_Q$	difference in quadrupolar splittings
$\Delta\nu^{CT}$	breadth of the central-transition powder pattern
$\Delta\nu_Q$	first-order quadrupolar splitting
ε	small increment of a fractional coordinate
ε_0, $^1\varepsilon_n$	ground state and excited state energies
η	quadrupolar asymmetry parameter
η_J	asymmetry of the *J* coupling tensor
θ_R	rotation angle
κ	skew of the chemical shift tensor
λ	scaling factor for the lattice energy in the calculation of the cost function
$\mathbf{\Lambda}$	matrix of eigenvalues of the rate matrix
$\boldsymbol{\mu}$	magnetic moment
μ_0	permeability constant
ν_0	Larmor frequency
ν_Q	quadrupolar frequency
$\nu^{S(2)}_{DD}$	second-order quadrupolar-dipolar cross-term shift
ν^{S}_{DD}	dipolar splitting
$\boldsymbol{\rho}$	density matrix
σ	magnetic shielding constant
$\boldsymbol{\sigma}$	magnetic shielding tensor
ς	step length in least-squares refinement
$\sigma^{(S)}$	uncertainty in the predicted EFG tensor components of S

σ_{11}, σ_{22}, σ_{33}	magnetic shielding tensor principal components
σ_{d}	diamagnetic magnetic shielding constant
σ_{p}	paramagnetic magnetic shielding constant
σ_{ref}	magnetic shielding constant of a reference compound
σ_{xx}, σ_{yy}, σ_{zz}	Cartesian components of the magnetic shielding tensor
$\sigma_{X\text{-}Y}$	A σ bond between the atoms X and Y
χ^2	cost function
χ^2 (δ_{iso}), χ^2 (CSA)	cross-validated, chemical shift and CSA-based, cost functions
χ^2(EFG), χ^2(energy)	EFG and DFT-computed lattice energy contributions to the cost function
Ω	chemical shift tensor span
ω_R	angular spinning frequency

Part I: Introduction and Objectives

Chapter 1.1: A General Introduction to Nuclear Magnetic Resonance

Nuclear magnetic resonance (NMR) spectroscopy had a humble beginning in the study of the structure of atomic nuclei. Like the electron, it was known that atomic nuclei also possessed spin and that a nuclear magnetic absorption signal could be detected due to the splitting of the different magnetic energy levels in the presence of a large applied magnetic field, known as the Zeeman effect.[1] This absorption signal was first detected by Rabi using a molecular beam of LiCl[2] and, after much hard work by Gorter,[3] the NMR phenomenon was eventually discovered independently by Purcell, Torrey, and Pound[4] as well as by Bloch, Hansen, and Packard.[5] At the time, the new spectroscopic technique was purely of interest to fundamental physicists; the only use which was proposed for the new method was for the standardisation of magnetic fields and the measurement of nuclear magnetic moments.

The discovery of the chemical shift, in NH_4NO_3,[6] and later the discovery of the *J* coupling interaction, in $NaSbF_6$,[7] demonstrated the rich structural information that could be obtained with the method. Discovering that the resonance frequencies were affected by the structure of the molecules disappointed physicists, who couldn't use the technique to measure accurate magnetic moments, but sparked interest amongst chemists which are largely responsible for the development of modern NMR spectroscopy.

Today, NMR spectroscopy has become an integral part of any academic, government, or industrial chemistry research centre. NMR spectroscopy is routinely used to solve the structures of small organic molecules for which a vast array of powerful NMR experiments, such as DEPT,[8] COSY,[9] HMQC,[10] and INADEQUATE[11] have been developed. With the advent of ever more powerful magnetic fields, NMR spectroscopy has also been expanded to solving the complex 3D structures of large macromolecules such as proteins[12-14] and RNA.[15] NMR spectroscopy has also been expanded for medical imaging purposes[16-18] (i.e., nuclear magnetic resonance imaging (NMRI)). The letter 'N' from NMRI was, however, soon dropped since the word 'nuclear' may cause anxiety for some patients.

NMR spectroscopy of solid samples is largely less developed than that of liquid samples due to the presence of anisotropic broadening that is not averaged in a powdered sample.[19] The presence of this broadening is both a blessing and a curse since it makes it possible to access a wealth of chemical information that is inaccessible in solution, but at the expense of spectral resolution. Although molecular species such as organic molecules are better studied in solution, some samples, such as large proteins,[20] glasses,[21] heterogeneous catalysts,[22] pharmaceuticals,[23] and porous materials,[24] may only be studied in solid forms. Since NMR spectroscopy does not require any long range periodicity, it can also be applied to powdered or amorphous samples for which diffraction experiments cannot yield atomic-level structural information.[25] Solid-state NMR also has a distinct advantage over liquid-state NMR for studying quadrupolar nuclei (nuclei with spin $I > 1/2$), which correspond to 3/4 of the NMR-active nuclei in the periodic table, due to the slower nuclear-spin relaxation in the solid state, which often broadens the NMR lines beyond detection in the liquid state.[26]

In this first chapter, the main principles of NMR spectroscopy will be introduced. The quantum mechanical description of NMR spectroscopy will also be discussed and the theory and experiments used for solid-state NMR spectroscopy will be presented. For much of the work discussed in this thesis, density functional theory (DFT) calculations were used to complement the results obtained using NMR spectroscopy. The DFT methods of relevance to this thesis are also introduced in this chapter.

1.1.1 The Zeeman Interaction

The nucleus at the heart of the atom is composed of protons, which possess a positive charge, and neutrons, that do not possess a charge; both particles have a spin quantum number of 1/2. Nuclides with an odd number of either neutrons, protons, or both possess a non-zero nuclear spin quantum number and magnetic moment; these are known as NMR-active nuclei. Nuclides with an odd number of protons or neutrons have a half-integer spin quantum number and those with an odd number of protons and neutrons have an integer spin quantum number.[27]

Nuclei with a non-zero spin have an intrinsic angular momentum (**I**) that is rigidly tied to the magnetic moment (**μ**) of the nucleus. A given nucleus with a spin quantum number of I has $2I + 1$ energy levels with magnetic quantum numbers (m) ranging from I to $-I$. These quantum states are normally degenerate; however, the degeneracy of the states is lifted in the presence of an applied external magnetic field; this is known as the Zeeman interaction.[28] This interaction is described by the Zeeman Hamiltonian ($\hat{H}_Z$) below and is depicted in Figure 1.1.[29]

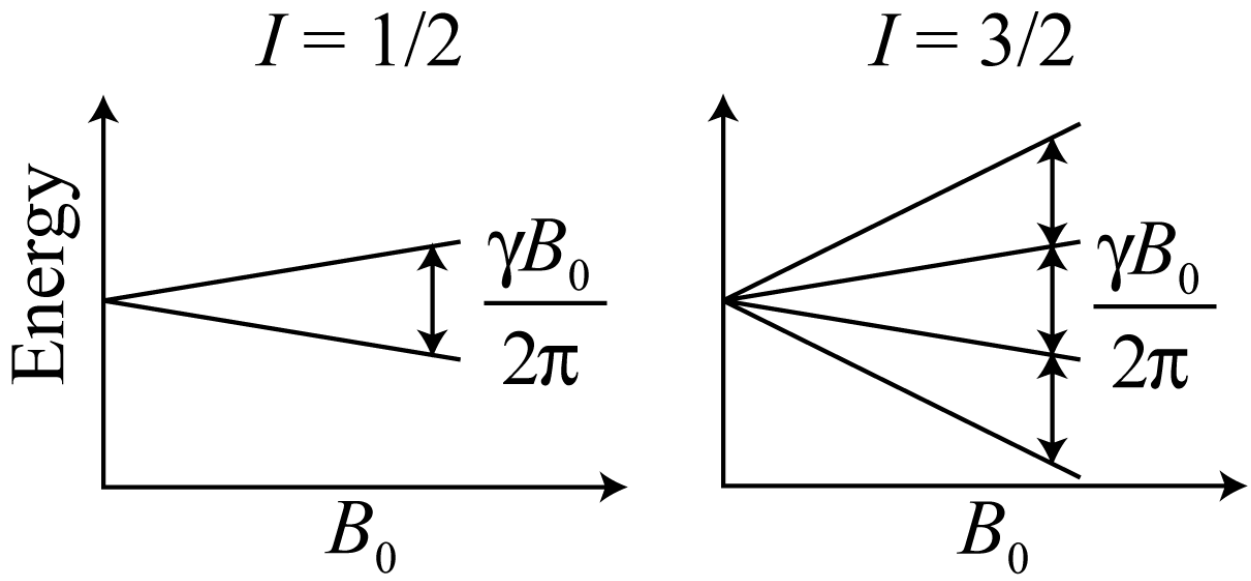

Figure 1.1. Depiction of the Zeeman splitting for hypothetical spin-1/2 and spin-3/2 nuclei with identical magnetogyric ratios. Note that in the presence of a non-zero quadrupolar interaction, the Zeeman energy levels for the spin-3/2 nucleus are not degenerate in the absence of a magnetic field.

(1.1) $\hat{H}_Z = \frac{\gamma B_0}{2\pi}\hat{I}_z$

In the above expression B_0 is the strength of the applied magnetic field, γ is the magnetogyric ratio of the nucleus (γ = **μ**/**I**), and $\hat{I}_z$ is an angular momentum operator which simply returns the value of m when operating on a spin wave function. The properties of the most common spin angular momentum operators are listed below. The Dirac bra-ket notation will be used throughout this thesis.[19]

(1.3) $\hat{I}_z|m\rangle = m|m\rangle$

(1.4) $\hat{I}^2|m\rangle = I(I+1)|m\rangle$

(1.5) $\hat{I}_+ |m\rangle = (\hat{I}_x + i\hat{I}_y)|m\rangle = \sqrt{I(I+1) - m(m+1)}\,|m+1\rangle$

(1.6) $\hat{I}_- |m\rangle = (\hat{I}_x - i\hat{I}_y)|m\rangle = \sqrt{I(I+1) - m(m-1)}\,|m-1\rangle$

The size of the splitting between the Zeeman energy levels is known as the Larmor frequency (ν_0).[27]

(1.7) $\nu_0 = \frac{\gamma B_0}{2\pi}$

NMR spectroscopy involves the excitation and detection of transitions between the various energy levels that are separated by the Zeeman splitting and resonate at the Larmor frequency. This interaction is very weak and appears in the radio frequency (rf) part of the electromagnetic spectrum. Nuclei with a spin quantum number of 0, such as ^{12}C, ^{16}O, and ^{32}S, do not couple with applied magnetic fields and are thus NMR-silent.

1.1.2 Pulsed NMR Spectroscopy

When atomic nuclei are exposed to an applied magnetic field they begin to precess at the Larmor frequency since the force to align the spins with the field is countered by the angular momentum of the nucleus. This is analogous to the precessional motion of a gyroscope, for which there is macroscopic angular momentum as opposed to spin. The sense of the precession is dependent on the sign of $\boldsymbol{\mu}$ and is depicted in Figure 1.2.[27]

The fluctuations in the local magnetic field of the nucleus perturb its precession and eventually leads to the alignment of the spin polarization axis of the nuclei with the applied magnetic field. This is known as spin-lattice relaxation and the rate at which thermal equilibrium is reached is characterized by the relaxation time constant T_1. The nuclei with a

positive product of μ and m will have their spin polarization axes aligned parallel with $\mathbf{B}_0$ whereas those with a negative product of μ and m will have spin polarization axes aligned antiparallel with the magnetic field.

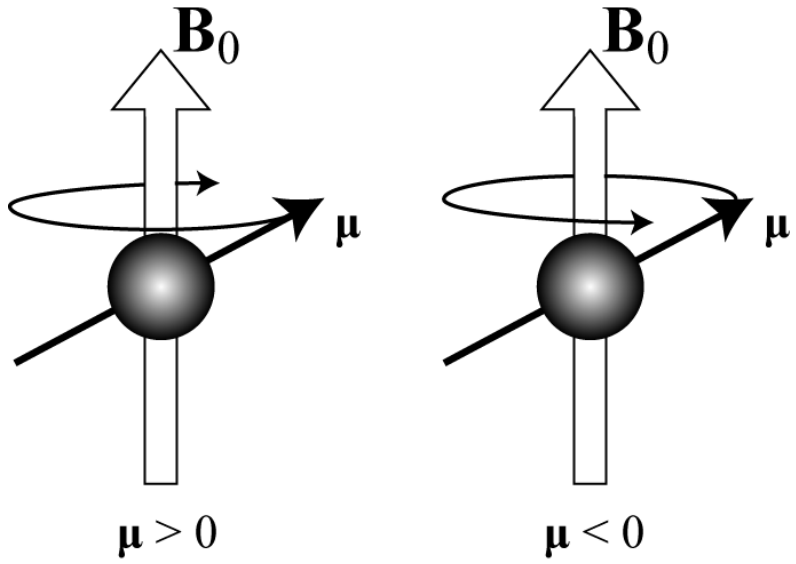

Figure 1.2. Directions of the precession of nuclear spins in the presence of a large applied magnetic field ($\mathbf{B}_0$).

The minute excess of nuclei in the lower energy level will lead to the formation of a bulk magnetization (**M**) which is aligned with $\mathbf{B}_0$; only this excess population of the lower energy level(s) can be detected using NMR spectroscopy. If we consider a set of one million ^{1}H nuclei (I = 1/2) in a magnetic field of 9.4 T, such that their Larmor frequency is of 400 MHz, at room temperature, the lower energy level will only contain 32 more spins than the other energy level (see equation 1.8). In principle, only these 32 out of one million ^{1}H nuclei are detectable using NMR.

$$(1.8)\quad \frac{P(1/2)}{P(-1/2)} = \exp\left(\frac{E(-1/2) - E(1/2)}{kT}\right) = \exp\left(\frac{400\text{MHz}}{2.0836618\text{x}10^{10}\,\text{Hz/K}\cdot 298\text{K}}\right) = 1.000064421$$

This bulk magnetization also precesses about the large applied magnetic field at the Larmor frequency. It is then useful to introduce a rotating frame of reference that precesses about $\mathbf{B}_0$ at the Larmor frequency.[19] In this rotating frame of reference, the effects of the large Zeeman interaction are completely removed and thus the theoretical description only needs to focus on the smaller perturbations to the Zeeman interaction. The Hamiltonian describing the system is then simplified from $\hat{H} = \hat{H}_Z + \hat{H}^{(1)}$, where $\hat{H}^{(1)}$ corresponds to a small perturbation, to $\hat{H} = \hat{H}^{(1)}$; this is pictorially represented in Figure 1.3. All further discussions in this thesis will assume a rotating frame of reference.

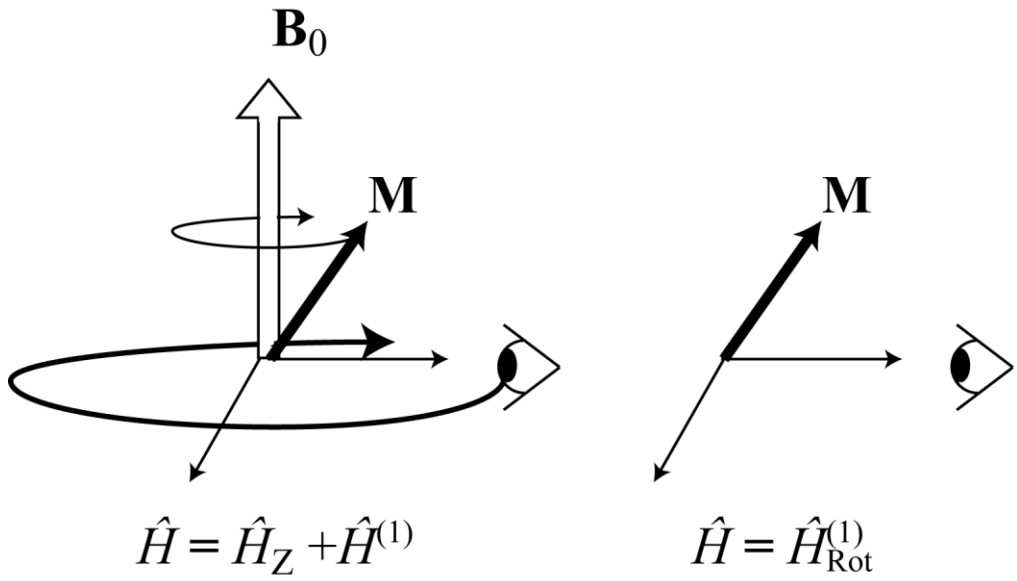

Figure 1.3. Depiction of the rotating frame of reference: on the left the bulk magnetization is shown precessing about $\mathbf{B}_0$ at the Larmor frequency and on the right the observer is also rotating at the Larmor frequency. In this frame of reference **M** is no longer precessing and the effects of $\hat{H}_Z$ are removed.

The magnetization may be manipulated by the use of rf pulses which resonate at the Larmor frequency. The interaction of **M** with the rf pulses is described by the rf Hamiltonian ($\hat{H}_{rf}$).[30]

$$\hat{H}_{rf}(t) = \frac{-\gamma B_1}{2\pi}\left[M_x \cos(\omega_{rf} t - \phi) - M_y \sin(\omega_{rf} t - \phi)\right] \quad (1.9)$$

In the above expression B_1 corresponds to the strength of the magnetic field component of the rf pulse, M_x and M_y are the components of the magnetization along x and y, respectively, ω_{rf} is the offset of the rf pulse from the resonance, and ϕ is the phase of the pulse.

The impact of the rf pulse is to momentarily introduce an oscillating magnetic field ($\mathbf{B}_1$) that can be decomposed into components that rotate about $\mathbf{B}_0$ at the Larmor frequency. In the rotating frame of reference, this is seen as a small static magnetic field in the transverse plane with a phase of ϕ. In the rotating frame of reference, **M** then precesses about $\mathbf{B}_1$ until the pulse is turned off, as depicted in Figure 1.4.

A basic pulsed NMR experiment uses a single 90° pulse, meaning that the magnetization vector is rotated by 90° such that it is left in the transverse plane, perpendicular to the magnetic field. In this plane, the magnetization will precess at the Larmor frequency and this precession can be detected by the induction it creates in a coil oriented perpendicularly with respect to the magnetic field. This signal is known as the free induction decay (FID). A Fourier transform of the cosine-modulated FID can then be performed to obtain the NMR spectrum.[31] Several more complex pulse sequences can be performed in order to extract additional information or increase the sensitivity of the experiment, some of these shall be discussed later in the text.

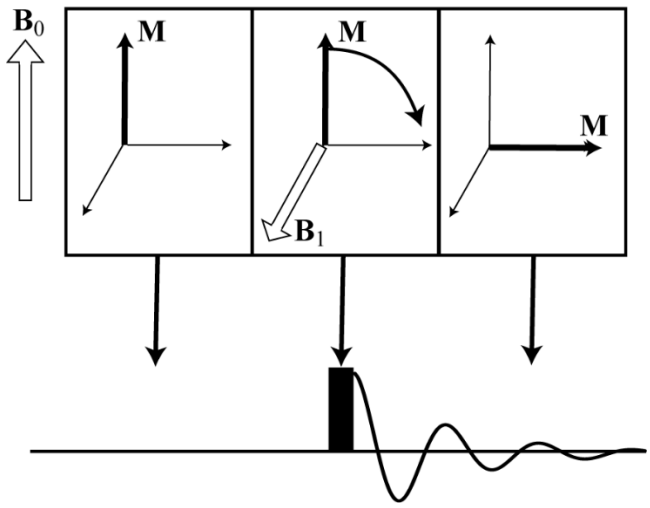

Figure 1.4. Depiction of the effect of an rf pulse on the bulk magnetization of a sample. On the top, a vector diagram shows the bulk magnetization vector at different time points of the pulse sequence. Prior to the application of a rf pulse, the magnetization is aligned with the magnetic field. A rf pulse then rotates the bulk magnetization onto the transverse plane and is then turned off to allow the free precession of the magnetization.

1.1.3 NMR Interactions

The main NMR interaction, the Zeeman interaction, *vide supra*, only depends on the physical properties of the nucleus and the applied magnetic field and does not discriminate between nuclei in different chemical environments. Luckily, the other atomic nuclei and electrons in a molecule or material also interact with the nuclei, albeit much more weakly. The internal NMR interactions affect the Zeeman energy levels, and thus the resonance frequency, making it possible to discriminate between different NMR signals and gain insight into the chemical structure of a material.[6]

1.1.3.1 Magnetic Shielding

The electrons in a molecule respond to the application of a magnetic field and can partially shield a nucleus from the magnetic field. The Zeeman Hamiltonian, when the effects of magnetic shielding (MS) are taken into consideration, can be rewritten as follows:[27]

$$\hat{H}_{Z+S} = (1-\sigma)\frac{\gamma B_0}{2\pi}\hat{I}_z \quad (1.10)$$

where σ is the magnetic shielding constant which is, in principle, different for every chemically distinct nucleus in a sample. σ can be either negative or positive and thus the magnetic field can be either reduced or amplified at the nuclear site, depending on its chemical environment. According to Ramsey's theory for nuclear shielding,[32] there are two mechanisms that are responsible for the MS of a nuclear site, the diamagnetic shielding (σ_d) and paramagnetic shielding (σ_p) mechanisms. Diamagnetic shielding involves the shielding of nuclei by the electrons in the ground state wave function and is usually smaller than the paramagnetic shielding, with the exception of some of the lightest elements. The following expression describes the diamagnetic shielding.

$$\sigma_d^{\alpha\beta} = \left(\frac{\mu_0}{4\pi}\right)\left(\frac{e^2}{2m}\right)\langle 0|\sum_k \frac{r^2\delta_{\alpha\beta} - r_{k\alpha}r_{k\beta}}{r_k^3}|0\rangle \quad (1.11)$$

In this expression $\langle 0|$ represents the ground state wave function, k is an index for an electron, r is the distance between the electron and the nucleus, α and β are indices representing a Cartesian direction, and $\delta_{\alpha\beta}$ is the Kronecker delta.

Since there is a dependence on α and β, it can be seen that MS is in fact anisotropic. The electron distribution along a Cartesian axis α is different than it is along β and thus, unless there is some sort of symmetry, the MS will also be different along α and β.

The paramagnetic shielding is usually the dominant shielding mechanism and involves the promotion of electrons from the ground state electronic wave function ($\langle 0|$) into an excited state wave function ($\langle n|$).

$$(1.12)\quad \sigma_{\mathrm{p}}^{\alpha\beta} = -\left(\frac{\mu_0}{4\pi}\right)\left(\frac{e^2}{2m^2}\right)\sum_{\mathrm{n}\neq 0}\left[\frac{\langle 0|\sum_{\mathrm{k}} \mathrm{r}_{\mathrm{k}}^{-3}\hat{l}_{\mathrm{k}\alpha}|n\rangle\langle n|\sum_{\mathrm{k}}\hat{l}_{\mathrm{k}\beta}|0\rangle + \langle 0|\sum_{\mathrm{k}}\hat{l}_{\mathrm{k}\beta}|n\rangle\langle n|\sum_{\mathrm{k}}\mathrm{r}_{\mathrm{k}}^{-3}\hat{l}_{\mathrm{k}\alpha}|0\rangle}{{}^1\varepsilon_n - \varepsilon_0}\right]$$

The operators $\hat{l}_{\mathrm{ki}}$ are angular momentum operators that effectively rotate a ground state atomic orbital that can then overlap with an unoccupied orbital.[33,34] This rotation increases the magnitude of the magnetic field in the direction of the rotation and 'deshields' the nucleus. For this mechanism to be significant, the difference in energy between the ground state (ε_0) and excited state ($^1\varepsilon_{\mathrm{n}}$) wave functions needs to be small.

The orientation dependence of the MS interaction, as seen in equations 1.11 and 1.12, is not evident in the Hamiltonian written in equation 1.10. The Zeeman-shielding Hamiltonian can then be rewritten as:[30]

$$(1.13)\quad \hat{H}_{Z+S} = \frac{\gamma}{2\pi}\mathbf{I}\cdot(\mathbf{1}-\boldsymbol{\sigma})\cdot\mathbf{B}_0 = \frac{\gamma}{2\pi}\left(\hat{I}_{\mathrm{x}},\hat{I}_{\mathrm{y}},\hat{I}_{\mathrm{z}}\right)\begin{pmatrix} 1-\sigma_{\mathrm{xx}} & \sigma_{\mathrm{xy}} & \sigma_{\mathrm{xz}} \\ \sigma_{\mathrm{yx}} & 1-\sigma_{\mathrm{yy}} & \sigma_{\mathrm{yz}} \\ \sigma_{\mathrm{zx}} & \sigma_{\mathrm{zy}} & 1-\sigma_{\mathrm{zz}} \end{pmatrix}\begin{pmatrix} 0 \\ 0 \\ B_0 \end{pmatrix}$$

where **σ** is a second rank tensor representing the shielding interaction. **σ** can have up to nine independent components; however, this number can be reduced to six if the antisymmetric part, which doesn't affect the NMR spectrum, is ignored.[35] This simplification is also known as the secular approximation, or the first-order perturbation, since only the terms that commute with the larger Zeeman interaction are maintained. The secular Zeeman-shielding Hamiltonian is the following:

$$\hat{H}_{Z+S}^{(1)} = (1-\sigma_{zz})\frac{\gamma B_0}{2\pi}\hat{I}_z \quad (1.14)$$

where σ_{zz} is the shielding along the direction of the applied magnetic field and is typically calculated as follows:[36]

$$\sigma_{zz} = \sigma_{11}\sin\theta\cos\phi + \sigma_{22}\sin\theta\sin\phi + \sigma_{33}\cos^2\theta \quad (1.15)$$

where σ_{ii} are the principal components (eigenvalues) of the magnetic shielding tensor and ϕ and θ are the polar angles that define the orientation of the MS tensor in the Cartesian coordinate system. The principal components of the MS tensor are ordered as: $\sigma_{33} \geq \sigma_{22} \geq \sigma_{11}$.

MS cannot, unfortunately, be measured directly. Instead we can only measure the shielding of a substance with respect to reference compound, this is known as the chemical shift (CS, δ) and is defined as follows.[19]

$$\delta_{ii} = \frac{\sigma_{ref} - \sigma_{ii}}{1-\sigma_{ref}} \quad (1.16)$$

In equation 1.16, σ_{ref} is the shielding constant of a reference sample, for example tetramethylsilane is used for ^{1}H, ^{13}C, and ^{29}Si NMR, σ_{ii} is a MS tensor component and δ_{ii} is the corresponding CS tensor component. The CS, as well as MS, are expressed in units of parts per million (ppm). The CS of a primary reference is set to 0 ppm.

The CS is importantly used to solve molecular structures since it is extremely sensitive to the chemical environment. Signals from different functional groups in a molecule appear in different CS ranges and the effects of varying groups are largely additive.

In solution, the rapid isotropic tumbling of the molecules averages the anisotropy of the chemical shift interaction such that only the isotropic part of **δ** can be measured, the isotropic chemical shift (δ_{iso}).

(1.17) $$\delta_{iso} = (\delta_{11} + \delta_{22} + \delta_{33})/3$$

In solids, however, molecular tumbling is highly restricted and molecules can usually be approximated as being immobile. The anisotropic interactions then aren't averaged and the spectral resonance appears at δ_{zz} as opposed to δ_{iso}. Typically, experiments are also performed on powdered samples as opposed to single crystals; very large crystals are necessary for NMR experiments due to the low sensitivity of the technique (see equation 1.8). Powders are composed of a large number of small crystallites whose θ and ϕ angles relating the orientation of the CS tensor to the magnetic field are different. It is then necessary to perform what is known as a powder average and sum over the chemical shifts of all possible crystallite orientations and scale the intensity by the probability of finding a crystallite with that orientation.[37] The NMR spectrum for a powdered sample is then given by:

(1.18) $Spectrum = \int_0^{2\pi} \int_0^{\pi} \delta_{zz}(\theta,\phi) \sin\theta d\phi d\theta$

where the intensity of a given orientation in the sum is scaled by sinθ in order to take into consideration the fact that orientations with θ near 90° are more probable than those at 0°; this is illustrated in Figure 1.5.

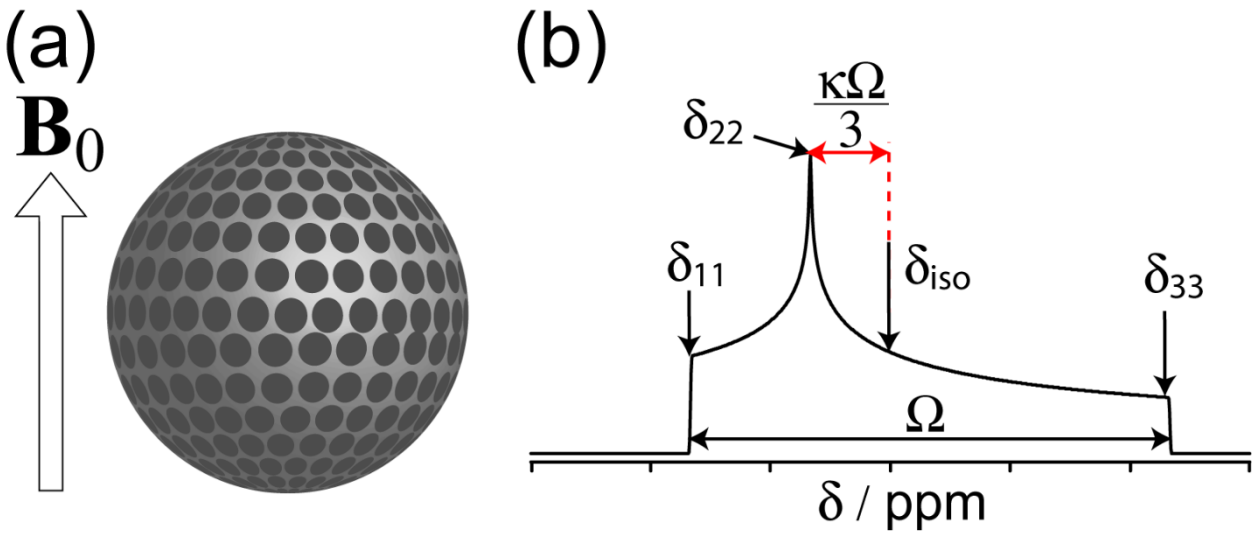

Figure 1.5. (a) The probability of finding δ_{33} at different orientations is depicted; more circles can be lined along the equator than at the poles and thus a polar angle θ of 90° is more probable than 0°. (b) Powder pattern broadened by chemical shift anisotropy. Arrows are used to indicate the critical points of the powder pattern and illustrate the δ_{iso}, Ω, and κ parameters.

The NMR spectrum is a broad line shape, as opposed to a single resonance, that has some fine features which can be fit to determine the principal components of the CS tensor (see Figure 1.5). δ_{iso} can however be easily determined using magic angle spinning (MAS) experiments, *vide infra*, and thus it is useful to define the δ_{iso}, the span (Ω), and the skew (κ)

of the CS tensor instead of using the eigenvalues exclusively.[38] The Ω is used to quantify the breadth of the powder pattern:

(1.19) $\Omega = \sigma_{33} - \sigma_{11} \approx \delta_{11} - \delta_{33}$

and κ is used to characterise the asymmetry of the CS tensor.

(1.20) $\kappa = \frac{3(\sigma_{iso} - \sigma_{22})}{\Omega} \approx \frac{3(\delta_{22} - \delta_{iso})}{\Omega}$

A κ of 1 or -1 represents CS tensors that are axially symmetric; however, the equivalent tensor element differ depending on the sign of κ. Axial symmetry requires that the atom in question possesses a rotation symmetry axis of order three or higher.[39]

1.1.3.2 Quadrupolar Interaction

Nuclei with a spin quantum number greater than 1/2 are quadrupolar. These nuclei have an asymmetric charge distribution and thus an electric quadrupole moment (Q).[26] A positive Q indicates that the nucleus is prolate whereas Q is negative when the nucleus is oblate. The Q can also couple with the electric field gradient (EFG) that is generated by the electrons and the nuclei in a molecule. Unlike the Zeeman interaction, which is a magnetic interaction, the quadrupolar interaction is an electrostatic interaction and can be quite strong. Additionally, since the Q is aligned with **I**, the quadrupolar interaction affects the Zeeman energy levels, and thus, the NMR spectrum. The Hamiltonian describing this interaction can be written as follows.[40]

(1.21) $\hat{H}_{\mathrm{Q}} = \frac{eQ}{6I(2I-1)} \mathbf{I} \cdot \mathbf{V} \cdot \mathbf{I} = \frac{eQ}{6I(2I-1)} \left(\hat{I}_{\mathrm{x}}, \hat{I}_{\mathrm{y}}, \hat{I}_{\mathrm{z}}\right) \begin{pmatrix} V_{\mathrm{xx}} & V_{\mathrm{xy}} & V_{\mathrm{xz}} \\ V_{\mathrm{yx}} & V_{\mathrm{yy}} & V_{\mathrm{yz}} \\ V_{\mathrm{zx}} & V_{\mathrm{zy}} & V_{\mathrm{zz}} \end{pmatrix} \begin{pmatrix} \hat{I}_{\mathrm{x}} \\ \hat{I}_{\mathrm{y}} \\ \hat{I}_{\mathrm{z}} \end{pmatrix}$

In the preceding expression, **V** is the EFG tensor which, like **σ**, is a second-rank tensor, however **V** is symmetric and traceless and can thus only have a maximum of five independent elements. **V** can be easily calculated using the charge distribution of the electrons and the nuclei as follows.[41]

$$(1.22)\quad V_{\alpha\beta} = \sum \frac{ne(3\alpha\beta - \delta_{\alpha\beta} r^2)}{r^5}$$

In equation 1.22 r represents the distance between a charged particle and the nucleus, α and β are Cartesian indices, $\delta_{\alpha\beta}$ is the Kronecker delta and n is the charge of the particle generating the EFG.

Like the MS (or CS) tensor, the EFG tensor is typically diagonalised and parameterised using its eigenvalues which are ordered as $V_{33} \geq V_{22} \geq V_{11}$. However, since the EFG tensor is traceless, according to the Laplace equation:

$$(1.23)\quad V_{11} + V_{22} + V_{33} = 0$$

only two parameters are necessary to characterize the magnitude and asymmetry of the EFG tensor: the quadrupolar coupling constant (C_Q) and the asymmetry parameter (η).

$$(1.24)\quad C_Q = \frac{eQV_{33}}{h}$$

$$(1.25)\quad \eta = \frac{V_{11} - V_{22}}{V_{33}}$$

The asymmetry parameter can take values ranging from 0 to 1 where a η of zero represents an axially symmetric EFG tensor.

The secular part (or first-order perturbation) of $\hat{H}_Q$ can be written as follows:[42]

$$\hat{H}_Q^{(1)} = \frac{C_Q\left(3\hat{I}_z^2 - \hat{I}^2\right)}{8I(2I-1)}\left[(3\cos\theta - 1) + \eta\sin^2\theta\cos 2\phi\right] \quad (1.26)$$

Since the $\hat{I}_z$ operator, which returns the value of the quantum number m (see equation 1.3), is squared, the first order quadrupolar perturbation of the 1/2 and -1/2 states is equal. Of the allowed single quantum transitions (selection rule of $\Delta m = \pm 1$), the m = 1/2 to -1/2 transition is unaffected by the quadrupolar interaction to first order. This transition, known as the central transition (CT), is then much sharper than the other single quantum transitions, which are known as the satellite transitions (ST). This is depicted in Figure 1.6. The CT may also be manipulated independently when using low-power rf pulses if the pulse durations are scaled by $1/(I + 1/2)$; these are known as CT-selective pulses.[43]

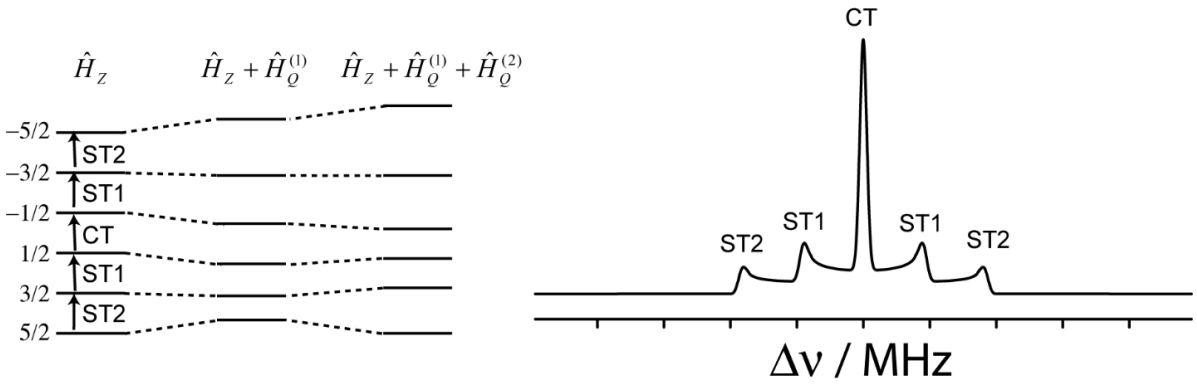

Figure 1.6. (left) Energy level diagram for a spin-5/2 nucleus in a magnetic field, the various single-quantum transitions are outlined. The effect of the inclusion of the first and second-order quadrupolar interaction are shown. On the right the NMR spectrum for a spin-5/2 nucleus is shown where a sharp CT resonance is flanked by the four quadrupole-broadened STs.

Since the quadrupolar interaction is often very strong, the first-order approximation is usually insufficient and a second-order perturbation needs to be evaluated. Recently it was demonstrated experimentally that higher perturbation orders are necessary to accurately reproduce the NMR spectra of some quadrupolar nuclei.[44,45] Unlike the first-order quadrupolar Hamiltonian, the second-order quadrupolar Hamiltonian does affect the central transition of a quadrupolar nucleus which is then broadened by the quadrupolar interaction. The STs are broadened to first-order and thus have a breadth that increases linearly with C_Q whereas the breadth of the CT ($\Delta\nu^{CT}$) depends on the square of C_Q and depends inversely on ν_0 (see equation 1.27).

$$\Delta\nu^{CT} = \frac{C_Q^2(25+22\eta+\eta^2)(I(I+1)-3/4)}{9\nu_0(2I(2I-1))^2} \quad (1.27)$$

There is then a significant advantage in using the highest possible magnetic fields when performing NMR experiments on half-integer quadrupolar nuclei since the breadth of the CT will be reduced.[46]

The effect of the asymmetry parameter is to change the appearance of the line shape. Theoretical CT and ST line shapes are shown in Figure 1.7 as a function of the value of η.

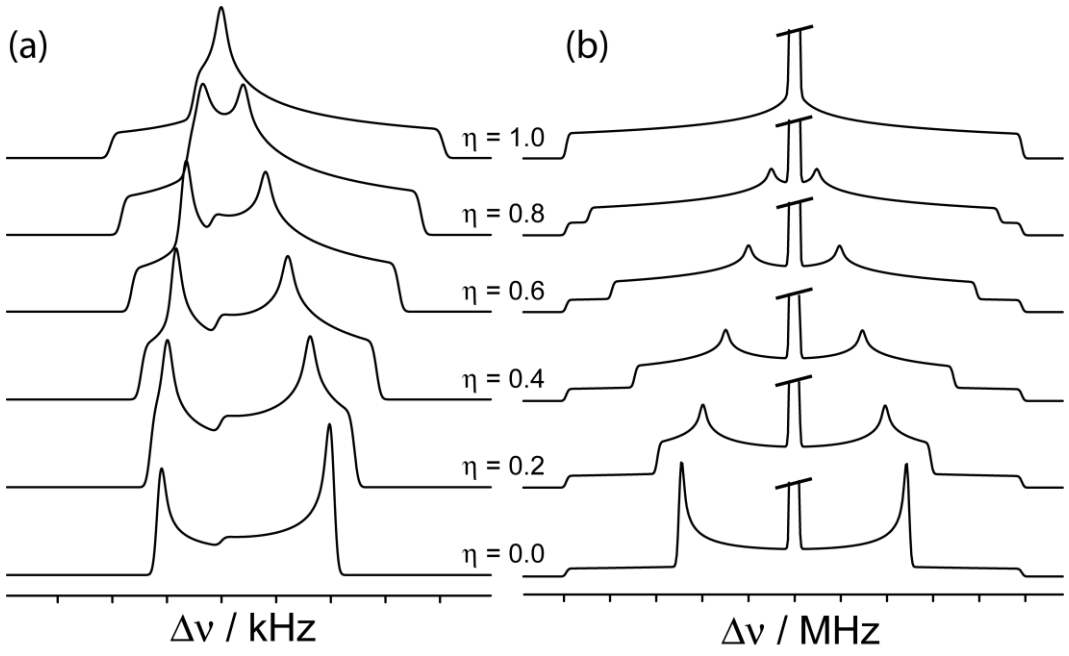

Figure 1.7. Theoretical CT line shapes (a) as well as the corresponding ST line shapes (b) of a spin-3/2 nucleus as a function of the value of η.

Of course, the chemical shift anisotropy can also have a significant impact on the line shape. In this case, the contributions from the second-order quadrupolar interaction only need to be summed with the contribution from equation 1.15. The polar angles (θ and ϕ) are however, in principle, different for the CS and EFG tensors, unless molecular symmetry forces them to share the same principal axis frames.[47,48] The orientation of the CS tensor is then related to that of the EFG tensor by a series of rotations about the z, y, and z axes by angles of α, β, and γ, respectively; these are known as the Euler angles. The angles α and γ can take values ranging from 0 to 360° whereas β can range from 0 to 180°. The definition of these angles is shown pictorially in Figure 1.8.

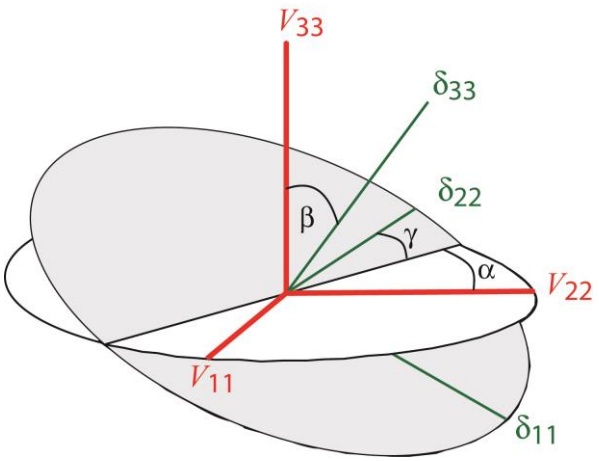

Figure 1.8. Definition of the Euler angles relating the orientation of the CS tensor with respect to the EFG tensor.

1.1.3.3 Spin-Spin Coupling

Nuclei can magnetically couple with each other, much like the coupling with an applied magnetic field caused by the Zeeman interaction. There are two spin-spin coupling interactions, the direct dipolar interaction and the indirect nuclear spin-spin coupling (*J*) interaction. Dipolar coupling involves the coupling of the magnetic dipoles directly through space. This interaction depends only on the motionally averaged inverse cube of the internuclear distance between the spins and thus measuring dipolar coupling can be used to obtain strong distance restraints.[49-51] The dipolar coupling Hamiltonian, in its principal axis frame (the internuclear vector), is written as follows.[52]

$$\hat{H}_{\mathrm{D}} = -R_{\mathrm{DD}}(\mathbf{S}\cdot\mathbf{D}\cdot\mathbf{I}) = -R_{\mathrm{DD}}\left(\hat{S}_{\mathrm{x}},\hat{S}_{\mathrm{y}},\hat{S}_{\mathrm{z}}\right)\begin{pmatrix}-1 & 0 & 0\\ 0 & -1 & 0\\ 0 & 0 & 2\end{pmatrix}\begin{pmatrix}\hat{I}_{\mathrm{x}}\\ \hat{I}_{\mathrm{y}}\\ \hat{I}_{\mathrm{z}}\end{pmatrix} \quad (1.28)$$

In equation 1.28 R_{DD} is the dipolar coupling constant and *S* and *I* are the two coupled nuclei. R_{DD} is defined as:

$$(1.29)\quad R_{DD} = \left(\frac{\mu_0}{4\pi}\right)\left(\frac{\gamma_S \gamma_I}{2\pi}\right)\left\langle r_{S,I}^{-3}\right\rangle$$

where γ_S and γ_I are the magnetogyric ratios of nuclei *S* and *I* and $r_{S,I}$ is the internuclear distance between *S* and *I*. The secular part of $\hat{H}_D$ is the following, assuming a heteronuclear spin pair.

$$(1.30)\quad \hat{H}_D^{(1)} = -R_{DD}(3\cos^2\theta - 1)\hat{S}_Z\hat{I}_Z$$

The $3\cos^2\theta$-1 dependence in equation 1.30, where θ is the angle between the magnetic field and the internuclear vector, averages to zero in the isotropic motions of a liquid and thus the dipolar coupling information is inaccessible in solution. In the solid state, however, dipolar coupling leads to the formation of the Pake doublet (see Figure 1.9).[53]

J coupling involves the coupling of two nuclei through the electrons and is particularly large when a covalent interaction connects the atoms. There are four mechanisms responsible for *J* coupling: the diamagnetic spin-orbital (DSO), paramagnetic spin-orbital (PSO), spin dipole (SD), and Fermi contact (FC) mechanisms. DSO and PSO are analogous to the diamagnetic and paramagnetic shielding and involve the coupling of two nuclei through the orbital angular momentum of the electrons. SD involves the direct dipolar interaction of a nucleus with an electron and FC involves the interaction of the nuclei with an electron situated on the nuclei.[54] Only orbitals with orbital angular momentum can contribute to DSO and PSO and only orbitals with a significant *s*-character can contribute to FC since only those orbitals have a finite probability of finding the electron on the nucleus.

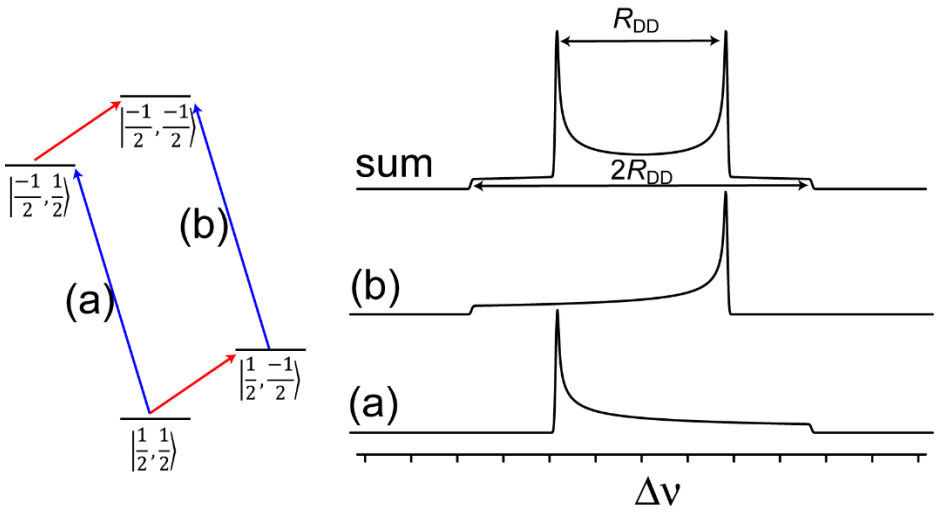

Figure 1.9. (left) Energy level diagram for a two-spin system displaying the allowed transitions for both of the coupled nuclei in red and blue. On the right, the powder pattern known as the Pake doublet is shown which is a combination of two powder patterns (a and b) for the cases when the nucleus is coupled to the *m* = 1/2 or -1/2 state of the other nucleus.

The *J* coupling Hamiltonian is very similar to the dipolar coupling Hamiltonian; however, the *J* coupling tensor can have up to nine independent tensor elements.[55]

$$(1.31)\quad \hat{H}_J = (\mathbf{S}\cdot\mathbf{J}\cdot\mathbf{I}) = \left(\hat{S}_x,\hat{S}_y,\hat{S}_z\right)\begin{pmatrix} J_{xx} & J_{xy} & J_{xz} \\ J_{yx} & J_{yy} & J_{yz} \\ J_{zx} & J_{zy} & J_{zz} \end{pmatrix}\begin{pmatrix} \hat{I}_x \\ \hat{I}_y \\ \hat{I}_z \end{pmatrix}$$

Unlike the dipolar coupling tensor, the *J* coupling tensor isn't traceless and thus has an isotropic component (J_{iso}) that remains measurable in solution NMR experiments and leads to the characteristic multiplets of the NMR signals. The J_{iso} can be used to gain insight

into the bonds in the molecule and forms the basis for many NMR experiments such as DEPT,[8] COSY,[9] HMQC,[10] and INADEQUATE.[11]

The J coupling tensor can be diagonalised to obtain the three principal components (J_{11}, J_{22}, and J_{33}) of the tensor and their orientations. These are ordered as $|J_{33}\text{-}J_{iso}| \geq |J_{11}\text{-}J_{iso}| \geq |J_{22}\text{-}J_{iso}|$ and are usually parameterised using the isotropic J coupling constant (J_{iso}), the anisotropy (ΔJ), and asymmetry η_J.

(1.32) $$J_{iso} = (J_{11} + J_{22} + J_{33})/3$$

(1.33) $$\Delta J = J_{33} - (J_{11} + J_{22})/2$$

(1.34) $$\eta_J = (J_{22} - J_{11})/(J_{33} - J_{iso})$$

The largest principal component of **J** is however usually oriented along the internuclear vector and it is often reasonable to assume an η_J of zero.[56] In that case, the anisotropic part of the J coupling tensor cannot be separated from the dipolar coupling tensor and only an effective dipolar coupling constant (R_{eff}) can be measured.

(1.35) $$R_{eff} = R_{DD} - \Delta J/3$$

1.1.4 The Wave Function Method in NMR

The previous sections discussed many of the interactions which are encountered when performing solid-state NMR experiments, the solutions to which were obtained by using the secular approximation or perturbation theory. Much of the work in this thesis involves cases for which the use of perturbation expansions is unreasonable or impractical. The wave function method for NMR will be introduced in this section and provides one of

many, and perhaps the simplest, exact solutions to solving an arbitrary spin Hamiltonian and simulating an NMR spectrum.

A complete basis set for a spin system can be obtained from the possible values of *m* for a given system. For example, the basis set for a single spin-3/2 nucleus is as follow:[57]

$$(1.36)\quad \textit{Basis set} = \begin{bmatrix} |-3/2\rangle \\ |-1/2\rangle \\ |1/2\rangle \\ |3/2\rangle \end{bmatrix}$$

If multiple spins make up the spin system, then products of the single spin basis functions can be used. For example, if there are two spin-1/2 nuclei, the basis functions are the following.[58]

$$(1.37)\quad \textit{Basis set} = \begin{bmatrix} |-1/2,-1/2\rangle \\ |-1/2,1/2\rangle \\ |1/2,-1/2\rangle \\ |1/2,1/2\rangle \end{bmatrix}$$

Note that the size of the basis set grows exponentially with the size of the system and that it is currently unfeasible to perform exact simulations of spin systems on the order of 20 spin-1/2 nuclei, although new approximative methods show promise in performing nearly exact simulations of hundreds of spins.[59]

The Hamiltonian can then be expressed in matrix form by evaluating the expectation value of the Hamiltonian for every pair of two basis functions.

$$(1.38)\quad \mathbf{H} = \begin{bmatrix} \langle 1|\hat{H}|1\rangle & \langle 1|\hat{H}|2\rangle & \cdots & \langle 1|\hat{H}|N\rangle \\ \langle 2|\hat{H}|1\rangle & \langle 2|\hat{H}|2\rangle & & \langle 2|\hat{H}|N\rangle \\ \vdots & & \ddots & \vdots \\ \langle N|\hat{H}|1\rangle & \langle N|\hat{H}|2\rangle & \cdots & \langle N|\hat{H}|N\rangle \end{bmatrix}$$

If the basis functions correspond to the true wave functions of the system, then the Hamiltonian will be diagonal and its diagonal elements would correspond to the energy levels. Note that these diagonal elements correspond to the energy levels calculated using the secular approximation. If the off-diagonal elements are non-zero, then the matrix needs to be diagonalised by performing a unitary transformation as follows.

$$(1.39)\quad \mathbf{P}^{-1}\mathbf{H}\mathbf{P} = \mathbf{E}$$

In equation 1.39, **P** is a matrix whose columns correspond to the eigenvectors and **E** is a diagonal matrix whose diagonal elements are the eigenvalues (energy levels). The eigenvectors correspond to the wave function associated to a given energy level (eigenvalue) that is expanded in the selected basis set:[60]

$$(1.40)\quad |m\rangle = \sum_{n} (b_{n,m} + ic_{n,m})|n\rangle$$

where n is an index for a basis function and $b_{n,m}$ and $c_{n,m}$ correspond to the real and imaginary components of the eigenvector. Since the Hamiltonian is Hermitian, the energy levels are always real however the wave functions are often imaginary. The eigenvalues can be used to determine the NMR resonance frequencies and the eigenvectors can be used to calculate other properties. For example, the intensity of a given resonance between states m_1 and m_2 can be calculated as follows using equations 1.3-1.6:[61]

(1.41) $Intensity \propto \left| \left\langle m_1 \left| \hat{I}_+ + \hat{I}_- \right| m_2 \right\rangle \right|^2$.

1.1.5 The Density Matrix

The wave function method can be applied to simulate simple, time-independent, problems, however that is often insufficient. If the result of a sequence of rf pulses needs to be calculated, or if we are dealing with a spinning sample, then the time dependence of the Hamiltonian needs to be taken into consideration explicitly. The most common method for solving the time-dependent Schrödinger equation in NMR experiments is with the use of the density matrix (**ρ**). The density matrix, expressed in a Zeeman basis set (see equations 1.36 and 1.37), is a matrix whose diagonal elements represent the relative population of a given state and the off-diagonal elements are known as coherences (transitions). For example, for a single spin-3/2 nucleus, the density matrix is written as:[58]

(1.42) $$\boldsymbol{\rho} = \begin{bmatrix} -3/2 & ST & DQ & TQ \\ ST & -1/2 & CT & DQ \\ DQ & CT & 1/2 & ST \\ TQ & DQ & ST & 3/2 \end{bmatrix}.$$

In the **ρ** above, the coherences for the central transition (CT), satellite transitions (ST), double-quantum coherences (DQ) and triple quantum coherences (TQ) are indicated. At thermal equilibrium **ρ** is diagonal since none of the coherences have been excited.

In order to simulate the time dependence of an NMR experiment it is useful to introduce the propagator (**U**) which is simply the imaginary exponential of the Hamiltonian (equation 1.38).

(1.43) $\mathbf{U}(t) = \exp(-i\,\mathbf{H}(t))$

Note that the exponential of a matrix is simply the exponential of all its elements. The propagator for the application of an on resonance rf pulse, that induces a rotation of the magnetization of φ, to a spin-1/2 nucleus is the following. During delays in the pulse sequence, the system evolves according to the relevant internal spin Hamiltonians (equations 1.14, 1.21, 1.28, and 1.31).

(1.44) $\mathbf{U}_{\text{rf}} = \begin{bmatrix} \cos(\varphi/2) & -i\sin(\varphi/2) \\ -i\sin(\varphi/2) & \cos(\varphi/2) \end{bmatrix}$

If the Hamiltonian is not diagonal, then the propagator is given by the following, where **P** is the matrix of eigenvectors of **H** and **E** is the diagonal matrix containing its eigenvalues (see equation 1.39).[57]

(1.45) $\mathbf{U}(t) = \mathbf{P}\exp(-i\,\mathbf{E}(t))\mathbf{P}^{-1}$

The calculation of the density matrix under the application of a given propagator is calculated using the following unitary transformation:

(1.46) $\boldsymbol{\rho}(t) = \mathbf{U}(t)\boldsymbol{\rho}(0)\mathbf{U}^{-1}(t)$

and the expectation value of an operator (**Q**), such as the signal intensity, according to equation 1.41, can be calculated according to:

(1.47) $\langle Q \rangle(t) = Tr\{\boldsymbol{\rho}(t)\mathbf{Q}\}.$

In 1.47, *Tr* indicates that the trace (sum of the diagonal elements) is calculated.

When multiple pulses are applied, or if we have a spinning sample, it is necessary to separate the propagator into a series of small time increments:[62]

$$\rho(t_N) = U(0,t_1)U(t_1,t_2)\ldots U(t_{N-1},t_N)\rho(0)U^{-1}(t_{N-1},t_N)\ldots U^{-1}(t_1,t_2)U^{-1}(0,t_1). \quad (1.48)$$

With the density matrix approach, any NMR experiment can be simulated exactly, including the effects of rf pulses.

1.1.6 Solid-State NMR Experiments

1.1.6.1 Magic Angle Spinning (MAS)

The technique known as magic angle spinning (MAS) was discovered independently by Andrew, Bradbury, and Eades[63] as well as by Lowe[64] in the late 1950s. The technique uses fast mechanical rotations of a sample to average first-order broadening interactions such as dipolar coupling and CSA to obtain high-resolution, solution-like, NMR spectra of solid samples.

The rotation of a sample is better described with the use of spherical tensors as opposed to Cartesian ones. The general form of a spherical tensor Hamiltonian is as follows:[65]

$$\hat{H}_\lambda = C_\lambda \sum_l \sum_{m=l}^{-l} (-1)^m R^\lambda_{l,-m} T^\lambda_{l,m'} \quad (1.49)$$

where λ is the interaction in question, C^λ is a fundamental constant, and $R^\lambda_{l,-m}$ and $T^\lambda_{l,m'}$ are the space and spin part of the Hamiltonian, respectively. l represents the rank of the tensor, the isotropic part has an l of 0, the antisymmetric part has an l of 1, and the anisotropic part has an l of 2. The space part can be expanded as follows:

(1.50) $$R^{\lambda}_{l,m} = \sum_{m'} D^{l}_{m',m}(\alpha,\beta,\gamma)\rho^{\lambda}_{l,m'}$$

where $D^{l}_{m,m'}$ is a Wigner rotation matrix and the values of C^{λ}, $T^{\lambda}_{l,m'}$, and $\rho^{\lambda}_{l,m'}$ are tabulated elsewhere.[66] The Wigner rotation matrix is used to rotate the principal axis frame of the tensor into the lab frame (the magnetic field) with a set of Euler angles (α,β,γ). To take into consideration the rotation of the sample, it is only necessary to include an additional Wigner rotation matrix:[67]

(1.51) $$R^{\lambda}_{l,m} = \sum_{m'} D^{l}_{m'',m'}(\omega_R t,\theta_R,0) D^{l}_{m',m}(\alpha,\beta,\gamma)\rho^{\lambda}_{l,m'}$$

where ω_R is the spinning frequency, t is time, and θ_R is the angle of the rotor with respect to the magnetic field. The Wigner rotation matrix for the rotation (considering only the anisotropic, $l = 2$ part) can be expanded as:

(1.52) $$D^{(2)}_{m'',m'}(\omega_R t,\theta_R,0) = e^{-im''\omega_R t} d^{(2)}_{m'',0}(\theta_R)$$

where m' was set to zero to satisfy the secular approximation. When time averaging over a rotor cycle, the only remaining term is $d^{(2)}_{0,0}$ which is equal to $\frac{1}{2}(3\cos^2\theta_R - 1)$. This term is equal to zero when the spinning axis is set to 54.74° with respect to the magnetic field. $d^{(2)}_{0,0}$ is also known as the second-order Legendre polynomial of $\cos\theta_R$. All rank 2 (first-order) anisotropic interactions are then averaged to zero by the technique of magic angle spinning, yielding solution-like NMR spectra of solids. Simulated MAS NMR spectra are shown in Figure 1.10.

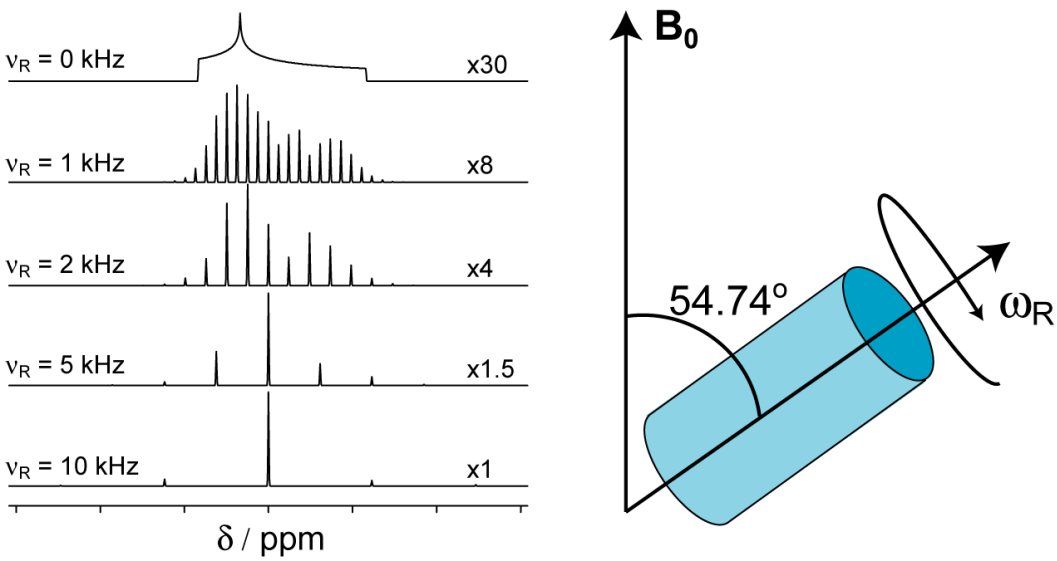

Figure 1.10. Theoretical NMR spectra for an arbitrary spin-1/2 nucleus are shown on the left as a function of the MAS rate. The spinning sidebands change position as the spinning rate is increased whereas the isotropic peak does not. A scheme of a MAS rotor is shown on the right where the spinning axis is tilted away from the magnetic field by the magic angle.

It is shown in Figure 1.10 that the broad powder pattern is split into a series of sharp resonances that are known as spinning sidebands.[68] These are separated from the isotropic resonance by the spinning frequency. The isotropic peak is usually identified by acquiring spectra at multiple spinning rates as its position is independent of the spinning frequency, unlike the spinning sidebands.

The second-order quadrupolar interaction behaves as a spherical tensor of rank 4 and thus the simplified space part of the Hamiltonian under sample spinning simplifies to:

$$(1.53)\quad R^{\lambda}_{l,0} = R^{\lambda(\mathrm{LAB})}_{0,0} + \sum_{m'} D^{2}_{m',0}(\omega_R t, \theta_R, 0) R^{\lambda(\mathrm{LAB})}_{2,0} + \sum_{m'} D^{4}_{m',0}(\omega_R t, \theta_R, 0) R^{\lambda(\mathrm{LAB})}_{4,0} .$$

There is then a dependency on the second, as well as the fourth-order Legendre polynomial, which is equal to $1/8(35\cos^4\theta_R - 30\cos^2\theta_R + 3)$. This term, unfortunately, does not average to zero when θ_R is set to 54.74° and thus MAS cannot fully average the broadening caused by the second-order quadrupolar interaction. The breadth of the anisotropic CT line shape is then only reduced by about a factor of 3, as shown in Figure 1.11.[69] Also shown in Figure 1.11 is the dependence of the MAS CT line shape as a function of the η. The effects of CSA are however completely removed by MAS.

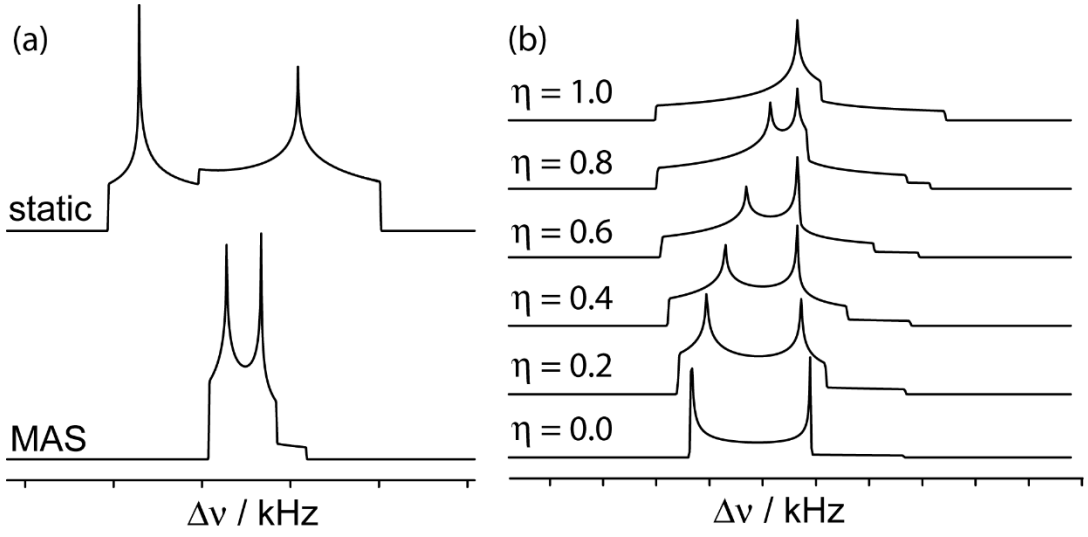

Figure 1.11. (a) The effect of MAS on the CT powder pattern of a quadrupolar nucleus is illustrated, showing that the anisotropic broadening is only reduced by a factor of 3. (b) Appearances of the MAS CT line shapes are shown as a function of the value of η.

1.1.6.2 Double-Rotation (DOR)

As seen in equation 1.53, in order to average the second-order quadrupolar interaction, it is necessary to spin the samples about two angles simultaneously to eliminate the dependence on the second- and fourth-order Legendre polynomials whose magic angles

are of 54.74° and 30.56° or 70.12°, respectively. This extremely mechanically challenging method has been developed and is known as double-rotation (DOR), see Figure 1.12.[70,71] For DOR experiments, the sample is packed in a small rotor, known as the inner rotor, that is inserted into the larger outer rotor. High pressure gas is fed into the outer rotor from its extremities in order to spin both rotors simultaneously.[72] The newest models can only achieve outer and inner rotor spinning frequencies of 2.2 and 8 kHz, respectively, whereas the DOR probe used for this work can be spun at frequencies of 1.1 and 5 kHz for the outer and inner rotors, respectively.

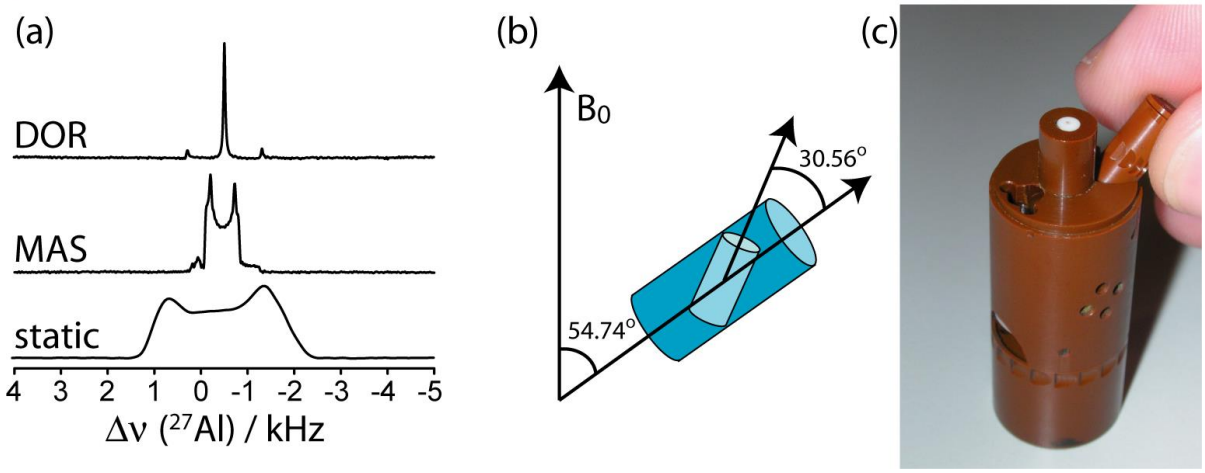

Figure 1.12. (a) A comparison of the ^{27}Al static, MAS, and DOR NMR spectra are shown. A scheme of a typical DOR rotor is shown in (b) and a photo of the DOR rotors used for this work is shown in (c).

DOR makes it possible to acquire high-resolution, solution-like, NMR spectra for half-integer quadrupolar nuclei in a single dimension. Although other two-dimensional methods such as multiple-quantum MAS (MQMAS)[73] and satellite-transition MAS (STMAS)[74] have been designed to acquire high-resolution NMR spectra using conventional

NMR equipment, DOR offers tremendous sensitivity advantages[75] and enables the acquisition of high-resolution 2D correlation spectra.[76,77] A comparison of the static, MAS, and DOR ^{27}Al ($I(^{27}\text{Al})$ = 5/2) NMR spectra of aluminium acetylacetonate are shown in Figure 1.12.

1.1.6.3 Cross-Polarization

The NMR signals from dilute nuclei can be enhanced with a simple polarization transfer technique known as cross-polarization (CP), see Figure 1.13.[78,79] In the CP experiment, the magnetization from an abundant, high-γ, nucleus, which is usually ^{1}H, is transferred to a less sensitive nucleus, such as ^{13}C. The sensitivity enhancement is two-fold; the Boltzmann population of the nucleus of interest is increased due to the ^{1}H's higher magnetogyric ratio, and the repetition time can be reduced since ^{1}H generally has shorter relaxation times. More scans can then be acquired during a given time period.

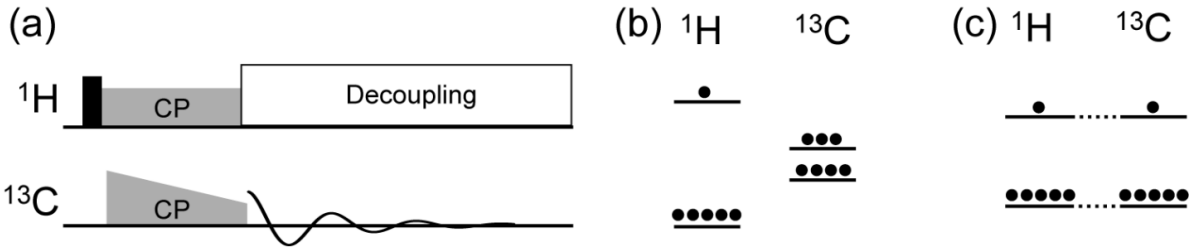

Figure 1.13. (a) A depiction of the CP pulse sequence is shown. An initial 90° pulse excites the ^{1}H spins and the magnetization is then transferred to ^{13}C using two contact pulses (gray). The signal is then detected on the ^{13}C channel while the ^{1}H spins are decoupled. In (b) and (c) the energy levels are shown at equilibrium and during the contact pulse, respectively.

The pulse sequence for the CP experiment is depicted in Figure 1.13 where the excitation pulse is applied to the abundant spins and long spin locking pulses are then applied to equalise the resonance frequency of the two nuclei in the rotating frame (i.e. identical nutation frequency). This is known as the Hartmann-Hahn match. The larger magnetization of the abundant spins can then be transferred to the dilute spins and the NMR signal can be acquired.

1.1.6.4 The Spin Echo

The length of the FID, that is acquired after the application of an rf pulse, is inversely proportional to the line width of the signal in the NMR spectrum. In solid samples, and, more importantly, static samples, the duration of the FID can be extremely short due to the very broad anisotropic line shapes that are obtained. The short length of the FID becomes an issue if one considers that many of the first data points in the FID are lost while the rf pulse rings down, a period known as the dead time. In order to obtain reliable spectral line shapes, it is necessary to acquire the beginning of the FID; this is done with the use of a spin echo.[80]

The spin echo pulse sequence involves the application of two pulses, a 90° and a 180° pulse, that are separated by a certain delay (see Figure 1.14). The 90° pulse excites single-quantum coherences and rotates the magnetization vector into the transverse plane. During the delay the signal dephases due to the different resonance frequencies in the sample. The 180° pulse inverts the magnetization vectors, which maintain their initial precessional frequencies, and thus lead to an echo when the inter-pulse delay is repeated.[81] This is illustrated in Figure 1.14.

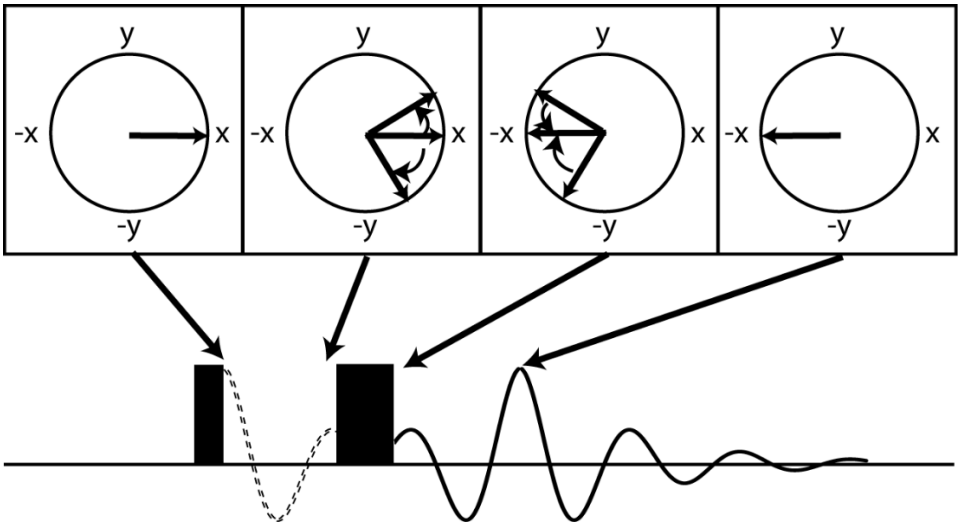

Figure 1.14. Scheme depicting a spin echo. A 90° pulse (of phase -y) is applied to rotate the magnetization into the transverse plane (viewed from the z axis). During the delay the magnetization dephases and a 180° pulse (of phase -y) is used to invert the magnetization. The signal is refocused after waiting an equal delay and the beginning of the FID can be recorded.

Echoes may also be formed when two 90° pulses are applied; these are known as Solomon echoes.[82] Solomon echo experiments have broader excitation bandwidths and produce more reliable line shapes at the expense of a loss of signal since only half of the signal is refocused by a 90° pulse.[80]

Multiple echoes may also be acquired with the Carr Purcell Meiboom Gill (CPMG) pulse sequence[83,84] in order to increase the signal to noise ratio of an NMR spectrum (see Figure 1.15). The train of spin echoes acquired with the CPMG method can be Fourier transformed directly to obtain a spectrum whose intensity is condensed into a manifold of sharp spikelets that mimics the line shape of the NMR spectrum. The echoes may also be

summed in order to yield a conventional NMR spectrum with a higher signal to noise ratio. This method is also referred to as the quadrupolar CPMG (QCPMG) method when it is applied to a quadrupolar nucleus using CT-selective pulses.[85]

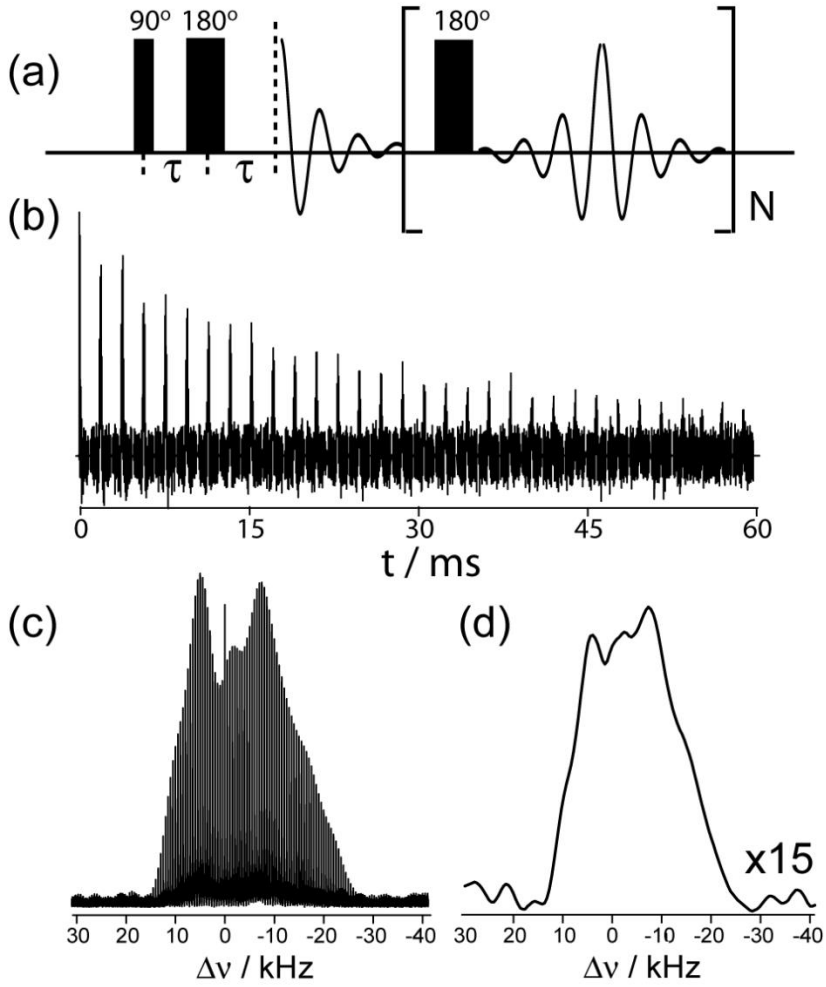

Figure 1.15. (a) The (Q)CPMG pulse sequence is depicted. An example echo train from a ^{91}Zr QCPMG NMR experiment is shown in (b) and the Fourier transform of the echo train is shown in (c), forming a spikelet spectrum. The Fourier transform of the first echo (equivalent to a spin echo experiment) is shown in (d) and has a much lower signal/noise ratio.

1.1.6.5 Ultra-Wideline NMR

If the size of the quadrupolar interaction (or CSA) is very large, it may not be possible to acquire the whole NMR spectrum with a single rf transmitter offset. This is the case since square rf pulses have a limited excitation bandwidths and the probe itself is only sensitive to frequencies within a certain range. These ultra-wideline NMR spectra must then be acquired in pieces using a series of rf transmitter offsets; this is known as the variable offset cumulative spectrum (VOCS) acquisition method.[86] An example spectrum acquired using the VOCS method is shown in Figure 1.16.

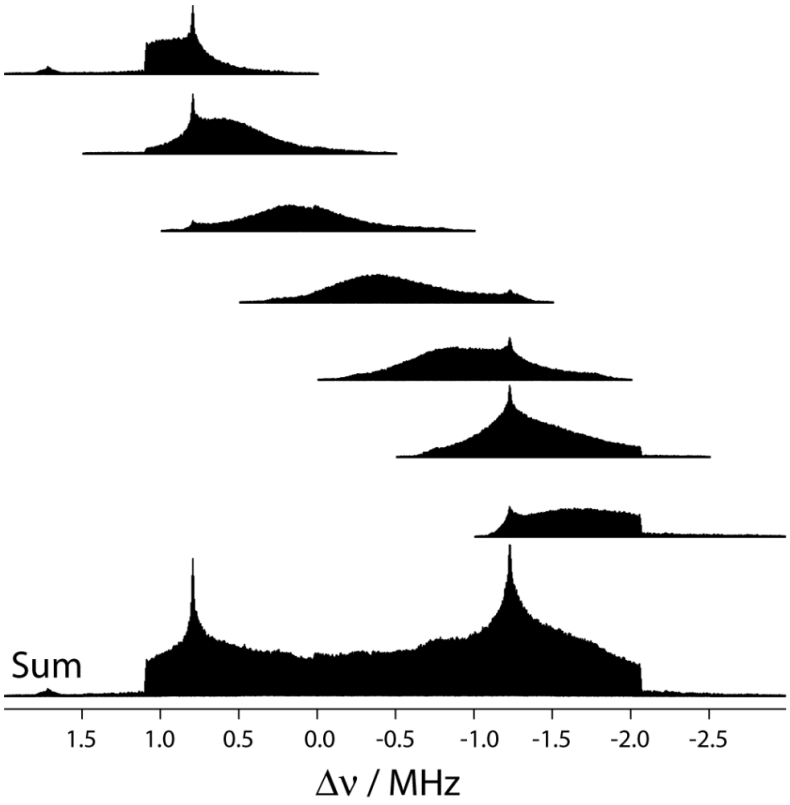

Figure 1.16. An example ^{35}Cl NMR spectrum acquired using the VOCS method is shown. The top traces show each of the individual sub-spectra and their sum (on the bottom trace) shows the full CT powder pattern.

Another way to increase the excitation bandwidth is to use chirped (frequency-swept) rf pulses as opposed to square, monochromatic, rf pulses. Recently it was shown that wideband uniform rate smooth truncation (WURST)[87] shaped rf pulses can be used to excite broad powder patterns.[88] WURST pulses generate a linear frequency sweep and can be used to excite powder patterns as broad as 1 MHz with a single rf transmitter offset. In principle larger excitation bandwidths are possible; however the probe bandwidth becomes the main limitation.

Since the pulse produces a linear frequency sweep, all isochromats in a powder pattern are excited sequentially, as opposed to simultaneously. The WURST echoes are then frequency dispersed and mimic the shape of the powder pattern.[88,89] In order to obtain absorptive NMR spectra acquired using WURST pulses it is necessary to apply either a second-order phase correction or to calculate the magnitude of the NMR spectrum.[90]

WURST pulses have also been applied in a QCPMG fashion (the WURST-QCPMG pulse sequence, see Figure 1.17) in order to excite broad powder patterns and maintain the sensitivity advantages of the QCPMG method.[91]

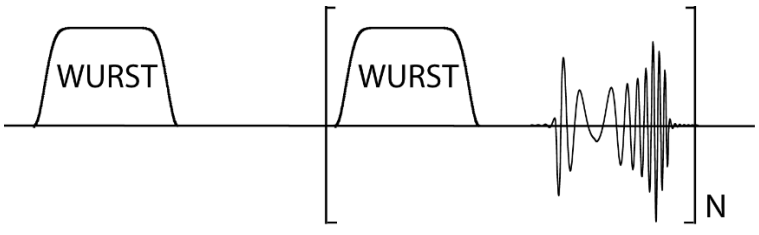

Figure 1.17. The WURST-QCPMG pulse sequence is depicted where a train or WURST pulses are applied to acquire a series of frequency dispersed echoes.

1.1.7 Density Functional Theory

Quantum chemical calculations are of tremendous use to complement experimental NMR parameters and gain insight into the origin of a given NMR parameter in order to relate it to a feature of the chemical or electronic structure. Density functional theory (DFT) is an ideal method for this purpose since it is often sufficiently accurate in reproducing NMR parameters without having the computational demands of higher-level *ab initio* wave function methods.

DFT, which expresses the electronic energy of a system as a function of the electron density, is, in principle, an exact theory;[92] however, the exact functional is not known. DFT is then commonly performed using the Kohn-Sham formalism[93] which, usually, uses atomic-centered orbitals as basis functions and calculates the kinetic and Coulombic energies as is done in the Hartree-Fock method. The exchange and correlation energies are then calculated using an approximate exchange-correlation potential that can use the electron density (local density approximation, LDA),[94] the gradient of the electron density (generalised gradient approximation, GGA),[95] the kinetic energy density (meta-GGA),[96] and the Hartree-Fock exchange energy (hybrid DFT)[97] as input parameters. The Kohn-Sham energy and electron density can then be used to calculate the EFG, MS, and *J*-coupling tensors.[98] Typically, these calculations are performed on discrete molecules or cluster models centered around the atom on interest. Longer range effects, which are important for the calculation of the EFG tensor, must then be ignored. The projector-augmented wave (PAW) DFT method[99] (*vide infra*) can be used to efficiently simulate an infinite crystal and include these longer range effects in accurate calculations of NMR parameters. The use of cluster models however

makes it possible to include relativistic effects, with the use of the zeroth-order regular approximation (ZORA),[100] which are very important in the calculation of the NMR parameters for heavy elements. NMR parameters calculated with the use of cluster model calculations can also be analysed with the use of natural localised molecular orbitals (NLMO)[101] which can shed light into the origins of a given NMR parameter.[102-104]

1.1.7.1 The Zeroth-Order Regular Approximation

The electrons in the elements of the fourth row and below of the periodic table kinetic energies that approach the speed of light. For these elements, relativistic effects can have a large impact on their chemistry and physical properties.[105] For example, relativistic effects are responsible for the color of gold and the fact that mercury is a liquid at room temperature. A useful approximate Hamiltonian for the full four-component relativistic Hamiltonian is the ZORA Hamiltonian.[100]

The ZORA method incorporates two components, the scalar and spin-orbit relativistic components. Scalar relativistic effects contract and stabilise of the *s* and *p* orbitals while destabilising the *d* and *f* orbitals. Scalar relativistic effects are, for example, responsible for the inert pair effect in the heavier main group elements. Spin-orbit relativistic effects are responsible for the splitting of orbitals due to the coupling of the electron spin with the angular momentum of the orbitals. Spin-orbit relativistic effects are known to be particularly important in the calculation of NMR parameters and are the reason why atoms bound to iodine, for example, are shielded while those bound to the lighter halogens are deshielded. This effect is known as the heavy atom-light atom (HALA) effect.[106]

1.1.7.2 Natural Localised Molecular Orbitals

The traditional solution to the Fock (or Kohn-Sham) self-consistent field (SCF) equations use a set of highly delocalised orbitals known as canonical molecular orbitals (CMOs). The CMOs are the MOs that chemist are most familiar with and are heavily used to analyse chemical reactions, but they are not the only solution to the SCF equations. Any combination of the CMOs to form a new orthonormal set of orbitals is also acceptable. These new MOs would have the same electronic energy, and can be used to calculate any property, such as NMR interaction tensors. One such set of molecular orbitals are the natural localised molecular orbitals (NLMOs).[101]

To construct the NLMOs, the electron density is first fit with the use of highly localised (strictly one or two (rarely more) centers) MOs known as natural bonding orbitals (NBOs).[107] All possible bonding schemes are trialed to determine the best set of NBOs. NBOs are arranged to represent a quantum-mechanical description of Lewis-type structures with orbitals representing the core functions, lone pairs, and bonds.

The NBOs are then relaxed in order to include the delocalisation that is necessary to represent the electron density in the system. This final change leads to the semi-localised NLMOs which are very similar to their parent NBOs, but are acceptable solutions to the SCF equations. A comparison of typical CMOs, NBOs and NLMOs is shown in Figure 1.18, using cyclohexane as an example.

Using the Amsterdam density functional (ADF) program[108] it is possible to decompose contributions to the EFG,[104] MS,[103] and *J*-coupling[102] tensors in terms of the NLMOs. This is a very powerful method as it enables us to isolate contributions to the

observable NMR properties from individual bonds or lone pairs. A greater understanding of a given NMR observable can then be obtained which can be used to gain insights into the electronic structures of unknown compounds whose NMR spectra can be measured.

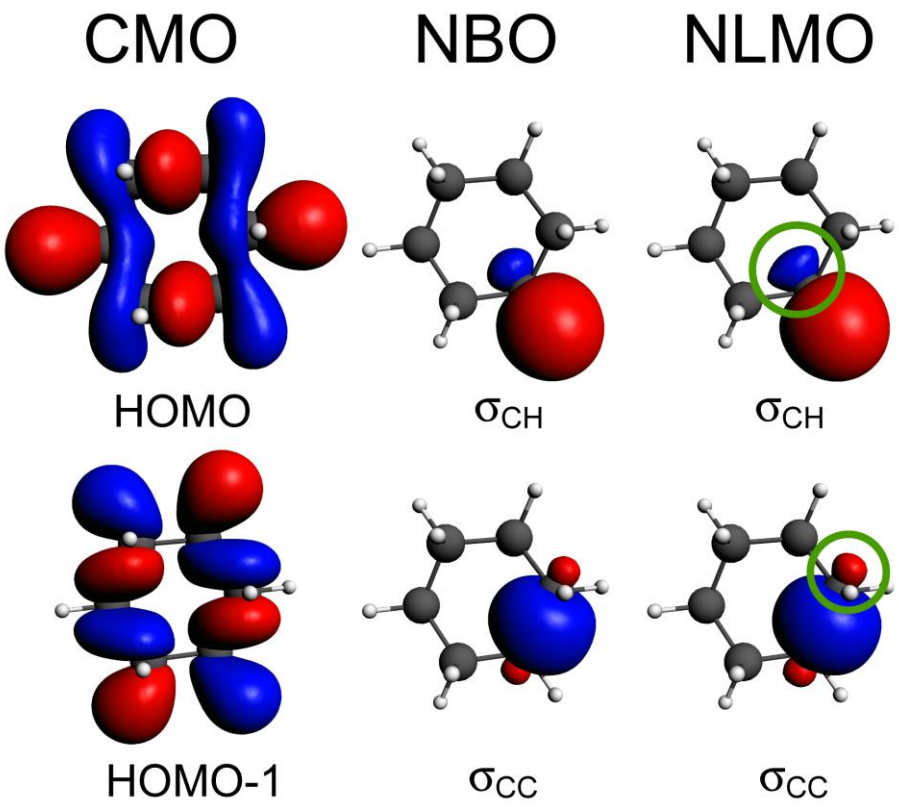

Figure 1.18. A comparison of some CMOs, NBOs, and NLMOs calculated for cyclohexane at the PBE/DZP level of theory. It can be seen that the CMOs are highly delocalised and difficult to interpret whereas the NBOs and NLMOs represent bonds as in Lewis structures. The NLMOs show some degree of delocalisation that is absent in the corresponding NBOs; this is most clearly seen in the circled regions.

1.1.7.3 Projector Augmented Wave DFT

Many systems cannot be accurately represented with the use of cluster models since they form networks in the solid state. Long range effects are also very important when calculating the EFG tensor since it has an r^{-3} dependence (see equation 1.22). The PAW method[99] provides a computationally efficient approach to representing infinite solids. The unit cell (smallest repeating unit in a crystalline system) is used as an input structure and plane waves (which are periodic 3D functions) are used as basis functions instead of atom-centered basis sets. Although plane waves are fairly poor basis functions, and a large number of them are necessary to accurately represent the electron density, the use of fast Fourier transforms accelerates the solution of the SCF equations. The calculations are also accelerated with the use of pseudopotentials.

Chemistry is mainly dominated by the valence electrons that participate in bonding interactions whereas the core electrons remain untouched. The description of the wave function near the core is however very computationally demanding, necessitating a large number of plane waves to represent the oscillations associated with the high kinetic energy of core electrons. In the PAW method, the wave function within a certain radius from the nucleus is replaced by a smooth function known as a pseudopotential. The smoother profile of the pseudopotential lowers the demand for a large number of plane waves, and thus the computational cost. A depiction of a pseudopotential is shown in Figure 1.19. The PAW methods allows for a reconstruction of the core functions following the SCF which is important for calculating NMR properties which depend on the electron density near the core.

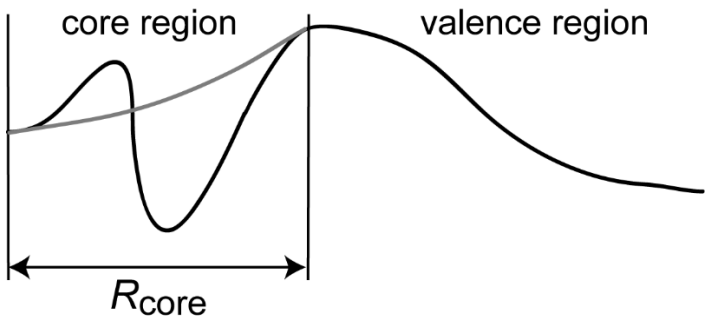

Figure 1.19. A schematic representation of a pseudopotential. The all-electron wave function is shown in black whereas in the core region (defined by R_{core}) also depicts a pseudopotential (lighter grey).

Both the EFG[109] and the MS tensors can be calculated using the PAW method however the gauge-including PAW (GIPAW)[110] method is necessary to restore the spatial translational invariance that is lost with the application of a magnetic field. The GIPAW method is equivalent to the GIAO[111] or IGLO[112] methods used in gas-phase DFT calculations. The GIPAW formalism has also been recently expanded for the calculation of *J* coupling tensors[113] and the inclusion of scalar relativistic effects, with the use of the ZORA method;[114] however, these options are currently not available to the public.

1.1.8 Objectives

The use of solid-state NMR for the determination or refinement of crystalline structures, NMR crystallography,[115,116] has gained much popularity among the scientific community. Although the technique is still in its infancy, NMR crystallography can, in principle, enable one to solve the high resolution crystal structure of a material without resulting to single-crystal diffraction methods, which cannot be used in cases where large single crystals cannot be grown.

It has been shown that the crystal structures of organic molecular species can be determined with the use of ^{1}H spin diffusion rates[117-119] as well as with the explicit use of chemical shifts.[120] The chemical shifts have also been used as a structure selection parameter when solving crystal structures with the use of crystal structure prediction software.[121,122] Anisotropic ^{13}C chemical shift tensors have also been used as a structural constraint in the refinements of the crystal structures of organic molecules[123] and proteins.[124]

The crystal structures of framework materials, such as zeolites[125,126] and aluminophosphates,[127,128] have also been solved with the use of through-space correlation NMR experiments. Similarly to the molecular species, it was additionally demonstrated that the crystal structures of zeolites could be refined with the use of ^{29}Si chemical shift tensors.[129,130] Many NMR crystallographic methods combine NMR with numerous other techniques such as powder X-ray diffraction, elemental analysis, DFT calculations, and crystal structure prediction. It is however important to develop methods that make use of quadrupolar nuclei due to their significant presence in the periodic table, specifically in materials chemistry.

The first objective of this thesis is to design and implement new NMR crystallographic methods that can be applied to systems containing quadrupolar nuclei. In the second part of the thesis, a method developed for the refinements of crystal structures that uses experimentally-determined EFG tensor components, and those predicted using PAW DFT, as a constraint is presented. This method is then applied to the refinement of the crystal structures of the non-linear optical material $Na_2Al_2B_2O_7$ (chapter 2.2), some sodium pyrophosphates (chapter 2.3), and the near-zero thermal expansion material $ZrMgMo_3O_{12}$ (chapter 2.4).

Spin-spin coupling interactions can be used to characterise the bonding motifs in a material (*J* coupling) or measure internuclear distances (dipolar coupling). Measuring spin-spin coupling then yields very powerful structural information. Spin-spin coupling interactions are however rather weak, when compared to the quadrupolar interaction, which has limited the measurement of spin-spin coupling between pairs of quadrupolar nuclei. Reliable methods have, however, been designed for the measurement of spin-spin coupling between a spin-1/2 and a quadrupolar nucleus.[131-134]

The second objective of this thesis is to design new methods to measure spin-spin coupling in pairs of quadrupolar nuclei that can be used to gain unprecedented structural and electronic information. In the third part of the thesis, such methods, which are based on using either DOR NMR (chapters 3.1 and 3.3) or multiple pulse experiments (chapters 3.4 and 3.5), are described. These techniques can be used to provide valuable spin-spin coupling data that directly yield unambiguous structural information. The technique developed for the simulation of the DOR spectra is also expanded to produce software capable of simulating exact static NMR spectra of quadrupolar nuclei at any applied magnetic field (chapter 3.2). This program, known as the QUadrupolar Exact SofTware (QUEST), is now being widely distributed to other members of the scientific community.

References

[1] Gorter, C. J. *Physica* **1936**, *3*, 995-998.

[2] Rabi, I. I.; Zacharias, J. R.; Millman, S.; Kusch, P. *Phys. Rev.* **1938**, *53*, 318.

[3] Gorter, C. J.; Broer, L. J. F. *Physica* **1942**, *9*, 591-596.

[4] Purcell, E. M.; Torrey, H. C.; Pound, R. V. *Phys. Rev.* **1946**, *69*, 37-38.

[5] Bloch, F.; Hansen, W. W.; Packard, M. *Phys. Rev.* **1946**, *70*, 474-485.

[6] Proctor, W. G.; Yu, F. C. *Phys. Rev.* **1950**, *77*, 717.

[7] Proctor, W. G.; Yu, F. C. *Phys. Rev.* **1951**, *81*, 20-30.

[8] Doddrell, D. M.; Pegg, D. T.; Bendall, M. R. *J. Magn. Reson.* **1982**, *48*, 323-327.

[9] Aue, W. P.; Bartholdi, E.; Ernst, R. R. *J. Chem. Phys.* **1976**, *64*, 2229-2246.

[10] Bax, A.; Griffey, R. H.; Hawkins, B. L. *J. Magn. Reson.* **1983**, *55*, 301-315.

[11] Bax, A.; Freeman, R.; Frenkiel, T. A. *J. Am. Chem. Soc.* **1981**, *103*, 2102-2104.

[12] Kumar, A.; Ernst, R. R.; Wüthrich, K.; *Biochem. Biophys. Res. Commun.* **1980**, *95*, 1-6.

[13] Marion, D.; Kay, L. E.; Sparks, S. W.; Torchia, D. A.; Bax, A. *J. Am. Chem. Soc.* **1989**, *111*, 1515-1517.

[14] Pervushin, K.; Riek, R.; Wider, G.; Wüthrich, K. *Proc. Nat. Acad. Sci USA* **1997**, *94*, 12366-12371.

[15] Fürtig, B.; Richter, C.; Wöhnert, J.; Schwalbe, H. *ChemBioChem*, **2003**, *4*, 936-962.

[16] Lauterbur, P. C. *Nature* **1973**, *242*, 190-191.

[17] Kumar, A.; Welti, D.; Ernst, R. R. *J. Magn. Reson.* **1975**, *18*, 69-83.

[18] Damadian, R.; Goldsmith, M.; Minkoff, L. *Physiol. Chem. & Phys.* **1977**, *9*, 97-100, 108.

[19] Duer, M. J. *Introduction to Solid-State NMR Spectroscopy*, Blackwell Publishing Ltd: Oxford, 2004.

[20] Petkova, A. T.; Ishii, Y.; Balbach, J. J.; Antzutkin, O. N.; Leapman, R. D.; Delaglio, F.; Tycko, R. *Proc. Nat. Acad. Sci. USA* **2002**, *99*, 16742-16747.

[21] Maekawa, H.; Maekawa, T.; Kawamura, K.; Yokokawa, T. *J. Non-Cryst. Solids* **1991**, *127*, 53-64.

[22] Samantaray, M. K.; Alauzun, J.; Gajan, D.; Kavitake, S.; Mehdi, A.; Veyre, L.; Lelli, M.; Lesage, A.; Emsley, L.; Copéret, C.; Thieuleux, C. *J. Am. Chem. Soc.* **2013**, *135*, 3193-3199.

[23] Apperley, D. C.; Fletton, R. A.; Harris, R. K.; Lancaster, R. W.; Tavener, S.; Threlfall, T. L. *J. Pharm. Sci.* **1999**, *88*, 1275-1280.

[24] Fyfe, C. A.; Feng, Y.; Grondey, H.; Kokotailo, G. T.; Gies, H. *Chem. Rev.* **1991**, *91*, 1525-1543.

[25] Eckert, H. *Prog. Nucl. Magn. Reson. Spectrosc.* **1992**, *24*, 159-293.

[26] Wasylishen, R. E.; Ashbrook, S. E.; Wimperis, S. *NMR of Quadrupolar Nuclei in Solid Materials*, John Wiley & Sons: Chichester, 2012.

[27] Levitt, M. H. *Spin Dynamics, second edition*, John Wiley & Sons: Chichester, 2009.

[28] Zeeman, P. *Phil. Mag. Ser. 5* **1897**, *44*, 55-60.

[29] Smith, S. A.; Palke, W. E.; Gerig, J. T. *Concepts Magn. Reson.* **1992**, *4*, 107-144.

[30] Smith, S. A.; Palke, W. E.; Gerig, J. T. *Concepts Magn. Reson.* **1992**, *4*,181-204.

[31] Ernst, R. R.; Anderson, W. A. *Rev. Sci. Instrum.* **1966**, *37*, 93-102.

[32] Ramsey, N. F.; *Phys. Rev.* **1950**, *78*, 699-703.

[33] Jameson, C. J.; Gutowsky, H. S. *J. Chem. Phys.* **1964**, *40*, 1714-1724.

[34] Bernard, G. M.; Eichele, K.; Wu, G.; Kirby, C. W.; Wasylishen, R. E. *Can. J. Chem.* **2000**, *78*, 614-625.

[35] Robert, J. B.; Wiesenfeld, L. *Phys. Rep.* **1982**, *86*, 363-401.

[36] Duncan, T. M. *J. Phys. Chem. Ref. Data* **1987**, *16*, 125-151.

[37] Edén, M. *Concepts Magn. Reson. A* **2003**, *18*, 24-55.

[38] Mason, J. *Solid State Nucl. Magn. Reson.* **1993**, *2*, 285-288.

[39] Bechmann, M.; Sebald, A. *Symmetry Effects at the Local Level in Solids*, in: Harris, R. K.; Wasylishen, R. E., Eds. *eMagRes*, John Wiley & Sons, 2009.

[40] Man, P. P., *Quadrupolar Interactions*, in: Harris, R. K.; Wasylishen, R. E., Eds. *eMagRes*, John Wiley & Sons, 2009.

[41] Koller, H.; Engelhardt, G.; Kentgens, A. P. M.; Sauer, J. *J. Phys. Chem.* **1994**, *98*, 1544-1551.

[42] Vega, A. J., *Quadrupolar Nuclei in Solids*, in: Harris, R. K.; Wasylishen, R. E., Eds. *eMagRes*, John Wiley & Sons, 2009.

[43] Samoson, A.; Lippmaa, E. *Phys. Rev. B* **1983**, *28*, 6567-6570.

[44] Widdifield, C. M.; Bryce, D. L. *J. Phys. Chem. A* **2010**, *114*, 10810-10823.

[45] Widdifield, C. M.; Bain, A. D.; Bryce, D. L. *Phys. Chem. Chem. Phys.* **2011**, *13*, 12413-12420.

[46] Gan, Z.; Gor'kov, P.; Cross, T. A.; Samoson, A.; Massiot, D. *J. Am. Chem. Soc.* **2002**, *124*, 5634-5635.

[47] Power, W. P.; Wasylishen, R. E.; Mooibroek, S.; Pettitt, B. A.; Danchura, W. *J. Phys. Chem.* **1990**, *94*, 591-598.

[48] Cheng, J. T.; Edwards, J. C.; Ellis, P. D. *J. Phys. Chem.* **1990**, *94*, 553-561.

[49] Gullion, T.; Schaefer, J. *J. Magn. Reson.* **1989**, *81*, 196-200.

[50] Lee, Y. K.; Kurur, N. D.; Helmle, M.; Johannessen, O. G.; Nielsen, N. C.; Levitt, M. H. *Chem. Phys. Lett.* **1995**, *242*, 304-309.

[51] Jaroniec, C. P.; Filip, C.; Griffin, R. G. *J. Am. Chem. Soc.* **2002**, *124*, 10728-10742.

[52] Wasylishen, R. E. *Dipolar & Indirect Coupling Basics*, in: Harris, R. K.; Wasylishen, R. E., Eds. *eMagRes*, John Wiley & Sons, 2009.

[53] Pake, G. E. *J. Chem. Phys.* **1948**, *16*, 327-336.

[54] Ramsey, N. F. *Phys. Rev.* **1953**, *91*, 303-307.

[55] Harris, K.J.; Bryce, D. L.; Wasylishen, R. E. *Can. J. Chem.* **2009**, *87*, 1338-1351.

[56] Bryce, D. L.; Dorval Courchesne, N. M.; Perras, F. A. *Solid State Nucl. Magn. Reson.* **2009**, *36*, 182-191.

[57] Edén, M. *Concepts Magn. Reson. A* **2003**, *17*, 117-154.

[58] Stejskal, E. O.; Memory, J. D. *High Resolution NMR in the Solid State*, Oxford University Press, Oxford, 1994.

[59] Edwards, L. J.; Savostyanov, D. V.; Welderufael, Z. T.; Lee, D.; Kuprov, I. *J. Magn. Reson.* **2014**, *243*, 107-113.

[60] Alarcón, S. H.; Olivieri, A. C.; Harris, R. K. *Solid State Nucl. Mgan. Reson.* **1993**, *2*, 325-334.

[61] Harris, R. K. *Nuclear Magnetic Resonance Spectroscopy: A Physicochemical View*, Pearson Education, Ltd., 2005, p. 46.

[62] Edén, M.; Lee, Y. K.; Levitt, M. H. *J. Magn. Reson. Ser. A* **1996**, *120*, 56-71.

[63] Andrew, E. R.; Bradbury, A.; Eades, R. G. *Nature*, **1958**, *182*, 1659.

[64] Lowe, I. J.; *Phys. Rev. Lett.* **1959**, *2*, 285-287.

[65] Maricq, M. M.; Waugh, J. S. *J. Chem. Phys.* **1979**, *70*, 3300-3316.

[66] Chandra Shekar, S.; Jerschow, A. *Tensors in NMR*, in: Harris, R. K.; Wasylishen, R. E., Eds. *eMagRes*, John Wiley & Sons, 2009.

[67] Haeberlen, U. *High-Resolution NMR in Solids: Selective Averaging*, Academic Press, Waltham, 1976.

[68] Herzfeld, J.; Roufosse, R. A.; Haberkorn, R. A.; Griffin, R. G.; Glimcher, M. J. *Philos. Trans. R. Soc. Lond., B* **1980**, *289*, 459-469.

[69] Kundla, E.; Samoson, A.; Lippmaa, E. *Chem. Phys. Lett.* **1981**, *83*, 229-232.

[70] Samoson, A.; Lippmaa, E.; Pines, A. *Mol. Phys.* **1988**, *65*, 1013-1018.

[71] Chmelka, B. F.; Mueller, K. T.; Pines, A.; Stebbins, J.; Wu, Y.; Zwanziger, J. W. *Nature*, **1989**, *339*, 42-43.

[72] Samoson, A.; Pines, A. *Rev. Sci. Instrum.* **1989**, *60*, 3239-3241.

[73] Frydman, L.; Harwood, J. S. *J. Am. Chem. Soc.* **1995**, *117*, 5367-5368.

[74] Gan, Z.; *J. Am. Chem. Soc.* **2000**, *122*, 3242-3243.

[75] Howes, A. P.; Anupõld, T.; Lemaitre, V.; Kukol, A.; Watts, A.; Samoson, A.; Smith, M. E.; Dupree, R. *Chem. Phys. Lett.* **2006**, *421*, 42-46.

[76] Hung, I.; Howes, A. P.; Anupõld, T.; Samoson, A.; Massiot, D.; Smith, M. E.; Brown, S. P.; Dupree, R. *Chem. Phys. Lett.* **2006**, *432*, 152-156.

[77] Brinkmann, A.; Kentgens, A. P. M.; Anupõld, T.; Samoson, A. *J. Chem. Phys.* **2008**, *129*, 174507.

[78] Pines, A.; Gibby, M. G.; Waugh, J. S. *J. Chem. Phys.* **1972**, *56*, 1776-1777.

[79] Stejskal, E. O.; Schaefer, J.; Waugh, J. S. *J. Magn. Reson.* **1977**, *28*, 105-112.

[80] Bodart, P. R.; Amoureux, J.-P., Dumazy, Y.; Lefort, R. *Mol. Phys.* **2000**, *98*, 1545-1551.

[81] Hahn, E. L. *Phys. Rev.* **1950**, *80*, 580-594.

[82] Solomon, I. *Phys. Rev.* **1958**, *110*, 61-65.

[83] Carr, H. Y.; Purcell E. M. *Phys. Rev.* **1954**, *94*, 630-638.

[84] Meiboom, S.; Gill, D. *Rev. Sci. Instrum.* **1958**, *29*, 688-691.

[85] Larsen, F. H.; Skibsted, J.; Jakobsen, H. J.; Nielsen, N. C. *J. Am. Chem. Soc.* **2000**, *122*, 7080-7086.

[86] Bureau, B.; Silly, G.; Buzaré, J. Y.; Legein, C.; Massiot, D. *Solid State Nucl. Magn. Reson.* **1999**, *14*, 181-190.

[87] Kupče, E.; Freeman, R. *J. Magn. Reson. Ser. A* **1995**, *115*, 273-276.

[88] Bhattacharyya, R.; Frydman, L. *J. Chem. Phys.* **2007**, *127*, 194503.

[89] O'Dell, L. A. *Solid State Nucl. Magn. Reson.* **2013**, *55-56*, 28-41.

[90] Hung, I.; Gan, Z. *J. Magn. Reson.* **2010**, *204*, 256-265.

[91] O'Dell, L. A.; Schurko, R. W. *Chem. Phys. Lett.* **2008**, *464*, 97-102.

[92] Hohenberg, P.; Kohn, W. *Phys. Rev.* **1964**, *136*, B864-B871.

[93] Kohn, W.; Sham, L. J. *Phys. Rev.* **1965**, *140*, A1133-A1138.

[94] Vosko, S. H.; Wilk, L.; Nusair, M. *Can. J. Phys.*, **1980**, *58*, 1200-1211.

[95] Perdew, J. P.; Burke, K.; Ernzerhof, M. *Phys. Rev. Lett.* **1996**, *77*, 3865-3868.

[96] Tao, J.; Perdew, J. P.; Staroverov, V. N.; Scuseria, G. E. *Phys. Rev. Lett.* **2003**, *91*, 146401.

[97] Becke, A. D. *J. Chem. Phys.* **1993**, *98*, 1372-1377.

[98] Kaupp, M.; Buhl, M.; Malkin, V. G. *Calculation of NMR and EPR Parameters: Theory and Applications*, John Wiley & Sons, ltd., Chichester, 2004.

[99] Blöchl, P. E.; *Phys. Rev. B* **1994**, *50*, 17953-17979.

[100] van Lenthe, E.; Baerends, E. J.; Snijders, J. G. *J. Chem. Phys.* **1993**, *99*, 4597-4610.

[101] Reed, A. E.; Weinhold, F. *J. Chem. Phys.* **1985**, *83*, 1736-1740.

[102] Autschbach, J. *J. Chem. Phys.* **2007**, *127*, 124106.

[103] Autschbach, J. *J. Chem. Phys.* **2008**, *128*, 164112.

[104] Autschbach, J. Zheng, S.; Schurko, R. W. *Concepts Magn. Reson. A* **2010**, *36*, 84-126.

[105] Autschbach, J. *J. Chem. Phys.* **2012**, *136*, 150902.

[106] Kaupp, M.; Malkina, O. L.; Malkin, V. G.; Pyykkö, P. *Chem. Eur. J.* **1998**, *4*, 118-126.

[107] Foster, J. P.; Weinhold, F. *J. Am. Chem. Soc.* **1980**, *102*, 7211-7218.

[108] te Velde, G.; Bickelhaupt, F. M.; Baerends, E. J.; Fonseca Guerra, C.; van Gisbergen, S. J. A.; Snijders, J. G.; Ziegler, T. *J. Comput. Chem.* **2001**, *22*, 931-967.

[109] Zwanziger, J. W. *Computing Electric Field Gradient Tensors*, in: Harris, R. K.; Wasylishen, R. E., Eds. *eMagRes*, John Wiley & Sons, 2009.

[110] Pickard, C. J.; Mauri, F. *Phys. Rev. B* **2001**, *63*, 245101.

[111] Ditchfield, R. *Mol. Phys.* **1974**, *27*, 789-807.

[112] Schindler, M.; Kutzelnigg, W. *J. Chem. Phys.* **1982**, *76*, 1919-1933.

[113] Joyce, S. A.; Yates, J. R.; Pickard, C. J.; Mauri, F. *J. Chem. Phys.* **2007**, *127*, 204107.

[114] Yates, J. R.; Pickard, C. J; Payne, M. C.; Mauri, F. *J. Chem. Phys.* **2003**, *118*, 5746-5753.

[115] Harris, R. K.; Wasylishen, R. E.; Duer, M. J. *NMR Crystallography*, John Wiley & Sons, Chichester, 2009.

[116] Martineau, C.; Senker, J.; Taulelle, F. *Annu. Rep. Nucl. Magn. Reson. Spectrosc.* **2014**, *82*, 1-57.

[117] Elena, B.; Emsley, L. *J. Am. Chem. Soc.* **2005**, *127*, 9140-9146.

[118] Elena, E.; Pintacuda, G.; Mifsud, N.; Emsley, L. *J. Am. Chem. Soc.* **2006**, *128*, 9555-9560.

[119] Pickard, C. J.; Salager, E.; Pintacuda, G.; Elena, B.; Emsley, L. *J. Am. Chem. Soc.* **2007**, *129*, 8932-8933.

[120] Santos, S. M.; Rocha, J.; Mafra, L. *Cryst. Growth Des.* **2013**, *13*, 2390-2395.

[121] Salager, E.; Day, G. M.; Stein, R. S.; Pickard, C. J.; Elena, B.; Emsley, L. *J. Am. Chem. Soc.* **2010**, *132*, 2564-2566.

[122] Baias, M.; Widdifield, C. M.; Dumez, J.-N.; Thompson, H. P. G.; Cooper, T. G.; Salager, E.; Bassil, S.; Stein, R. S.; Lesage, A.; Day, G. M.; Emsley, L. *Phys. Chem. Chem. Phys.* **2013**, *15*, 8069-8080.

[123] Witter, R.; Sternberg, U.; Hesse, S.; Kondo, T.; Koch, F.-T.; Ulrich, A. S. *Macromolecules* **2006**, *39*, 6125−6132.

[124] Wylie, B. J.; Schwieters, C. D.; Oldfield, E.; Rienstra, C. M. *J. Am. Chem. Soc.* **2009**, *131*, 985-992.

[125] Brouwer, D. H.; Darton, R. J.; Morris, R. E.; Levitt, M. H. *J. Am. Chem. Soc.* **2005**, *127*, 10365-10370.

[126] Brouwer, D. H.; Cadars, S.; Eckert, J.; Liu, Z.; Terasaki, O.; Chmelka, B. F. *J. Am. Chem. Soc.* **2013**, *135*, 5641-5655.

[127] Bouchevreau, B.; Martineau, C.; Mellot-Draznieks, C.; Tuel, A.; Suchomel, M. R.; Trébosc, J.; Lafon, O.; Amoureux, J.-P.; Taulelle, F. *Chem. Mater.* **2013**, *25*, 2227-2242.

[128] Bouchevreau, B.; Martineau, C; Mellot-Draznieks, C.; Tuel, A.; Suchomel, M. R.; Trébosc, J.; Lafon, O.; Amoureux, J.-P.; Taulelle, F. *Chem. Eur. J.* **2013**, *19*, 5009-5013.

[129] Brouwer, D. H.; Enright, G. D. *J. Am. Chem. Soc.* **2008**, *130*, 3095-3105.

[130] Brouwer, D. H. *J. Am. Chem. Soc.* **2008**, *130*, 6306-6307.

[131] Massiot, D.; Fayon, F.; Alonso, B.; Trébosc, J.; Amoureux, J.-P. *J. Magn. Reson.* **2003**, *164*, 160-164.

[132] Amoureux, J.-P.; Trébosc, J.; Wiench, J. W.; Massiot, D. Pruski, M. *Solid State Nucl. Magn. Reson.* **2005**, *27*, 228-232.

[133] Lu, X.; Lafon, O.; Trébosc, J.; Amoureux, J.-P. *J. Magn. Reson.* **2012**, *215*, 34-49.

[134] Nimerovsky, E.; Gupta, R.; Yehl, J.; Li, M.; Polenova, T.; Goldbourt, A. *J. Magn. Reson.* **2014**, *244*, 107-113.

Part II: NMR Crystallographic Structure Refinements of Materials with the Use of the EFG Tensor

NMR crystallography, namely techniques designed for obtaining new crystallographic information with the use of solid-state NMR spectroscopy, has grown immensely in the past decade.[1,2] It has been demonstrated that the site symmetry[3] or even the space group[4] of a given crystal could be obtained with the use of NMR measurements. Whole crystal structures of organic compounds,[5-10] proteins,[11] and framework materials[12-17] have been determined with the use of NMR data. Crystal structure refinement methods[18-25] have also been developed which use solid-state NMR data in order to obtain accurate atomic coordinates for the atoms in a given system.

All these studies, however, make almost exclusive use of the spin-1/2 nuclei in the sample, such as ^{1}H, ^{13}C, ^{29}Si, and ^{31}P. For these nuclei, it is relatively easy to obtain dipolar coupling information that can be used to solve a structural model, or to obtain chemical shift anisotropy information to refine the structure. Crystallography is however particularly important in materials chemistry. High temperature syntheses are often used and only powdered samples can be obtained. Unlike single-crystal diffraction experiment, it is unnecessary to have large single crystals in order to perform solid-state NMR experiments. Unfortunately, many materials do not contain elements with spin-1/2 isotopes and instead

have a large proportion of quadrupolar nuclei such as $^{6/7}$Li, ^{11}B, ^{17}O, ^{23}Na, ^{27}Al, and transition metal elements (which are mostly quadrupolar nuclei). For these nuclei, it isn't possible to apply the previously developed NMR crystallographic methods since it is generally impossible to measure accurate dipolar or CSA information for these nuclei; that information is obscured by the dominant quadrupolar interaction. For many nuclei, it is then only possible to determine the components of the EFG tensor, along with the number of individual sites of a given element, by using NMR spectroscopy. Most materials have fairly simple, and high-symmetry, crystal structures and thus the unit cell dimensions and the space group can typically be determined with the use of powder X-ray diffraction (PXRD).[26] Using software such as FOX[27] or TOPAS[28] it may also be possible to solve a structural model using the PXRD data, however it is often necessary to optimize this model in some way in order to obtain a chemically reasonable structure. The following chapters will describe a strategy for the refinement of crystal structures using the EFG tensor as a constraint and its application to a series of different materials.

Chapter 2.1: Hybrid NMR/DFT Crystal Structure Refinement Method

2.1.1 Description of Refinement Strategy

2.1.1.1 Introduction

Although limited reports show that the EFG tensor can be used directly in order to obtain improved atomic coordinates,[29,25] no general systematic approach for crystal structure refinement using EFG tensor components has found general applicability. Even though it cannot be related to the crystallographic structure as directly or simply as the dipolar coupling interactions, the EFG tensor is extremely sensitive to the local environment surrounding the atom.[25-32] Unlike the chemical shift interaction, the EFG tensor is a ground state property and is thus very computationally inexpensive to calculate;[33] low-level calculations often yield very accurate results. The calculation of the EFG tensor also does not significantly increase the computational time of standard single-point DFT calculations. The addition of an experimentally-determined EFG tensor constraint into standard, DFT-based, crystal structure refinements wouldn't therefore increase the computational time and would lead to more accurate, and experimentally-relevant, crystal structures.

In this chapter, we present a methodology for crystal structure refinement using EFG tensor components. In our approach, the differences between the empirically corrected projector-augmented wave (PAW) density functional theory (DFT)[34-37] calculated EFG tensor components and those measured experimentally using solid-state NMR are minimized using a least-squares procedure. The approach is further improved if the lattice energy from

the PAW DFT calculations is also used as a restraint in the minimization procedure. This hybrid experimental-theoretical approach is important given that the vast majority of NMR-active nuclides found in inorganic compounds and functional materials are quadrupolar. We validate this technique using α-Al_2O_3 for which high quality single-crystal ^{17}O and ^{27}Al NMR data exist.

2.1.1.2 Calibration

PAW DFT calculations have been shown to provide highly precise EFG tensor parameters, yet the data are almost always systematically overestimated or underestimated by a given factor when compared to experiment.[38,39] This may be empirically corrected with the use of a common scaling factor. This correction implicitly accounts for possible systematic deficiencies in the computational method, including the nature of the pseudopotentials used. Since the computations are carried out at 0 K, the calibration also inherently accounts for small effects due to vibrational averaging of the experimental EFG tensor parameters, since these data are acquired at room temperature. Fortunately, however, it is known experimentally for molecules containing second- and third-row elements, such as those considered here, that vibrational effects on the EFG are typically negligible. For example, the change in the ^{23}Na quadrupolar coupling constant in NaF(g) undergoing a transition from the $v = 0$ to $v = 1$ vibrational state is only 1.3%,[40] and for NaCl(s) this change is just under 1%.[41] We choose these molecules for discussion because the atomic masses are comparable to those presently under study, and because of the availability of very precise data for specific vibrational states. While these data are not directly transferrable to solids, it is nevertheless reasonable to suppose that vibrational corrections to the EFG tensors for comparable nuclei in the current work will be small (typically less than our experimental

errors). Recent molecular dynamics studies show that motions can partially average the EFG tensor[42] but this is empirically accounted for in the scaling factors mentioned above, at least to a first approximation. Incidentally, vibrational corrections to shielding constants (which are not used as restraints) may be up to several ppm in certain cases (e.g., ^{25}Mg and ^{17}O in MgO); however, this is over a temperature range of up to 1000°C.[43] Corrections to shielding for atoms such as ^{31}P, ^{13}C, and ^{1}H can be important to consider over smaller temperature ranges.[44,45] We also note that recent NMR crystallographic refinements of zeolite structures (where atoms of similar mass to those studied presently are considered, i.e., Si, O) neglected vibrational corrections to the 0 K computed ^{29}Si chemical shift tensors and were nevertheless extremely successful.[19-22]

In order to determine the appropriate scaling factors we have performed PAW DFT calculations (using CASTEP software[35]) of the ^{11}B, ^{17}O, ^{23}Na, ^{25}Mg, ^{27}Al, ^{91}Zr, and ^{95}Mo EFG tensor parameters of some model compounds whose crystal structures are known with high precision. For ^{11}B, the calibration compounds were: lithium diborate,[46,47] datolite,[48,47] danburite,[49,47] colemanite,[50,47] and sodium tetraborate decahydrate.[51,47] In the case of ^{17}O, coesite,[52,53] α-Al_2O_3,[54,55] and forsterite,[56,57] were used in order to calibrate the PAW DFT EFG calculations. For ^{23}Na, sodium nitrate,[58,59] zektzerite,[60,61] and sodium thiosulfate[62,63] were used as calibration compounds. α- and β-magnesium sulfate,[64] magnesium acetylacetonate,[65] magnesium acetate,[66] magnesium molybdate,[67] magnesium hydroxide,[68] magnesium vanadate,[69] and magnesium tungstate[70] were used to calibrate the ^{25}Mg EFG tensor calculations.[71] α-Al_2O_3,[54,72] topaz,[73,74] YAG,[75,76] and andalusite[77] were used in the case of ^{27}Al. The ^{91}Zr EFG tensor calculations were calibrated using Ba_2ZrF_8,[78,79] K_2ZrF_6,[80,79] *m*- and *o*-zirconium oxide,[81-83] sodium zirconate,[84,85] Na_2ZrSiO_5,[86,87]

$Na_5Zr_2F_{13}$,[88,79] zirconium chloride,[79,89] zirconium iodide,[79,90] and zirconium silicate.[91] Finally, the PAW DFT calculations of the ^{95}Mo EFGs were calibrated using the data for potassium molybdate,[92,93] ammonium molybdate (mP60 and mS60),[94,95] lead molybdate,[96,92] and zinc molybdate.[97,94] These compounds were selected since they all have highly accurate and precise EFG tensor parameters derived from single-crystal NMR or other techniques.

For all nuclei under study, an excellent linear correlation was observed between the experimental and calculated EFG tensor parameters. In all cases, the calculated EFG tensor parameters either overestimated or underestimated the experimental ones by scaling factors ranging from 0.93 for ^{91}Zr to 1.166 for ^{11}B. This discrepancy likely originates from a combination of errors in the quadrupole moments that were used[98] as well as the frozen core approximation used in the PAW method. The plots showing the correlation between the calculated and experimental EFG tensor parameters are shown in Figure 2.1. From the linear correlation in these plots we can extract the factors by which it is necessary to scale the calculated EFG tensor parameters for the structure refinement purposes. These scaling factors, as well as their standard deviations, are given in Table 2.1.

Table 2.1. Scaling factors describing the linear correlations between the PAW DFT calculated EFG tensor parameters and the experimental ones

nucleus	slope
^{11}B	1.166 ± 0.001
^{17}O	1.029 ± 0.007
^{23}Na	1.12 ± 0.08
^{25}Mg	1.14 ± 0.04
^{27}Al	1.01 ± 0.02
^{91}Zr	0.93 ± 0.04
^{95}Mo	1.11 ± 0.02

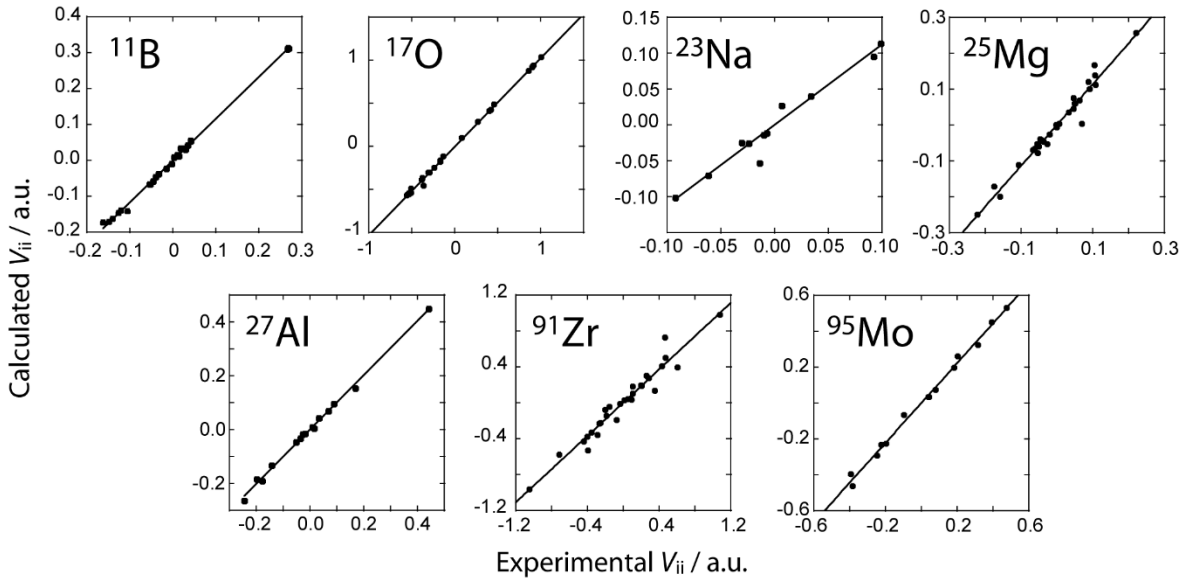

Figure 2.1. Correlations between the calculated and experimental EFG tensor principal components for a test set of compounds (a.u. are atomic units). The experimental error bars are within the size of the symbols.

Based upon these data, we can judge the quality of a given crystal structure (which is not part of the test set) on the basis of the agreement between its EFG tensor components and those which are predicted using the scaled PAW DFT calculations. The cost function defining the quality of the structure, χ^2, depends on the square of the difference between the calculated and experimental EFG tensor parameters, and is scaled by the experimental uncertainty and the standard deviation from the fits in Figure 2.1. The lattice energy is also readily available from the PAW DFT calculations and may be added in an attempt to increase the quality of the refined structure. The expression describing χ^2 is given below.

$$\chi^2 = \sum_{S=1}^{N}\sum_{i=1}^{3}\left(\frac{\frac{V_{ii}^{(S)calc}}{\alpha^{(S)}} - V_{ii}^{(S)exp}}{\sigma^{(S)}}\right)^2 + \left(\frac{E - E^{opt}}{\lambda}\right)^2 \quad (2.1)$$

In this expression, the terms $V_{ii}^{(S)}$, where 'i' can take values of 1, 2, or 3, are the principal components of the EFG tensor for the nucleus denoted 'S', $\sigma^{(S)}$ is the sum of the experimental uncertainty, which is specific to each measurement, and that from Table 2.1, $\alpha^{(S)}$ is the slope from Table 2.1, E is the lattice energy of a test structure, E^{opt} is the lattice energy of the pure DFT energy-minimized structure, and λ is a scaling factor which is determined empirically. This expression contains a single variable parameter, λ. If λ tends towards 0 then the result will be the DFT minimum energy structure. Similarly, if the value of λ tends towards infinity, then a purely NMR-optimized structure will result. The reasoning behind the formulation of eq. 2.1 is that the EFG tensor data alone do not provide enough information to determine the atomic coordinates: the problem is in general underdetermined. By incorporating a DFT-computed energy term, it can be ensured that the experimental data are not over-fitted. The best structures will, of course, require a high weighting of the experimental data so that they remain experimentally-based structures; however, it is important not to over-interpret the correlations from Figure 2.1 and "force" the structure into yielding a perfect agreement with the DFT-computed EFG tensor parameters. Incorporating the lattice energy then ensures that the structures remain reasonable. In practice, an adequate starting value for λ can be deduced logically, if one supposes that near equal weighting needs to be given to both the NMR and the energy terms of eq. 2.1. The inclusion of the EFG term (which reflects experimental data obtained at room temperature) also allows for adjustments of the 0 K pure DFT structure as the refinement progresses.

It should be pointed out that, since E^{opt} is defined to be representative of the lowest energy structure obtainable with DFT, one could envisage the possibility that the initial optimization finds only a local minimum and that the true structure lies at a lower global

minimum energy, but would be characterized by a higher value of χ^2 because of the dependence of this term on the square of the difference in energies (eq. 2.1). This could be a problem for large molecules with many degrees of freedom, e.g., rotable bonds, or for any system where there is reason to believe that the initial structural model is severely problematic. Regardless of the above comments, the cost function in eq. 2.1 emphasizes the fact that the NMR data are refining an initial structural model; appropriate choice of the parameter λ through calibration (*vide infra*) will allow required changes in the structure to obtain the lowest overall value of χ^2, not necessarily the lowest values for each of the two terms in equation 2.1 independently (i.e. χ^2(EFG) and χ^2(DFT)).

2.1.1.3 Refinement Procedure

For the refinement, an initial "guess" structure is geometry-optimized using PAW DFT to yield the lowest energy while maintaining the space group and unit cell parameters determined using XRD. The lattice energy for this structure is taken as E^{opt}. This structure is then systematically modified to create an additional 3*N* crystal structures (*N* being the number of crystallographically distinct sites in the crystal structure) where in each of those 3*N* structures, a single fractional coordinate is increased by a small stepping value, typically 0.0001. The total number of structures can be reduced if certain atoms are located on crystallographic special positions; this is the case for some of the examples in the following chapters. PAW DFT calculations of all the EFG tensors are then performed on each of the new 3*N* structures, and the value of χ^2 for each of these structures is evaluated according to eq. 2.1. Using these data, the structure will be iteratively refined in order to minimize the value of χ^2. Since the number of decimal places given for the EFG tensor components in the

CASTEP output files is small, an efficient least-squares minimization procedure such as the Gauss-Newton algorithm could not be applied. Instead, the stepping direction vector (**p**) was determined as follows, which corresponds to the method of steepest descent:[99]

(2.2) $p_w = \chi^2_w - \chi^2_{w+\varepsilon}$.

In this expression, the optimal relative change in a given coordinate (p_w), where 'w' is a given fractional coordinate value (along either the a, b, or c dimensions), is given as the difference between the initial structure's χ^2 and the value of χ^2 of the structure in which a given coordinate was increased by a value of ε. In this fashion, the stepping vector (**p**), for which each component is defined as the value of p_w for every coordinate, will then point in a direction towards the structure with the minimum value of χ^2.

A line search is then performed along the direction of the vector **p**. The new crystal structure is then determined as the structure having the lowest value of χ^2 along this vector. In practice this is done by determining a series of new structures which vary in the step length by a parameter, ς:

(2.3) $w_{new} = w + \varsigma p_w$.

PAW DFT calculations of V_{ii} and E are then performed on each of the resulting structures in order to evaluate their new χ^2. From this set, the best structure (lowest value of χ^2) is kept and is passed to the next iteration. This is repeated until self-consistency is achieved and the value of χ^2 does not change by a significant amount. This was determined to be the case when the value of χ^2 reached a minimum with respect to changes of 0.0001 in all fractional coordinates. The process is illustrated in Figure 2.2.

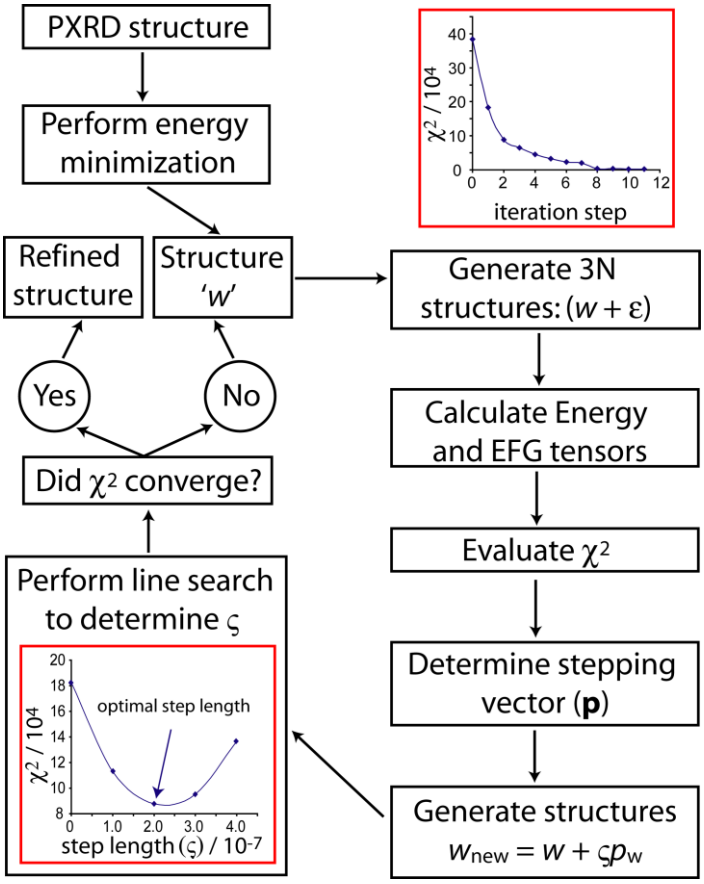

Figure 2.2. Flow chart summarizing the optimization procedure described in this chapter. Graphs showing the convergence of χ^2 and an example line search are shown in red boxes.

2.1.2 α-Al_2O_3

We decided to test the hypothesis that the incorporation of both NMR parameters and energy would yield comparable or higher quality structures than either NMR-refined structures alone, DFT-optimized structures alone, or PXRD structures, as judged by the agreement with an accepted high-quality single crystal X-ray structure. For this purpose, we chose to optimize the structure of α-Al_2O_3 since single crystal NMR data exist for ^{27}Al as well as for ^{17}O. We note that due to the crystal symmetry and space group, there are only two coordinates to be optimized. Several different optimizations were performed using (i)

only the EFG tensor parameters as restraints, (ii) only the DFT energy, (iii) as well as hybrid experimental-theoretical optimizations with different values for λ. The DFT structure was used as a starting point for the NMR crystallographic refinements. The results from these optimizations are summarized in Figure 2.3. An important difference between the present approach and some of the previously published NMR crystallographic approaches for spin-1/2 nuclei is that the experimental NMR data are used as restraints in the refinement process, as opposed to being used to cross-validate purely *ab initio* or DFT-generated structures.

From these data it may be seen that if only the NMR parameters are used (i.e., $\lambda \rightarrow \infty$), then we can artificially "force" the structure into perfect agreement with the NMR data. However, this procedure produces a converged structure which differs from the X-ray structure as is evident from the brown squares in Figure 2.3. As judged by the root-mean-square deviation (RMSD) between all the fractional coordinates, the structure which was optimized using the NMR parameters alone is of higher quality than the DFT-energy optimized structure which is shown as the dashed red line in Figure 2.3. This immediately demonstrates the value of incorporating experimental data into purely computational structure optimization procedures.

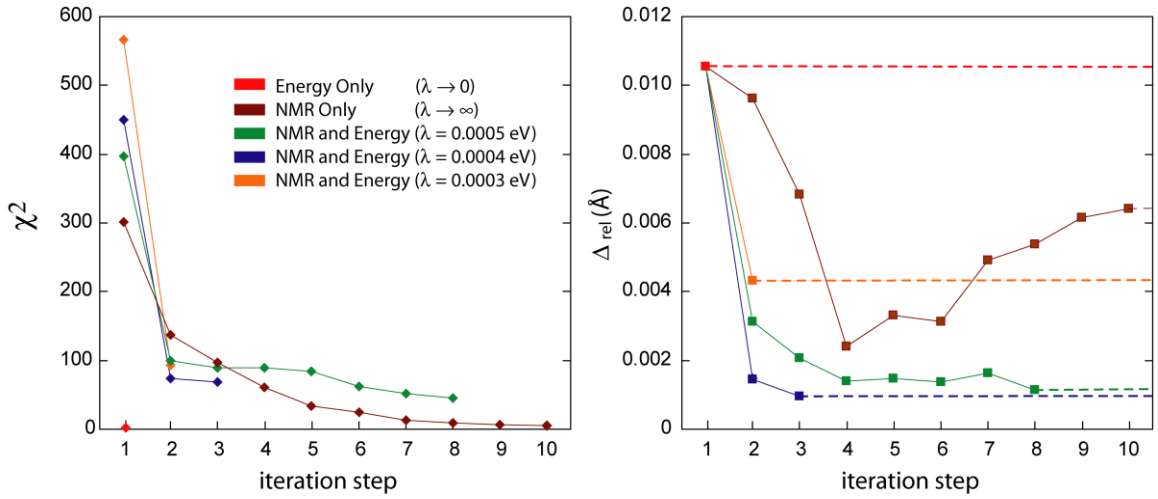

Figure 2.3. Comparison of the χ^2 (filled diamonds, left), along with the relative difference in fractional coordinates, Δ_{rel}, (filled squares, right) between the X-ray structure and the intermediate structure at a given optimization step for α-Al_2O_3 using different weightings for the lattice energy (see eq. 2.1). Dotted lines are used to guide the eye to the Δ_{rel} axis, which indicates the difference between the single crystal X-ray structure (Δ_{rel} = 0) and the various optimized structures.

When the DFT lattice energy and EFG tensor data are both included as refinement restraints, the resulting structure is a compromise between the DFT- and NMR-optimized structures. In this case it is impossible for χ^2 to be 0 since we are forced to compromise and simultaneously find the best agreement with both the NMR data and the lattice energy. We observed that χ^2 converged to some value which is, of course, dependent on λ; but, the resulting 'hybrid' structure was in much better agreement with the accepted single-crystal X-ray structure than with either the pure NMR or the pure DFT energy optimized structures in all cases. The best structure, as assessed by the RMSD to the single-crystal X-ray structure, was obtained with a λ value of 0.0004 eV. The fractional coordinates of this structure

differed from those of the single crystal X-ray structure by an RMSD of only 0.002 Å. For remaining discussions, the concept of a 'best structure' is that with the lowest overall value of χ^2 (eq. 2.1) using the optimized λ value of 0.0004 eV.

The robustness of the method was then tested by distorting the crystal structure of α-Al_2O_3 and optimizing this structure anew. This was done by rounding all the single crystal XRD fractional coordinates of the Al and O sites to one significant digit to maintain the same topology. The final structure, after only 4 iteration steps (λ = 0.0004 eV), was essentially indistinguishable from that obtained during the first refinement process (see Figure 2.4), thereby offering some level of validation regarding the reliability and robustness of the method.

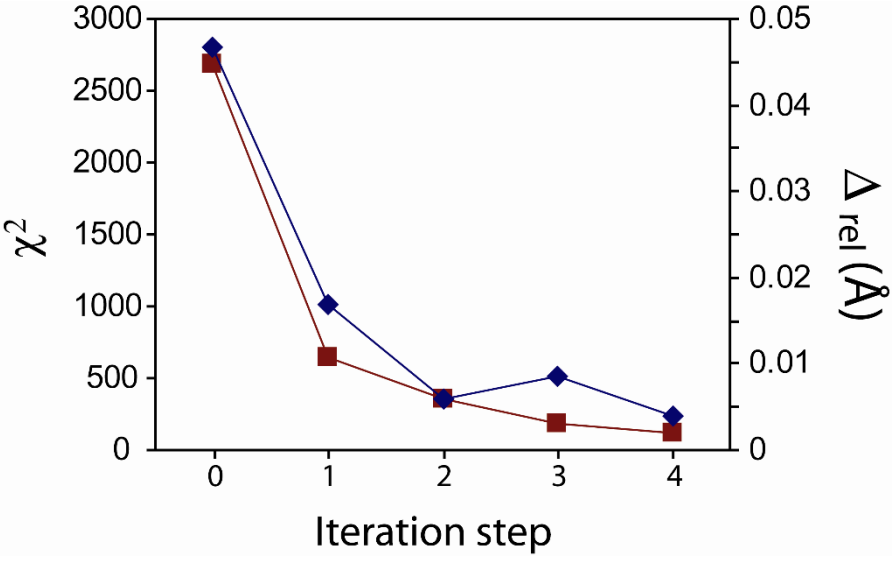

Figure 2.4. Graph showing the convergence of the relative difference in fractional coordinates (Δ_{rel}) of the intermediate structure and those from the single crystal X-ray analysis (blue diamonds),[54] and the convergence of the χ^2 (red squares) for a distorted starting structure of α-Al_2O_3.

2.1.3 Conclusions

A new NMR crystallographic method that incorporates the use of DFT energy and NMR-determined EFG tensor components as constraints in a crystal structure refinement is proposed. This hybrid experimental-theoretical method recognizes that often the structure refinement problem is underdetermined on the basis of only experimental NMR data, and refines the fractional coordinates in a given crystal structure to yield the highest agreement between PAW DFT calculated EFG tensor parameters and those which are measured experimentally. This method is widely applicable and can be applied to any sample containing quadrupolar nuclei. The methodology is also general and could be implemented in combined structure refinement protocols using chemical shift, dipolar, and EFG tensors.

Chapter 2.2: Crystal Structure Refinement and Cross-Validation of Sodium Aluminoborate

2.2.1 Introduction

Sodium aluminoborate is a compound with the empirical formula $Na_2Al_2B_2O_7$, which belongs to the family of non-linear optics materials of the form $A_2E_2B_2O_7$, where A and E can be several combinations of first, second, and third group metal ions.[100-104] $Na_2Al_2B_2O_7$ was first reported in 1971, although only poor-quality PXRD data were presented and no attempt was made to solve the structure.[100] The structure was later noted as being isostructural with $Na_2Ga_2B_2O_7$ and was subsequently refined using Rietveld techniques;[101,102] however, the result was unfortunately of poor quality. The difficulties of diffraction techniques at solving this structure mainly arise from the instability of the crystals[105] that lead to stacking faults and crystal twinning. Later studies attempted to improve the crystal structure of $Na_2Al_2B_2O_7$ using single-crystal X-ray and Rietveld techniques while accounting for crystal twinning[106] and stacking faults,[107] respectively. These stacking faults arise since reflections of the unit cell along the c axis leads to small energy differences and the BO_3 trigonal planes can arrange either in a staggered or an eclipsed fashion with each other. The unit cell for the most stable conformation is shown in Figure 2.5. Even after several reinvestigations of the structure of $Na_2Al_2B_2O_7$, a high-quality structure remains elusive due to the limitations of diffraction methods for this sample.

NMR offers a particularly attractive alternative for such systems since NMR parameters are especially sensitive to the local atomic environment. The effects of the

stacking faults on the observed NMR data are expected to be negligible since the bulk of the nuclei in a powder sample will not be located at such interfaces. The EFGs at the various crystallographic sites will then be a reasonable representation of the effects of an infinite periodic lattice even though the actual sample will contain stacking faults. This point is validated through the sharp NMR line shapes observed experimentally (*vide infra*). Additionally, we can work directly with the powder produced when the material is synthesized and not have to worry about growing single crystals.

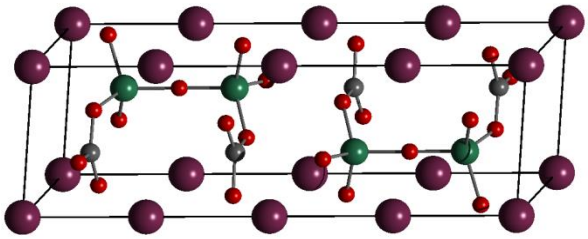

Figure 2.5. Unit cell of the staggered conformation of $Na_2Al_2B_2O_7$ shown along the crystallographic *b* axis. The sodium atoms are purple, aluminium is green, boron is grey, and oxygen is red.

2.2.2 Solid-State NMR

We have performed ^{11}B, ^{17}O, ^{23}Na, and ^{27}Al magic-angle spinning (MAS) NMR experiments on $Na_2Al_2B_2O_7$ in applied magnetic fields of 21.1 T, 11.7 T, and 4.7 T in order to extract the EFG tensor parameters at all atomic positions. Sample spectra are shown in Figure 2.6 along with their simulations.

2.2.2.1 ^{11}B NMR

The ^{11}B MAS NMR spectrum of the central transition is characteristic of a single boron site in a position of axial EFG symmetry. This is consistent with the local site

symmetry determined from PXRD[102] which indicates that the boron site in $Na_2Al_2B_2O_7$ lies on a crystallographic C_3 axis. The moderately large quadrupolar coupling constant (C_Q) is consistent with trigonal planar geometry at boron.[47,108]

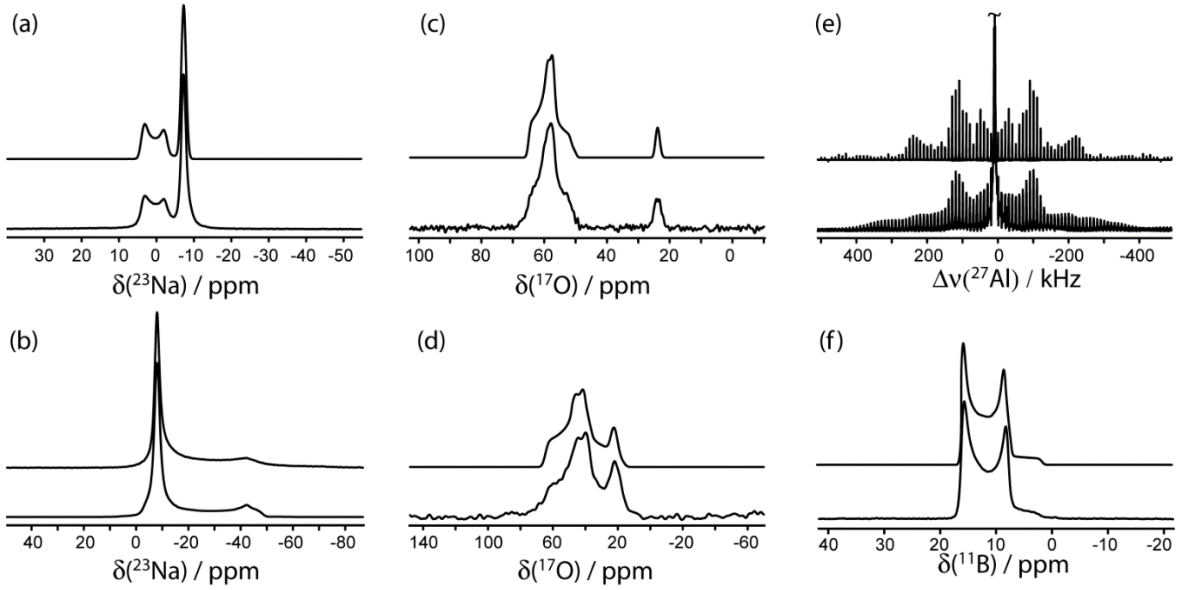

Figure 2.6. MAS NMR spectra of $Na_2Al_2B_2O_7$. In (a) and (b), the ^{23}Na MAS NMR spectra acquired at 11.7 and 4.7 T respectively are shown. The ^{17}O NMR spectra acquired on an isotopically-enriched sample at 21.1 and 11.7 T are shown in (c) and (d), respectively. The ^{27}Al SATRAS NMR spectrum acquired at 11.7 T is shown in (e) and the ^{11}B MAS NMR spectrum acquired at 11.7 T is shown in (f). In all cases the experimental NMR spectrum is shown on the bottom trace and the simulation using the parameters from Table 2.2 is shown in the top trace.

2.2.2.2 ^{23}Na NMR

The two crystallographically distinct sodium sites[102] can be easily distinguished in the ^{23}Na MAS NMR spectra (Figure 2.6(a), (b)). One of the two sites has a very small C_Q of

0.33 MHz and the other site has a somewhat larger C_Q of 1.9 MHz. Since the second site presents a second-order quadrupolar-broadened line shape, the spectrum could be fit directly to extract the NMR parameters; however, this was not the case for the first site. Since no line shape is observed, even at 4.7 T, for this sodium site, the parameters cannot be reliably extracted using any single spectrum. Fortunately, according to the PXRD space group,[102] this sodium site lies on a crystallographic C_3 axis. Since, if we assume axial symmetry, the observed spectral shift of the central transition (δ), is magnetic field dependent and is fully defined by the C_Q and δ_{iso} parameters, as described in the following expression,[109] we can directly extract the NMR parameters from the NMR spectra acquired at multiple fields.

$$(2.4)\quad \delta = \delta_{iso} - \frac{3C_Q^2}{40\nu_0 I^2(2I-1)^2}\left(I(I+1)-\frac{3}{4}\right)\frac{10^6\,Hz}{\nu_0}$$

In this expression, I corresponds to the spin quantum number of the nucleus (I = 3/2 in the case of ^{23}Na) and ν_0 corresponds to the Larmor frequency which depends directly on the applied magnetic field strength. The parameters are summarized in Table 2.2. The impact of a possible distribution of ^{23}Na chemical shifts was assessed with ^{23}Na double-rotation NMR and found to be negligible ($\leq$ 0.3 ppm).

2.2.2.3 ^{17}O NMR

The ^{17}O MAS NMR spectra of $Na_2Al_2B_2O_7$ are shown in Figure 2.6 (c) and (d). Both crystallographically distinct sites can be distinguished in the NMR spectra and assigned unambiguously using their relative intensities since there are 6 O1 sites for every O2 site. The EFG tensor parameters for the O1 site can be extracted directly from the spectrum by fitting the second-order quadrupolar line shape. In the case of the O2 site however, multiple

field data were necessary to extract the quadrupolar parameters as the line shape could not be fit. Luckily, since the O2 site lies on a crystallographic C_3 axis, equation 2.4 could be used, as was done for ^{23}Na, with the exception that I is 5/2 in this case. If this were not the case, the structure refinement procedure would need to use the quadrupolar product ($P_Q = C_Q(1+\eta^2/3)^{1/2}$) instead of the EFG tensor components as this would be the only measurable parameter.

Table 2.2. NMR parameters for the six crystallographic sites in $Na_2Al_2B_2O_7$ determined from the spectral data in Figure 2.6

site	δ_{iso} / ppm	C_Q / MHz[a]	η[a]
Al	70.3 ± 0.1	-1.65 ± 0.03	0.05 ± 0.05
Na1	5.5 ± 0.5	-1.9 ± 0.1	0.1 ± 0.1
Na2	-7.1 ± 0.2	-0.33 ± 0.05	0
B	18.3 ± 0.2	2.63 ± 0.01	0.00 ± 0.05
O1	65.0 ± 0.5	-3.7 ± 0.1	0.77 ± 0.05
O2	24.5 ± 0.5	-1.4 ± 0.3	0

[a]All sites other than O1 are C_3 symmetric and thus have axially symmetric EFG tensors.

2.2.2.4 ^{27}Al NMR

The centerband of the ^{27}Al NMR spectrum did not have a second-order line shape. In order to extract the EFG tensor information we decided to acquire the satellite transitions (primarily ±3/2 to ±1/2) under MAS conditions. This is sometimes referred to as satellite transition spectroscopy (SATRAS) in the literature.[110,111] Unlike the more commonly observed central transition, the satellite transitions are affected by the quadrupolar interaction to first order and are thus much broader. This makes it possible to measure accurate quadrupolar coupling constants in cases where the EFGs are weak. This approach was not used in the case of ^{23}Na and ^{17}O due to the small number of sidebands (^{23}Na), or the low sensitivity (^{17}O). The ^{27}Al SATRAS NMR spectrum acquired at 11.7 T under 10 kHz MAS is shown in Figure 2.6 (e) along with the fit. The parameters are given in Table 2.2.

2.2.3 *Crystal Structure Refinement*

Chemical shift anisotropy (CSA) parameters for quadrupolar nuclei could also potentially be used as restraints in the refinement process, as has been done for spin-1/2 nuclei. However, the strong dipolar coupling between the abundant ^{27}Al, ^{11}B, and ^{23}Na spins in $Na_2Al_2B_2O_7$ made it impossible to precisely measure CSA from the stationary NMR spectra of these quadrupolar nuclei, even in an applied magnetic field of 21.1 T. Similarly, isotropic chemical shifts were not used due to the much larger computational expense relative to EFG tensor calculations (the chemical shifts were used instead for an independent cross-validation procedure, *vide infra*).

A DFT geometry optimization (energy minimization) was performed with CASTEP using the original powder X-ray crystal structure[102] of $Na_2Al_2B_2O_7$ as a starting point. This structure was then refined as described earlier using χ^2 instead of only the DFT-computed lattice energy as a minimization function. For all optimizations, the space group and unit cell parameters were fixed to those determined using PXRD. We note that due to the crystal symmetry and space group, there are five coordinates to be optimized.

Table 2.3. Values of χ^2 obtained for the different structures of NABO as well as the RMSD between those structures and the NMR crystallographic one

Structure	RMSD (Å)[a]	χ^2 (total)	χ^2 (energy)	χ^2 (EFG)	χ^2 (δ_{iso})[c]
He, PXRD[101]	0.055	2.23×10^7	2.22×10^7	1.35×10^5	1.70×10^4
Gao, PXRD[106]	0.058	1.96×10^7	1.92×10^7	3.87×10^5	1.81×10^4
He, Single Crystal XRD[105]	0.023	3.84×10^5	3.72×10^5	1.11×10^4	7605
DFT energy optimized ($\lambda \rightarrow 0$)	0.002	625	0	625	7025
NMR optimized[b] ($\lambda \rightarrow \infty$)	0.001	374	6	368	7017
NMR and energy optimized ('NMR crystallographic structure' (λ = 0.0004 eV))	0	373	0.6	372.4	6982

[a] These RMSDs were calculated using only the five variable crystallographic positions. The RMSDs including the coordinates which are fixed by symmetry are 52.7% smaller. The RMSDs stated in this table are with respect to the λ = 0.0004 eV structure.

[b] 'NMR optimized' structure refers to an optimization using EFG data, without including the lattice energy as a minimization parameter.

[c] Cross-validated χ^2 values for chemical shifts; chemical shifts were not used as restraints in any of the refinements.

Two refinements were performed: (i) using only the NMR parameters ($\lambda \rightarrow \infty$), and (ii) a combination of the NMR parameters and the DFT lattice energy. Since λ cannot be optimized on the sample itself in this case, the optimal value of 0.0004 eV, which was determined using α-Al_2O_3 (see Chapter 2.1), was used. For this particular sample, this places a larger weighting on the EFG tensor parameters than what was done for α-Al_2O_3 since we have NMR data for six nuclear sites in this case instead of two as in the case of α-Al_2O_3. However, the optimal value for λ should remain fairly constant between similar compounds of the same elements. When more NMR data are present, a stronger weighting will be given to the NMR parameters whereas the lattice energy will become more important if the NMR data are sparse. Similarly, if the experimental error on the EFG tensor parameters is large, as may be the case if only low quality NMR data can be acquired, then the lattice energy will contribute more to χ^2.

In the case of $Na_2Al_2B_2O_7$, unlike with α-Al_2O_3 (see chapter 2.1), the structure which was optimized using only the NMR data could not converge to a χ^2 of 0. Since in the case of $Na_2Al_2B_2O_7$ there are 12 independent EFG tensor parameters instead of 4, the competition between these becomes more severe and a structural change which may improve the agreement of one calculated parameter can have a negative effect on another.

The results of the various optimizations are summarized in Table 2.3. The total value of χ^2 is listed along with the contributions from the energy term and the EFG term independently (terms 1 and 2 from eq. 2.1). Several points are worth discussing. First, the values of χ^2 for all of the previously proposed XRD structures follow the expected trend, as the SCXRD structure has a lower value of χ^2 than do the PXRD structures, with the NMR crystallography structure (i.e. the structure which was refined using both NMR and lattice

energy data) exhibiting the lowest overall χ^2. The original PXRD structure[102] is characterized by a χ^2 of 2.23 x 10^7 whereas the agreement with experimental EFG data is improved for the single crystal X-ray structure using a twinned crystal (Table 2.3). Second, it is seen that the energy term is largely responsible for the large values of χ^2 for all X-ray structures. Only for the structures with the lowest overall values of χ^2 (the DFT, NMR, and hybrid DFT/NMR structures) do the contributions to χ^2 from the EFG term become dominant in determining the overall value of χ^2. It is important to recall here that the relative values of the two contributions to χ^2 are determined entirely by the optimized value of λ which was determined during the calibration procedure; therefore, it is not particularly surprising that the pure energy term appears to do "most of the work" in optimizing the structure, with the EFG tensor parameters becoming more important during the final 'fine-tuning' stages of the structure refinement. Third, it is seen that the pure DFT, pure NMR, and hybrid DFT/NMR refinements result in structures and χ^2 values which are all very similar. Encouragingly, this implies that the NMR-only refinement did not result in a distortion in the structure simply to satisfy the experimental data, as could happen if the problem is severely underdetermined. This is encouraging because it shows that initial structural models (either from X-ray or from DFT) can be refined directly against experimental EFG tensor data. Nevertheless, since the energy is calculated by default during EFG tensor calculations, the hybrid DFT/NMR method is not significantly more costly in terms of computational time, and has the added benefit of allaying any concerns about structures being over-fit to the experimental data. The inclusion of the lattice energy in the optimization did not improve the value of χ^2 beyond what was obtained using NMR parameters alone (i.e., 374 vs 373). However, the structures which are optimized using

experimental NMR data have χ^2 values which are lower than the structure which is optimized using DFT alone (χ^2 = 625). Thus, while it is clear that the improvements offered by the hybrid approach are small in this case, there is nevertheless an improvement in the value of χ^2 when NMR data are incorporated into the refinement procedure (i.e. NMR-only or DFT/NMR). The RMSDs between the refined NMR crystallographic structure and the X-ray structures are non-trivial; however, it is not surprising that they are small (0.02 – 0.06 Å). It is interesting to note that the order of χ^2 follows the expected trend that the PXRD structures are the worst, followed by the single-crystal XRD structure, the DFT lattice energy minimized structure, and then the NMR crystallographic one. While the DFT-energy-minimized structure, the NMR-only structure, and the NMR crystallographic structure are all equivalent within experimental error when judged by their RMSDs, the latter two structures provide better agreement with the experimental NMR data. This point is further discussed in the context of cross-validation against both EFG and chemical shift data (*vide infra* and Table 2.3).

Table 2.4. Fractional coordinates from the NMR crystallographic refinement and those determined X-ray diffraction

coordinate[a]	NMR crystallography (DFT+EFG) structure	PXRD structure of He[102]	PXRD structure of Gao[107]	SCXRD structure[106]
Al 'z' coordinate	0.6381	0.6374	0.6349	0.63991
B 'z' coordinate	0.1031	0.0978	0.100	0.1040
O1 'x' coordinate	0.9614	0.9704	0.976	0.9612
O1 'y' coordinate	0.6100	0.6087	0.598	0.6029
O1 'z' coordinate	0.8968	0.8916	0.8971	0.8952

[a] The remaining coordinates are fixed by symmetry (atoms on special positions).

The final fractional coordinates (from the NMR and energy optimization) are given in Table 2.4 and are compared to the coordinates generated from PXRD data. Very small

changes in the fractional atomic coordinates induce very large changes in the calculated EFG tensor parameters. This is a clear demonstration of the sensitivity of NMR to local structure and shows why it is of interest to include experimental data, even if DFT structures seem to be quite accurate in many cases. This fact also indicates that the accuracy of the resulting fractional coordinates is likely to be high, perhaps as good as 0.002 Å as was noted in the case of α-Al_2O_3. The ^{27}Al EFG tensor parameters are by far the most sensitive to the atomic coordinates. In order to ensure that the differences in the fractional coordinates are not simply due to temperature-induced vibrational effects, ^{27}Al MAS NMR experiments were performed at 9.4 T with temperatures ranging from 0°C to 40°C. By comparison, the X-ray studies were performed at 25°C. No change in the SATRAS line shape was observed in this temperature range. Similarly, no change was observed in the ^{23}Na NMR spectrum over the same temperature range. We can thus conclude that the fractional coordinates are not particularly sensitive to small temperature variations near ambient temperatures. Even though the energy-minimized and NMR crystallographic structures differ by a RMSD of only 0.002 Å in this case, we believe that it is advantageous to use experimental data when solving or refining crystal structures when this is possible.

2.2.4 Cross-Validation

Cross-validation is a technique whereby a test set of data from an experimental dataset is excluded from a refinement process, a structure is refined, and then the excluded test set is predicted from the refined structure. This is a common technique in X-ray crystallography, where an R_{free} parameter is reported.[112-114] Solution NMR studies of proteins also use the method with NMR data.[115] The method is particularly important in

cases where experimental data are sparse. In order to probe the accuracy and variability of the fractional coordinates of $Na_2Al_2B_2O_7$ determined with our refinement method, we have performed a full cross-validation against the experimental EFG data. Briefly, a series of NMR crystallographic refinements were performed while excluding the EFG tensor parameters of one of the six atomic sites (the test set). The final structure from one of these refinements is used in a CASTEP calculation of the EFG tensors for the omitted site. This process is repeated six times, using a different test set in each case. In all cases the resulting structures were very similar to the one reported in Table 2.4. For example, the fractional coordinates predicted for an atom when its EFG tensor parameters were omitted from the optimization procedure varied by 0.00041 to 0.00004. The EFG tensor parameters which are predicted when they are omitted from the structure refinement were also very similar, and may be quantified using χ^2. The χ^2 which is calculated using these predicted NMR parameters was of 2057, which is, of course, larger than the χ^2 of 373 which was obtained when including all the EFG tensor parameters, and the χ^2 of 625 from the energy-minimized structure. This is however a significant improvement over the XRD structures. The successful prediction of the correct EFG tensor parameters from the cross-validation demonstrated that the structure is acceptable and that the NMR data are not being grossly over-interpreted. A graph showing the comparison of the experimental and scaled calculated EFG tensor parameters from the PXRD structure, the NMR crystallography structure and those predicted using the cross-validation is shown in Figure 2.7. Unfortunately it is not particularly meaningful to report a cross-validation quality factor (analogous to the *Q* value used for NMR residual dipolar coupling refinements of biomolecules)[115] due to the limited number of data points for each type of nuclide.

Since the isotropic chemical shifts were omitted from the optimization procedure they can also be used as an independent test of the quality of the end structure. The GIPAW DFT computed isotropic magnetic shieldings were calculated for all the structures discussed in the text. In order to quantify the agreement between structures, the χ^2 values associated with isotropic chemical shifts were calculated using equation 2.1 by using isotropic chemical shifts instead of EFG tensor components. The χ^2 value obtained for the chemical shifts of two PXRD structures are on the order of 1.8×10^4 whereas those of the single crystal X-ray structure and of the refined structures are less than half this value. We can therefore show, with the use of independent parameters, that the NMR crystallographic structure shows improved agreement with all experimental NMR observables which are available. Additionally, it is interesting to note that the NMR crystallographic structure also predicted the chemical shifts more accurately than both the NMR and DFT structures. This supports the fact that the incorporation of both DFT energy and EFG tensor parameters leads to higher quality crystal structures than either of the two methods alone.

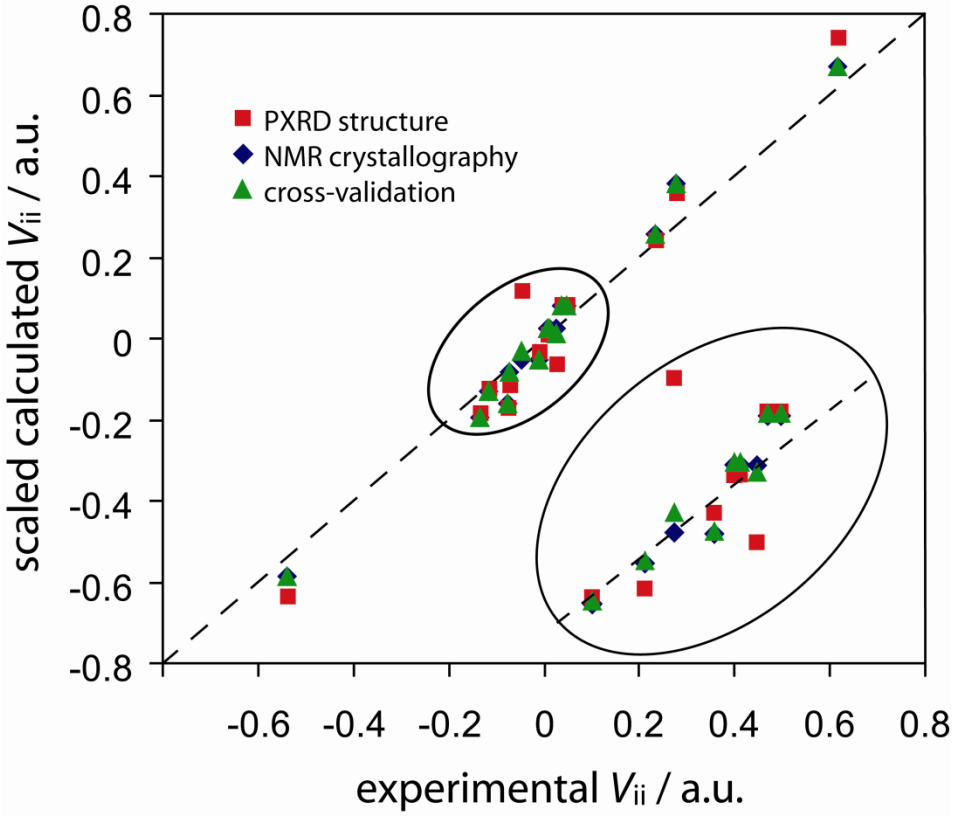

Figure 2.7. Comparison of the scaled calculated EFG tensor parameters from He's PXRD structure[102] (red squares), NMR crystallography (blue diamonds), and cross-validation (green triangles) with those measured experimentally.

2.2.5 Conclusions

This chapter presented the application of our NMR crystallographic method for the crystal structure refinement of $Na_2Al_2B_2O_7$. This sample is plagued by crystal twinning and stacking faults which have rendered the determination of accurate fractional coordinates using diffraction methods highly difficult. Accurate fractional coordinates have been determined using ^{11}B, ^{17}O, ^{23}Na and ^{27}Al solid-state NMR data. The refined structures have been verified using a systematic cross-validation procedure. It was found in the case of $Na_2Al_2B_2O_7$ that refinement against experimental EFG tensor parameters alone yielded a

structure of similar quality as a purely DFT-optimized structure. One time-saving advantage of the method, when compared to other NMR crystallographic techniques, is that the structure is refined against EFG tensor parameters (which are significantly computationally quicker to calculate than shielding tensors) and then validated against independent shielding tensor data, which only need to be calculated once. The simultaneous incorporation of the DFT energy and the EFG tensor parameters as constraints improved the final refined crystal structure, when compared to the NMR- or DFT-refined crystal structures.

2.2.6 Experimental

2.2.6.1 Sample Preparation

Aluminium oxide and boric acid were purchased from Strem chemicals, sodium bicarbonate was purchased from Aldrich, and 10% ^{17}O labeled water was purchased from Spectra Stable Isotopes (Columbia, MD). All were used without further purification.

Sodium aluminoborate was prepared by grinding 200 mg of Al_2O_3, 342.6 mg of H_3BO_3, and 329.6 mg of $NaHCO_3$ together. This mixture was then placed in a crucible and heated to 300°C for 5 hours followed by a 5 hour heating period at 500°C, and finally a heating period of 3 days at 900°C. Several intermediate grindings were performed to ensure the homogeneity of the reaction mixture.[107] The sample was heated at 200°C for several hours prior to NMR experiments to ensure the staggered form of $Na_2Al_2B_2O_7$ was maintained.

An approximately 10% ^{17}O labeled sample of sodium aluminoborate was prepared by recrystallizing 126.5 mg of boric acid from 10% ^{17}O-labeled water prior to the reaction. The

appropriate molar ratios of non-labeled Al_2O_3 and $NaHCO_3$ were added and the same procedure as was described above was used.

For all NMR experiments, the sample was powdered and tightly packed into either 4 mm or 7 mm o.d. zirconium oxide rotors. The experiments performed at 11.7 T used a Bruker AVANCE 500 NMR spectrometer, those at 9.4 T used a Bruker AVANCE III 400 NMR spectrometer, and those at 4.7 T used a Bruker AVANCE III 200 NMR spectrometer. The experiments performed at 21.1 T used the AVANCE II 900 NMR spectrometer at the National Ultra-high Field NMR Facility for Solids in Ottawa.

2.2.6.2 ^{27}Al NMR

The ^{27}Al SATRAS NMR spectrum of $Na_2Al_2B_2O_7$ was acquired at 11.7 T ($\nu_0(^{27}Al)$ = 130.3 MHz) using a 4 mm triple resonance MAS probe. A spinning frequency of 10 kHz was used and a simple pulse and acquire method was applied. A pulse length of 1.0 μs was used along with a 2 MHz spectral window and 2522 scans. The variable temperature ^{27}Al SATRAS NMR experiments were performed at 9.4 T ($\nu_0(^{27}Al)$ = 104.3 MHz) using a 4 mm triple resonance MAS probe with an 8 kHz spinning frequency, a 0.5 μs pulse length, a 0.5 s recycle delay, and a total of 240 scans. The chemical shifts were referenced to aqueous aluminium nitrate (δ = 0 ppm).

2.2.6.3 ^{23}Na NMR

^{23}Na MAS NMR experiments were performed at 11.7 T ($\nu_0(^{23}Na)$ = 132.3 MHz) under 10 kHz MAS. The spectrum was generated with the simple pulse and acquire method using a 60 μs central transition selective excitation pulse, a 0.5 s recycle delay, and a total of 60 scans. A ^{23}Na NMR spectrum was acquired at 4.7 T ($\nu_0(^{23}Na)$ = 52.8 MHz) using a 7 mm

triple resonance MAS probe. A 5 kHz MAS spinning frequency was used along with a 1.75 μs excitation pulse, a 4 s recycle delay, and a total of 128 scans. The chemical shifts were referenced to dilute NaCl using solid NaCl as a secondary reference (δ = 7.21 ppm).

2.2.6.4 ^{11}B NMR

^{11}B MAS NMR experiments were performed at 11.7 T ($\nu_0(^{11}B)$ = 160.5 MHz) using a 4 mm triple resonance MAS probe and a 10 kHz spinning frequency. A rotor synchronized Hahn-echo sequence was used with a 1.4 μs 90° excitation pulse and a 4 s recycle delay. A total of 32 scans were collected. The echo was subsequently left shifted to obtain the correct phase information. The chemical shifts were referenced to $F_3B{\cdot}O(C_2H_5)_2$ using sodium borohydride as a secondary reference (δ = -42.06 ppm).

2.2.6.5 ^{17}O NMR

^{17}O NMR experiments were performed at 11.7 T using a 4 mm triple resonance MAS probe and a 10 kHz spinning frequency. The simple pulse and acquire method was used with a 5.5 μs central transition selective excitation pulse, a 4 s recycle delay, and 39320 scans. The spectrum acquired at 21.1 T used a 4 mm double resonance MAS probe and a 12.5 kHz spinning frequency. The pulse and acquire method was used with a 2 μs central transition selective excitation pulse, a 4 s recycle delay, and a total of 13840 scans. The chemical shifts were referenced to liquid D_2O (δ = 0 ppm).

The MAS NMR spectra were fit with the use of WSOLIDS1[116] in order to extract the chemical shift and EFG tensor information. The satellite transition sidebands from the ^{27}Al NMR spectrum of $Na_2Al_2B_2O_7$ were fit using SIMPSON.[117]

2.2.6.7 DFT Calculations and Structure Refinement

All (GI)PAW DFT calculations were performed with CASTEP NMR (ver. 4.1) using the exchange correlation functional of Perdew Burke and Ernzerhof (PBE)[118] and a 6x6x2 k-point grid. A kinetic energy cutoff of 610 eV was used for all the NMR calculations; however, this value was set to 450 eV for the geometry optimization. The intermediate structures in the geometry optimization procedure were all generated using an in house C program which used the theory described in chapter 2.1. A total of 518 PAW DFT calculations of EFG tensor parameters were performed for this study. Each PAW DFT calculation took several hours and, on average, one optimization step for a given compound was performed per day. The absolute magnetic shieldings used for the comparison between calculated and experimental chemical shifts were calculated using the same structures which were used for the calibration of the EFG tensor calculations (see chapter 2.1).

The space group used in all cases is *P-31c* and the lattice parameters for the optimized structures and the original PXRD structure[102] are a = 4.8113 Å and c = 15.2781 Å. The cell lengths in the SCXRD structure[106] are a = 4.8010 Å and c = 15.2425 Å and those for the PXRD structure of Gao[107] are a = 4.80760 Å and c = 15.2684 Å

Chapter 2.3: Incorporating Dipolar, Shielding, and Quadrupolar Information for the Crystal Structure Refinement of Sodium Diphosphates

2.3.1 Introduction

Most of the NMR crystallographic methods focus on the measurement of dipolar coupling for pairs of spin-1/2 nuclei. This is the case since dipolar coupling can yield an internuclear distance directly that can be used as a strong, unambiguous, structural restraint. As was shown in Chapter 2.2, the EFG tensor can be easily measured for quadrupolar nuclei and can be used to refine existing structural models and obtain more accurate crystal atomic coordinates. The combination of EFG tensor information with dipolar coupling information would, in principle, yield crystal structures with even higher accuracy. Dipolar coupling information would also alleviate issues with respect to the resonance assignments that may arise in cases when multiple resonances of a given element are present. Qualitative information on the distances between quadrupolar nuclei can be obtained, with high resolution, using spin diffusion (SD) DOR NMR;[119-121] the spin diffusion build-up rate has been shown to be correlated to the dipolar coupling strength.[122] Obtaining quantitative dipolar coupling information is, however, difficult and remains an active area of research.[123-131] The incorporation of chemical shift tensor information into least-squares crystal structure refinements, using the GIPAW method, may also improve the refined crystal structures; however, this is currently too computationally demanding.

In this work, we analyze the crystal structures of sodium pyrophosphate[132] ($Na_4P_2O_7$) and trisodium hydrogen pyrophosphate monohydrate[133] ($Na_3HP_2O_7 \cdot H_2O$) using ^{31}P and ^{23}Na MAS NMR, ^{23}Na DOR and 2D SDDOR NMR, as well as PXRD. These compounds were selected due to their importance as calibration standards for various spectroscopic methods including ^{31}P dipolar recoupling experiments,[134] ^{23}Na MQMAS NMR spectroscopy,[135,136] X-ray photoelectron spectroscopy,[137,138] and Raman spectroscopy.[139] For many of these applications, the knowledge of accurate bond lengths is key in the interpretation of the data. The structures are iteratively refined in order to improve the overall agreement between the experimental SDDOR, EFG tensor, and shielding tensor data, and those data predicted from a test structure. The EFG tensors are predicted for a given test structure using PAW DFT calculations[34,35,37,38,140] and the DFT lattice energy is also used as a structural restraint. The ^{31}P chemical shift tensor data and ^{23}Na isotropic chemical shifts, predicted with the use of GIPAW DFT,[36] are then used to independently cross-validate the test structures. In the case of $Na_3HP_2O_7 \cdot H_2O$, SSNMR and DFT data are also used to locate the position of the hydrogen atoms that couldn't be detected using PXRD.[133] In a related study, a combined ^{23}Na NMR and PXRD technique has been used to solve the structure of Na_2HPO_4;[141] however, the NMR parameters were not used in the refinement process. We additionally determine the crystal structure of the nonahydrate $Na_3HP_2O_7 \cdot 9H_2O$ from single crystal (SC) XRD and compare it to the refined crystal structure of $Na_3HP_2O_7 \cdot H_2O$. This structure provides an independent verification of the structural changes to the pyrophosphate anion upon NMR crystallographic refinements.

2.3.2 Spin Diffusion DOR (SDDOR)

In complex spin systems, dipolar coupling interactions can typically only be probed with the use of 2D correlation NMR experiments. In the case of quadrupolar nuclei, this means that double-rotation is necessary since the spectral overlap in MAS-based methods precludes the measurement of dipolar coupling in multiple-spin systems. There are two homonuclear correlation methods that have been proposed for DOR NMR. The first technique, SDDOR, uses the natural dipolar-mediated spin diffusion of the magnetization to generate correlations between sites that are close to each other in space. The second technique uses symmetry-based recoupling pulse sequences to excite 2-spin double-quantum coherences. The double-quantum technique can provide more direct dipolar coupling information and makes it possible to provide correlations between equivalent sites but the technique is significantly less sensitive than SDDOR. The SDDOR pulse sequence is depicted in Figure 2.8, along with an example ^{23}Na SDDOR NMR spectrum for sodium deoxycytidine monophosphate (dCMP).[121]

Extracting dipolar coupling information from spin diffusion data is, unfortunately, very challenging. In principle, spin diffusion involves the complicated spin dynamics between hundreds of atoms and cannot be modeled quantum mechanically, particularly for quadrupolar nuclei, due to the computational cost. In the case of ^{1}H and ^{31}P NMR, spin diffusion has been modelled approximately using the kinetic rate matrix approach. This approach is based on the fact that the spin diffusion between two isolated spins is approximately exponential, as was also shown in the case of ^{23}Na SDDOR NMR

experiments on monunucleotides.[121] The rate matrix however makes it possible to simulate multiple-spin dynamics.

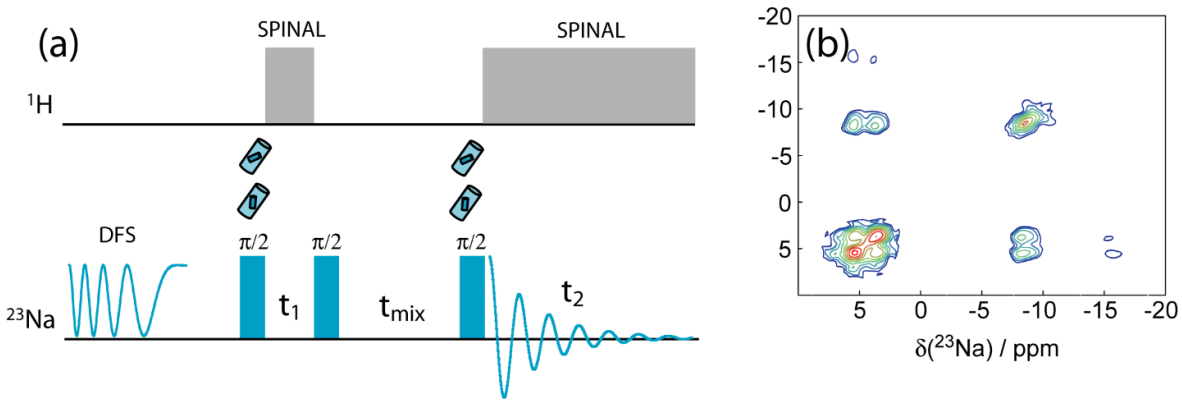

Figure 2.8. (a) The SDDOR pulse sequence is shown; a 90° pulse excites single-quantum coherences that evolve during t_1 and are then reconverted into zero-quantum coherences for the duration of the mixing time (t_{mix}) with a second 90° pulse until the signal is detected with a third 90° pulse. A double-frequency sweep (DFS) pulse is used to enhance the CT NMR signal. The first and third pulses are rotor-synchronized to remove the odd-ordered sidebands. ^{1}H decoupling is used during both t_1 and t_2. An example ^{23}Na SDDOR NMR spectrum is shown in (b) where the correlations between the three ^{23}Na resonances appear off the diagonal.

The rate of spin diffusion under spinning conditions is proportional to the square of the dipolar coupling between the spins.[142] Macroscopic spin diffusion can then be summarized in a rate matrix, **K**, with individual elements represented as:

$$k_{i,j} = \sum_{\lambda} \frac{A}{\left(r_{i,j}^{6}\right)_{\lambda}} \quad (2.5)$$

where *i* and *j* are nuclei residing in different sites, $r_{i,j}$ is the distance separating the nuclei, *A* is a constant that incorporates the magnetogyric ratios of the nuclei and the spin-rate dependence of the spin diffusion. *A* is typically optimized to best fit the data. In this work, a sum over all spins within 30 Å was used.

The diagonal elements of the spin diffusion rate matrix, **K**, are calculated as:

$$k_{ii} = -\sum_{i \neq j} k_{i,j} \quad (2.6)$$

such that the sum of the elements in the rows of the rate matrix is zero. The effects of spin diffusion, including relayed spin diffusion, which may be important in these samples, can then be simulated as follows:

$$P_{i,j} = B_{i,j}\left[\mathbf{X}\exp(-\mathbf{\Lambda}\cdot t_{mix})\mathbf{X}^{-1}\right]_{i,j} \quad (2.7)$$

In the equation above, $P_{i,j}$ corresponds to the cross-peak intensity in an SDDOR experiment, **Λ** is a matrix containing the eigenvalues of **K** along the diagonal, **X** is the matrix of eigenvectors of **K**, t_{mix} is the mixing time and $B_{i,j}$ is an experimentally optimized constant. For spin-1/2 nuclei, $B_{i,j}$ corresponds to the equilibrium magnetization of *j*; however, this cannot be used for quadrupolar nuclei since the asymptotic cross-peak intensities depend on the EFG tensors of the nuclei, as well as their relative orientations.[122]

This approach then permits the simulation of spin diffusion build-up curves directly using a crystal structure. Only the absolute scaling of the spin diffusion rates (*A*) and the relative asymptotic cross-peak intensities ($B_{i,j}$) need to be optimized. In order to avoid an over-interpretation of the data and provide a more rigorous test of the rate matrix method for quadrupolar nuclei, the spin diffusion build-up curves for all compounds in this work,

measured under similar experimental conditions, were simulated simultaneously using a single value of *A*.

The potential issues caused by rapid relaxation of the quadrupolar nuclei are alleviated by normalising the cross-peak as follows in both the experiments and the simulations:

$$P_{i,j}^{norm} = \frac{P_{i,j} + P_{j,i}}{P_{i,i} + P_{j,j} + P_{i,j} + P_{j,i}} \quad (2.8)$$

2.3.3 Sodium Pyrophosphate ($Na_4P_2O_7$)

The crystal structure of $Na_4P_2O_7$ has been solved using SCXRD at 22°C and it was reported that it crystallizes in the orthorhombic $\mathbf{P}2_12_12_1$ space group (a = 9.367 Å, b = 5.39 Å, and c = 13.48 Å).[132] There is one molecule in the asymmetric unit and all the phosphorus, sodium, and oxygen sites are inequivalent. The NMR parameters of the ^{31}P[143] and ^{23}Na[136] nuclei in $Na_4P_2O_7$ are already known with high precision as this is a standard sample for setting up ^{23}Na MQMAS[135,136] as well as ^{31}P dipolar-recoupling NMR experiments.[134]

Table 2.5. ^{23}Na NMR parameters for $Na_4P_2O_7$

site[a]	δ_{iso} / ppm	C_Q / MHz	η
Na1	5.52 ± 0.15	2.08 ± 0.05	0.26 ± 0.05
Na2	1.96 ± 0.15	2.30 ± 0.05	0.70 ± 0.05
Na3	10.41 ± 0.15	2.90 ± 0.05	0.47 ± 0.05
Na4	6.36 ± 0.15	3.22 ± 0.08	0.56 ± 0.06

[a] See the main text for details relating to the assignment of the resonances.

Although ^{31}P NMR is a valuable spectroscopic tool, the chemical shift tensor is mainly sensitive to covalent bonding at short distances and may not be the most suitable probe for longer-range crystal packing effects.[144] There are, however, four inequivalent

sodium sites that may be probed *via* ^{23}Na NMR, see Figure 2.9. Unlike the phosphorus atoms, where the local phosphorus-oxygen bonds largely determine the ^{31}P NMR parameters, the sodium cations do not engage in covalent bonding. The environment surrounding the sodium cations is potentially more variable and one would expect the ^{23}Na NMR parameters to change notably as a function of the structure.[145] In principle, the EFGs could also be probed using ^{17}O, which is also quadrupolar; however, in practice isotopic enrichment is required, the spectral resolution may be poor, and spectral assignment can be quite difficult.[146,147]

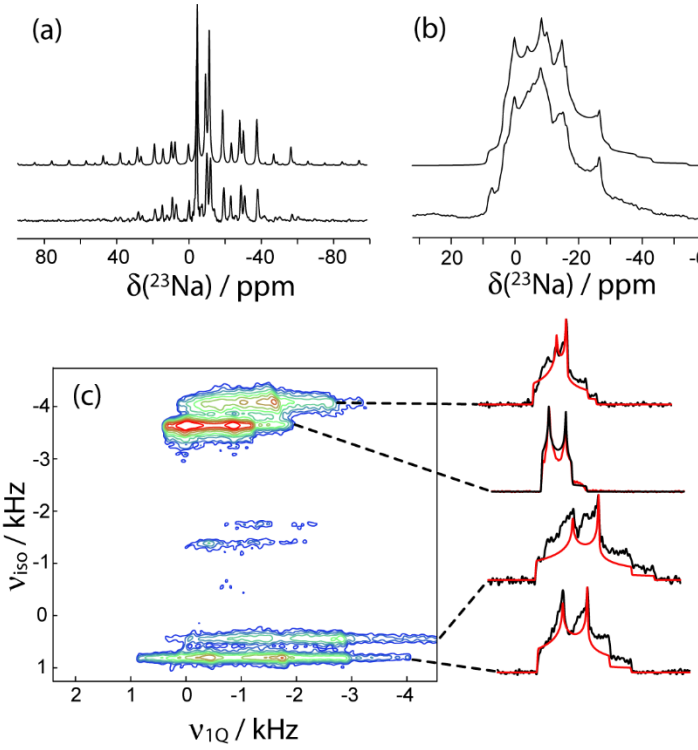

Figure 2.9. The ^{23}Na NMR spectra of $Na_4P_2O_7$. In (a), the DOR NMR spectrum and its simulation are shown and, similarly, the MAS NMR spectrum is shown in (b). The MQMAS NMR spectrum is shown in (c) where simulations of the anisotropic slices are shown. All spectra were simulated using the known ^{23}Na NMR parameters.[136]

2.3.3.1 Solid-State NMR

The ^{23}Na EFG tensor parameters for $Na_4P_2O_7$ may be extracted with the use of MAS, MQMAS, and DOR NMR spectra and are known with high precision from the literature[136] (see Table 2.5). In order to use these parameters as restraints for a crystal structure refinement it is however necessary to correctly assign the resonances to their respective crystallographic sites. In this case, Na1 and Na4 could be unambiguously assigned to the first and fourth resonances, respectively (see Figure 2.9 and 2.10), using the PAW DFT calculated EFG tensor parameters. The calculated EFG tensor parameters for Na2 and Na3 are very similar and EFGs cannot be used to confidently assign the resonances. However, Na2 and Na3 have distinctly different chemical shifts which can be assigned using GIPAW DFT calculated isotropic magnetic shielding values.

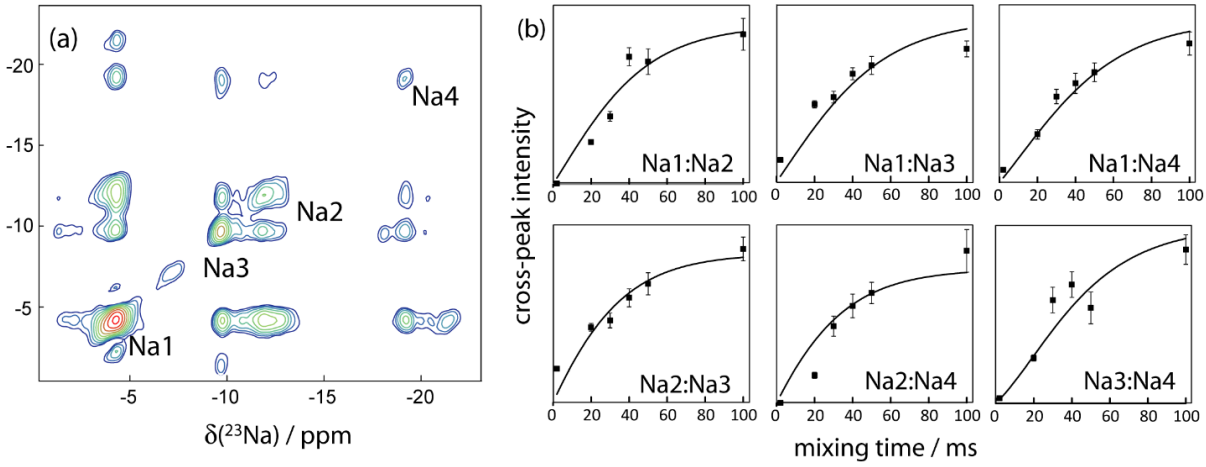

Figure 2.10. (a) ^{23}Na SDDOR NMR spectrum of $Na_4P_2O_7$ with a 50 ms mixing time. (b) Spin diffusion build-up curves for the different pairs of sodium sites.

We have performed ^{23}Na 2D SDDOR NMR experiments that provide high-resolution, through-space, ^{23}Na chemical shift correlation spectra. The DOR NMR spectra

(see, for example, Figure 2.9) show four well-resolved resonances of $Na_4P_2O_7$ as well as a number of spinning sidebands, the intensities of which are related to the EFG tensor parameters. The integrated intensities of the sideband patterns are in agreement with the equal occupancy of the four sites from the SCXRD structure. It can be seen in the SDDOR NMR spectrum in Figure 2.10a that all of the resonances are correlated to each other. As was discussed by Edén and Frydman,[122] and by us,[121] the intensities of the cross peaks are not directly correlated to the internuclear distances and therefore the former cannot be used as a quantitative structural restraint. However, the rate at which the cross peaks grow in intensity as the mixing time is increased depends, to a good approximation, only on the dipolar coupling constant.[122] For example, this information was used to assign the ^{23}Na DOR NMR resonances in sodium deoxyuridine monophosphate.[121]

The build-up curves for the various cross-peaks for $Na_4P_2O_7$ are shown in Figure 2.10b. The curves are fit assuming first-order rate kinetics for the spin diffusion process and relayed spin diffusion is modeled using the rate matrix method. This approach predicts the spin diffusion build-up curves using only the crystal structure as input. The data in Figure 2.10b were simultaneously fit with the data for $Na_3HP_2O_7{\cdot}H_2O$ and $Na_3HP_2O_7{\cdot}9H_2O$ (*vide infra*) in order to further restrain the fits. It can be seen that the rate matrix approach models spin diffusion in quadrupolar spin systems rather well (correlation coefficient, R, is 0.95), providing further support of the resonance assignment. In this particular example, however, the rate of spin diffusion is similar for all cross-peaks and these spectra couldn't have been used to assign the resonances in the absence of GIPAW DFT data. This nonetheless demonstrates that SDDOR NMR, along with proper spin diffusion modelling, may be used to provide distance constraints for NMR crystallographic purposes.

2.3.3.2 Crystal Structure Refinement

Once all resonances have been assigned, a crystal structure refinement can be performed. In a first refinement step, a simple energy minimization of the SCXRD structure is performed using DFT. This induced a significant change in the structure (RMSD of 0.012 Å) and a decrease in energy of 0.086 eV, which is above the thermally accessible energy at room temperature of 0.013 eV. The agreement between the experimental and calculated PXRD patterns remained fairly constant upon refinement; the χ^2 value for the PXRD data, which is calculated using FOX software,[27] increased from 1.69×10^4 to 1.72×10^4. The agreement between the experimental and PAW DFT predicted EFG tensor components is however significantly better; the χ^2 value for the ^{23}Na EFGs decreased from 166 to 55 (see Table 2.6).

Table 2.6. Values of χ^2 for different structures of $Na_4P_2O_7$

model	χ^2	RMSD /Å[e]	χ^2(^{23}Na EFG)[a]	χ^2(^{31}P δ_{ii})[b,d]	χ^2(^{23}Na δ_{iso})[c,d]	χ^2(PXRD)[d]
SCXRD	4.63×10^4	0.013	166	9.2	26	1.69×10^4
DFT-refined	55	0.001	55	8.6	19	1.72×10^4
NMR/DFT-refined	41	0	41	8.9	18	1.72×10^4

[a] This term is incorporated in the χ^2 parameter used for the refinement.

[b] The GIPAW DFT calculated ^{31}P chemical shifts were scaled by 0.796.[150]

[c] The GIPAW DFT calculated ^{23}Na chemical shifts were scaled by 0.897.[150]

[d] These values are used for cross-validation purposes only and were not included in the refinement process.

[e] Root-mean-square deviation of the *fractional* coordinates relative to the NMR/DFT-refined structure.

The DFT-refined structure was further refined against the ^{23}Na EFG tensor data in order to improve the agreement between the scaled DFT calculated EFG tensor components and those that are measured experimentally.

Table 2.7. Comparison of the SCXRD (ref. 132) and NMR/DFT-refined fractional coordinates of $Na_4P_2O_7$

	SCXRD			NMR/DFT-refined		
	x	y	z	x	y	z
Na1	0.7225	0.4992	-0.0168	0.7233	0.4991	-0.0165
Na2	0.7419	0.4848	0.2360	0.7408	0.4850	0.2354
Na3	0.3721	0.4961	0.1545	0.3716	0.4967	0.1537
Na4	0.9154	-0.0268	0.1674	0.9165	-0.0388	0.1671
P1	0.5570	0.0113	-0.1061	0.5575	0.0100	-0.1066
P2	0.5638	-0.0223	0.1113	0.5647	-0.0217	0.1118
O1	0.6102	0.0971	0.0040	0.6111	0.0984	0.0038
O2	0.5944	0.2338	-0.1693	0.5937	0.2341	-0.1706
O3	0.6453	-0.2131	-0.1339	0.6470	-0.2152	-0.1338
O4	0.3990	-0.0447	-0.1019	0.3992	-0.0481	-0.1017
O5	0.6764	0.0803	0.1805	0.6777	0.0822	0.1811
O6	0.5705	-0.3017	0.1009	0.5711	-0.3024	0.1015
O7	0.4154	0.0744	0.1333	0.4152	0.0763	0.1334

The resulting NMR/DFT-refined structure only differed from the pure DFT-refined structure by a RMSD of 0.001 Å. A summary of the RMSDs between all the structures mentioned in this text and the final NMR/DFT-refined structure, as well as the χ^2 values, is given in Table 2.6. The fractional coordinates for all the atoms in this structure are listed in Table 2.7 and are compared to those from the SCXRD structure. It can be seen that the agreement between the predicted and experimental EFG tensor components is significantly improved after the NMR/DFT-refinement (χ^2 of 41). The agreement with PXRD data also improved slightly; however, the results remain indistinguishable from those of the DFT-refined structure. The NMR/DFT refined crystal structure for $Na_4P_2O_7$ is in good agreement

with PXRD data, as well as in a much better agreement with the DFT energy term and with the ^{23}Na EFG tensors.

The ^{23}Na isotropic chemical shifts (δ_{iso}) and ^{31}P chemical shift tensor components (δ_{ii}, where i = 1, 2, or 3) were not included directly in the refinement procedure due to the computational cost of calculating the corresponding magnetic shielding tensors, but these data may be used to cross-validate the proposed crystal structure. The ^{23}Na δ_{iso} values are determined with the use of MQMAS, MAS, and DOR NMR (Table 2.5), as described in the literature.[136] The ^{31}P chemical shift tensor components were determined using slow MAS. In Table 2.6, the cost functions calculated with the use of the ^{23}Na chemical shifts ($\chi^2(^{23}\text{Na}\ \delta_{iso})$) and ^{31}P chemical shift tensor components ($\chi^2(^{31}\text{P}\ \delta_{ii})$) are listed. Both cost functions are notably lower for the DFT-refined structure than they are for the SCXRD structure. The cost function for the ^{23}Na chemical shifts has also improved when the EFGs were used as constraints for the refinement whereas the agreement with the ^{31}P CSA remained fairly constant. This is further evidence that the NMR/DFT-refined structure is of higher quality than the DFT-refined structure alone, despite the very small RMSD between these two structures. By comparing the $\chi^2(^{31}\text{P}\ \delta_{ii})$ values for the three structures it is also apparent that ^{31}P NMR is far less sensitive to the structural changes than ^{23}Na NMR. As mentioned earlier, this is due to the cations' lack of covalent interactions which would dominate all NMR properties.

The structural changes upon refinement were largely uniform. The pyrophosphate anion showed some non-negligible structural changes, which may impact the expected spectroscopic properties. The P-O-P angle changed from 127.5° in the SCXRD structure to 127.1° in the DFT-refined structure and 127.2° in the NMR/DFT-refined structure. The

bridging O-P bond lengths changed from 1.637 ± 0.007 Å to 1.647 ± 0.009 Å and 1.647 ± 0.007 Å in the SCXRD, DFT-, and NMR/DFT-refined structures, respectively. Finally, the terminal O-P bond lengths changed from 1.513 ± 0.001 Å to 1.521 ± 0.002 Å and 1.521 ± 0.003 Å in the XRD, DFT-, and NMR/DFT-refined structures, respectively. Generally, all the bond lengths are increased by approximately 0.01 Å relative to the SCXRD structure. This change is larger than the reported experimental error in the diffraction measurement; however, this difference may also be caused by the different timescales of NMR and XRD measurements. The inclusion of NMR data affected all the bond lengths on average by 0.001 Å.

2.3.4 Trisodium Hydrogen Pyrophosphate Monohydrate ($Na_3HP_2O_7 \cdot H_2O$)

The crystal structure of $Na_3HP_2O_7 \cdot H_2O$ has been solved *ab initio* with the use of PXRD by Ivashkevich and co-workers.[133] They showed that $Na_3HP_2O_7 \cdot H_2O$ crystallizes in the **P**$2_1/n$ space group with the following unit cell dimensions: a = 10.4242 Å, b = 6.8707 Å, c = 10.0837 Å, and β = 99.2258°. There is one molecule in the asymmetric unit and thus there are two inequivalent phosphorus sites and three inequivalent sodium sites. However, due to the low resolution of the technique, it is often impossible to obtain a truly high resolution structure from PXRD alone. Additionally, the positions of the hydrogen atoms are unknown since these are often effectively invisible in XRD measurements. A combination of PAW DFT calculations and NMR measurements may be applied to refine and improve the PXRD structure of Ivashkevich.

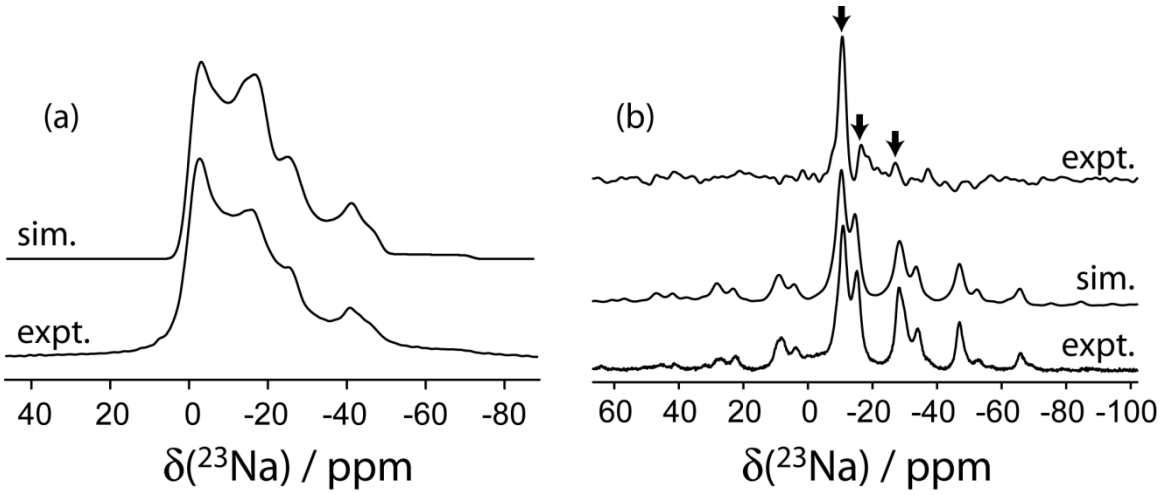

Figure 2.11. ^{23}Na MAS (a) and DOR (b) NMR spectra for $Na_3HP_2O_7 \cdot H_2O$. In (b), the bottom trace is the experimental NMR spectrum and the middle trace is the simulation. The experimental AMBASSADOR[148] spectrum is shown in the top trace of (b) where three arrows mark the positions of the three sodium resonances.

2.3.4.1 Solid-State NMR

The ^{23}Na DOR NMR spectrum of $Na_3HP_2O_7 \cdot H_2O$ is shown in Figure 2.11b, where it can be seen that there are at least two resolved resonances in the DOR spectrum, one of which has an intensity twice that of the other. The PXRD structure indicates three chemically distinct sodium sites and therefore, we expect to see three resonances in the DOR NMR spectrum. Due to the large number of sidebands, it is likely that a resonance overlaps with the sideband of another. With our DOR probe it was not possible to improve the resolution by increasing the spinning frequency and thus we used the recently described AMBASSADOR experiment which can completely remove the sidebands in DOR spectra.[148] From the AMBASSADOR spectrum it can be seen that there are three resonances. As expected, one of the resonances overlapped with the sidebands of another.

The ^{23}Na MAS NMR spectrum is shown in Figure 2.11a, where three overlapping second-order quadrupolar line shapes are observed. By using the DOR shifts ($\delta_{\mathrm{DOR}} = \delta_{\mathrm{iso}} - \frac{C_{\mathrm{Q}}^2(1+\eta^2/3)}{40}\frac{10^6\,\mathrm{Hz}}{\nu_0}$), it was possible to fit the MAS line shape with three chemically distinct sites and extract their chemical shifts and EFG tensor parameters (see Table 2.8). The simulation parameters were then confirmed by simulating the DOR sideband patterns (see Figure 2.11b).

Table 2.8. ^{23}Na NMR parameters for $Na_3HP_2O_7{\cdot}H_2O$

site[a]	δ_{iso} / ppm	C_{Q} / MHz	η
Na1	4.0 ± 0.5	2.55 ± 0.1	0.15 ± 0.1
Na2	1.0 ± 0.5	3.60 ± 0.05	0.20 ± 0.06
Na3	6.5 ± 0.5	3.1 ± 0.1	0.10 ± 0.05

[a] See the main text for details relating to the assignment of the resonances.

^{23}Na SDDOR NMR experiments were also performed on this sample. An example SDDOR spectrum is shown in Figure 2.12a and the build-up curves of the cross-peaks' intensities are shown in Figure 2.12b. The spin diffusion rates are very similar for all the pairs of sodium sites, which is nicely reproduced in the simulated build-up curves calculated using the rate matrix approach. However, the calculated ^{23}Na EFG tensor components are much larger than the experimentally determined ones which indicates that the sodium ions' crystallographic positions could be improved by further structural refinements.

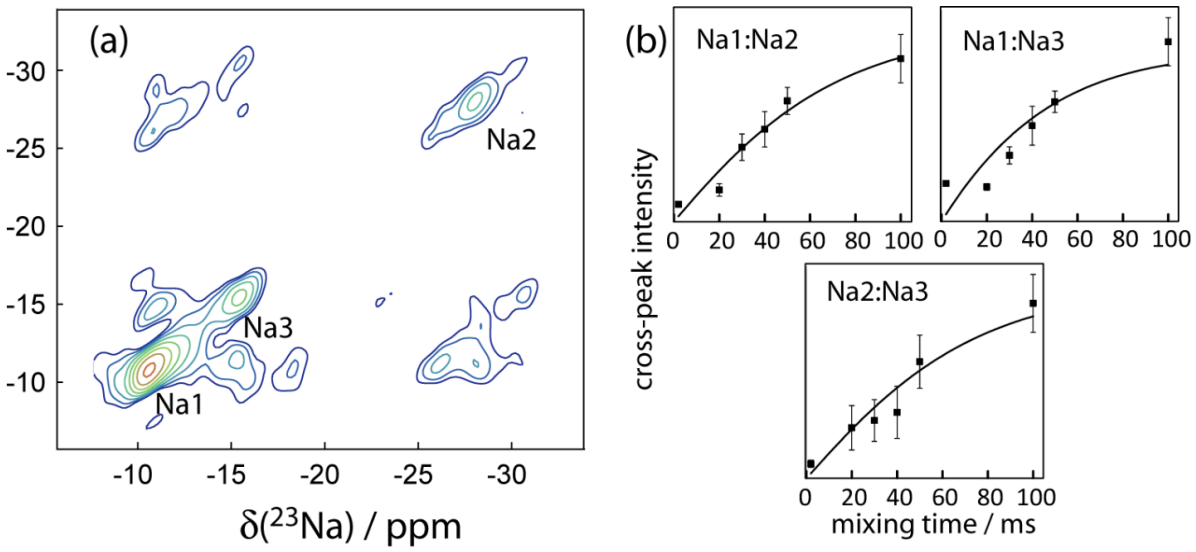

Figure 2.12. (a) ^{23}Na SDDOR NMR spectrum of $Na_3HP_2O_7{\cdot}H_2O$ with a 50 ms mixing time. (b) Spin diffusion build-up curves for the different pairs of sodium sites.

^{31}P slow-MAS NMR spectra were also acquired to extract the ^{31}P chemical shift tensor components. There are two chemically inequivalent phosphorus sites that may be assigned to the two phosphorus atoms in the pyrophosphate anions. Unlike in the case of anhydrous $Na_4P_2O_7$ where the two phosphorus sites were nearly indistinguishable by NMR, in this case the isotropic resonances are well separated and the chemical shift anisotropy is markedly different. The chemical shift tensor spans (Ω) are quite similar and yet the skews (κ) are of opposite signs, see Table 2.9. This large difference is to be expected as one of the phosphorus sites bears an 'OH' moiety.

Table 2.9. ^{31}P NMR parameters for the three compounds studied

sample	site	δ_{iso} / ppm	Ω / ppm	κ
$Na_4P_2O_7$[a]	P1/P2	2.7 ± 0.5	140 ± 10	-0.69 ± 0.05
$Na_3HP_2O_7{\cdot}H_2O$	P1	-2.7 ± 0.1	150 ± 10	-0.23 ± 0.05
	P2	-5.1 ± 0.1	180 ± 10	0.08 ± 0.05
$Na_3HP_2O_7{\cdot}9H_2O$	P1	-5.2 ± 0.1	175 ± 10	0.11 ± 0.05
	P2	-2.6 ± 0.1	156 ± 10	-0.27 ± 0.05

[a] These values were also reported in ref 143.

2.3.4.2 Crystal Structure Refinement

The positions of the hydrogen atoms in this compound are unknown. It can be assumed that two of the hydrogen atoms are located on the water molecule and the remaining hydrogen atom is located on the pyrophosphate. It was hypothesized that the latter hydrogen atom may be located on either the O2 or O4 site and that a hydrogen bond would connect the two as these have a short internuclear distance in the PXRD structure.[133] We have generated models placing the hydrogen on the two different oxygen sites. Those structures were then optimized using PAW DFT which placed the hydrogen on the O2 oxygen in both cases. This represents a low temperature, static structure.

Table 2.10. Values of χ^2 for different structures of $Na_3HP_2O_7 \cdot H_2O$

model	$\chi^2(^{23}Na$ EFG)	RMSD / Å[d]	ΔE / eV	$\chi^2(^{31}P\ \delta_{ii})^{a,c}$	$\chi^2(^{23}Na\ \delta_{iso})^{b,c}$	$\chi^2(PXRD)^c$
PXRD	287	0.117	0.112	34	1.4	1.40×10^4
DFT-refined	121	0.003	0	25	40	2.74×10^4
NMR-refined	100	0	0.017	22	35	2.77×10^4

[a] The GIPAW DFT calculated ^{31}P chemical shifts were scaled by 0.796.[150]

[b] The GIPAW DFT calculated ^{23}Na chemical shifts were scaled by 0.897.[150]

[c] These values are used for cross-validation purposes only and were not included in the refinement process.

[d] Root-mean-square deviation of the *fractional* coordinates relative to the NMR-refined structure.

The overall changes as a result of the DFT optimization of the PXRD structure were non-negligible (RMSD of 0.117 Å) and the change in lattice energy of 0.112 eV is also significant. By refining the crystal structure using the PAW DFT energy, the agreement between the experimental and predicted ^{23}Na EFG tensors and ^{31}P chemical shift tensors improved (see Table 2.10). In this case, due to the large difference between the three sodium

sites' EFG tensor parameters, the ^{23}Na resonances could be unambiguously assigned using the PAW DFT calculated values. The agreement for the ^{23}Na chemical shifts is, however, worse. This is deemed to be fortuitous as ^{23}Na chemical shifts are typically not reproduced with the level of accuracy seen here for the PXRD structure.[149] The RMSD in the predicted ^{23}Na chemical shifts is typically 2.3 ppm,[150,149] which is similar to the total range of chemical shifts in this sample.

Table 2.11. Comparison of the PXRD (ref. 133) and NMR-refined fractional coordinates of $Na_3HP_2O_7{\cdot}H_2O$

	PXRD			NMR-refined		
	x	y	z	x	y	z
Na1	0.2254	0.646	0.5519	0.2186	0.6387	0.5535
Na2	-0.2423	0.62	0.7559	-0.2377	0.6375	0.7607
Na3	0.053	0.862	0.7541	0.0575	0.8537	0.7518
P1	0.184	0.1691	0.5146	0.1844	0.1628	0.5164
P2	0.0216	0.3402	0.6964	0.0182	0.3374	0.6954
O1	0.1523	0.112	0.3641	0.1551	0.1083	0.3699
O2	0.2143	-0.027	0.5939	0.2149	-0.0250	0.6056
O3	0.2812	0.321	0.5512	0.2868	0.31523	0.5543
O4	0.0914	0.542	0.7224	0.1014	0.5239	0.7168
O5	0.0637	0.187	0.7961	0.0581	0.1889	0.8067
O6	-0.1253	0.391	0.6622	-0.1257	0.3822	0.6695
O7	0.0426	0.247	0.557	0.0471	0.2429	0.5538
O8	-0.0562	0.707	0.94	-0.0804	0.7939	0.9282
H1	N/A	N/A	N/A	0.2017	0.4989	0.8138
H2	N/A	N/A	N/A	0.4474	0.7361	0.5251
H3	N/A	N/A	N/A	0.4282	0.5651	0.4241

Attempts to further refine the DFT-refined structure using both the DFT energy and ^{23}Na EFG tensors as restraints simultaneously, as done for $Na_4P_2O_7$, were not productive due to the relative sparsity of experimental restraints. The DFT-refined structure was nonetheless further refined using only the ^{23}Na EFG tensors as restraints; the fractional coordinates for this NMR-refined structure, as well as the Rietveld-refined structure, are listed in Table 2.11. The lack of a covalent bonding environment for the cations renders

their NMR parameters especially sensitive to the crystal packing whereas, for the pyrophosphate anion, the bonds between the phosphorus and the oxygen atoms largely dictate the ^{31}P chemical shift tensor. The PXRD patterns calculated using the Rietveld-refined or the NMR-refined structures are virtually indistinguishable.

There were some small changes in the structure of the pyrophosphate anion upon refinement. The P-O-P bond angle increased from 127.0° to 128.8° and 128.6° in the DFT and NMR-refined structures respectively. The average bridging P-O bond lengths increased from 1.639 Å to 1.641 Å with DFT refinement; however, they decreased to 1.636 Å when the EFG tensors were used as restraints. Similarly, the O-H bond length decreased from 1.109 Å to 1.104 Å with the NMR refinement and the hydrogen bond length between the pyrophosphate molecules decreased from 1.325 Å to 1.323 Å. The P-OH bond length also decreased from 1.582 Å to 1.576 Å upon NMR refinement; the value in the Rietveld-refined structure is 1.573 Å. Lastly the terminal P-O bond lengths increased from 1.515 Å ± 0.019 Å to 1.527 ± 0.028 Å when the EFG tensors were used as constraints; the value is 1.521 ± 0.051 Å in the Rietveld-refined structure.

It is well known that generalized gradient approximation (GGA) DFT functionals tend to underestimate the strengths of chemical bonds[151] and perform poorly for weak interactions.[152] Approaches such as these which include experimental data as restraints in DFT-based optimizations may be useful in overcoming such shortcomings.

It is difficult to determine in this case whether the additional, NMR-based, refinements of the DFT-refined structure improved the crystal structure, especially since the two are of comparable energy at room temperature (see Table 2.10). Comparing the quality

of predicted observables that are not used in the refinement process may however be helpful. From the data in Table 2.10, it is clear that both the ^{23}Na chemical shifts and ^{31}P chemical shift tensors provide superior cross-validation of the NMR-refined structure relative to the DFT-refined structure whereas the PXRD data cannot distinguish between the two structures. This conclusion is further supported by comparing the structure of the pyrophosphate anion with that in the nonahydrate form, *vide infra*.

2.3.5 Trisodium Hydrogen Pyrophosphate Nonahydrate ($Na_3HP_2O_7{\cdot}9H_2O$)

2.3.5.1 Crystal Structure

The crystal structure of $Na_3HP_2O_7{\cdot}9H_2O$, like many other diphosphate salts, is unknown. We were however able to obtain large crystals of $Na_3HP_2O_7{\cdot}9H_2O$ which enabled us to solve the structure using SCXRD (see Figure 2.13). There is one pyrophosphate molecule in the asymmetric unit as well as three inequivalent sodium sites. Since a transition from the nonahydrate to the monohydrate salt occurs when the solid is heated, or placed under a vacuum,[165] it may be anticipated that the crystal packing for the two salts is similar. That is indeed found to be the case since, as in the monohydrate salt, the pyrophosphate anions form hydrogen-bonded "zigzag" chains; however, the spacing between the anions is much greater in the case of the nonahydrate.

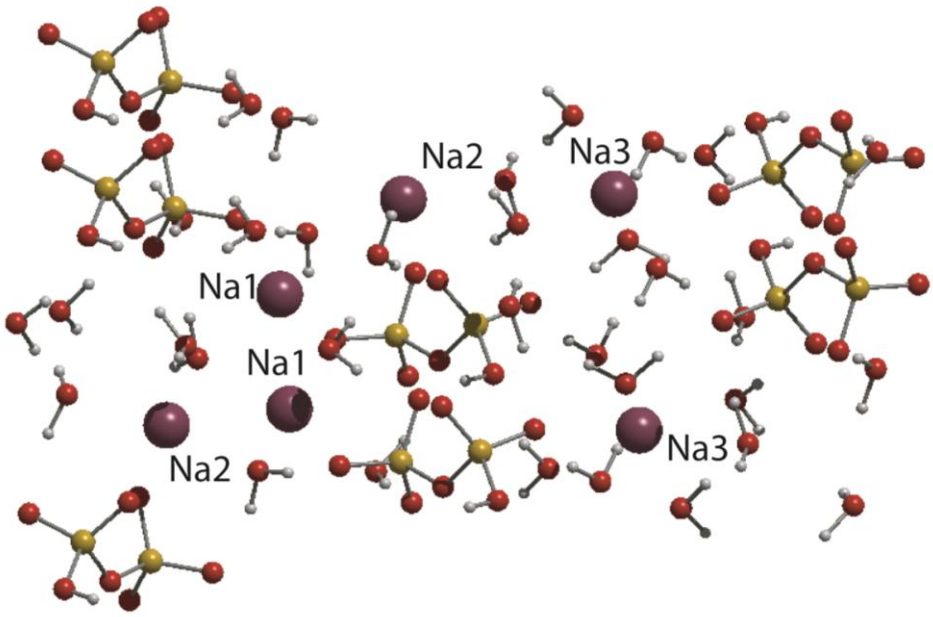

Figure 2.13. A partial view of the packing in the crystal structure of $Na_3HP_2O_7 \cdot 9H_2O$ along the *a* axis showing the three different sodium sites.

The geometry of the pyrophosphate anion in the nonahydrate is quite similar to that obtained from the DFT- or NMR-refinements of the Rietveld refined structure of the monohydrate salt. The bridging P-O-P angle for the pyrophosphate anion in the nonahydrate is essentially identical to the value obtained from the NMR-refined structure of the monohydrate. The RMSD of the bond lengths between the DFT- and NMR-refined structures of the monohydrate salt, when compared to the SCXRD structure of the nonahydrate salt, are 0.12 and 0.05 Å, respectively. The RMSD of the bond angles between the DFT- and NMR-refined structures of the monohydrate salt, when compared to the structure of the nonahydrate, are 3.23° and 3.26°, respectively. This independent structural cross-validation of the pyrophosphate anion using SCXRD on a different hydrate further

suggests that the NMR-refined structure of $Na_3HP_2O_7 \cdot H_2O$ is of higher quality than the original PXRD and the DFT-refined structure.

2.3.5.2 Solid-State NMR

The unit cell of the nonahydrate is elongated along the *b* axis when compared to the monohydrate salt and layers of pyrophosphate anions are separated by highly hydrated regions (Figure 2.13). One of the sodium sites is located in these highly hydrated regions whereas the other two are in close proximity to each other (3.45 Å separation) and coordinated to the oxygen atoms of the pyrophosphate anion (see Figure 2.13). The ^{23}Na DOR NMR spectra of this compound were acquired at magnetic fields of 9.4 and 4.7 T (see Figure 2.14a). At 9.4 T, two resonances were observed, one of which had twice the integrated intensity of the other. Since the DOR shifts are magnetic field-dependent, *vide supra*, a DOR NMR spectrum at a lower magnetic field was able to provide improved resolution and distinguish between the three sodium sites with equal integrated intensities. From these data, the quadrupolar product and isotropic chemical shifts may also be extracted (see Table 2.12); however, we also used MQMAS NMR to refine the final values of C_Q and η, as shown in Figure 2.14c.

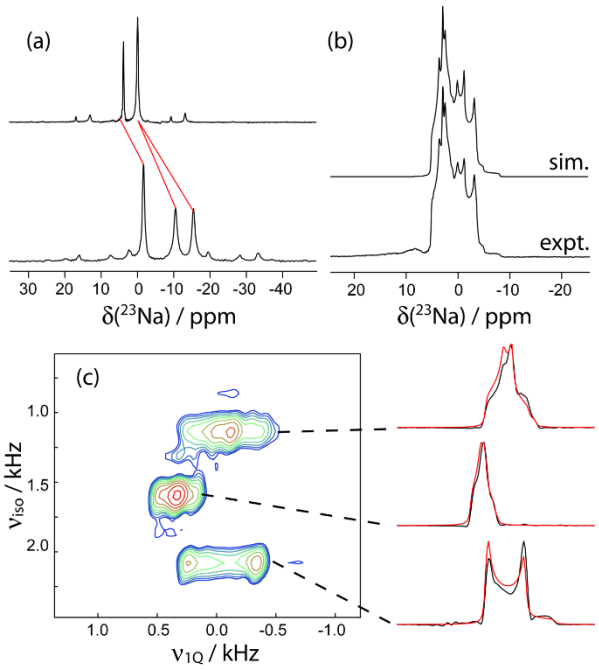

Figure 2.14. ^{23}Na DOR (a), MAS (b), and MQMAS (c) NMR spectra for $Na_3HP_2O_7{\cdot}9H_2O$ are shown along with their simulations. In (a), the ^{23}Na DOR NMR spectra acquired at 9.4 T and 4.7 T are shown in the top and bottom traces, respectively; all other spectra were acquired at 9.4 T.

Table 2.12. ^{23}Na NMR parameters for $Na_3HP_2O_7{\cdot}9H_2O$

site[a]	δ_{iso} / ppm	C_Q / MHz	η
Na1	5.25 ± 0.05	0.85 ± 0.02	0.68 ± 0.04
Na2	4.5 ± 0.1	1.50 ± 0.02	0.07 ± 0.03
Na3	3.1 ± 0.1	1.16 ± 0.02	0.67 ± 0.03

[a] See the main text for details relating to the assignment of the resonances.

A SDDOR NMR spectrum with a mixing time of 50 ms was acquired at a magnetic field of 4.7 T, where the three resonances are well resolved (see Figure 2.15). It can be seen that two of the resonances are correlated with each other, whereas the third resonance is not correlated to either of the first two sites. It is then possible to unambiguously assign the resonance which is not correlated to the other sites to Na3, since Na3 is isolated in the

crystal structure and coordinated only by water molecules. The other two sites are 3.45 Å apart and a cross-peak in the SDDOR spectrum is expected. Other SDDOR experiments with varying mixing times were performed at 9.4 T where the sole cross-peak is still well resolved. The build-up curve for this cross-peak is very well reproduced by the rate matrix method (see Figure 2.15c). The predicted build-up curved for the correlations to Na3 are also shown in Figure 2.15c and show that the cross-peak intensity would be negligible at mixing times which are experimentally feasible.

Curiously, a strong correlation between the Na-Na distances and their spin diffusion rate constants was observed previously for sodium dUMP where the sodium concentration is low (4.4×10^{-3} Å^{-3});[121] however, for the present samples, the spin diffusion rates seem to be only weakly correlated to the internuclear distances. In these samples, relayed spin diffusion becomes important due to the high concentration of sodium (e.g., 23.5×10^{-3} Å^{-3} in $Na_4P_2O_7$). The SDDOR data could nonetheless be very well fit with the use of the rate matrix method in order to unambiguously assign the sodium sites in $Na_3HP_2O_7 \cdot 9H_2O$. This application of accurate, structure-based, modeling of spin diffusion involving quadrupolar nuclei demonstrates that SDDOR may be useful for qualitative homonuclear distance measurements involving quadrupolar nuclei. This consideration may be of importance in glass chemistry where ^{11}B SDDOR NMR has been used to establish connectivities.[120] Quantum mechanical simulations may be necessary to simulate the spin diffusion processes sufficiently accurately in order to extract quantitative distance restraints.[153]

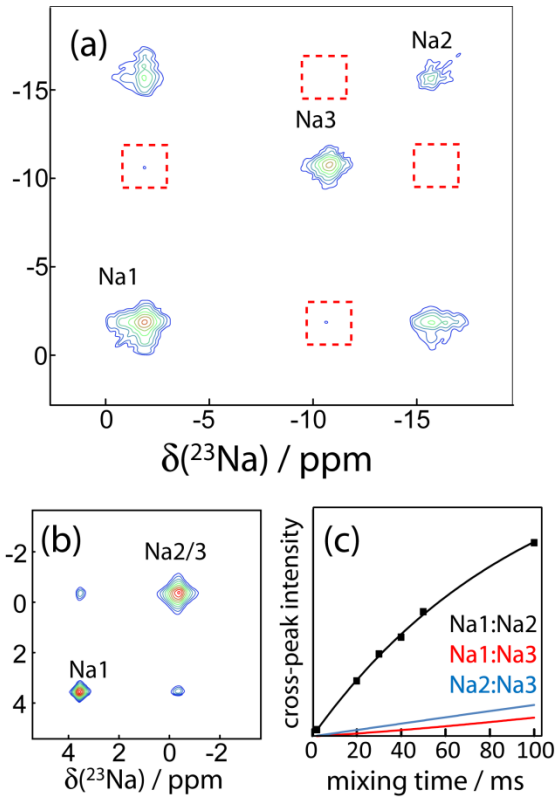

Figure 2.15. ^{23}Na SDDOR NMR spectra of $Na_3HP_2O_7{\cdot}9H_2O$ acquired at 4.7 T (a) and 9.4 T (b) with 50 ms mixing times are shown. In (a), boxes indicate the missing cross-peaks. The spin diffusion build-up curve for the visible cross-peak is shown in (c) along with the simulated build-up curves for the missing correlations (red and blue lines).

The ^{31}P slow-MAS NMR spectrum was also acquired for the nonahydrate where the two phosphorus sites are again clearly resolved. The isotropic chemical shifts and chemical shift anisotropies are very similar to those obtained for the monohydrate (see Table 2.9). This demonstrates that the chemical shift tensors are more sensitive to anion structure than to the overall crystallographic packing. As mentioned earlier, the NMR of the cations is especially well-suited to report on the crystallographic packing due to their lack of covalent interactions. The EFG tensor is also more sensitive to long range ordering, and has a r^{-3}

dependence,[154] than the magnetic shielding tensor, which is mostly sensitive to the immediate coordination of the atom. As anticipated for the nonahydrate, a good agreement between the calculated and experimental chemical shift and EFG tensor values is obtained without further structural refinement as a high quality SCXRD structure is available. The value of $\chi^2(^{23}\text{Na, EFG})$ is 221, the value of $\chi^2(^{23}\text{Na}, \delta_{iso})$ is 232, and the value of $\chi^2(^{31}\text{P}, \delta_{ii})$ is 50.

2.3.5.3 ^2H NMR

We have also performed ^{2}H NMR experiments on uniformly deuterated samples of the monohydrated and nonahydrated forms of $Na_3HP_2O_7$. The resonances from the water and the pyrophosphate hydrogens are clearly resolved in the two-dimensional one-pulse (TOP)[155,156] projection (see Figure 2.16). A large chemical shift (15 ppm) is observed for the pyrophosphate hydrogen resonance due to hydrogen bonding between neighboring anions. The chemical shift of the water signal in the monohydrate salt is also at a higher chemical shift, when compared to the nonahydrate, indicating a stronger hydrogen bonding environment. There is, however, a shoulder at higher frequency on the water resonance from the nonahydrate, suggesting that some of the water molecules are more strongly hydrogen bonded, and thus, less mobile. From variable-temperature static quadrupolar echo experiments, it can also be clearly seen that the water and pyrophosphate hydrogen are highly dynamic, specifically in the nonahydrate salt (see Figure 2.16). The dynamics of the water molecules in the nonahydrate salt are necessary for the seamless transition to the monohydrate salt when the sample is heated or placed under a vacuum.[165]

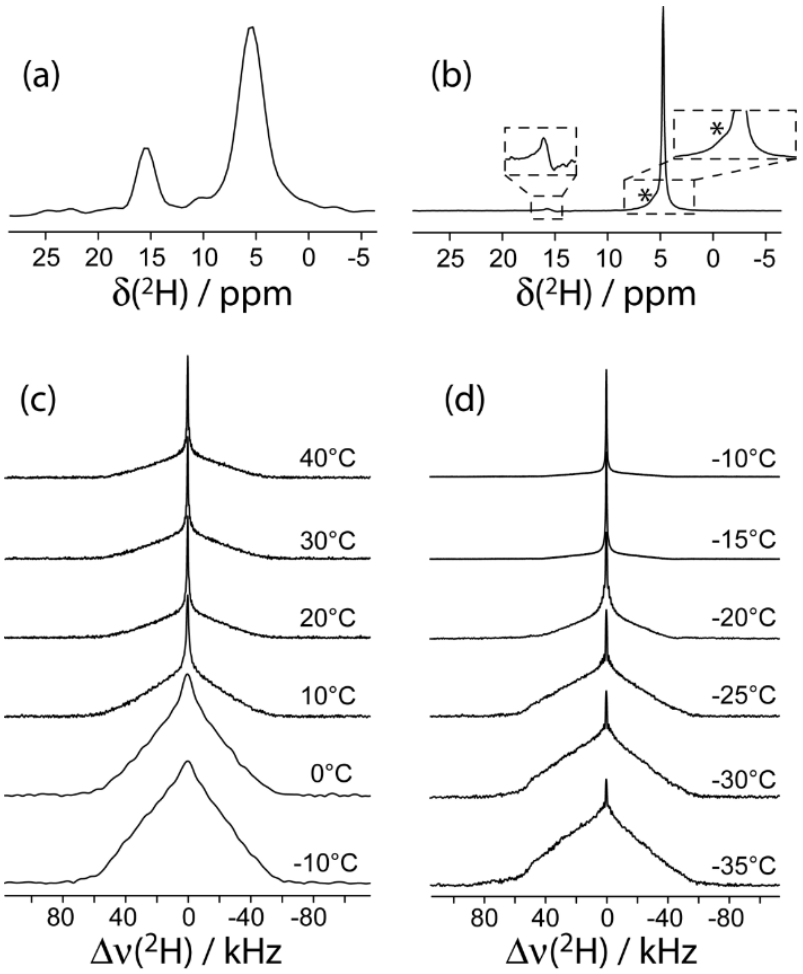

Figure 2.16. ^{2}H NMR spectra for $Na_3HP_2O_7 \cdot H_2O$ (a, c) and $Na_3HP_2O_7 \cdot 9H_2O$ (b, d) are shown. In (a) and (b), the centerbands of the ^{2}H MAS NMR spectra at room temperature are shown using TOP processing. In (b), an asterisk marks a shoulder to higher frequency on the water resonance. In (c) and (d), the temperature dependence of the ^{2}H NMR spectra of stationary samples are shown.

The dynamics of water molecules in crystalline solids are generally dominated by two-fold flips which would lead to a quadrupolar asymmetry parameter of near unity for ^{2}H in the limit of rapid exchange,[157,158] similar to our lowest temperature spectra in Figure 2.16. These two-fold flips would not affect the ^{23}Na EFG tensors as both conformations are

equivalent from the sodium's point of view. Isotropic hydrogen motions, which may occur from the transfer of hydrogen atoms to neighbouring molecules at higher temperatures, could potentially have an impact on the ^{23}Na EFG tensors.[159] However, it is known that partial averaging of the second-order quadrupolar broadening by dynamic motions (in the kHz range) does not change the second-order quadrupole shift (which would be affected by much faster motions in MHz range).[160-162] It would then be expected that the multiple-field DOR NMR data would be inconsistent with the MAS NMR data if dynamics were important, which is not the case. All MAS and DOR data (second-order quadrupolar shifts and second-order line shapes) can be successfully simulated using a single set of quadrupolar parameters. Water dynamics therefore have a negligible effect on the ^{23}Na EFG tensors.

2.3.6 Conclusions

We have investigated the crystalline structures of three sodium pyrophosphate salts with the use of XRD, SSNMR, and periodic DFT calculations. The crystal structure of $Na_4P_2O_7$ was improved with the use of ^{23}Na EFG tensors. The availability of homonuclear ^{23}Na distance restraints obtained from SDDOR experiments was useful to validate the DFT-based resonance assignments. The NMR parameters for the sodium cations were found to be much more sensitive to the crystallographic structure than are the ^{31}P NMR parameters, which are largely dependent on the anion's local structure. This is important considering that most approaches to NMR crystallography currently focus on utilising the isotropic chemical shifts or the chemical shift anisotropy alone.

The crystal structure of $Na_3HP_2O_7{\cdot}H_2O$ was also refined with the use of DFT as well as ^{23}Na EFG tensors determined using SSNMR. Using DFT, we were additionally able to

determine the positions of the hydrogen atoms which could not be located using PXRD. Although the structures that were refined using DFT and the ^{23}Na EFG parameters are very similar, the latter more accurately reproduces the experimental ^{23}Na chemical shifts and the ^{31}P chemical shift anisotropy. The structure of the pyrophosphate anion in the NMR-refined structure is also in better agreement with that solved using SCXRD for the nonahydrate form.

We also demonstrated that the rate matrix analysis of spin diffusion, previously used to obtain distance information for spin-1/2 nuclei[5,163,164] can also be applied to quadrupolar nuclei undergoing double-rotation. The rate of spin diffusion was consistent for all three samples in this study and permitted the assignment of the sodium sites in $Na_3HP_2O_7 \cdot 9H_2O$. The need for a reliable resonance assignment method is necessary for the application of any NMR crystallographic method.

2.3.7 Experimental

2.3.7.1 Sample Preparation

$Na_4P_2O_7$ and pyrophosphoric acid ($H_4P_2O_7$) were purchased from Aldrich and used without further purification. To prepare the hydrates of $Na_3HP_2O_7$, 964.5 mg of $Na_4P_2O_7$ and 215.2 mg of $H_4P_2O_7$ were dissolved in a minimum quantity of D_2O. The solutions were then mixed in an ice bath for five minutes. A polycrystalline sample of the monohydrate salt was obtained from isothermal crystallization of the solution at 85°C and its purity was verified with the use of PXRD. Large crystals of the nonahydrate salt were obtained from isothermal crystallization of the same solution at 4°C.[165] These were left in solution and

were only filtered and dried minutes before performing the SCXRD and NMR measurements.

2.3.7.2 X-Ray Diffraction

PXRD measurements were performed using a Rigaku Ultima IV diffractometer with Cu Kα radiation (wavelength of 1.54184 Å) and the Bragg-Brentano geometry. Intensity measurements were performed from a 2θ diffraction angle of 5° to 70° in steps of 0.02° at a rate of 1°/min for $Na_4P_2O_7$ and from 10° to 50° for $Na_3HP_2O_7 \cdot H_2O$.

2.3.7.3 Solid-State NMR

Solid-state NMR experiments were performed at external magnetic fields of 9.4 T or 4.7 T using Bruker Avance III NMR spectrometers. Powdered samples were tightly packed into either 4 mm ZrO_2 MAS rotors or 4.3 mm vespel DOR inner rotors for the MAS and DOR NMR experiments, respectively. ^{23}Na chemical shifts were referenced to NaCl(s) at 7.21 ppm and ^{31}P chemical shifts were referenced to ammonium dihydrogen phosphate at 0.81 ppm (primary standards: 1 M NaCl(aq) and 85% phosphoric acid).

^{31}P MAS NMR spectra were acquired using a 4 kHz MAS frequency and a Bloch decay pulse sequence. A 3.5 μs excitation pulse was used along with a 10 s recycle delay for the $Na_3HP_2O_7$ hydrates and a 20 s recycle delay for $Na_4P_2O_7$. The MAS sideband patterns were iteratively fit using the DMfit program.[166]

The ^{23}Na MAS NMR spectra were acquired using a Bloch decay pulse sequence with a 30 μs central transition selective excitation pulse and a recycle delay of 2 s for the $Na_3HP_2O_7$ hydrates and 4 s for anhydrous $Na_4P_2O_7$. ^{23}Na MQMAS NMR experiments were

acquired using the soft pulse added mixing (SPAM) pulse sequence.[167] The excitation, conversion, and detection pulses lasted 4.0, 1.5, and 30 μs, respectively. For $Na_4P_2O_7$, 84 echoes and 48 anti-echoes were acquired and for $Na_3HP_2O_7 \cdot 9H_2O$ 128 echoes and anti-echoes were acquired. The MAS spectral line shapes were simulated using the WSolids program.[116]

^{23}Na DOR NMR experiments were acquired using a Bruker HP WB 73A DOR probe with 4.3 mm inner rotors and a 14 mm outer rotor. The outer rotor spinning frequencies varied between 700 and 1000 Hz and the inner rotor spinning was monitored with the use of an oscilloscope. The rotor-synchronized odd-ordered sideband suppression method[168] was used with a 15 μs central transition selective excitation pulse. A sideband-free DOR NMR spectrum was also acquired for $Na_3HP_2O_7 \cdot H_2O$ using the 'angle modification before acquisition to suppress sidebands acquired in DOR' (AMBASSADOR) total suppression of sidebands (TOSS) experiment.[148,169] The DOR NMR spectra were simulated using extended Floquet theory with a program that uses the Gamma programming library.[170-172]

^{23}Na SDDOR NMR spectra were acquired with rotor synchronization in both dimensions.[173,174] A double-frequency sweep (DFS)[135] pulse sweeping from 900 to 250 kHz in 4.5 ms was used for all the SDDOR experiments. Multiple experiments with mixing times of 2, 20, 30, 40, 50, and 100 ms were carried out for each sample. The recycle delay was set to 2 s for all DOR NMR experiments. 132 t_1 increments of 100 μs were acquired for the SDDOR spectra of $Na_4P_2O_7$ whereas 92 were acquired for $Na_3HP_2O_7 \cdot H_2O$. For $Na_3HP_2O_7 \cdot 9H_2O$, 32 t_1 increments of 400 μs were acquired and covariance processing[175,176] was used to generate the spectrum at 9.4 T and 24 t_1 increments of 500 μs were acquired for the SDDOR spectrum at 4.7 T. Covariance processing was used in this case in order to

increase the rate of convergence and reduce the experiment times because the lines were very sharp (< 30 Hz). Two-dimensional deconvolution of the spectra was used to extract the peak intensities.

^{2}H MAS NMR spectra were acquired at 9.4 T using a Bruker 4 mm triple-resonance MAS NMR probe while spinning at 4 kHz. A rotor-synchronized quadrupolar echo pulse sequence was used with a 6.3 μs 90° pulse length. The static experiments utilized the same pulse sequence with a 30 μs echo delay.

2.3.7.4 DFT Calculations

(GI)PAW DFT calculations were performed using the CASTEP-NMR program[140] (ver. 4.1) using the generalized gradient approximation (GGA) exchange correlation functional of Perdew, Burke, and Ernzerhof (PBE).[118] All calculations were performed with the use of on-the-fly generated ultrasoft pseudopotentials, a 610 eV kinetic energy cut-off and the default "ultrafine" *k*-point grids.

Chapter 2.4: NMR-Driven Crystal Structure Solution and Refinement of the Near-Zero Thermal Expansion Material Zirconium Magnesium Molybdate

2.4.1 Introduction

Zirconium magnesium molybdate ($ZrMgMo_3O_{12}$) is a member of a class of near-zero thermal expansion materials[177-179] of the form $A_2M_3O_{12}$ which was prepared by Carl P. Romao, a graduate student in the group of Mary Anne White at Dalhousie University.[180-183] The development of materials that do not expand when heated is of great importance for the fabrication of parts for precision engineering and nanodevices, to name a few examples. Unfortunately, as is the case for the case of $ZrMgMo_3O_{12}$, the synthesis of these materials generally forms microcrystalline powders from which it is impossible to extract single crystals and determine the crystalline structure from SCXRD. However, the determination of the crystalline structures of these materials is of paramount importance in understanding the mechanisms of near-zero thermal expansion. For example, it has been noticed that the coefficient of thermal expansion in the $A_2M_3O_{12}$ materials is strongly correlated to the polyhedral distortions about the *A* cations.[184,185]

The NMR crystallographic method discussed in this part of the thesis is particularly well suited for the determination of a high-resolution crystal structure of $ZrMgMo_3O_{12}$ since the EFG tensors of the ^{17}O, ^{25}Mg, ^{91}Zr, and ^{95}Mo sites can be extracted using conventional solid-state NMR methods. The quadrupolar coupling constant has also been shown to be very strongly correlated to the polyhedral distortion about a metal site, [186,187] a parameter that

is believed to be central to the mechanism of thermal expansion in this system. The number of sites that are observed for each element can also serve as a constraint when determining the appropriate space group and validate a structural model; this approach has been termed NMR-driven crystallography.[16,17] NMR crystallography has in particular been shown to be particularly useful in helping to elucidate the mechanism responsible for negative thermal expansion in other materials.[188-190]

In this chapter, the *ab initio* crystal structure solution of $ZrMgMo_3O_{12}$ using PXRD techniques will be discussed. This structure is then refined with the use of the Rietveld method and, subsequently, with the use of the EFG tensor components of the metal sites, as determined using solid-state NMR methods, in conjunction with DFT calculations. The final crystal structure is then cross-validated with the use of the ^{17}O NMR parameters which were omitted from the crystal structure refinement.

2.4.2 Crystal Structure Solution

The free objects in crystallography program (FOX)[27] was used to solve a structural model for $ZrMgMo_3O_{12}$ using standard PXRD data. Three molybdate polyhedra as well as single magnesium and zirconium atoms were included in the structure solution. It was not possible to reach convergence using the *Pnma* space group, which had been predicted by Le Bail analysis,[181] and so the *Pna21* space group (a subgroup of *Pnma*) was trialed. This corresponds to the approximate symmetry of the DFT-solved structure of $HfMgW_3O_{12}$[191] and is in agreement with the number of sites observed in the NMR experiments, *vide infra*. Using this space group, it was possible to consistently obtain the same model structure, as seen in Figure 2.17a.

Using the Rigaku PDXL software, a Rietveld refinement of a FOX-determined structural model was performed. This improved the agreement of the crystal structure with PXRD (see Figure 2.17b), as well as making it chemically more reasonable, however many of the bond lengths and angles were still very odd. For example, some Zr-O bond lengths were as long as 3 Å and some O-Mo-O angles were as large as 157°. The Rietveld refinement did, however, permit us to obtain accurate unit cell dimensions for this compound ($a = 9.5737$, $b = 9.4800$, $c = 13.1739$, and $\alpha = \beta = \gamma = 90°$).

The Rietveld-refined crystal structure was then refined using PAW DFT in order to obtain a chemically reasonable structural model. This structure is similar to the structure of $Sc_2W_3O_{12}$[192] and features cation ordering where the Mg and Zr cations are ordered in separate channels, much like $HfMgW_3O_{12}$.[191]

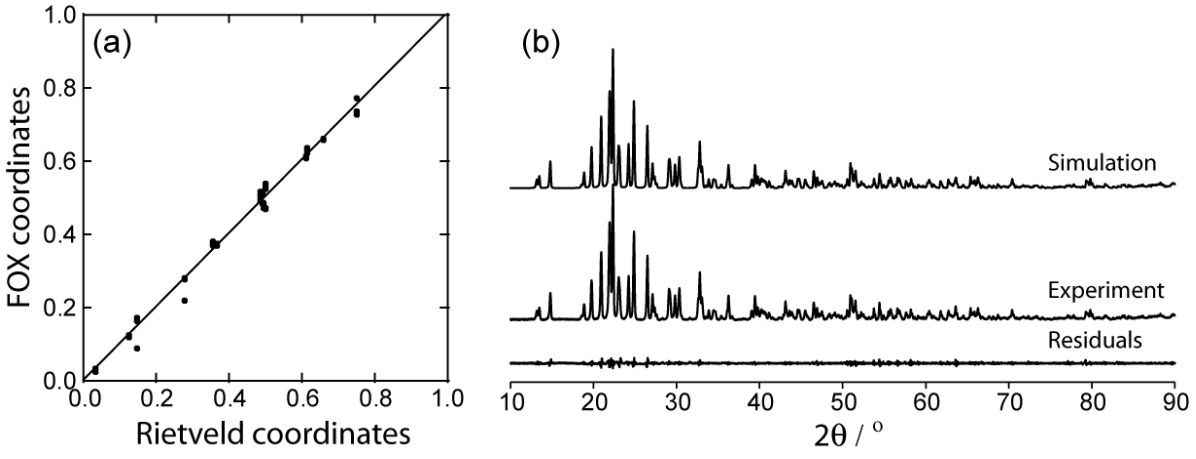

Figure 2.17. (a) Correlation between the fractional coordinates of the metal nuclei that were calculated with five independent FOX runs and the Rietveld-refined coordinates. (b) Graphs showing the powder X-ray diffraction pattern as well as the predicted pattern from the Rietveld-refined crystal structure and the residuals. The PXRD data were acquired by Carl P. Romao at Dalhousie University.

2.4.3 Solid-State NMR

2.4.3.1 ^{25}Mg, ^{91}Zr, and ^{95}Mo NMR

We have acquired a series of multiple-field ^{25}Mg, ^{91}Zr, and ^{95}Mo solid-state NMR spectra in order to extract the chemical shifts and EFG tensor parameters of all the metal centers in the compound. ^{25}Mg MAS spectra were acquired at applied magnetic fields of 9.4 and 21.1 T; these spectra and their simulations are shown in Figure 2.18; the simulations parameters are given in Table 2.13. Static ^{91}Zr NMR spectra were acquired at 9.4 T and 21.1 T. We were also able to acquire a ^{91}Zr MAS NMR spectrum at 21.1 T. These spectra and the simulations are given in Figure 2.18 and the simulation parameters are listed in Table 2.13. We have lastly acquired ^{95}Mo MAS NMR spectra at 9.4, 11.7, and 21.1 T, these are shown in Figure 2.18. In order to aid in the simulation of these complex spectra containing three overlapping second-order line shapes we also acquired the satellite transition signals at 11.7 T which have a higher resolution. The satellite transition centerband was detected using the two-dimensional one-pulse (TOP) processing trick.[155,156] An MQMAS NMR spectrum was also acquired at 21.1 T which confirms the quadrupolar products obtained from the line shape simulations. The simulation parameters are given in Table 2.13. The detection of three distinct ^{95}Mo NMR signals is in agreement with the *Pna21* space group and supports this lower symmetry space group. When the EFG tensor parameters, listed in Table 2.13, are compared to those obtained for the same elements in other compounds, it is evident that these metal sites have very small quadrupolar interactions. This is indicative that the coordination polyhedra of these Mg, Zr, and Mo sites is nearly perfectly octahedral or tetrahedral; the quadrupolar coupling constant is often well correlated to the strain of the polyhedra.[186,187]

Table 2.13. NMR parameters for all the sites in the crystal structure of $ZrMgMo_3O_{12}$

Site	δ_{iso} / ppm	$\lvert C_Q \rvert$[a] / MHz	η
Mg	-17.4 ± 0.5	0.80 ± 0.05	0.7 ± 0.1
Zr	-1 ± 5	5.3 ± 0.2	0.55 ± 0.05
Mo1	-241.0 ± 0.5	1.00 ± 0.05	1.0 ± 0.1
Mo2	-240.8 ± 0.5	0.92 ± 0.05	0.4 ± 0.1
Mo3	-250.7 ± 0.5	0.85 ± 0.05	0.63 ± 0.1
O1, O6, O7	653.52 ± 0.03	1.3 ± 0.1	--
O4	645.4 ± 0.4	1.3 ± 0.5	--
O8, O10	638.39 ± 0.04	1.3 ± 0.2	--
O11	503.4 ± 0.2	1.8 ± 0.4	--
O5, O9	493.1 ± 0.3	2.0 ± 0.5	--
O2, O12	483.1 ± 0.1	1.9 ± 0.3	--
O3	473.40 ± 0.2	1.8 ± 0.4	--

[a] Note that this value corresponds to the quadrupolar product for the oxygen sites as the value of η could not be determined.

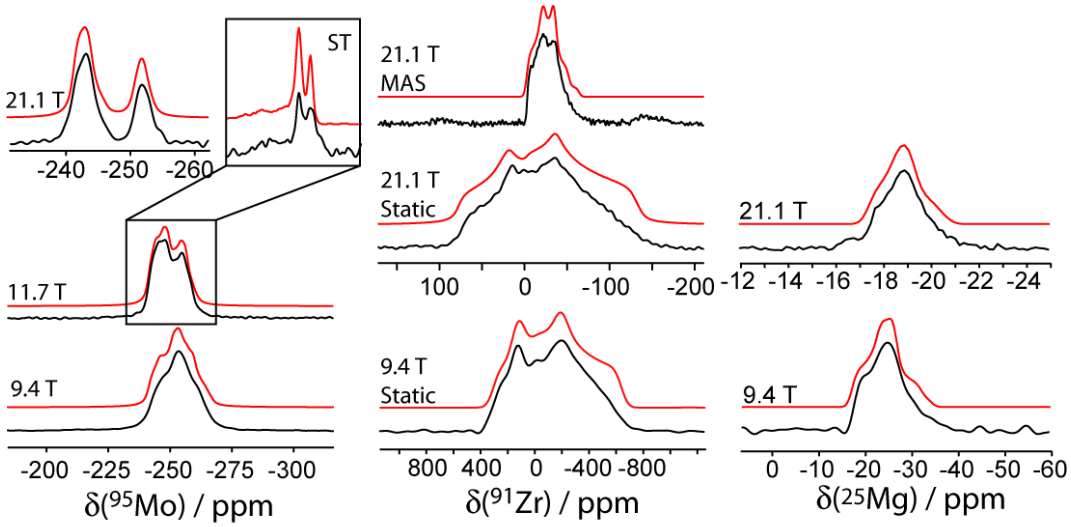

Figure 2.18. ^{95}Mo MAS NMR spectra (left) acquired at applied magnetic fields of 9.4, 11.7, and 21.1 T, as indicated on the spectra. An inset is shown showing the satellite transitions sidebands from the 11.7 T spectrum generated using the TOP method. The ^{91}Zr static and MAS NMR spectra acquired at 9.4 and 21.1 T are shown in the middle. The ^{25}Mg MAS NMR spectra acquired at 9.4 and 21.1 T are shown on the right. In all cases the experimental spectra are shown in black and the simulations are shown in red.

2.4.3.2 Crystal Structure Refinement

In order to further refine the DFT-refined crystal structure of $ZrMgMo_3O_{12}$ and correct the potential inaccuracies in the strain of the polyhedra, we sought to include the experimental EFG tensor components as constraints in the refinement. As was discussed in the experimental section, and as is shown in Figure 2.1, the EFG tensor parameters are very well reproduced using PAW DFT calculations once the appropriate scaling factor is taken into consideration. The quality of a trial crystal structure can then be assessed experimentally using a cost function (χ^2), as defined in equation 2.1 (see chapter 2.1 for more details).

Table 2.14. Cost functions (χ^2) and RMSD of the various model structures from the NMR-refined crystal structure

Structure	χ^2	RMSD / Å
FOX structure	2.04×10^{12}	0.5 ± 0.2
Rietveld-refined	1.21×10^{12}	0.24
DFT-refined	934.5	0.0014
NMR-refined	613.1	0

It can be seen in Table 2.14 that there is a significant decrease in χ^2 when going from the FOX structure ($\chi^2 = 2.04 \times 10^{12}$) to the Rietveld-refined structure ($\chi^2 = 1.21 \times 10^{12}$) and finally the DFT-refined structure ($\chi^2 = 934.5$). While optimizing the fractional coordinates to minimize the χ^2 value is was then possible to lower its value to 613.1. There is an overall RMSD improvement in the fractional coordinates of 0.5 ± 0.2 Å from the FOX coordinates, 0.24 Å from the Rietveld coordinates and 0.0014 Å from the DFT coordinates, in agreement with the improvements in the χ^2 parameter. A graphical comparison of the quality of the predicted EFG tensor components is shown in figure 2.19. It can be seen that the Rietveld structure grossly overestimates the size of the EFG tensor components due to its unnatural

polyhedral distortions. There is a great improvement in the agreement with experiment with the DFT-refined structure and the NMR-refined structure. It can be seen that the scatter of the points in this linear plot are comparable to those obtained using the calibration compounds, showing that the quality of the NMR-refined crystal structure must be similar to that which could be obtained using single-crystal X-ray diffraction. The fractional coordinates for the atoms in this structure are given in Table 2.15.

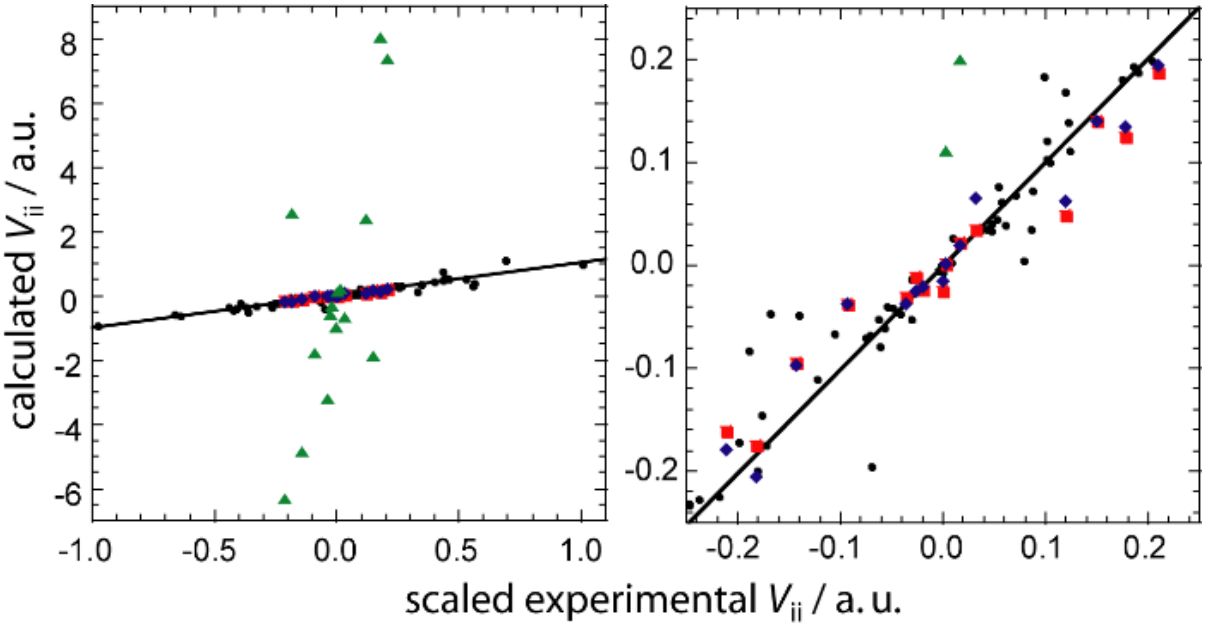

Figure 2.19. Correlations of the calculated EFG tensor components with the appropriately scaled experimental EFG tensor components for all metal nuclei in $ZrMgMo3O_{12}$. The calibration data are shown as black circles, the data calculated using the Rietveld-refined structure are shown as green triangles, the data calculated using the DFT-refined structure are shown as red triangles and the data from the NMR-refined structure are shown as blue diamonds. An expansion of the central region of the graph is shown on the right.

Although experimental data were used in solving and refining this crystal structure, it

is important to also cross-validate the model structure in order to ensure that the data were not over-fit (see chapter 2.2). This is typically done in diffraction experiments,[112,113] as well as in protein NMR structure solutions,[115] by repeating the refinement process while omitting some of the data.

Table 2.15. Fractional coordinates for the atoms in the NMR-refined structure of $ZrMgMo_3O_{12}$

Atom	x	y	z
Zr1	0.0361	0.4975	0.6156
Mg1	0.4628	0.5000	0.3732
Mo1	0.7485	0.2766	0.4844
Mo2	0.1303	0.6607	0.3510
Mo3	0.6105	0.3623	0.1410
O1	0.1065	0.8418	0.3548
O2	0.8772	0.3912	0.5407
O3	0.0227	0.5846	0.2526
O4	0.3243	0.3357	0.3961
O5	0.0870	0.5858	0.4722
O6	0.3052	0.6306	0.3248
O7	0.4953	0.4392	0.2260
O8	0.5756	0.4293	0.0207
O9	0.1691	0.3277	0.5829
O10	0.6206	0.3740	0.4238
O11	0.2116	0.5984	0.6752
O12	-0.0857	0.6742	0.6410

2.4.3.3 ^{17}O NMR

Due to the sparsity of the NMR data in this case, and the computational demand of this approach, it is favourable to validate the crystal structure using data which were completely excluded from the refinement process. Chemical shifts have been used in the previous chapters as these are typically too computationally expensive to be used as refinement parameters in periodic DFT calculations but are relatively well reproduced in single-point calculations. In this case, the ^{17}O NMR data were omitted from the refinement

process and can be used for cross-validation purposes since the ^{17}O chemical shifts are well known to being very sensitive to the distance between the oxygen and the cations.[193]

The ^{17}O MAS and MQMAS NMR spectra are shown in Figure 2.20 where it can be seen that there are two general chemical shift regions containing multiple resonances. A first group of resonances centered around 630 ppm features three resonances that, once deconvoluted, integrate to line intensities of 2.9, 0.8 and 2.5, when decreasing in chemical shift. The second group, centered at 480 ppm, has four identifiable resonances that have integrated intensities of 0.97, 1.92, 1.99, and 0.98. It can then be concluded that each group contains six independent resonances, which is in agreement with the proposed structural model. Using GIPAW DFT calculations we can assign the lower chemical shift sites to the oxygen sites that are coordinated to zirconium whereas the sites with the higher chemical shift are coordinated to magnesium.

Due to the spherical nature of the O^{2-} anion, the oxygen sites have very small quadrupolar coupling constants and thus neither the chemical shift values nor the quadrupolar coupling constants can be determined by line shape fitting of a single spectrum. The center of gravity of the resonances depends however on the inverse square of the Larmor frequency. By acquiring a series of ^{17}O MAS NMR spectra at varying magnetic field strengths, namely 9.4, 16.4, and 21.1 T, it is possible to extract the isotropic chemical shift values and quadrupolar products ($P_Q = C_Q(1+\eta^2/3)^{1/2}$) for all sites. By plotting the apparent chemical shifts as a function of the inverse square of the Larmor frequency it is possible to form linear plots where the intercept is the isotropic chemical shift.[136] The P_Q value can be extracted from the slope of the graphs as $(\text{slope}/-6000)^{1/2}$. As it was possible to acquire an MQMAS spectrum for one set of the resonances at an applied magnetic field of

16.4 T that data was also included. In order to include MQMAS data it is however necessary to use the universal chemical shift referencing method of Amoureux[194] and scale the Larmor frequency by -10/17.[136] The ^{17}O MAS and MQMAS NMR spectra are shown in Figure 2.20 along with the linear fits of the of the magnetic field dependence of the peak positions; the extracted δ_{iso} and P_Q valued are also listed in Table 2.13.

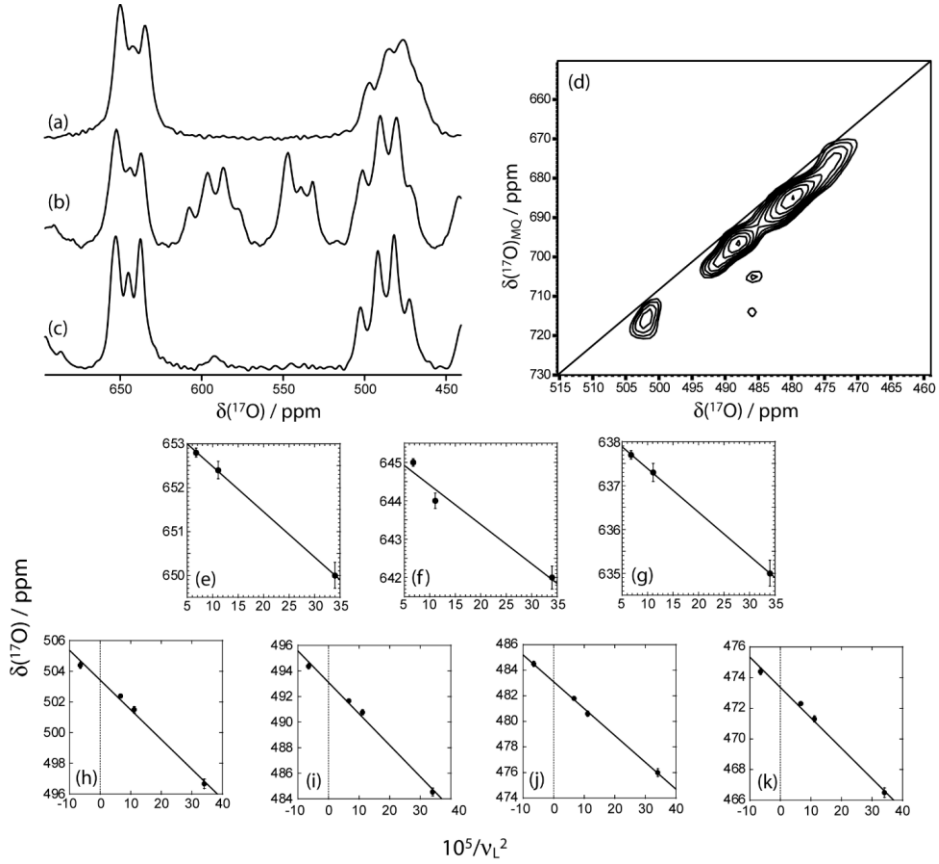

Figure 2.20. ^{17}O MAS NMR spectra acquired at applied magnetic fields of (a) 9.4 T, (b) 16.4 T, and (c) 21.1 T are shown. The MQMAS NMR spectrum acquired at 16.4 T is shown in (d). The plots correlating the apparent shifts as a function of the inverse of the Larmor frequency squared are shown in (e)-(k); the MQMAS data were included by scaling the value of $1/\nu_0^2$ by -10/17. Dr. Ulrike Werner-Zwanziger is acknowledged for having acquired the MAS and MQMAS NMR spectra at 16.4 T.

The oxygen sites that are bound to magnesium have smaller quadrupolar products of 1.3 MHz whereas the sites that are bound to zirconium have P_Q values of 1.8 to 2.0 MHz. This is in agreement with the fact that oxygen atoms would have a more covalent interaction with zirconium than magnesium, thus altering the spherical symmetry of the O^{2-} anion and increasing the P_Q. The plots in Figure 2.21 show the correlation between the calculated and experimental quadrupolar products as well as chemical shifts. There is a very good agreement between the calculated and experimental values for both parameters. The slope of best fit for the P_Q products is of 1.04 which is very close to the expected slope of 1.029 from the calibration and the P_Q values are slightly better reproduced using the NMR-refined structure ($R^2 = 0.9979$) than the DFT-refined structure ($R^2 = 0.9976$).

Surprisingly, the ^{17}O chemical shifts weren't reproduced quantitatively, although the relative shifts for each of the two groups of resonances were well reproduced. It is however well known that spin-orbit induced relativistic effects (heavy atom, light atom affect, HALA) can have a large impact on the chemical shifts of lighter elements.[195] We have then decided performed cluster model DFT calculations using the two-component zeroth-order regular approximation (ZORA) method to include scalar and spin-orbit relativistic effects. These calculations predict that there is a -47 ppm relativistic shift for the oxygen sites connected to a Mo and a Zr site whereas the relativistic shift is of only -27.5 ppm for those connected to Mo and Mg. As seen in Figure 2.21 the inclusion of this relativistic shift to the GIPAW results improves the slope from 0.7 to 0.8 and improves the correlations coefficients from 0.9946 to 0.9975. It is expected that full, four-component, relativistic DFT calculations would further improve the slope of the plot. Also, as was the case with the P_Q values, the isotropic chemical shifts are better reproduced by the NMR-refined structure than the DFT-

refined structure, which has a correlation coefficient of 0.9967.

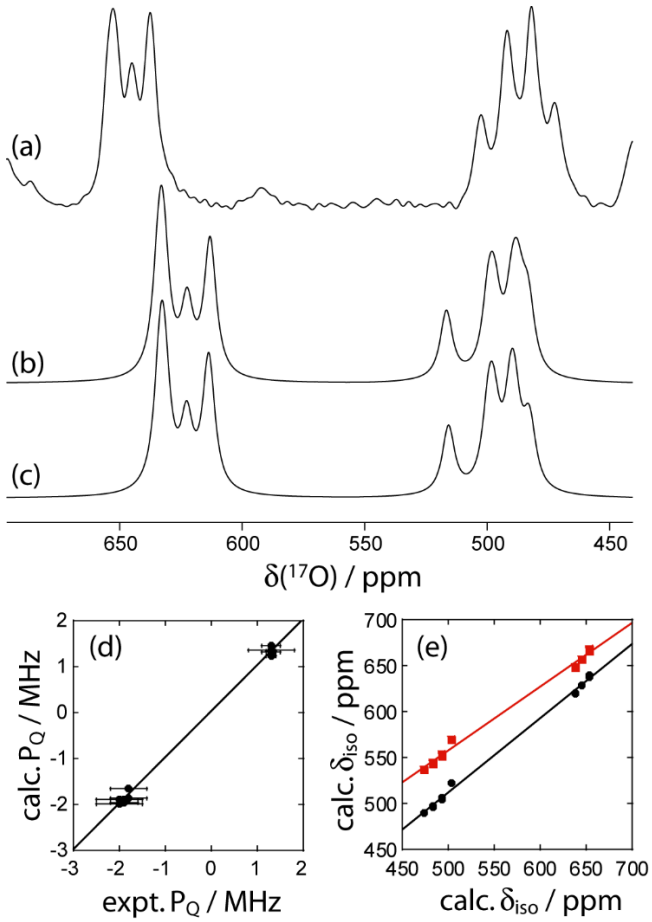

Figure 2.21. The ^{17}O MAS NMR spectrum acquired at 21.1 T (a) is overlaid with the predicted ^{17}O NMR spectra using the DFT-refined structure (b) and the NMR-refined structure (c). The correlations between the calculated and experimental P_Q (d) and δ_{iso} (e) values are also shown. In (d) the red squares correspond to the GIPAW DFT calculated data whereas the black circles show the calculated shifts which were scaled by their respective relativistic shifts.

The improvement in the predicted ^{17}O NMR spectra can also be visualised by observing the predicted ^{17}O NMR spectra, see Figure 2.21. It can be seen that the spread of the high chemical shift resonances is reduced in the NMR-refined structure, when compared

with the DFT-refined structure, in agreement with the experimental spectrum. Additionally, the lowest chemical shift resonance is significantly better reproduced by the NMR-refined crystal structure than the DFT-refined crystal structure which predicts that it would significantly overlap with its neighbouring resonance. The quality of the correlation plots in Figures 2.19 and 2.21 demonstrate the quality of the final NMR-refined crystal structure. These also show that DFT-based crystal structure refinements can be improved by the explicit inclusion of experimental data, such as EFG tensor components, which would lead, notably, to more accurate polyhedral distortions.

2.4.4 Conclusions

The crystal structure of $ZrMgMo_3O_{12}$, a near-zero thermal expansion material has been solved *ab initio* with the use of an NMR-driven crystallography approach which incorporates NMR derived crystallographic information into a PXRD crystal structure solution procedure. A Rietveld refinement was performed in order to extract accurate unit cell parameters; however, the coordinates weren't of sufficient accuracy. A hybrid NMR/DFT-based crystal structure refinement procedure, as described in chapter 2.1, was then applied in order to obtain accurate fractional coordinates for all the atoms in the crystal structure.

The quality of this NMR crystallographic crystal structure was then compared to that of the DFT- and Rietveld-refined structures using the EFG tensor components of the metal centers. ^{17}O NMR experiments, on an isotopically enriched sample, were also performed in order to cross-validate the structure since the ^{17}O NMR data was not used for the structural refinement. Notably, the ^{17}O NMR data were in better agreement with the NMR-refined

crystal structure than one that was refined using the DFT energy alone. The high quality crystal structure that was obtained for this material may then be compared to that of analogous materials in order to better understand the mechanism of near-zero thermal expansion, and, notably, the correlation between the coefficients of thermal expansion and the polyhedral distortions of the AO_6 octahedra.

2.4.5 Experimental

All samples were prepared by Carl P. Romao, a graduate student in the group of Mary Anne White at Dalhousie University.

2.4.5.1 ^{25}Mg NMR

The ^{25}Mg MAS NMR spectrum at 9.4 T ($\nu_0(^{25}Mg)$ = 24.5 MHz) was acquired using a Hahn echo sequence preceded by a double-frequency (DFS) pulse sweeping from 300 to 20 kHz in 5 ms for signal enhancement.[135,196] The sample was spun at 5 kHz using a 7 mm low-γ MAS probe. The central transition (CT) selective 90° and 180° pulses lasted 12 and 24 μs, respectively and the echo delay was of 200 μs. A total of 14504 scans were acquired with a 4 s recycle delay. The chemical shifts were referenced to a saturated $MgCl_2$ solution.

The ^{25}Mg MAS NMR spectrum at 21.1 T ($\nu_0(^{25}Mg)$ = 55.1 MHz) was acquired using a simple Bloch decay sequence with a 3 μs CT-selective excitation pulse. The sample was spun at 10 kHz using a 4 mm low-γ MAS probe. A total of 712 scans were accumulated with a 2 s recycle delay.

2.4.5.2 ^{91}Zr NMR

A static ^{91}Zr NMR spectrum was acquired at 9.4 T ($\nu_0(^{91}Zr)$ = 37.2 MHz) using a Hahn echo sequence preceded by a DFS pulse sweeping from 1 MHz to 100 kHz in 5 ms. The data was acquired on a 7 mm solenoid probe using 35992 scans and a 0.5 s recycle delay. A 5 μs CT-selective 90° pulse was used along with a 50 μs echo delay. The chemical shifts were referenced to a dichloromethane solution of Cp_2ZrCl_2.

A static ^{91}Zr NMR spectrum was acquired at 21.1 T ($\nu_0(^{91}Zr)$ = 83.7 MHz) using a Hahn echo sequence preceded by a DFS pulse sweeping from 1 MHz to 50 kHz in 2 ms. A 3 μs CT-selective 90° pulse was used along with a 30 μs echo delay. The data was acquired on a 4 mm MAS probe using 6250 scans and a 1 s recycle delay. An MAS NMR spectrum was also acquired at 21.1 T spinning at 10 kHz. The same experimental parameters were used, however, the echo delay was increased to 100 μs for rotor synchronization and a total of 2560 scans were accumulated.

2.4.5.3 ^{95}Mo NMR

The ^{95}Mo MAS NMR spectrum at 9.4 T ($\nu_0(^{95}Mo)$ = 26.1 MHz) was acquired using a Hahn echo sequence preceded by a double-frequency (DFS) pulse sweeping from 800 to 50 kHz in 5 ms for signal enhancement. The sample was spun at 5 kHz using a 7 mm low-γ MAS probe. The central transition (CT) selective 90° and 180° pulses lasted 8 μs and 16 μs, respectively and the echo delay was of 200 μs. A total of 18968 scans were acquired with a 8 s recycle delay. The chemical shifts were referenced to a 2 M solution of Na_2MoO_4.

A ^{95}Mo MAS NMR spectrum was also acquired at 11.7 T ($\nu_0(^{95}Mo)$ = 32.6 MHz) using a Hahn echo sequence preceded by a double-frequency (DFS) pulse sweeping from 1

MHz to 80 kHz in 5 ms for signal enhancement. The sample was spun at 10 kHz using a 4 mm low-γ MAS probe. The central transition (CT) selective 90° and 180° pulses lasted 6.67 μs and 13.34 μs, respectively and the echo delay was of 100 μs. A total of 11528 scans were acquired with a 10 s recycle delay.

A ^{95}Mo MAS NMR spectrum was also acquired at 21.1 T ($\nu_0(^{95}Mo)$ = 58.6 MHz) using a Bloch decay sequence. The sample was spun at 10 kHz using a 4 mm low-γ MAS probe. The central transition (CT) selective excitation pulse lasted 3 μs. A total of 128 scans were acquired with a 5 s recycle delay. An MQMAS NMR spectrum[197] was also acquired using the three-pulse sequence with a z-filter.[198] The excitation, conversion, and detection pulses lasted 8 μs, 3 μs, and 20 μs, respectively. A total of 45 t_1 increments of 100 μs were acquired with 240 scans each.

2.4.5.4 ^{17}O NMR

A ^{17}O MAS NMR spectrum was acquired at 9.4 T using 13.5 kHz MAS with a 4 mm triple resonance MAS probe. A 0.6 μs excitation pulse was used and a baseline correction was applied to remove the effects from the pulse ring-down. 44548 scans were summed with a 1 s recycle delay. Chemical shifts were referenced to water.

^{17}O MAS NMR spectra were also acquired at 21.1 T using a 2.5 mm MAS probe. The optimal spinning frequency was of 26 kHz which avoided any overlap between the sidebands, the centerbands, and a peak from ZrO_2 in the rotor. 148000 scans were acquired with a 0.5 s recycle delay.

Static ^{71}Zr NMR spectra were fit using the QUEST program,[199] whereas DMfit[166] was used to fit the MAS NMR spectra. The two-dimensional-one-pulse procedure, used to sum the spinning sidebands, is implemented in the DMfit program.[156]

2.4.5.5 DFT Calculations and Structure Refinement

All PAW and GIPAW DFT calculations were performed using the CASTEP program (ver. 3.2 or 4.1).[34,37,38,140] The GGA functional of Perdew, Burke, and Ernzerhof (PBE)[118] was used for all the DFT calculations. A 3x3x2 k-point grid was used along with a 610 eV kinetic energy cut-off. On-the-fly generated ultrasoft pseudopotentials were used for all atoms.

The accuracy of the PAW DFT predicted EFG tensor components was determined by performing calculations on model systems with known crystal structures and EFG tensor parameters. This makes it possible to also determine the factors by which the PAW DFT calculations systematically over- or underestimate the EFG tensor components for each element. This over- or underestimation of the EFG tensor components generally arises from the use of pseudopotentials to replace the core functions and is not present in all-electron DFT calculations (see chapter 2.1). It is important to include this factor when refining crystal structures using experimental EFG tensor parameters and PAW DFT calculated ones otherwise the polyhedral distortions would be under- or over-estimated. Our calibration curves for ^{17}O, ^{25}Mg, ^{91}Zr, and ^{95}Mo are shown in chapter 2.1. From these curves, we determined that the calculated EFG tensor parameters need to be scaled by 1.029 ± 0.007 for ^{17}O, 1.14 ± 0.04 for ^{25}Mg, 0.93 ± 0.04 for ^{91}Zr, and 1.11 ± 0.02 for ^{95}Mo. These curves also demonstrate that the PAW DFT calculated EFG tensor components are highly accurate for

all the elements in this system and that a similar accuracy should be expected for $ZrMgMo_3O_{12}$. An inferior quality of the PAW DFT calculated EFG tensor components is an indication that the fractional coordinates are inaccurate.

The geometry optimization of the crystal structure was performed with fixed unit cell dimensions. The NMR/DFT-refinement of the crystal structure was subsequently performed using a steepest descent least-squares minimization of the χ^2 parameter, as described in chapter 2.1. All DFT calculations in the refinement process calculated only the EFG due to its significantly lower computational cost, when compared to the magnetic shielding. Convergence was achieved after 3 iteration steps, which corresponds to a total of 174 PAW DFT calculations for the refinement of the crystal structure.

Relativistic DFT calculations were performed using the Amsterdam density functional (ADF) program.[200] Two-component (scalar and spin-orbit) relativistic effects were included using the zeroth-order regular approximation (ZORA),[201] as implemented in ADF. Calculations with and without relativistic effects were performed on M-O-Mo (M being either Mg or Zr) clusters and the difference in chemical shifts between the two is the spin-orbit ZORA relativistic shift. Calculations on larger clusters generally had SCF convergence issues; this is a known problem for transition metal oxide systems. Calculations were performed using the revPBE GGA functional[202] and the ZORA/TZ2P Slater basis set.[203]

References

[1] Harris, R.K.; Wasylishen, R.E.; Duer, M.J., Eds.; *NMR Crystallography*; John Wiley & Sons: Chichester, UK, 2009.

[2] Martineau, C.; Senker, J.; Taulelle, F. *Annu. Rep. NMR Spectrosc.* **2014**, *82*, 1-57.

[3] Senker, J.; Seyfarth, L.; Voll, J. *Solid State Sci.* **2004**, *6*, 1039-1052.

[4] Taulelle, F. *Solid State Sci.* **2004**, *6*, 1053-1057.

[5] Elena, B.; Emsley, L. *J. Am. Chem. Soc.* **2005**, *127*, 9140-9146.

[6] Elena, B.; Pintacuda, G.; Mifsud, N.; Emsley, L. *J. Am. Chem. Soc.* **2006**, *128*, 9555-9560.

[7] Pickard, C.J.; Salager, E.; Pintacuda, G.; Elena, B.; Emsley, L. *J. Am. Chem. Soc.* **2007**, *129*, 8932-8933.

[8] Salager, E.; Stein, R.S.; Pickard, C.J.; Elena, B.; Emsley, L. *Phys. Chem. Chem. Phys.* **2009**, *11*, 2610-2621.

[9] Santos, S. M.; Rocha, J.; Mafra, L. *Cryst Growth Des.* **2013**, *13*, 2390-2395.

[10] Salager, E.; Day, G.M.; Stein, R.S.; Pickard, C.J.; Elena, B.; Emsley, L. *J. Am. Chem. Soc.* **2010**, *132*, 2564-2566.

[11] Luchinat, C.; Parigi, G.; Ravera, E.; Rinaldelli, M. *J. Am. Chem. Soc.* **2012**, *134*, 5006-5009.

[12] Brouwer, D.H.; Darton, R.J.; Morris, R.E.; Levitt, M.H. *J. Am. Chem. Soc.* **2005**, *127*, 10365-10370.

[13] Martineau, C.; Mellot-Draznieks, C.; Taulelle, F. *Phys. Chem. Chem. Phys.* **2011**, *13*, 18078-18087.

[14] Martineau, C.; Bouchevreau, B.; Tian, Z.; Lohmeier, S.-J.; Behrens, P.; Taulelle, F. *Chem. Mater.* **2011**, *23*, 4799-4809.

[15] Brouwer, D. H.; Cadars, S.; Eckert, J.; Liu, Z.; Terasaki, O.; Chmelka, B. F. *J. Am. Chem. Soc.* **2013**, *135*, 5641-5655.

[16] Bouchevreau, B.; Martineau, C.; Mellot-Draznieks, C.; Tuel, A.; Suchomel, M. R.; Trébosc, J.; Lafon, O.; Amoureux, J.-P.; Taulelle, F. *Chem. Mater.* **2013**, *25*, 2227-2242.

[17] Bouchevreau, B.; Martineau, C.; Mellot-Draznieks, C.; Tuel, A.; Suchomel, M. R.; Trébosc, J.; Lafon, O.; Amoureux, J.-P.; Taulelle, F. *Chem. Eur. J.* **2013**, *19*, 5009-5013.

[18] Witter R.; Sternberg, U.; Hesse, S.; Kondo, T.; Koch, F.-T., Ulrich, A.S. *Macromolecules* **2006**, *39*, 6125-6132.

[19] Brouwer, D.H.; Enright, G.D. *J. Am. Chem. Soc.* **2008**, *130*, 3095-3105.

[20] Brouwer, D.H. *J. Am. Chem. Soc.* **2008**, *130*, 6306-6307.

[21] Brouwer, D.H. *J. Magn. Reson.* **2008**, *194*, 136-146.

[22] Cadars, S.; Brouwer, D.H.; Chmelka, B.F. *Phys. Chem. Chem. Phys.* **2009**, *11*, 1825-1837.

[23] Wylie, B.J.; Schwieters, C.D.; Oldfield, E.; Rienstra, C.M. *J. Am. Chem. Soc.* **2009**, 131, 985-992.

[24] Wylie, B.J.; Sperling, L.J.; Nieuwkoop, A.J.; Franks, W.T.; Oldfield, E.; Rienstra, C.M. *Proc. Natl. Acad. Sci. U.S.A.* **2011**, *108*, 16974-16979.

[25] Widdifield, C.M.; Bryce, D.L. *Phys. Chem. Chem. Phys.* **2009**, *11*, 7120-7122.

[26] Dutour, J.; Guillou, N.; Huguenard, C.; Taulelle, F.; Mellot-Draznieks, C.; Férey, G. *Solid State Sci.*, **2004**, *6*, 1059-1067.

[27] Favre-Nicolin, V.; Černý, R. *J. Appl. Cryst.* **2002**, *35*, 734-743.

[28] Coelho, A.A. *J. Appl. Cryst.* **2003**, *36*, 86-95.

[29] Wang, X.; Adhikari, J.; Smith, L. J. *J. Phys. Chem. C* **2009**, *113*, 17548-17559.

[30] Hansen, M.R.; Madsen, G.K.H.; Jakobsen, H.J.; Skibsted, J. *J. Phys. Chem. A* **2005**, *109*, 1989-1997.

[31] Zhou, B.; Giavani, T.; Bildsøe, H.; Skibsted, J.; Jakobsen, H.J. *Chem. Phys. Lett.* **2005**, *402*, 133-137.

[32] Hansen, M.R.; Madsen, G.K.H.; Jakobsen, H.J.; Skibsted, J. *J. Phys. Chem. B* **2006**, *110*, 5975-5983.

[33] Zwanziger, J. W. *Computing Electric Field Gradient Tensors*, in: Harris, R. K.; Wasylishen, R. E., Eds. *eMagRes*, John Wiley & Sons, 2009.

[34] Clark, S.J.; Segall, M.D.; Pickard, C.J.; Hasnip, P.J.; Probert, M.I.J.; Refson, K.; Payne, M.C. *Z. Kristallogr.* **2005**, *220*, 567-570.

[35] Segall, M.D.; Lindan, P.J.D.; Probert, M.J.; Pickard, C.J.; Hasnip, P.J.; Clark, S.J.; Payne, M.C. *J. Phys. : Condens. Matter* **2002**, *14*, 2717-2744.

[36] Pickard, C.J.; Mauri, F. *Phys. Rev. B* **2001**, *63*, 245101.

[37] Profeta, M.; Mauri, F.; Pickard, C.J. *J. Am. Chem. Soc.* **2003**, *125*, 541-548.

[38] Charpentier, T. *Solid State Nucl. Magn. Reson.* **2011**, *40*, 1-20.

[39] Chapman, R.P.; Bryce, D.L. *Phys. Chem. Chem. Phys.* **2009**, *11*, 6987-6998.

[40] Cederberg, J.; Kang, L.; Conklin, C.; Berger, E. *J. Mol. Spectrosc.* **2010**, *263*, 142-144.

[41] De Leeuw, F. H.; van Wachem, R.; Dymanus, A. *J. Chem. Phys.* **1970**, *53*, 981-984.

[42] Dračínský, M.; Hodgkinson, P. *CrystEngComm* **2013**, *15*, 8705.

[43] Rossano, S.; Mauri, F.; Pickard, C. J.; Farnan, I. *J. Phys. Chem. B* **2005**, *109*, 7245-7250.

[44] Dumez, J.-N.; Pickard, C. J. *J. Chem. Phys.* **2009**, *130*, 104701.

[45] Davies, E.; Duer, M. J.; Ashbrook, S. E.; Griffin, J. M. *J. Am. Chem. Soc.* **2012**, *134*, 12508-12515.

[46] Adamiv, V.T.; Burak, Y.V.; Teslyuk, I.M. *J. Alloys Compd.* **2009**, *475*, 869-873.

[47] Hansen, M.R.; Vosegaard, T.; Jakobsen, H.J.; Skibsted, J. *J. Phys. Chem. A* **2004**, *108*, 586-594.

[48] Ivanov, Y.V.; Belokoneva, E.L. *Acta Cryst. B* **2007**, *63*, 49-55.

[49] Downs, J.W.; Swope, R.J. *J. Phys. Chem.* **1992**, *96*, 4834-4840.

[50] Burns, P.C.; Hawthorne, F.C. *Can. Mineral.* **1993**, *31*, 297-304.

[51] Levy, H.A.; Lisensky, G.C. *Acta Cryst B* **1978**, *34*, 3502-3510.

[52] Levien, L.; Prewitt, C.T. *Am. Mineral.* **1981**, *66*, 324-333.

[53] Grandinetti, P.J.; Baltisberger, J.H.; Farnan, I.; Stebbins, J.F.; Werner, U.; Pines, A. *J. Phys. Chem.* **1995**, *99*, 12341-12348.

[54] Tsirelson, V.G.; Antipin, M.Y.; Gerr, R.G.; Ozerov, R.P.; Struchkov, Y.T. *Phys. Stat. Sol. A* **1985**, *87*, 425-433.

[55] Brun, E.; Derighetti, B.; Hundt, E.E.; Niebuhr, H.H. *Phys. Lett. A* **1970**, *31*, 416-417.

[56] Kirfel, A.; Lippmann, T.; Blaha, P.; Schwarz, K.; Cox, D.F.; Rosso, K.M.; Gibbs, G.V. *Phys. Chem. Miner.* **2005**, *32*, 301-313.

[57] Fritsch, R.; Brinkmann, D.; Hafner, S.S.; Hosoya, S.; Lorberth, J.; Roos, J. *Phys. Lett. A* **1986**, *118*, 98-102.

[58] Paul, G.L.; Pryor, A.W. *Acta Cryst. B* **1971**, *27*, 2700-2702.

[59] Vosegaard, T.; Hald, E.; Daugaard, P.; Jakobsen, H.J. *Rev. Sci. Intrum.* **1999**, *70*, 1771-1779.

[60] Ghose, S.; Wan, C. *Am. Mineral.* **1978**, *63*, 304-310.

[61] Ghose, S.; Brinkmann, D.; Roos, J. *Phys. Chem. Miner.* **1989**, *16*, 720-724.

[62] Prasad, S.M.; Rani, A. *Acta Cryst. E* **2001**, *57*, i67-i69.

[63] Itoh, J.; Kusaka, R.; Yamagata, Y. *J. Phys. Soc. Jap.* **1954**, *9*, 209-218.

[64] Fortes, A. D.; Wood, I. G.; Vočadlo, L.; Brand, H. E. A.; Knight, K. S. *J. Appl. Cryst.* **2007**, *40*, 761-770.

[65] Arlett, R. H.; White, J. G.; Robbins, M. *Acta Cryst* **1967**, *22*, 315-320.

[66] Irish, D. E.; Semmler, J.; Taylor, N. J.; Toogood, G. E. *Acta Cryst C* **1991**, *47*, 2322-2324.

[67] Bekakin, V.V.; Klevtsova, R. F.; Gaponenko, L. A. *Sov. Phys. Crystallogr.* **1982**, *27*, 20-22.

[68] Catti, M.; Ferraris, G.; Hull, S.; Pavese, A. *Phys. Chem. Miner.* **1995**, *22*, 200-206.

[69] Krishnamachari, N.; Calvo, C. *Can. J. Chem.* **1971**, *49*, 1629-1637.

[70] Macavei, J.; Schulz, H. *Z. Kristallogr.* **1993**, *207*, 193-208.

[71] Pallister, P.J.; Moudrakovski, I. L.; Ripmeester, J. A. *Phys. Chem. Chem. Phys.* **2009**, *11*, 11487-11500.

[72] Vosegaard, T.; Jakobsen, H.J. *J. Magn. Reson.* 1997, *128*, 135-137.

[73] Gatta, G.D.; Nestola, F.; Bromiley, G.D.; Loose, A. *Am. Mineral.* **2006**, *91*, 1839-1846.

[74] Mizuno, M.; Aoki, Y.; Endo, K.; Greenidge, D. *J. Phys. Chem. Solids* **2006**, *67*, 705-709.

[75] Nakatsuka, A.; Yoshiasa, A.; Yamanaka, T. *Acta Cryst B*, **1999**, *55*, 266-272.

[76] Vosegaard, T.; Byriel, I.P.; Pawlak, D.A.; Wozniak, K.; Jakobsen, H.J. *J. Am. Chem. Soc.* **1998**, *120*, 7900-7904.

[77] Bryant, P.L.; Harwell, C.R.; Wu, K.; Fronczek, F.R.; Hall, R.W.; Butler, L.G. *J. Phys. Chem. A* **1999**, *103*, 5246-5252.

[78] Le Bail, A.; Laval, J.-P. *Eur. J. Solid State Inorg. Chem.* **1998**, *35*, 357-372.

[79] Pauvert, O.; Fayon, F.; Rakhmatullin, A.; Krämer, S.; Horvatić, M.; Avignant, D.; Berthier C.; Deschamps, M.; Massiot, D.; Bessada, C. *Inorg. Chem.* **2009**, *48*, 8709-8717.

[80] Hoppe, V. R.; Mehlhorn, B. *Z. Anorg. Allg. Chem.* **1976**, *425*, 200-208.

[81] Smith, D. K.; Newkirk, H. W. *Acta Cryst*. **1965**, *18*, 983-991.

[82] Kisi, E. H.; Howard, C. J. *J. Am. Ceram. Soc.* **1989**, *72*, 1757-1760.

[83] O'Dell, L. A.; Schurko, R. W. *Chem. Phys. Lett.* **2008**, *464*, 97-102.

[84] Claveris, J.; Foussier C.; Hagenmuller, P. *Bull. Soc. Chim. Fr.* **1966**, 244-246.

[85] Bastow, T. J.; Hobday, M. E.; Smith, M. E.; Whitfield, H. J. *Solid State Nucl. Magn. Reson.* **1994**, *3*, 49-57.

[86] Treushnikov, E. N.; Ilyukhin, V. V.; Belov, N. V. *Dokl. Akad. Nauk. SSSR* **1970**, *190*, 334-337.

[87] Bastow, T. J.; Hobday, M. E.; Smith, M. E.; Whitfield, H. J. *Solid State Nucl. Magn. Reson.* **1996**, *5*, 293-303.

[88] Herak, R. M.; Malčić, S. S.; Manojlovič, L. M. *Acta Cryst.* **1965**, *18*, 520.

[89] Krebs, V. B. *Z. Anorg. Allg. Chem.* **1970**, *378*, 263-272.

[90] Krebs, V. B.; Henkel, G.; Dartman, M. *Acta Cryst B* **1979**, *35*, 274-278.

[91] Bastow, T. J.; *J. Phys. Condens. Matter* **1990**, *2*, 6327-6330.

[92] Gatehouse, B. M.; Leverett, P. *J. Chem. Soc. A* **1969**, 849-854.

[93] Forgeron, M. A. M.; Wasylishen, R. E. *Phys. Chem. Chem. Phys.* **2008**, *10*, 574-581.

[94] Dittman, M.; Schweda, E. *Z. Anorg. Allg. Chem.* **1998**, *624*, 2033-2037.

[95] d'Espinose de Lacaillerie, J.-B.; Barberon, F.; Romanenko, K. V.; Lapina, O. B.; Le Pollès, L.; Gautier, R.; Gan, Z. *J. Phys. Chem. B* **2005**, *109*, 14033-14042.

[96] Leciejewicz, J. *Z. Kristallogr.* **1965**, *121*, 158-164.

[97] Reichelt, W.; Weber, T.; Söhnel, T. Däbritz, S. *Z. Anorg. Allg. Chem.* **2000**, *626*, 2020-2027.

[98] Pyykkö, P. *Mol. Phys.* **2008**, *106*, 1965-1974.

[99] Ruszczyński, A.; Nonlinear Optimization; Princeton University Press: Princeton, USA, 2006, p. 218

[100] Rza-Zade, P.F.; Abdullaev, G.K.; Samedov, F.R.; Zeinalova, K.K. *Russ. J. Inorg. Chem.* **1971**, *16*, 1221-1223.

[101] Corbel, G.; Leblanc, M. *J. Solid State Chem.* **2000**, *154*, 344-349.

[102] He, M.; Chen, X.L.; Zhou, T.; Hu, B.Q.; Xu, Y.P.; Xu, T. *J. Alloys Compd.* **2001**, *327*, 210-214.

[103] Chen, C.; Wang, Y.; Wu, B.; Wu, K.; Zeng, W.; Yu, L. *Nature* **1995**, *373*, 322-324.

[104] Atuchin, V.V.; Bazarov, B.G.; Gavrilova, T.A.; Grossman, V.G.; Molokeev, M.S.; Bazarova, Z.G. *J. Alloys Compd.* **2012**, *515*, 119-122.

[105] Meng, X.Y.; Gao, J.H.; Wang, Z.Z.; Li, R.K.; Chen, C.T. *J. Phys. Chem. Solids* **2005**, *66*, 1655-1659.

[106] He, M.; Kienle, L.; Simon, A.; Chen, X.L.; Duppel, V. *J. Solid State Chem.* **2004**, *177*, 3212-3218.

[107] Gao, J.H.; Xia, W.B.; Li, R.K. *J. Phys. Chem. Solids* **2007**, *68*, 536-540.

[108] Bryce, D.L.; Wasylishen, R.E.; Gee, M. *J. Phys. Chem. A* **2001**, *105*, 3633-3640.

[109] Mackenzie, K.J.D.; Smith, M.E. *Multinuclear Solid-State NMR of Inorganic Materials*; Elesevier Science: Oxford, UK, 2002.

[110] Jäger, C. In *NMR Basic Principles and Progress*; Diehl, P., Fluck, E., Günther, H., Kosfeld, R., Seelig, J., Eds.; Springer-Verlag: Berlin, 1994; Vol. 31, pp 133-170.

[111] Skibsted, J.; Nielsen, N.C.; Bildsøe, H.; Jakobsen, H.J. *J. Magn. Reson.* **1991**, *95*, 88-117.

[112] Brädén, C.-I.; Jones, T.A. *Nature* **1990**, *343*, 687-689.

[113] Brünger, A.T. *Nature* **1992**, *355*, 472-475.

[114] Brünger, A.T. *Methods Enzymol.* **1997**, *277*, 366-396.

[115] Cornilescu, G.; Marquardt, J.L.; Ottiger, M.; Bax, A. *J. Am. Chem. Soc.* **1998**, *120*, 6836-6837.

[116] Eichele, K.; Wasylishen, R.E. WSolids1: Solid-State NMR Spectrum Simulation Package v. 1.20.15, University of Tübingen, Tübingen, Germany, 2011.

[117] Bak, M.; Rasmussen, J.T.; Nielsen, N.C. *J. Magn. Reson.* **2000**, *147*, 296-330.

[118] Perdew, J.P.; Burke, K.; Ernzerhof, M. *Phys. Rev. Lett.* **1996**, *77*, 3865-3868.

[119] Hung, I.; Howes, A. P.; Anupõld, T.; Samoson, A.; Massiot, D.; Smith, M. E.; Brown S. P.; Dupree, R. *Chem Phys. Lett.* **2006**, *432*, 152-156.

[120] Howes, A. P.; Vedishcheva, N. M.; Samoson, A.; Hanna, J. V.; Smith, M. E.; Holland, D.; Dupree, R. *Phys. Chem. Chem. Phys.* **2011**, *13*, 11919-11928.

[121] Perras, F. A.; Korobkov, I.; Bryce, D. L. *Phys. Chem. Chem. Phys.* **2012**, *14*, 4677-4681.

[122] Edén, M.; Frydman, L. *J. Phys. Chem. B* **2003**, *107*, 14598-14611.

[123] Duer, M. J. *Chem. Phys. Lett.* **1997**, *277*, 167-174.

[124] Wi, S.; Frydman, L. *J. Chem. Phys.* **2000**, *112*, 3248-3261.

[125] Mali, G.; Kaučič, V.; Taulelle, F. *J. Chem. Phys.* **2008**, *128*, 204503.

[126] Perras, F. A.; Bryce, D. L. *J. Magn. Reson.* **2011**, *213*, 82-89.

[127] Wu, G.; Yamada, K. *Chem. Phys. Lett.* **1999**, *313*, 519-524.

[128] Wi, S.; Logan, J. W.; Sakellariou, D.; Walls, J. D.;. Pines, A. *J. Chem. Phys.* **2002**, *117*, 7024-7033.

[129] Wi, S.; Heise. H.; Pines, A. *J. Am. Chem. Soc.* **2002**, *124*, 10652-10653.

[130] Brinkmann, A. Edén, M. *Can. J. Chem.* **2011**, *89*, 892-899.

[131] Perras, F. A.; Bryce, D. L. *J. Chem. Phys.* **2013**, *138*, 174202.

[132] Leung, K. Y.; Calvo, C. *Can. J. Chem.* **1972**, *50*, 2519-2526.

[133] Ivashkevich, L. S.; Selevich, K. A.; Lyakhov, A. S.; Selevich, A. F.; Petrusevich, Y. I. *Z. Kristallogr.* **2002**, *217*, 73-77.

[134] Schmedt auf der Günne, J. *J. Magn. Reson.* **2003**, *165*, 18-32.

[135] Kentgens, A. P. M.; Verhagen, R. *Chem. Phys. Lett.* **1999**, *300*, 435-443.

[136] Engelhardt, G.; Kentgens, A. P. M.; Koller, H.; Samoson, A. *Solid State Nucl. Magn. Reson.* **1999**, *15*, 171-180.

[137] Asunskis, A. L.; Gaskell, K. J.; Asunskis, D. J.; Sherwood, P. M. A. *J. Vac. Sci. Technol. A* **2003**, *21*, 1126-1132.

[138] Atuchin, V. V.; Kesler, V. G.; Pervukhina, N. V. *Surf. Rev. Lett.* **2008**, *15*, 391-399.

[139] Popović, L.; de Waal, D. Boeyens, J. C. A. *J. Raman Spectrosc.* **2005**, *36*, 2-11.

[140] Bonhomme, C.; Gervais, C.; Babonneau, F.; Coelho, C.; Pourpoint, F.; Azaïs, T.; Ashbrook, S. E.; Griffin, J. M.; Yates, J. R.; Mauri, F.; Pickard, C. J. *Chem. Rev.* **2012**, *112*, 5733-5779.

[141] Baldus, M.; Meier, B. H.; Ernst, R. R.; Kentgens, A. P. M.; zu Altenschildesche, H. M.; Nesper, R. *J. Am. Chem. Soc.* **1995**, *117*, 5141-5147.

[142] Kubo, A.; McDowell, C. A. *J. Chem. Soc., Faraday Trans.* **1988**, *84*, 3713-3730.

[143] Griffiths, L.; Root, A.; Harris, R. K.; Packer, K. J.; Chippendale, A. M.; Tromans, F. R. *J. Chem. Soc. Dalton Trans.* **1986**, 2247-2251.

[144] Rothwell, W. P.; Waugh, J. S.; Yesinowski, J. P. *J. Am. Chem. Soc.* **1980**, *102*, 2637-2643.

[145] Koller, H.; Engelhardt, G.; Kentgens, A. P. M.; Sauer, J. *J. Phys. Chem.* **1994**, ***98***, 1544-1551.

[146] Prochnow, D.; Grimmer, A.-R.; Freude, D. *Solid State Nucl. Magn. Reson.* **2006**, *30*, 69-74.

[147] Vasconcelos, F.; Cristol, S.; Paul, J.-F.; Tricot, G.; Amoureux, J.-P.; Montagne, L.; Mauri, F.; Delevoye, L. *Inorg. Chem.* **2008**, *47*, 7327-7337.

[148] Perras, F. A.; Bryce, D. L. *J. Magn. Reson.* **2011**, *211*, 234-239.

[149] Charpentier, T.; Ispas, S.; Profeta, M.; Mauri, F.; Pickard, C. J. *J. Phys. Chem. B* **2004**, *108*, 4147-4161.

[150] Vasconcelos, F.; Cristol, S.; Paul, J.-F.; Montagne, L.; Mauri, F.; Delevoye, L. *Magn. Reson. Chem.* **2010**, *48*, S142-S150.

[151] Favot, F.; Dal Corso, A. *Phys. Rev. B* **1999**, *60*, 11427-11431.

[152] Wu, X.; Vargas, M. C.; Nayak, S.; Lotrich, V.; Scoles, G. *J. Chem. Phys.* **2001**, *115*, 8748-8757.

[153] Dumez, J.-N.; Butler, M. C.; Salager, E.; Elena-Herrmann, B. Emsley, L. *Phys. Chem. Chem. Phys.* **2010**, *12*, 9172-9175.

[154] Pound, R. V. *Phys. Rev.* **1950**, *79*, 685-702.

[155] Blümler, P.; Jansen, J. Blümich, B. *Solid State Nucl. Magn. Reson.* **1994**, *3*, 237-240.

[156] Massiot, D.; Hiet, J.; Pellerin, N.; Fayon, F.; Deschamps, M.; Steuernagel, S.; Grandinetti, P. J. *J. Magn. Reson.* **2006**, *181*, 310-315.

[157] Ketudat, S.; Pound, R. V. *J. Chem. Phys.* **1957**, *26*, 708-709.

[158] Soda, G.; Chiba, T. *J. Chem. Phys.* **1969**, *50*, 439-455.

[159] Moudrakovski, I. L.; Ratcliffe, C. I.; Ripmeester, J. A. *J. Am. Chem. Soc.* **2001**, *123*, 2066-2067.

[160] Kristensen, J. H.; Farnan, I. *J. Chem. Phys.* **2001**, *114*, 9608-9624.

[161] Schurko, R. W.; Wi, S.; Frydman, L. *J. Phys. Chem. A* **2002**, *106*, 51-62.

[162] Kurkiewicz, T.; Thrippleton, M. J.; Wimperis, S. *Chem Phys. Lett.* **2009**, *467*, 412-416.

[163] Robyr, P.; Tomaselli, M.; Straka, J.; Grob-Pisano, C.; Sutter, U. W.; Meier, B. H.; Ernst, R. R. *Mol. Phys.* **1995**, *84*, 995-1020.

[164] Karau, F. W.; Seyfarth, L.; Oekler, O.; Senker, J.; Landskron, K.; Schnick, W. *Chem. Eur. J.* **2007**, *13*, 6841-6852.

[165] Sarr, O.; Diop, L. *Spectrochimica Acta A*, **1987**, *43*, 999-1005.

[166] Massiot, D.; Fayon, F.; Capron, M.; King, I.; Le Calvé, S.; Alonso, B.; Durand, J.-O.; Bujoli, B.; Gan Z.; Hoatson, G. *Magn. Reson. Chem.* **2002**, *40*, 70-76.

[167] Gan, Z.; Kwak, H.-T. *J. Magn. Reson.* **2004**, *168*, 346-351.

[168] Samoson, A.; Lippmaa, E. *J. Magn. Reson.* **1989**, *84*, 410-416.

[169] Dixon, W. T. *J. Chem. Phys.* **1982**, *77*, 1800-1809.

[170] Baldus, M.; Levante, T. O.; Meier, B. H. *Z. Naturforsch.* **1994**, *49a*, 80-88.

[171] Smith, S. A.; Levante, T. O.; Meier, B. H.; Ernst, R. R. *J. Magn. Reson. Ser. A* **1994**, *106*, 75-105.

[172] Hung, I.; Wong, A.; Howes, A. P.; Anupõld, T.; Past, J.; Samoson, A.; Mo, X.; Wu, G.; Smith, M. E.; Brown, S. P.; Dupree, R. *J. Magn. Reson.* **2007**, *188*, 246-259.

[173] Samoson, A.; Anupõld, T. *Solid State Nucl. Magn. Reson.* **2000**, *15*, 217-225.

[174] Kentgens, A. P. M.; van Eck, E. R. H.; Ajithkumar, T. G. ; Anupõld, T.; Past, J.; Reinhold, A.; Samoson, A. *J. Magn. Reson.* **2006**, *178*, 212-219.

[175] Brüschweiler, R.; Zhang, F. *J. Chem. Phys.* **2004**, *120*, 5253-5260.

[176] Hu, B.; Amoureux, J.-P.; Trebosc, J.; Deschamps, M.; Tricot, G. *J. Chem. Phys.* **2008**, *128*, 134502.

[177] Miller, W.; Smith, C. W.; Mackenzie, D. S.; Evans, K. E. *J. Mater. Sci.* **2009**, *44*, 5441-5451.

[178] Lind, C. *Materials* **2012**, *5*, 1125-1154.

[179] Barrera, G. D.; Bruno, J. A. O.; Barron T. H. K.; Allan, N. L. *J. Phys. Condens. Matter* **2005**, *17*, R217-R252.

[180] Suzuki, T.; Omote, A. *J. Am. Ceram. Soc.* **2004**, *87*, 1365-1367.

[181] Marinkovic, B. A.; Jardim, P. M.; Ari, M.; de Avillez, R. R.; Rizzo, F.; Ferreira, F. F. *Phys. Stat. Sol. B* **2008**, *245*, 2514-2519.

[182] Song, W. B.; Liang, E.-J.; Liu, X.-S.; Li, Z.-Y.; Yuan, B.-H.; Wang, J.-Q. *Chin. Phys. Lett.* **2013** *30*, 126502.

[183] Gindhart, A. M.; Lind, C.; Green, M. *J. Mater. Res.* **2008**, *23*, 210-213.

[184] Marinkovic, B. A.; Ari, M.; de Avillez, R. R.; Rizzo, F.; Ferreira, F. F.; Miller, K. J.; Johnson, M. B.; White, M. A. *Chem. Mater.* **2009**, *21*, 2886-2894.

[185] Marinkovic, B. A.; Ari, M.; Jardim, P. M.; de Avillez, R. R.; Rizzo, F.; Ferreira, F. F. *Thermochim. Acta* **2010**, *499*, 48–53.

[186] Ghose, S.; Tsang, T. *Am. Mineral.* **1973**, *58*, 748-755.

[187] Burgess, K. M. N.; Xu, Y.; Leclerc, M. C.; Bryce, D. L. *J. Phys. Chem A* **2013**, *117*, 6561-6570.

[188] Hampson, M. R.; Hodgkinson, P.; Evans, J. S. O.; Harris, R. K.; King, I. J.; Allen, S.; Fayon, F. *Chem. Commun.* **2004**, 392-393.

[189] Hampson, M. R.; Evans, J. O.; Hodgkinson, P. *J. Am. Chem. Soc.* **2005**, *127*, 15175-15181.

[190] Hibble, S. J.; Chippindale, A. M.; Marelli, E.; Kroeker, S.; Michaelis, V. K.; Greer, B. J.; Aguiar, P. M.; Bilbé, E. J.; Barney, E. R.; Hannon, A. C. *J. Am. Chem. Soc.* **2013**, *135*, 16478-16489.

[191] Omote, A.; Yotsuhashi, S.; Zenitani, Y.; Yamada, Y. *J. Am. Ceram. Soc.* **2011**, *94*, 2285-2288.

[192] Evans, J. S. O.; Mary, T. A.; Sleight, A. *J. Solid State Chem.* **1998**, *137*, 148–160.

[193] Turner, G. L.; Chung, S. E.; Oldfield, E. *J. Magn. Reson.*, **1985**, *64*, 316-324.

[194] Amoureux, J.-P.; Huguenard, C.; Engelke, F.; Taulelle, F. *Chem. Phys. Lett.* **2002**, *356*, 497-504.

[195] Kaupp, M.; Malkina, O. L.; Malkin, V. G.; Pyykkö, P. *Chem. Eur. J.* **1998**, *4*, 118-126.

[196] Perras, F. A.; Viger-Gravel, J.; Burgess, K. M. N.; Bryce, D. L. *Solid State Nucl. Magn. Reson.* **2013**, *51-52*, 1-15.

[197] Frydman, L.; Harwood, J. S. *J. Am. Chem. Soc.* **1995**, *117*, 5367-5368.

[198] Amoureux, J.-P.; Fernandez, C.; Steuernagel, S. *J. Magn. Reson., Ser A* **1996**, *123*, 116-118.

[199] Perras, F. A.; Widdifield, C. M.; Bryce, D. L. *Solid State Nucl. Magn. Reson.* **2012**, *45-46*, 36-34.

[200] te Velde, G.; Bickelhaupt, F. M.; Baerends, E. J.; Fonseca Guerra, C.; van Gisbergen, S. J. A.; Snijders, J. G.; Ziegler, T. *J. Comput. Chem.* **2001**, *22*, 931-967.

[201] van Lenthe, E.; Baerends, E. J.; Snijders, J. G. *J. Chem. Phys.* **1993**, *99*, 4597-4610.

[202] Zhang, Y.; Yang, W. *Phys. Rev. Lett.* **1998**, *80*, 890.

[203] van Lenthe, E.; Baerends, E. J. *J. Comput. Chem.* **2003**, *24*, 1142-1156.

Part III: Spin-Spin Coupling Between Quadrupolar Nuclei

Spin-spin coupling interactions provide the most direct form of structural information in NMR experiments. Since the direct dipolar coupling interaction only depends on the motionally averaged inverse cube of the internuclear distance separating the two spins, it provides a quantitative and unambiguous structural constraint.[1] The measurement of dipolar coupling-based constraints forms the basis for protein structure solutions using the nuclear Overhauser effects (NOE).[2] In the solid state, distance measurements are commonly performed using dipolar recoupling techniques in order to solve the structures of proteins.[3,4] Similar approaches have also been used to solve the structures of zeolites,[5,6] aluminophosphates,[7,8] and organic compounds.[9,10] Indirect nuclear spin-spin coupling (*J* coupling), which is mediated by the electrons that form bonds, provides a direct spectroscopic measure of the connectivities in a systems, making it possible to map out the bonds in a molecule. A truly complete picture of the bonds and close intermolecular contacts in a material can then be obtained by measuring the *J* and dipolar coupling between all nuclei; rendering the structure solution of materials using NMR relatively straightforward. An NMR crystallographic structure solution technique based on graph theory has recently been proposed which uses this approach.[6,11]

A vast proportion of all the NMR-active nuclei are however quadrupolar for which it is difficult to obtain spin-spin coupling information. Several techniques have been

developed in order to measure dipolar or *J* coupling between a spin-1/2 nucleus and a quadrupolar nucleus.[12-18] Measuring spin-spin coupling between a pair of quadrupolar nuclei is however significantly more challenging and no generally applicable techniques have been presented. The spectral splittings cannot typically be observed directly in an NMR spectrum since the quadrupolar broadening often obscures any fine structure. Sophisticated NMR pulse sequences have also been proposed in order to measure dipolar coupling between quadrupolar nuclei, either using spin diffusion,[19-21] rotary resonance recoupling,[22] or symmetry-based recoupling,[23,24] however these techniques are limited to nuclei with weak quadrupolar coupling due to the complicated spin dynamics of quadrupolar nuclei,[25,26] and the need to perform magic angle spinning. Attempts to measure *J* coupling for pairs of quadrupolar nuclei using tailored pulse sequences have also been performed but have, unfortunately, been unsuccessful.[27,28]

We demonstrate that residual dipolar coupling (RDC) multiplets can be observed in the case of dipolar coupled quadrupolar nuclei if the quadrupolar broadening is removed with the use of DOR. Techniques used to simulate the MAS and DOR NMR spectra of dipolar coupled quadrupolar nuclei are developed and presented. The code used for the calculation of residual dipolar coupling has additionally been reorganised in order to simulate exact NMR spectra of quadrupolar nuclei. It is also demonstrated that spin-spin coupling can also be measured in homonuclear *J* coupled systems with the use of DOR. The implications of molecular symmetry on the *J* coupling multiplets are also described.

Specialised pulse sequences for the measurement of *J* coupling are then presented which provide a generally applicable approach to investigating spin-spin coupling between quadrupolar nuclei. This new technique is applied to the study of diboron systems, of

importance in β-boration reactions, in order to gain insights into the nature of the reactive B-B bond. It is lastly shown that the simple *J*-resolved experiment can be applied to measure both dipolar and *J* coupling in cases when the quadrupolar interaction is so large that the NMR spectrum cannot be acquired in a single piece. This approach shows particular promise in experimental studies of metal-metal bonds.

Chapter 3.1: Residual Dipolar Coupling Between Quadrupolar Nuclei

3.1.1 Introduction

When a quadrupolar interaction is present, the quantization axis of the quadrupolar nucleus is tilted with respect to the magnetic field, towards the largest principal component of the EFG tensor (V_{33}).[29] The dipolar interaction with a second spin is then incompletely averaged by both MAS and DOR and has direct effects on the observable NMR transition frequencies of the nuclei to which it is coupled. For spin-1/2 nuclei coupled to quadrupolar nuclei under MAS conditions, this leads to the appearance of residual dipolar coupling (RDC) multiplets.[30-38] These are easily measured in this case since all other broadenings from dipolar and chemical shift anisotropy interactions are removed by MAS. RDC have often been exploited for the ^{13}C-^{14}N spin pair, which directly yields chemical information in biomolecules such as the bond distance and the bonding environment of nitrogen because the ^{14}N quadrupolar coupling constant's (C_Q) sign and magnitude depend strongly on the nitrogen environment [31,32,36,38,39].

When a quadrupolar nucleus, which is coupled to another quadrupolar nucleus, is observed, second-order quadrupolar broadening is still dominant when performing MAS NMR experiments, which unfortunately obscures the RDC information. Since DOR averages all quadrupolar, chemical shift and dipolar broadening to their isotropic parts, only the second-order quadrupolar shift and the RDC remain, making the measurement of these splittings nearly trivial. This information may also be extracted with the use of MQMAS[40-44]

or satellite-transition MAS (STMAS),[45,46] albeit with more difficulty since time consuming 2D simulations are necessary and crystallite-specific intensity losses may hamper the experimentalist's ability to accurately fit the data.[40-44]

This chapter discusses the theory underlying dipolar and *J* coupling between pairs of quadrupolar nuclei in the presence of large quadrupolar interactions. It is demonstrated experimentally that heteronuclear dipolar and *J* coupling constants can be measured with ease using one-dimensional DOR NMR experiments, even in cases when one of the two coupled nuclei has a prohibitively large quadrupolar interaction. The theory developed for the description of RDC between quadrupolar spin pairs is then extended to the simulation of exact NMR spectra of quadrupolar nuclei and software capable of simulating all cases from NQR to high-field NMR is described (Chapter 3.2). This is notably applied to studying chlorine nuclei involved in covalent bonding within organic molecules.

3.1.2 Theory

In many cases of interest in NMR, quadrupolar nuclei are mainly affected by the quadrupolar interaction, along with the Zeeman interaction. Their spin physics can then be nearly completely explained with the use of the Zeeman-quadrupolar Hamiltonian ($\hat{H}_{Z+Q}$). The dipolar and *J* coupling interactions are typically relatively weak and can be treated as perturbations. $\hat{H}_{Z+Q}$ may be conveniently written as follows:[47]

$$\hat{H}_{Z+Q} = -\nu_I \hat{I}_Z + \frac{C_Q}{4I(2I-1)} \begin{bmatrix} \frac{1}{3}\sqrt{6}(3\hat{I}_z^2 - \hat{I}^2)V_0 + (\hat{I}_z\hat{I}_+ + \hat{I}_+\hat{I}_z)V_{-1} \\ -(\hat{I}_z\hat{I}_- + \hat{I}_-\hat{I}_z)V_{+1} + \hat{I}_+^2 V_{-2} + \hat{I}_-^2 V_{+2} \end{bmatrix}. \quad (3.1)$$

The spherical tensor components (V_m) may be expressed as:

(3.2) $V_{\mathrm{m}} = \sum_{\mathrm{m'}=-2}^{2} D^{(2)}_{\mathrm{m'},\mathrm{m}}(\phi,\theta,0) V_{\mathrm{m'}}^{\mathrm{PAS}}$

Where $D^{(2)}_{\mathrm{m'},\mathrm{m}}$ are Wigner rotation matrices and the principal axis system values of the spherical tensor components (V_m,$^{\mathrm{PAS}}$) are $-\eta/2$ for $V_{\pm 2}^{\mathrm{PAS}}$ and $\sqrt{3/2}$ for V_0^{PAS}, where η is the asymmetry parameter of the EFG tensor.[47]

In principle, Zeeman-type eigenstates are used for NMR; however, these are not eigenfunctions of (3.1) when the quadrupolar interaction is large. It is then necessary to diagonalize the Zeeman-quadrupolar Hamiltonian, using Zeeman basis functions, to calculate accurate NMR properties. Upon diagonalization, the exact eigenvalues and eigenvectors of the Hamiltonian can be obtained. The eigenvalues (energy levels) can be used to simulate exact NMR spectra of quadrupolar nuclei (*vide infra*); the eigenvectors can be used to calculate other properties such as dipolar coupling.[30] The true eigenfunctions of (3.1) may then be expressed as

(3.3) $|m\rangle = \sum_{n=-S}^{S} \left(b_{\mathrm{m,n}} + ic_{\mathrm{m,n}}\right)|n\rangle$

where $|m\rangle$ are the states of (3.1), $|n\rangle$ are the Zeeman basis functions, m is the magnetic quantum number, and $b_{\mathrm{m,n}}$ and $c_{\mathrm{m,n}}$ are the real and imaginary components of the eigenvectors of (3.1).

In this framework, the effects of dipolar coupling ($\nu^{\mathrm{S}}_{\mathrm{DD}}$) between two quadrupolar nuclei '*I*' and '*S*' on the central transition of '*S*' (m_{S} = 1/2 to -1/2) can be calculated as a first-order perturbation to the Zeeman-quadrupolar eigenstates.

(3.4) $\nu_{\mathrm{DD}}^{S} = \langle -1/2, m_{\mathrm{I}} | \hat{H}_{\mathrm{DD}} | -1/2, m_{\mathrm{I}} \rangle - \langle 1/2, m_{\mathrm{I}} | \hat{H}_{\mathrm{DD}} | 1/2, m_{\mathrm{I}} \rangle$

In principle, the effects of the quadrupolar interaction on both nuclei need to be included; in this situation, the full dipolar Hamiltonian is secular. The frequency shifts due to each of the terms in $\hat{H}_{\mathrm{DD}}$ may be calculated as follows using the eigenvectors (equation 3.3) determined by diagonalizing equation (3.1).

(3.5) $\langle m_{\mathrm{S}}, m_{\mathrm{I}} | \hat{A} | m_{\mathrm{S}}, m_{\mathrm{I}} \rangle = (3\cos^2\theta - 1)\langle S_{\mathrm{Z}} \rangle_{\mathrm{Re}} \langle I_{\mathrm{Z}} \rangle_{\mathrm{Re}}$

(3.6)
$$\langle m_{\mathrm{S}}, m_{\mathrm{I}} | \hat{B} | m_{\mathrm{S}}, m_{\mathrm{I}} \rangle = -\frac{1}{4}(3\cos^2\theta - 1)\left[\langle S_{-} \rangle_{\mathrm{Re}} \langle I_{+} \rangle_{\mathrm{Re}} - \langle S_{-} \rangle_{\mathrm{Im}} \langle I_{+} \rangle_{\mathrm{Im}} + \langle S_{+} \rangle_{\mathrm{Re}} \langle I_{-} \rangle_{\mathrm{Re}} - \langle S_{+} \rangle_{\mathrm{Im}} \langle I_{-} \rangle_{\mathrm{Im}}\right]$$

(3.7) $$\langle m_{\mathrm{S}}, m_{\mathrm{I}} | \hat{C} + \hat{D} | m_{\mathrm{S}}, m_{\mathrm{I}} \rangle = \frac{3}{2}(\sin\theta\cos\theta)\left[\left\{\langle S_{+} \rangle_{\mathrm{Re}} + \langle S_{-} \rangle_{\mathrm{Re}}\right\}\langle I_{\mathrm{Z}} \rangle_{\mathrm{Re}} + \left\{\langle I_{+} \rangle_{\mathrm{Re}} + \langle I_{-} \rangle_{\mathrm{Re}}\right\}\langle S_{\mathrm{Z}} \rangle_{\mathrm{Re}}\right]$$

(3.8)
$$\langle m_{\mathrm{S}}, m_{\mathrm{I}} | \hat{E} + \hat{F} | m_{\mathrm{S}}, m_{\mathrm{I}} \rangle = \frac{3}{4}(\sin^2\theta)\left[\langle S_{+} \rangle_{\mathrm{Re}} \langle I_{+} \rangle_{\mathrm{Re}} - \langle S_{+} \rangle_{\mathrm{Im}} \langle I_{+} \rangle_{\mathrm{Im}} + \langle S_{-} \rangle_{\mathrm{Re}} \langle I_{-} \rangle_{\mathrm{Re}} - \langle S_{+} \rangle_{\mathrm{Im}} \langle I_{+} \rangle_{\mathrm{Im}}\right]$$

The operators $\hat{A}$ to $\hat{F}$ from the previous equations correspond to the 'alphabet' terms in the dipolar Hamiltonian where:

(3.9) $\hat{H}_{\mathrm{DD}} = -R_{\mathrm{DD}}\left(\hat{A} + \hat{B} + \hat{C} + \hat{D} + \hat{E} + \hat{F}\right)$

The expectation values of the angular momentum operators used here are calculated as follows:

(3.10) $\langle S_{\mathrm{Z}} \rangle_{\mathrm{Re}} = \sum_{n=-S}^{S}\left[n({}^{\mathrm{S}}b_{\mathrm{m_S}n}^{2} + {}^{\mathrm{S}}c_{\mathrm{m_S}n}^{2})\right]$

(3.11) $\langle S_{\mathrm{Z}} \rangle_{\mathrm{Im}} = 0$

(3.12) $\langle S_{+} \rangle_{\mathrm{Re}} = \sum_{n=-S}^{S}\left[\sqrt{S(S+1) - n(n+1)}({}^{\mathrm{S}}b_{\mathrm{m_S},\mathrm{n}}\,{}^{\mathrm{S}}b_{\mathrm{m_S},\mathrm{n+1}} + {}^{\mathrm{S}}c_{\mathrm{m_S},\mathrm{n}}\,{}^{\mathrm{S}}c_{\mathrm{m_S},\mathrm{n+1}})\right]$

(3.13) $$\langle S_{+}\rangle_{\mathrm{Im}} = \sum_{n=-S}^{S}\left[\sqrt{S(S+1)-n(n+1)}\left({}^{S}c_{\mathrm{m_S},\mathrm{n}}\,{}^{S}b_{\mathrm{m_S},\mathrm{n}+1}-{}^{S}b_{\mathrm{m_S},\mathrm{n}}\,{}^{S}c_{\mathrm{m_S},\mathrm{n}+1}\right)\right]$$

(3.14) $$\langle S_{-}\rangle_{\mathrm{Re}} = \sum_{n=-S}^{S}\left[\sqrt{S(S+1)-n(n-1)}\left({}^{S}b_{\mathrm{m_S},\mathrm{n}}\,{}^{S}b_{\mathrm{m_S},\mathrm{n}-1}+{}^{S}c_{\mathrm{m_S},\mathrm{n}}\,{}^{S}c_{\mathrm{m_S},\mathrm{n}-1}\right)\right]$$

(3.15) $$\langle S_{-}\rangle_{\mathrm{Im}} = \sum_{n=-S}^{S}\left[\sqrt{S(S+1)-n(n-1)}\left({}^{S}c_{\mathrm{m_S},\mathrm{n}}\,{}^{S}b_{\mathrm{m_S},\mathrm{n}-1}-{}^{S}b_{\mathrm{m_S},\mathrm{n}}\,{}^{S}c_{\mathrm{m_S},\mathrm{n}-1}\right)\right]$$

In these expressions, *S* is the spin quantum number of the nucleus.

Under stationary conditions, the *A* term contributes the most to the dipolar coupling and the effects of the quadrupolar coupling on the dipolar splitting are negligible. Under MAS conditions, however, the *A* term (as well as the *B* term) is mostly averaged and the *C* and *D* components contribute the most to the spectrum since they are not averaged by MAS. For pairs of quadrupolar nuclei, the *B*, *E*, and *F* terms can also contribute to the spectrum but are generally smaller since they depend on the "tilting" of the magnetization vectors of both spins. The effects of MAS are included by averaging the dipolar frequencies over a rotor period. This is done by re-expressing the angular terms in equations 3.1 through 3.8 as follows:

(3.16) $$\cos\theta = \cos(54.74°)\cos\vartheta + \sin(54.74°)\sin\vartheta\cos(\omega t)$$

(3.17) $$\sin\theta\cos\phi = -\cos(54.74°)\sin\vartheta\cos\varphi + \sin(54.74°)\left[\cos\vartheta\cos\varphi\cos(\omega t) + \sin\varphi\sin(\omega t)\right]$$

(3.18) $$\sin\theta\sin\phi = \cos(54.74°)\sin\vartheta\sin\varphi + \sin(54.74°)\left[\cos\varphi\sin(\omega t) - \cos\vartheta\sin\varphi\cos(\omega t)\right]$$

where θ and ϕ are the polar angles representing the orientation of the EFG and dipolar tensors with respect to the magnetic field (see Figure 3.1) which have been reoriented in a partial MAS rotation, ϑ and φ are the parent polar angles (which are being powder averaged), ωt is the phase of the rotor, and 54.74° is the magic angle. Empirically, we noticed that at least 20 rotor phases are necessary to properly average the dipolar interaction

for the cases studied here. The averaging of the resonance frequencies yields 'infinite' spinning frequency MAS spectra. The spinning sidebands, which would require lengthy time domain simulations, are then not calculated and are in fact unnecessary for the interpretation of the NMR data.

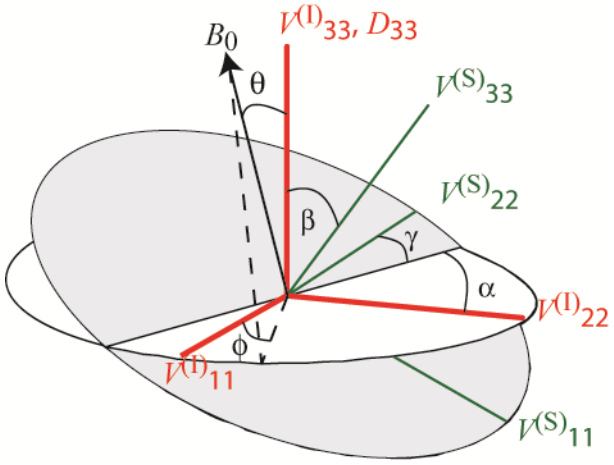

Figure 3.1. Image showing the definition of the Euler angles and polar angles used in this chapter. The nucleus labelled 'S' is the observed nucleus whereas the nucleus labelled 'I' is the perturbing nucleus. Notice that in all cases in this study, $V^{(I)}_{33}$ is always coincident with D_{33}.

For DOR NMR, where the sample is spun in a small rotor oriented at an angle of 30.56° with respect to the spinning axis of a larger rotor oriented at the magic angle,[48-51] the same process for averaging of the transition frequencies over the direction cosines can be done in a nested fashion. For this work, the transition frequencies for DOR were averaged using 90 rotor phases for each of the rotors (8100 orientations). The larger number of rotor phases necessary for DOR is compensated by the lack of a need to perform powder averaging.

To simulate the MAS and DOR NMR spectra of quadrupolar nuclei with RDC, the resonance frequency is calculated as the sum of the averaged dipolar coupling, the chemical shift, and the second-order quadrupolar shift (which is isotropic in the case of DOR). A custom graphical *C*/*C*++ program was written in order to simulate these NMR spectra. The MAS simulations used the powder averaging interpolation scheme of Alderman, Solum, and Grant for speed.[52] The relative orientation of the EFG and dipolar tensors is determined by a set of Euler angles. In this work, the ZYZ convention is used, consistent with the convention used in WSolids[53] (see Figure 3.1). In all cases, due to the symmetry of the compounds studied, it is assumed that the perturbing nucleus' EFG tensor is aligned with the dipolar tensor, and thus only a single set of Euler angles are defined.

3.1.3 Experimental Examples

We have studied the NMR spectra of four samples, the structures of which are shown in Figure 3.2. B-chlorocatecholborane (BcatCl), B-bromocatecholborane (BcatBr), trichloroborazine, and manganese catecholboryl pentacarbonyl (BcatMn) all contain quadrupolar heteronuclear spin pairs that can be probed by ^{11}B DOR and MAS NMR. The NMR spectra of the perturbing nucleus, the nucleus which is coupled to ^{11}B that affects the MAS and DOR spectra (i.e., $^{35/37}$Cl, $^{79/81}$Br, or ^{55}Mn), cannot be measured under MAS or DOR conditions due to the size of its quadrupolar interaction. The simulation of its NMR spectrum under stationary conditions, however, does aid in the simulation of the ^{11}B DOR and MAS NMR spectra because the RDC depends on the perturbing nucleus' quadrupolar coupling constant.

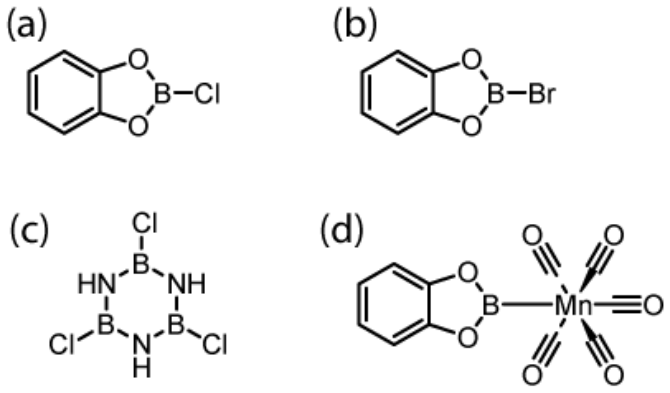

Figure 3.2. Chemical structures BcatCl (a), BcatBr (b), trichloroborazine (c), and BcatMn (d).

3.1.3.1 B-chlorocatecholborane

BcatCl contains a single ^{11}B site that is bound to a chlorine atom. Since the chlorine nucleus is involved in a covalent interaction with the boron, a large $^{35/37}$Cl C_Q is expected. The crystal structure has been solved by X-ray diffraction, according to which a static ^{35}Cl-^{11}B dipolar coupling constant of 713 Hz is to be expected.[54] There is a C_2 rotation axis along the chlorine-boron bond, which forces one principal component of both EFG tensors to be aligned along the bond. The approximate planar geometry of the molecule also fixes the remaining tensor components to be oriented either perpendicularly or within the plane of the molecule.

The ^{35}Cl and ^{37}Cl NMR spectra were acquired using the WURST-QCPMG[55] pulse sequence at an applied magnetic field of 21.1 T (see Figure 3.3a and b) to independently measure the chlorine quadrupolar interaction parameters. From these, a $|C_Q(^{35}Cl)|$ of 41.9 ± 0.1 MHz was obtained along with an η of 0.25 ± 0.03 and an isotropic chemical shift (δ_{iso}) of 50 ± 50 ppm. In this case, the small effects of dipolar coupling and CSA were safely ignored as the dipolar coupling constant is only 713 Hz whereas the central transition powder pattern

spans over 3 MHz. An upper limit for the span of the CS tensor of roughly 400 ppm can be estimated from the line shapes through simulations (not shown). Typical chlorine CS tensor spans are generally much less than 400 ppm[56]; gauge-including projector augmented wave (GIPAW) DFT calculations predict a chlorine CS tensor span of 246 ppm, which does not notably affect the line shape.

^{11}B DOR NMR spectra of BcatCl were acquired at 4.7 T (Figure 3.3c) using rotor synchronized acquisition to remove half of the sidebands.[57] At this magnetic field, the quadrupolar interaction for chlorine cannot be well described by second-order perturbation theory (for ^{35}Cl, $\nu_Q/\nu_0 = 1.16$) and an exact description of the quadrupolar interaction must be applied to simulate the ^{11}B NMR spectrum, as presented above. For this reason the DOR spectrum is in fact not the 1:1 doublet that is predicted by perturbation theory. By fitting the DOR spectrum using perturbation theory, the magnitude of the chlorine C_Q would be predicted as 36 MHz. The true C_Q of 41.9 MHz would then have been underestimated by 14 %. The actual spectrum is composed of eight peaks, shown in the bottom trace of Figure 3.3c, which correspond to the ^{11}B nucleus coupled to the four separate m_I levels of both ^{35}Cl and ^{37}Cl (natural abundances of 75.76 and 24.24 %, respectively). The fit as presented incorporates the ^{35}Cl and ^{37}Cl NMR parameters determined independently, and the dipolar coupling constant calculated from the crystal structure (note that the ratio of quadrupole moments $Q(^{37}\text{Cl})/Q(^{35}\text{Cl})$ is 0.788 and the ratio of magnetogyric ratios $\gamma(^{37}\text{Cl})/\gamma(^{35}\text{Cl})$ is 0.832). The $^{35/37}$Cl quadrupolar coupling constants are negative, as surmised from the broader low-frequency peak in the DOR NMR spectrum (the residual splitting is larger for those spin states (see Figure 3.3c)).

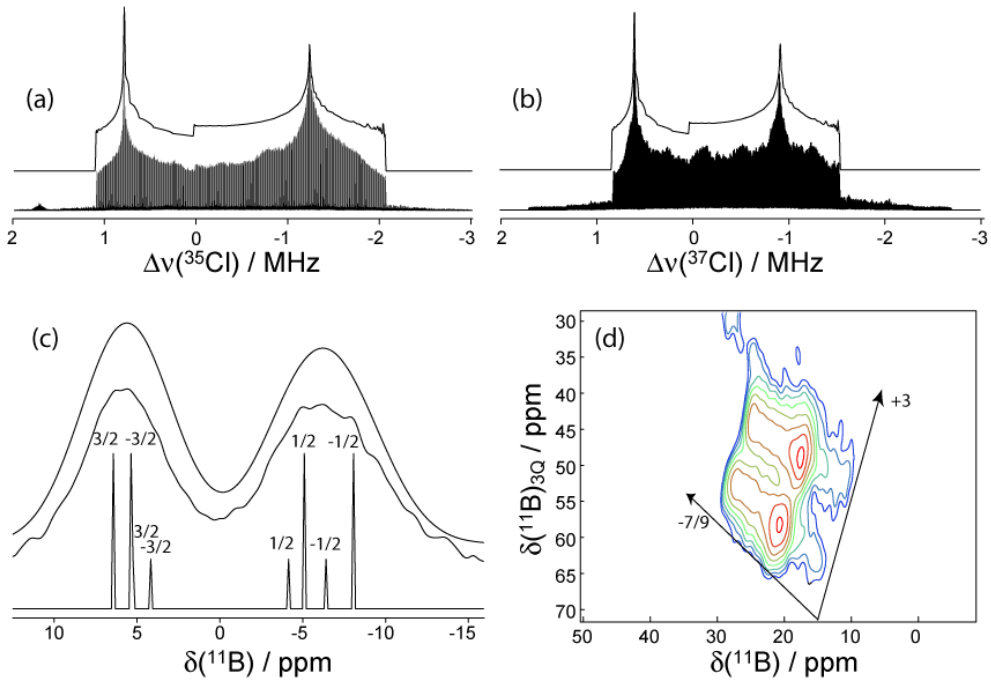

Figure 3.3. Experimental and simulated ^{35}Cl (a) and ^{37}Cl (b) static WURST-QCPMG NMR spectra for BcatCl are shown. In (c) the experimental and simulated ^{11}B synchronized DOR centerbands for BcatCl at 4.7 T are shown; the sidebands have been co-added into the centerband. The bottom trace is a simulation in the absence of line broadening in order to separate the eight resonances arising from the coupling to the four m_I states of ^{35}Cl (more intense lines) and ^{37}Cl (less intense lines). The m_I states to which these lines are attributed are annotated on the spectrum. The top trace includes 400 Hz of Lorentzian broadening. In (d) the ^{11}B MQMAS NMR spectrum of BcatCl acquired at 9.4 T is shown. Arrows have been inserted to indicate the pseudo-isotropic axis (-7/9) as well as the RDC axis (+3).

From the DOR spectrum, the sign of $C_Q(^{35/37}Cl)$ has thus been determined to be negative, something that cannot be easily obtained experimentally otherwise. The fact that one may obtain the sign of C_Q through dipolar coupling was noted by Casabella.[58] (It is

important to note that the high frequency peak can be made broader in the simulations with the introduction of a large isotropic *J* coupling constant, although in that case the MAS spectra (*vide infra*) could no longer be fit.) A ^{11}B MQMAS spectrum of BcatCl provides further evidence that this splitting originates from residual dipolar coupling, as the slope along the dimension which separates the two patterns is +3, in agreement with the work of Wimperis and coworkers[41] (see Figure 3.3d).

Since the quadrupolar interaction of the ^{11}B reintroduces the *B*, *E*, and *F* terms of the dipolar Hamiltonian, it would then also affect the splitting observed in the DOR NMR spectrum. We therefore obtained the ^{11}B MAS NMR spectra of BcatCl at four applied magnetic field strengths (Figure 3.4). The line shapes obtained have a large residual dipolar effect and we were only able to fit them using the approach discussed in the theory section (*vide supra*). The best fits of the spectra are given in Figure 3.4 and the fitting parameters are listed in Table 3.1. These fits were done using coincident chlorine EFG and dipolar PASs, although an Euler angle, β, of 90° relating the boron EFG to the chlorine EFG was necessary. Due to the symmetry of the molecule, this angle can only take the values 0° or 90°. A comparison of the simulated spectra with a β of 0° and 90° are shown in Figure 3.4b. It can be seen that when the two EFGs are coincident (β = 0°), the low frequency discontinuity at 9.4 T and 11.7 T is shifted to lower frequency. It is also seen that when γ takes a value of 90°, the powder pattern is severely skewed to lower frequency, which is inconsistent with the experimental data.

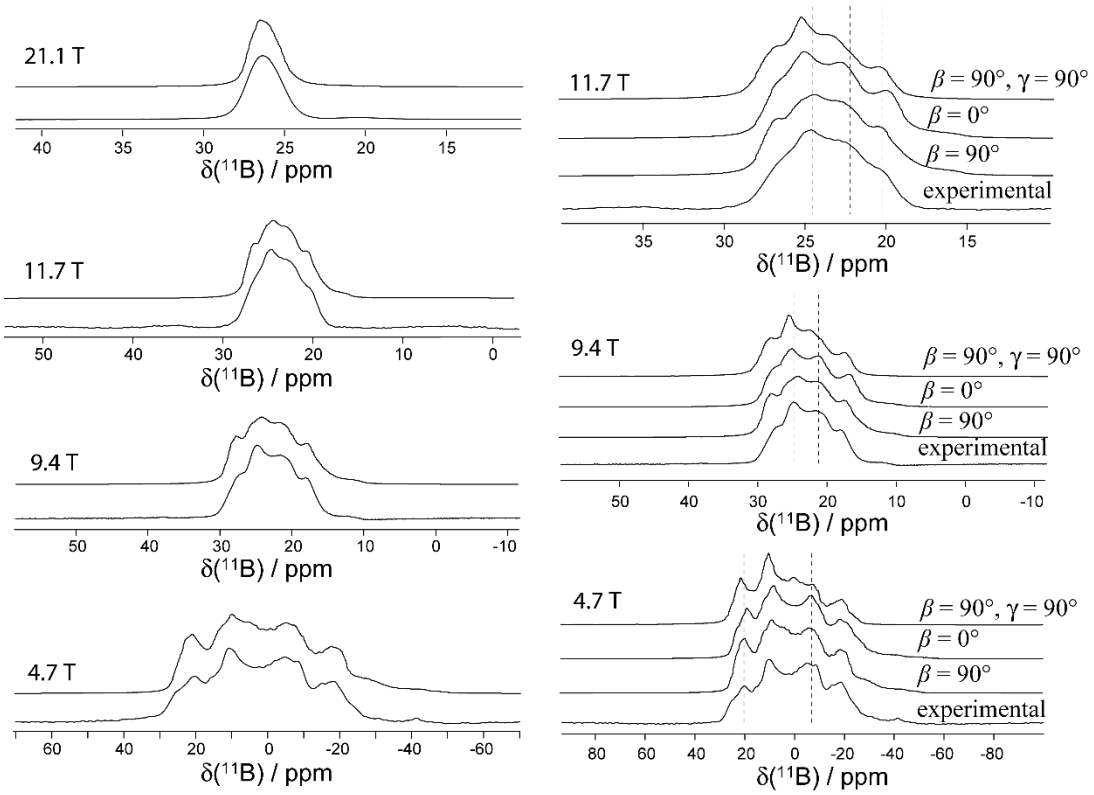

Figure 3.4. (left) Experimental (bottom traces) and simulated (top traces) ^{11}B MAS NMR spectra of BcatCl at four applied magnetic fields. The simulations were performed using the parameters listed in Table 3.1. (right) Comparison of the ^{11}B MAS NMR spectral simulations having coincident EFG tensors (β = 0°) or perpendicular V_{33} principal components (β = 90°). The best fits are deemed to be those where β = 90°. Simulations are also shown when γ is equal to 90°.

From these simulations, it was then possible to obtain the ^{11}B quadrupolar interaction tensor parameters, as well as the relative orientation of the ^{11}B and $^{35/37}$Cl EFG tensors. The ^{11}B quadrupolar parameters agree with those inferred from independent ^{10}B NMR studies (not shown). The possibility of $J(^{35/37}\text{Cl}, ^{11}\text{B})$ coupling affecting the spectra was also investigated. The anisotropy of the J coupling tensor (ΔJ) is included as a negligible part of

the effective dipolar coupling constant ($(\Delta J/3)/R_{\text{eff}} \approx 2$ % according to quantum chemical calculations, *vide infra*), whereas the isotropic J coupling (J_{iso}) must be considered separately, as a part of the coupling Hamiltonian as follows (considering only the secular part), $\hat{H}_{D+J} = J_{iso}\hat{S}_Z\hat{I}_Z + \hat{H}_D$. This effect simply induces a shift in the position of the various MAS subspectra. As these are already separated independently by the dipolar interaction, the effect of the sign of J_{iso} will also be important. Additional simulations show that, in this case, a positive value of $J(^{35/37}\text{Cl}, ^{11}\text{B})_{\text{iso}}$ shifts the positions of the discontinuities mostly towards low frequency, whereas the intensity of the discontinuity at -4.5 ppm decreases drastically if J_{iso} is negative. In our case, the best fits of the five ^{11}B NMR spectra are with an isotropic ^{11}B-$^{35/37}$Cl J coupling constant of -30 ± 15 Hz.

Table 3.1. Experimental and computed NMR parameters for BcatCl

parameter	experiment	(GI)PAW DFT	TPSS/QZ4P
$\delta_{\text{iso}}(\text{B})$ / ppm	28 ± 1	44.6[a]	40.8[a]
$\lvert C_Q(^{11}\text{B})\rvert$ / MHz	2.1 ± 0.1	2.4	2.1
$\eta(^{11}\text{B})$	0.15 ± 0.05	0.15	0.17
$\delta_{\text{iso}}(^{35}\text{Cl})$ / ppm	50 ± 50	120[b]	56[b]
$C_Q(^{35}\text{Cl})$ / MHz	-41.9 ± 0.1	-41.3	-34.8
$\eta(^{35}\text{Cl})$	0.25 ± 0.03	0.27	0.32
$R_{DD}(^{11}\text{B}, ^{35}\text{Cl})$ / Hz	713	--	--
$J(^{35}\text{Cl}, ^{11}\text{B})_{\text{iso}}$ / Hz	-30 ± 15	--	-17.7
α	0° [c]	3.9°	0°
β	90°	90°	90°
γ	0°	0°	0°

[a] Calculated using the absolute shielding of BF_3OEt_2 ($\sigma_{\text{iso}} = 110.9$ ppm).[59]

[b] Calculated using the absolute shielding of infinitely dilute Cl^- ($\sigma_{\text{iso}} = 975$ ppm).[60]

[c] The simulated spectra are not particularly sensitive to the value of α due to the small value of $\eta(^{11}\text{B})$; however, the best fits were obtained with a value of 0°.

As a final verification of our results, the experimental data are compared with the values calculated using standard gas-phase DFT calculation as well as PAW DFT.[61-63] The calculated EFG tensor parameters and chemical shifts are given in Table 3.1. These agree

very well with experiment, although there are some systematic overestimations in the PAW DFT calculations. These calculations notably provide some insight into the tensor orientations within the molecule frame. The chlorine EFG, in fact, shares the same PAS as the dipolar tensor and the largest principal component of the boron EFG (V_{33}) is perpendicular to the bond (i.e. $\beta = 90°$), while V_{11} orients parallel to the B-Cl bond ($\alpha = \gamma = 0°$). This shows that these calculations are able to reproduce fairly well the EFG tensor magnitudes for boron and chlorine as well as the tensor orientations. It was also possible to confirm the experimentally-determined negative sign of the chlorine C_Q using these calculations.

J coupling tensor calculations were also performed using the Amsterdam Density Functional software (ADF).[64-66] Scalar and spin-orbit relativistic effects were included using the zeroth-order regular approximation (ZORA).[67,68] These calculations predict a small and negative $J(^{35}Cl, ^{11}B)_{iso}$ of –17.7 Hz and a $\Delta J(^{35}Cl, ^{11}B)$ of 56.5 Hz. The computed value of $J(^{35}Cl, ^{11}B)_{iso}$ (both its magnitude and sign) is in agreement with experiment. The effect of the calculated ΔJ on the NMR spectra is in fact negligible and it is therefore not possible to obtain this parameter from our simulations for this compound due to the large $R_{DD}/\Delta J$ ratio of ~12.6.

3.1.3.2 B-bromocatecholborane

BcatBr, which is analogous to BcatCl, contains a boron-bromine bond. There are two quadrupolar isotopes of bromine, ^{79}Br and ^{81}Br, with high natural abundances (N.A. = 50.69 and 49.31 %, respectively) and large quadrupole moments (Q = 313 and 261.5 mb, respectively).[69] A large quadrupolar coupling at the bromine site in BcatBr is expected. The

dipolar and *J* coupling interactions to the bromine nuclei will then dominate the ^{11}B DOR NMR spectrum since all other interactions are removed by DOR. However, in order to extract any information from the ^{11}B NMR spectra, it is necessary to determine the EFG tensor parameters independently for the bromine nuclei since the $^{79/81}$Br-^{11}B RDC depends directly on C_Q($^{79/81}$Br) to first order.

The quadrupolar interactions for both bromine isotopes are much too large for the application of $^{79/81}$Br NMR spectroscopy to BcatBr; however, $^{79/81}$Br NQR spectroscopy is particularly apposite. The ^{81}Br and ^{79}Br NQR spectra of BcatBr are shown in Figure 3.5a and b, respectively, and depict single sharp resonances at their quadrupolar frequencies. Unfortunately, only the quadrupolar product ($P_Q = C_Q\sqrt{1+\eta^2/3}$) can be obtained with pure NQR spectroscopy for spin-3/2 nuclei since there is only a single NQR transition. We then performed ^{81}Br nutation NQR experiments, which makes it possible to measure η by recording the relative positions of the singularities on the nutation powder pattern as: $\eta = \frac{3(\nu_3-\nu_2)}{\nu_3+\nu_2}$, where ν_2 and ν_3 are the two highest-frequency singularities. (Figure 3.5c).[70]

This experiment also enabled us to determine the value of C_Q($^{79/81}$Br). From this spectrum we have determined a value of 0.25 ± 0.05 for η which means that the value of C_Q(^{81}Br) is 290.7 ± 1.0 MHz.

The ^{11}B DOR NMR spectra were acquired at 9.4 T with variable outer rotor spinning frequencies (700 to 1000 Hz) in order to identify the centerbands. This was necessary since the breadth of the RDC multiplet exceeds the maximum spinning speed achievable with our probe. The spectrum obtained with 700 Hz DOR is shown in Figure 3.5d. Six main resonances can be identified out of the total of eight resonances which are expected (four for

^{11}B nuclei coupled to each of the two isotopes of bromine); however, the intensities of two of the resonances are doubled. Even a qualitative simulation of the spectrum demonstrates that the sign of the bromine C_Q is positive, something that cannot be directly obtained with bromine NMR or NQR. As the first-order effects of the ^{11}B quadrupolar interaction on the RDC multiplet are null,[29] the DOR spectrum is fairly insensitive to the ^{11}B EFG tensor parameters. It may also be safely assumed that the largest principal component of the bromine EFG tensor is oriented along the boron-bromine bond, since the bromine is in a terminal chemical environment; this was also confirmed computationally, *vide infra*. The ^{11}B DOR NMR spectrum may then be simulated with only three adjustable parameters: the DOR shift ($\delta_{DOR} = \delta_{iso} + \delta_{QIS}$, where δ_{QIS} is the second-order quadrupolar-induced shift), the effective dipolar coupling constant ($R_{eff} = R_{DD} - \Delta J/3$, where ΔJ is the anisotropy of the J coupling tensor), and J_{iso}. The value of R_{DD} can be calculated with the use of X-ray diffraction data[54] (R_{DD}(^{11}B, ^{81}Br) = 1528 Hz) and the effects of J_{iso} can be included in the simulation by incorporating the isotropic J coupling Hamiltonian in the calculation. The effects of coupling to ^{79}Br were included simultaneously by scaling the appropriate quantities by the ratio of the magnetogyric ratios or quadrupole moments of the nuclei, where appropriate.

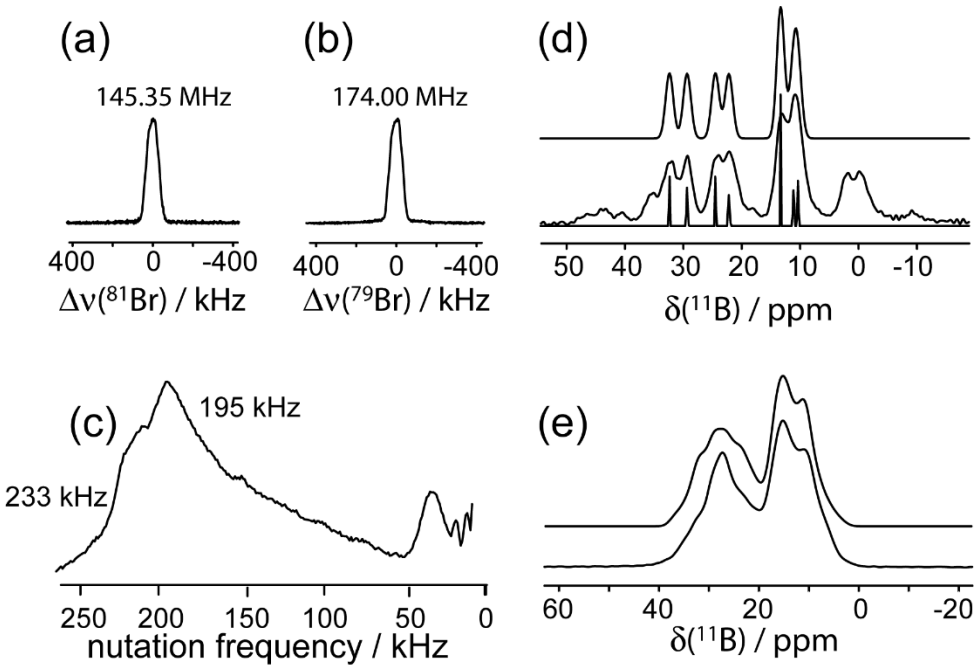

Figure 3.5. Nuclear resonance spectra of BcatBr. In (a) and (b) the ^{81}Br and ^{79}Br NQR spectra are shown, and in (c) the ^{81}Br nutation NQR powder pattern is shown. In (d) the ^{11}B DOR NMR spectrum is shown, in (e) the ^{11}B MAS NMR spectrum is shown. In cases where two spectra are overlaid, the top trace corresponds to the simulation. In (d), the bottom trace corresponds to the simulation of the DOR spectrum when line broadening is omitted. The peaks near 0 ppm as well as small shoulders on the main peaks in (d) are spinning sidebands.

It was not possible to simulate the spectrum in Figure 3.5d without the inclusion of both isotropic and anisotropic *J* coupling. For simplicity, the *J* coupling tensor was assumed to be axially symmetric and aligned along the boron-bromine bond. It is possible to extract the sign of both $J(^{11}B, ^{81}Br)_{iso}$ and $\Delta J(^{11}B, ^{81}Br)$ which are -75 ± 20 Hz and 500 ± 60 Hz, respectively (Table 3.2). The signs and magnitudes of these parameters are corroborated via DFT calculations, *vide infra*. The measurement of the anisotropy of the **J** tensor is typically

very difficult as it is often obscured by the dipolar coupling. Save for a very recent study by Jakobsen et al.,[71] this appears to be the first determination of ΔJ between quadrupolar nuclei using NMR spectroscopy, which opens the door to many more exciting studies. (It should be noted that many such values are available from molecular beam studies of diatomic molecules.[72,73]) Interestingly, the sign of the reduced J coupling constant is the same as that previously obtained for the analogous BcatCl, which suggests that the coupling tensors have similar origins.

Table 3.2. Experimental and computed NMR parameters for BcatBr

parameter	experiment	(GI)PAW DFT	TPSS/QZ4P
$\delta_{iso}(^{11}B)$ / ppm[a]	25.0 ± 0.5	48.5	39.1
$\lvert C_Q(^{11}B)\rvert$ / MHz	1.95 ± 0.1	2.33	2.03
$\eta(^{11}B)$	0.1 ± 0.1	0.21	0.21
$C_Q(^{81}Br)$ / MHz	290.7 ± 1.0	297.4	302.7
$\eta(^{81}Br)$	0.25 ± 0.05	0.24	0.28
$R_{DD}(^{11}B, ^{81}Br)$ / Hz	1528	--	--
$J_{iso}(^{11}B, ^{81}Br)$ / Hz	-75 ± 20	--	-137
$\Delta J(^{11}B, ^{81}Br)$ / Hz	500 ± 60	--	283
α / ° [b]	0	0	0
β / °	90	90	90
γ / °	0	-2	0

[a] The calculated ^{11}B shielding was converted to chemical shift using the absolute shielding scale (σ_{iso} = 110.9 ppm).[59]

[b] The Euler angles reorient the ^{11}B EFG axis frame into that of the bromine's EFG and dipolar interaction tensor frame. These were fixed to those predicted by symmetry considerations.

The ^{11}B MAS NMR spectrum of BcatBr acquired at 9.4 T is shown in Figure 3.5e along with its simulation. The parameters determined from DOR and NQR experiments (*vide supra*) reduce the fitting parameters for the MAS spectrum to the ^{11}B EFG tensor parameters and the orientation of this tensor with respect to the dipolar bond vector. It is then possible to easily determine the orientation of the ^{11}B EFG tensor with respect the dipolar vector: V_{33} is found to be perpendicular to the bond vector. This is characterized by

an Euler angle, β, relating the largest component of boron EFG tensor to the bromine's EFG tensor's principal axis frame (which has the same tensor orientation as the dipolar tensor), of 90°; the other two Euler angles were set to 0° and the spectrum is only moderately sensitive to their values.

This example clearly shows the wealth of information which is accessible from RDC between heteronuclear quadrupolar spin pairs under favourable conditions, such as R_{eff}, the sign of C_{Q}, the magnitude and sign of J_{iso} and ΔJ, as well as the orientation of EFG tensors with respect to a molecule fixed axis: the bond vector.

Density functional theory (DFT) calculations of the ^{11}B and $^{79/81}$Br EFG and magnetic shielding tensors for BcatBr were performed using both cluster-based DFT and the gauge-including projector-augmented wave (GIPAW) approach.[61] The calculated parameters are listed in Table 3.2 along with the experimentally-determined values. Both DFT methods reproduce the magnitudes and signs of the experimentally-determined EFG tensors and chemical shifts with reasonable accuracy; however, as previously noted, the GIPAW approach overestimates the value of $C_{\text{Q}}(^{11}\text{B})$ as well as the ^{11}B chemical shift (see chapter 2.1). The J coupling tensors were also calculated at the TPSS/QZ4P[74,75] level and reproduce the experimentally determined signs of J_{iso} and ΔJ; however, the magnitudes of both parameters are not reproduced within experimental error; this is not surprising as J coupling tensors are one of the most difficult properties to calculate and high-level correlated methods are often necessary.[76] The computed values of J_{iso} and ΔJ are satisfactory in comparison with experiment. Importantly, both methods correctly reproduce, and confirm, the experimentally determined sign of C_{Q} as well as the relative tensor orientations.

3.1.3.3 Trichloroborazine

Trichloroborazine contains three boron atoms, each of which is bound to a chlorine atom, similarly to BcalCl. Its ^{11}B NMR spectrum will then be greatly affected by the interactions of the ^{11}B nucleus with the chlorine nucleus. Effects due to coupling between ^{14}N and ^{11}B are also present; however, these are expected to be very small compared to the effects of interest. This is the case because of the small magnitude of the nitrogen EFG tensor (the PAW DFT calculated C_Q is of 1.30 MHz) and the orientation of the largest EFG tensor component relative to the B-N bond (β = 60°), for which the effects of the RDC are nearly absent.[77,78]

In the solid state, molecules of trichloroborazine have C_{2v} symmetry and there are thus two crystallographically inequivalent boron-chlorine spin-pairs with a stoichiometry of 2:1.[79] This is clearly seen in the ^{35}Cl WURST-QCPMG NMR[55] spectrum shown in Figure 3.6a. From this spectrum, the chlorine EFG tensor parameters could be determined: $|C_Q(^{35}Cl)|$ = 38.9 ± 0.1 MHz and 39.2 ± 0.1 MHz and η = 0.250 ± 0.005 and 0.335 ± 0.005 for the sites with relative intensities of 2 and 1 respectively, in agreement with the expected stoichiometry.

Similar to what was done for BcatCl, this independent information can be used to help simulate the ^{11}B DOR NMR spectrum since the number of adjustable parameters is reduced. In this case however, due to the presence of two crystallographically distinct but chemically equivalent boron sites, and the coupling to ^{14}N, much broader lines were obtained (when compared to BcatCl, see Figure 3.6b). A good fit was obtained assuming a single site with no anisotropy of the **J** tensor and a $J(^{11}B,^{35}Cl)_{iso}$ of -30 Hz (as was obtained for the

boron-chlorine spin pair in BcatCl). This is consistent with the fact that the bonding environment in both compounds is very similar.

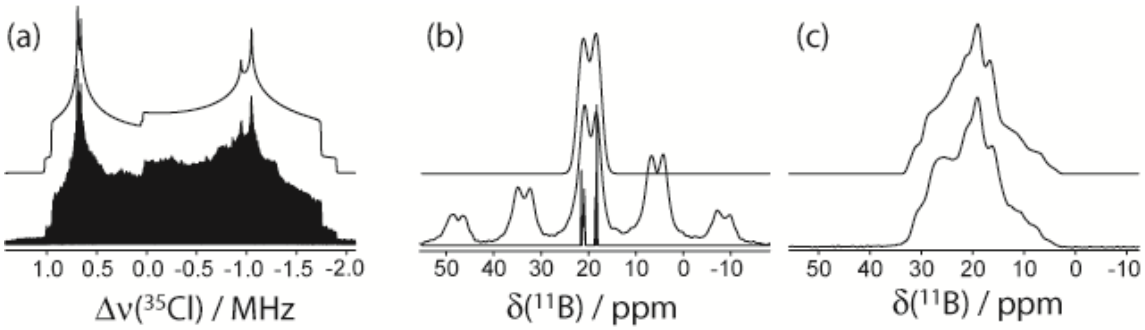

Figure 3.6. NMR spectra of trichloroborazine. In (a) the ^{35}Cl WURST-QCPMG NMR spectrum is shown (B_0 = 21.1 T), in (b) the ^{11}B DOR NMR spectrum is shown, and in (c) the ^{11}B MAS NMR spectrum is shown (both at B_0 = 9.4 T). In all cases the top trace corresponds to the simulation. In (b), the bottom trace corresponds to the simulation of the DOR spectrum when line broadening is omitted.

The ^{11}B MAS NMR spectrum of trichloroborazine is shown in Figure 3.6c. It was assumed that the largest component of the chlorine EFG tensor was aligned along the bond also in this case since it is a terminal chlorine; this assumption was confirmed using DFT (*vide infra*). Simulations of the ^{11}B NMR spectrum were however extremely sensitive to the orientation of the boron EFG tensor with respect to the B-Cl bond vector since the EFG asymmetry parameter is large in this case. It was possible to determine the orientation of the largest component of the ^{11}B EFG tensor with respect to the B-Cl bond vector with high precision: $\beta = 84 \pm 3°$. A summary of the simulation parameters is given in Table 3.3.

Table 3.3. Experimental and computed NMR parameters for trichloroborazine

parameter	experiment	(GI)PAW DFT	TPSS/QZ4P
$\delta_{iso}(^{11}B)$ / ppm[a]	31.0 ± 0.5	45.3 / 45.6	36.0 / 39.0
$\lvert C_Q(^{11}B)\rvert$ / MHz	2.47 ± 0.03	2.85 / 2.89	2.46 / 2.50
$\eta(^{11}B)$	0.78 ± 0.05	0.83 / 0.68	0.82 / 0.64
$\delta_{iso}(^{35}Cl)$[c] / ppm[b]	200 ± 50	150	91
$C_Q(^{35}Cl)$[c] / MHz	-39.2 ± 0.1	-36.6	-38.9
$\eta(^{35}Cl)$[c]	0.335 ± 0.005	0.443	0.345
$\delta_{iso}(^{35}Cl)$[d] / ppm	200 ± 50	160	106
$C_Q(^{35}Cl)$[d] / MHz	-38.9 ± 0.1	-37.3	-39.8
$\eta(^{35}Cl)$[d]	0.250 ± 0.005	0.255	0.308
$R_{DD}(^{11}B, ^{35}Cl)$ / Hz	690	--	--
$J_{iso}(^{11}B, ^{35}Cl)$ / Hz	-30 ± 30	--	-16
α / °[e]	0	-2	0
β / °	84 ± 3	88	89
γ / °	0	2	0

[a] The calculated ^{11}B shielding was converted to chemical shift using the absolute shielding scale (σ_{iso} = 110.9 ppm).[59]

[b] The calculated ^{35}Cl shielding was converted to chemical shift using the absolute shielding scale (σ_{iso} = 975 ppm).[60]

[c] These parameters belong to the chlorine site having a stoichiometry of 1.

[d] These parameters belong to the chlorine site having a stoichiometry of 2.

[e] The Euler angles reorient the ^{11}B EFG axis frame into that of the chlorine's EFG and dipolar interaction tensor frames. The angles α and γ were fixed to those predicted using symmetry considerations.

It is interesting to note, that the chlorine's η is larger in trichloroborazine than it was in BcatCl since the boron atoms in trichloroborazine are a part of a π-conjugated system. The effect of π back-bonding from the chlorine decreases the axial nature of the bond and increases the asymmetry of the EFG. Both conventional DFT and GIPAW DFT calculations of the relevant NMR parameters were also performed for trichloroborazine and are in good agreement with experiment. The calculated parameters are listed in Table 3.3 along with the experimentally determined values.

3.1.3.4 Manganese Catecholboryl Pentacarbonyl

BcatMn contains a boron-manganese bond where spin-spin coupling between ^{11}B and ^{55}Mn (N.A. = 100% and Q = 330 mb)[69] is expected to affect the ^{11}B NMR spectra since manganese centers in this type of chemical environment are known to have large quadrupolar interactions (i.e., C_Q as large as 64.3 MHz).[80,81] The ^{55}Mn static VOCS Solomon echo[82] NMR spectrum is shown in Figure 3.7a. There is some overlap with an impurity of dimanganese decacarbonyl due to the extreme moisture and air sensitivity of BcatMn; however, the singularities corresponding to BcatMn are clearly resolved from those of the impurity. The spectrum was simulated using both quadrupolar and chemical shift anisotropy interactions. The orientation between the EFG and chemical shift tensors was fixed to that calculated using DFT (*vide infra*). It was then possible to determine a $|C_Q(^{55}Mn)|$ value of 46.6 ± 0.2 MHz and an η of 0.17 ± 0.02. These data are used to aid in the simulation of the ^{11}B NMR spectra.

The ^{11}B DOR NMR spectrum of BcatMn is shown in Figure 3.7b. A doublet with unequal intensities is observed from which the sign of $C_Q(^{55}Mn)$ may be easily determined to be negative using spectral simulations. As ^{55}Mn has a positive value of Q, this points to the manganese having a mostly oblate coordination environment, i.e., a coordination environment in between octahedral and square pyramidal.[83] If we assume that the ligands are purely σ-donors, this suggests that the interactions between manganese and its carbonyl ligands are stronger than the interaction between manganese and the catecholboryl ligand. This insight into the nature of the interactions with the ligands could not have been obtained from ^{55}Mn NMR alone or from diffraction data. From the DOR NMR spectrum it is also

possible to measure a small, positive, J_{iso} of 10 ± 5 Hz; ΔJ has no measurable effect on the NMR spectrum.

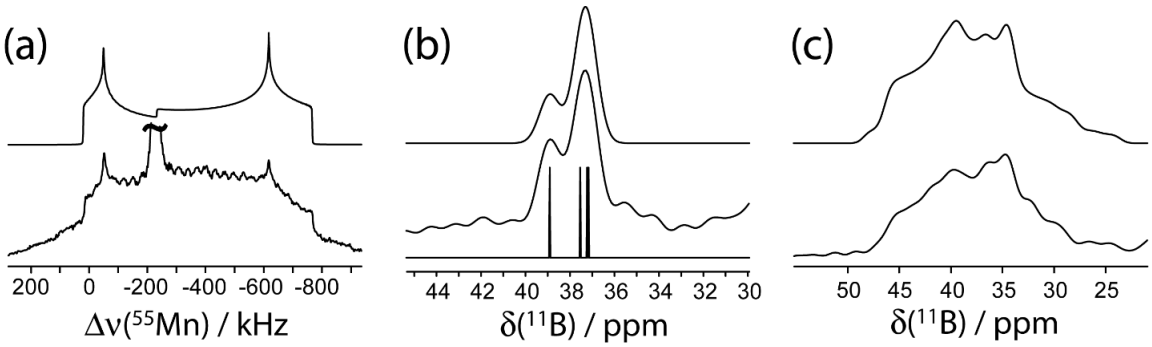

Figure 3.7. NMR spectra of BcatMn. In (a) the ^{55}Mn solid-echo NMR spectrum is shown (peak due to an impurity of dimanganese decacarbonyl goes off scale). In (b) the ^{11}B DOR NMR spectrum is shown and in (c) the ^{11}B MAS NMR spectrum is shown. In all cases, the top trace corresponds to the simulation. In (b), the bottom trace corresponds to the simulation of the DOR spectrum when line broadening is omitted. B_0 = 9.4 T.

The ^{11}B MAS NMR spectrum of BcatMn, shown in Figure 3.7c, demonstrates clear signs of RDC; however, the main broadening interaction is clearly the ^{11}B quadrupolar coupling. The largest component of the ^{55}Mn EFG tensor is assumed to be oriented along the boron-manganese bond due to the pseudo-C_4 symmetry about the bond. The largest component of the ^{11}B EFG tensor was also assumed to be perpendicular to the bond, as was measured for BcatCl and BcatBr. It is interesting to note that the dipolar information could likely also be obtained using double-resonance NQR methods, as was done for $DMn(CO)_5$.[84] These results are also in agreement with our DFT calculations (*vide infra*). A summary of the simulation parameters is given in Table 3.4.

DFT calculations using a cluster model were also performed on this sample; however, we were unable to obtain a reliable manganese pseudopotential for GIPAW DFT calculations. The calculated parameters are listed in Table 3.4. It can be seen that the EFG tensor parameters are very well reproduced and that the size and sign of J_{iso} are reproduced by the DFT calculation. A small ΔJ of 49.6 Hz is predicted; however, such a small ΔJ has no measurable effect on the NMR spectrum.

Table 3.4. Experimental and computed NMR parameters for BcatMn

parameter	experiment	TPSS/QZ4P
$\delta_{iso}(^{11}B)$ / ppm[a]	48.5 ± 0.3	57.2
$\lvert C_Q(^{11}B)\rvert$ / MHz	2.47 ± 0.07	2.47
$\eta(^{11}B)$	0.58 ± 0.05	0.38
δ_{iso} (^{55}Mn) / ppm	2580 ± 50	--
$C_Q(^{55}Mn)$ / MHz	-46.6 ± 0.2	-46.8
$\eta(^{55}Mn)$	0.17 ± 0.02	0.35
κ	0 ± 0.5	-0.14
Ω / ppm	250 ± 50	163
α / ° [b]	270	265
β / °	90	81
γ / °	0	10
$R_{DD}(^{11}B, ^{55}Mn)$ / Hz	1022	--
$J_{iso}(^{11}B, ^{55}Mn)$ / Hz	10 ± 5	15
α / ° [c]	270	276
β / °	90	89
γ / °	330	329

[a] The calculated ^{11}B shielding was converted to chemical shift using the absolute shielding scale (σ_{iso} = 110.9 ppm).[59]

[b] The Euler angles reorient the ^{55}Mn chemical shift tensor axis frame into that of the EFG tensor frame. The angles were determined using the DFT values as initial guesses.

[c] The Euler angles reorient the ^{11}B EFG axis frame into that of the manganese's EFG and dipolar interaction tensor frames. The angles were determined using the DFT values as initial guesses.

3.1.4 Conclusions

It has been demonstrated that residual dipolar splittings between pairs of quadrupolar nuclei can be easily measured and interpreted with the use of DOR NMR spectroscopy. Since DOR removes the effects of several broadening interactions simultaneously, only the isotropic chemical, second-order quadrupolar induced, and residual dipolar shifts affect the spectrum, and the dipolar and *J* coupling multiplets are easily analyzed. This provides an accurate approach for simultaneously measuring effective dipolar and *J* coupling constants in heteronuclear quadrupolar spin pairs. Additionally, the analysis of RDC multiplets also provides the sign of J_{iso}, ΔJ, and the C_Q of the perturbing nucleus, parameters which are difficult to obtain otherwise, given that the perturbing nucleus' $|C_Q|$ was independently measured using a different method. The spin-spin coupling may also be measured in cases when the quadrupolar interaction of one of the two coupled quadrupolar nuclei is prohibitively large. It is also necessary to understand these effect in order to avoid misinterpretation of DOR NMR spectra; a multiplet may be misassigned as a series of individual sites were these spin-spin coupling effects unknown.

3.1.5 Experimental

3.1.5.1 NMR Spectroscopy

Samples of BcatCl and BcatBr, were purchased from Aldrich and were used without further purification. Similarly, trichloroborazine was purchased from Strem and was used without further purification. BcatMn was prepared by reacting equimolar amounts of sodium manganese pentacarbonyl salt and B-chlorocatecholborane in dry toluene under an inert atmosphere using literature procedures.[85-87] The sodium manganese pentacarbonyl salt

was prepared by reacting manganese decacarbonyl with a 1 % Na/Hg amalgam in dry THF. All samples are moisture sensitive and were thus tightly packed into either vespel DOR rotors or zirconium oxide MAS rotors under an inert atmosphere.

All DOR NMR experiments were performed at 9.4 T using a Bruker AVANCE III console and a Bruker WB 73A DOR probe with a 14 mm outer rotor and a 4.3 mm inner rotor. Typically, experiments were performed with the outer rotor spin rate varied from 700 to 1000 Hz in order to identify the centerbands; the inner rotor spin rates are typically 4 to 5 times larger and cannot be independently varied. For all experiments, outer-rotor synchronization was used to remove the odd-ordered sidebands.[57] 20 kHz ^{1}H SPINAL-64 decoupling was also used for the ^{11}B DOR NMR experiments.[88] The ^{11}B DOR NMR experiments were performed using 20 μs CT selective excitation pulses, either 1 or 2 s recycle delays, and either 128 or 256 scans.

The ^{11}B MAS spectra were acquired using a Bruker AVANCE II 900 (21.1 T), Bruker AVANCE 500 (11.7 T), Bruker AVANCE III 400 (9.4 T) and Bruker AVANCE III 200 (4.7 T). Either a Hahn-echo (21.1 T) or a one-pulse acquisition (11.7 T, 9.4 T and 4.7 T) was used. The central-transition selective 90° pulse lengths were of 5 μs, 1.5 μs, 1 μs and 1.6 μs at 21.1 T, 11.7 T, 9.4 T and 4.7 T respectively. In all cases a 4 mm triple resonance MAS probe was used with a spin rate of 12 kHz. All ^{11}B NMR experiments were referenced to liquid $F_3B{\cdot}O(C_2H_5)_2$ using $NaBH_4$ as a secondary reference (δ_{iso} = -42.06 ppm).

The $^{35/37}$Cl WURST-QCPMG spectra were acquired using the Bruker AVANCE II 900 spectrometer operating at 21.1 T ($\nu_0(^{35}Cl)$ = 88.2 MHz) at the National Ultrahigh-Field NMR Facility for Solids in Ottawa using a double-resonance, 7 mm, static probe. Chemical

shifts were referenced using NH_4Cl as a secondary reference (δ_{iso} = 73.8 ppm). For ^{35}Cl, a 50 μs WURST shape sweeping 2 MHz was used; a total of 96 echoes where collected while proton decoupling; a recycle delay of 0.5 s and a spikelet separation of 5 kHz were used. Variable offset cumulative spectrum (VOCS) acquisition methods were also necessary.[82] Seven spectra, each taking 2048 scans, were acquired with a frequency step of 500 kHz. In the case of ^{37}Cl NMR, a 50 μs WURST shape sweeping 1 MHz was used. In this case the VOCS frequency steps were 400 kHz and 3072 scans were acquired for each piece.

The $^{79/81}Br$ NQR experiments were performed using a spin-echo sequence on a Bruker AVANCE III spectrometer equipped with a 4 mm triple resonance MAS probe. For the 1D experiments, the excitation pulse duration was 1 μs and the refocusing pulse was 2 μs. The 2D nutation experiment used 512 increments of 1 μs for the first pulse length in the spin echo experiment. The asymmetry parameter can then be determined from the nutation powder pattern singularities as: $\eta = \frac{3(\nu_3 - \nu_2)}{\nu_3 + \nu_2}$, where ν_2 and ν_3 are the two highest-frequency singularities.[70]

The ^{55}Mn solid echo NMR spectrum was acquired at 9.4 T using a Bruker AVANCE III spectrometer and a 4 mm triple channel MAS probe. A 1.75 μs CT selective excitation pulse was used with a 30 μs echo delay, a 2 s recycle delay, and 200 scans. A total of 12 VOCS subspectra were acquired with 100 kHz offsets. All ^{55}Mn NMR experiments were referenced to a 0.82 m solution of $KMnO_4$ in D_2O.

3.1.5.2 Density Functional Theory

Cluster model DFT calculations were performed using the ADF software package.[64,65] For all calculations the meta-GGA functional of Tao, Perdew, Staroverov, and Scuseria

(TPSS)[74] was used along with the ZORA/QZ4P Slater-type basis sets which are core triple-zeta, valence quadruple-zeta, and have four polarization functions.[203] The clusters consisted of a single molecule, the coordinates of which were extracted directly from the known crystal structures.

(GI)PAW DFT calculations of the EFG and magnetic shielding tensors were performed using the CASTEP NMR program[61] and the PBE exchange-correlation functional.[89] In all cases, a 610 eV kinetic energy cut-off was used along with the default 'ultra-fine' *k*-point grids. On-the-fly generated ultrasoft pseudopotentials were used on all atoms. For all cases, the published crystal structures were used without any modifications;[54,79,85,86,87] in the case of trichloroborazine however, the hydrogens needed to be added and were then subsequently optimized prior to performing the NMR calculation. The calculated boron[59] and chlorine[60] isotropic magnetic shielding constants were converted to chemical shifts with the use of an absolute shielding scale.

Chapter 3.2: The Quadrupolar Exact Software

3.2.1 Introduction

With the advent of higher field persistent magnets and the development of special pulse schemes designed to enhance the sensitivity of solid-state NMR experiments, quadrupolar nuclei that were once considered highly impractical to study by NMR are now being studied in the context of a wide range of applications.[90-101] The quadrupolar interaction operates in a molecule- or lattice-based frame, whereas the fundamental Zeeman interaction common to most NMR experiments operates in the lab frame which is imposed by an applied magnetic field. These two interactions have fundamentally different and independent foundations and two forms of nuclear resonance spectroscopy can be employed to study these nuclei. In nuclear quadrupole resonance (NQR), the quadrupolar interaction is the dominant interaction, while in NMR spectroscopy, the Zeeman interaction is assumed to be dominant. It is well known that when performing magnetic resonance experiments on real samples which possess quadrupolar nuclei, the intermediate region is ill-defined.[47,102-105] It has been common practice to use perturbation theory to analyze the spectra,[106,107] although these methods may not be valid in certain circumstances. As the solid-state NMR community pushes towards the study of nuclei with ever larger quadrupolar interactions (via large-*Q* nuclei and/or large EFGs) or smaller Zeeman interactions (for low-γ nuclei), perturbation theory treatments for isolated spins may no longer be useful and the use of exact solutions will become necessary in some cases. This has been demonstrated for some ^{127}I, $^{185/187}$Re, and ^{27}Al NMR spectra where a second-order perturbation theory model under the high-field approximation was shown to break down.[90,91,108,109] Several different approaches

to treating this problem have been proposed;[110-118] however, diagonalizing the Hamiltonian is likely the simplest solution to implement. Exact NMR/NQR solutions are also being used to study a wide range of interesting systems.[119-121]

To our knowledge, there is no generally available and user-friendly software which treats the Zeeman-quadrupolar Hamiltonian exactly, and includes contributions from chemical shift anisotropy. The software developed in order to simulate the residual dipolar coupling multiplets may however be adapted in order to form a fast and exact NMR/NQR simulation program with a graphical user interface (GUI). This program, called the QUadrupolar Exact SofTware (QUEST), can be used to simulate all cases in between NMR and NQR as well as predicts the correct intensity (and line shape) of overtone transitions.

3.2.2 Theory

Similarly as what is done in the case of RDC (see the theory section in Chapter 3.1), the first step in the simulation is to diagonalize the Zeeman-Quadrupole Hamiltonian (equation 3.1) in order to obtain the eigenvalues and eigenvectors of the system. In principle, the transition energy for all pairs of eigenvalues needs to be calculated since the state mixing that occurs in the presence of the quadrupolar interaction renders all transitions slightly allowed. The transition probability can then be calculated as:[122]

(3.19) $$\textit{Intensity} \propto \left| \left\langle n_1 \left| \hat{I}_X \sin\theta + \hat{I}_Z \cos\theta \right| n_2 \right\rangle \right|^2 .$$

In equation 3.19 the relative amplitude of a spectral resonance corresponding to a transition occurring between the n_1 and n_2 states is calculated; this expression is also known as Fermi's golden rule. This expression calculates the correct line intensity for any coil

orientation, where θ is the relative orientation of the coil with respect to the magnetic field.[122] This simple expression importantly calculates the correct overtone NMR and Zeeman-perturbed NQR line shapes, which is not the case if the intensities are not scaled appropriately. In the case of very broad powder NMR spectra, the effects of the differing Boltzmann populations of the isochromats in different parts of the powder pattern can also be taken into consideration when calculating the line intensities.

The effects of the chemical shift interaction, both isotropic and anisotropic, may also become important and these can be incorporated into the Hamiltonian as follows:

$$\hat{H}_{Z+Q} = -\nu_0(1+\delta_{ZZ})\hat{I}_z + \frac{C_Q}{4I(2I-1)}\begin{bmatrix}\frac{1}{3}\sqrt{6}(3\hat{I}_z^2-\hat{I}^2)V_0 + (\hat{I}_z\hat{I}_+ + \hat{I}_+\hat{I}_z)V_{-1} \\ -(\hat{I}_z\hat{I}_- + \hat{I}_-\hat{I}_z)V_{+1} + \hat{I}_+^2V_{-2} + \hat{I}_-^2V_{+2}\end{bmatrix} \quad (3.20)$$

where the component of the chemical shift tensor aligned with the magnetic field (δ_{ZZ}) is added. The value of δ_{ZZ} may be easily calculated using the chemical shift tensor components and the orientation of the tensor (using two polar angles, ϑ and φ).

$$\delta_{ZZ} = \delta_{11}\sin\vartheta\cos\varphi + \delta_{22}\sin\vartheta\sin\varphi + \delta_{33}\cos^2\vartheta \quad (3.21)$$

The relative orientation of the EFG and CS tensors also need to be defined since the polar angles for the two tensors may differ. This is done with the use of Euler angles (see introduction). In practice, this is done by rotating the magnetic field away from the chemical shift tensor with a series of consecutive rotations about the z, y, z axes by the Euler angles α, β, and γ with the following rotation matrix.

$$R(\alpha,\beta,\gamma) = \begin{bmatrix} cos\alpha cos\beta cos\gamma - sin\alpha sin\gamma & sin\alpha cos\beta cos\gamma + cos\alpha sin\gamma & -sin\beta cos\gamma \\ -cos\alpha cos\beta sin\gamma - sin\alpha cos\gamma & -sin\alpha cos\beta sin\gamma + cos\alpha cos\gamma & sin\beta sin\gamma \\ cos\alpha sin\beta & sin\alpha sin\beta & cos\beta \end{bmatrix} \quad (3.22)$$

These Euler angles correspond to the passive ZYZ convention as also specified in WSOLIDS[123] and which is explained in reference 124. The definition of these Euler angles is illustrated in Figure 1.8 in the introduction.

3.2.3 Software

There are several programs available which can be used to simulate the NMR line shapes associated with quadrupolar nuclei in powdered solids. These typically fall into two categories, the first being those which propagate the density matrix. Examples of such programs include GAMMA,[125] SIMPSON,[126] and SPINEVOLUTION,[127] and they may be used in order to calculate the full time domain data and simulate pulse sequences. These programs can take several minutes, hours, or even days to simulate a particular experiment or spectrum, and are mostly used to simulate magic angle spinning (MAS) NMR spectra, to test various pulses sequences, or to simulate multidimensional NMR experiments. The second class of simulation programs use simple mathematical expressions in order to calculate resonance frequencies directly and generate a simulation in a fraction of a second. Examples of such programs include WSOLIDS,[53] DMfit,[128] and QuadFit;[129] the latter specializes in the simulation of NMR spectra with distributions of NMR parameters, which is useful in the simulation of NMR spectra of amorphous solids. In order to efficiently generate simulated spectra, all of these programs use the high-field approximation. More specifically in the present context, they use formulas derived from second-order perturbation theory in order to treat the effects of the quadrupolar interaction on the Zeeman energy levels. This approach has been incredibly successful, since the commonly observed central transition (m = 1/2 to -1/2) in NMR is not affected by third-order effects.[130] As mentioned

earlier, although the second-order expressions are useful, they are sometimes invalid. Luckily, with the continued rapid increases in computer processing power, calculations of NMR spectra using diagonalization methods (i.e., 'exact' methods) can now be done routinely for small spin systems, and hence second-order perturbation theory is no longer the only convenient option. To the best of our knowledge, there exists no fast and user-friendly program capable of doing exact simulations of quadrupolar line shapes. As such, we have designed the first fast and graphical exact NMR simulation program for quadrupolar nuclei in powdered samples under static conditions, and which is oftentimes capable of calculating exact NMR spectra in under a second on a single processor.

QUEST is a C/C++ program we designed, using the theory described earlier, to simulate exact NMR/NQR spectra for quadrupolar nuclei. This program makes use of the fast diagonalization routines from the GNU scientific library,[131] as well as the efficient powder averaging scheme of Alderman, Solum and Grant (ASG).[52,132] To be more specific, a diagonalization and NMR calculation is performed for a large number of crystallite orientations. These are then organized and a linear interpolation is performed according to the ASG procedure in order to complete the powder averaging. The GUI contains a central plot of the NMR spectrum with the list of NMR parameters enumerated above it. A screen capture of the GUI is shown in Figure 3.8.

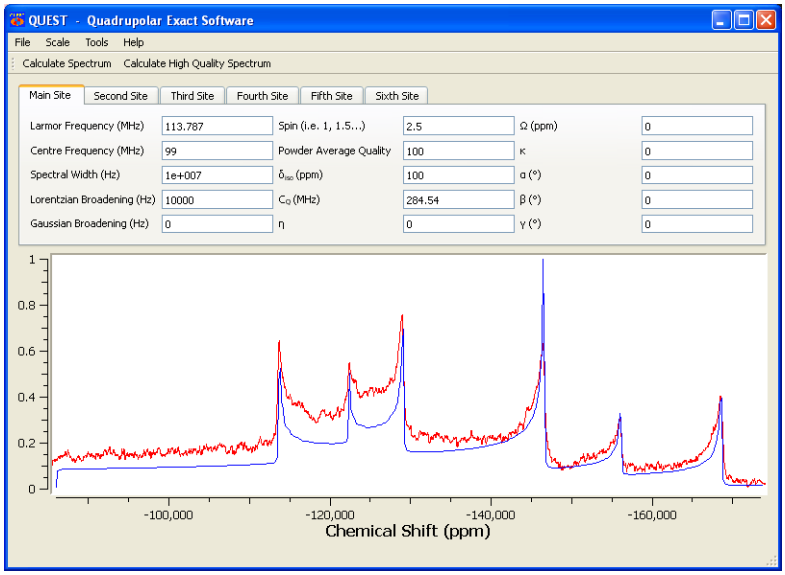

Figure 3.8. A screen shot of the QUEST program showing the layout of the GUI along with the simulation of an example spectrum.

The user can freely vary the EFG tensor parameters (C_Q and η) and the CS tensor parameters (δ_{iso}, Ω, κ), as well as their relative principal axis system orientations with the set of three Euler angles (α, β, γ). The Larmor frequency, center frequency, spectral width, and spin quantum number must also be set in the same window, and the ability to choose both Lorentzian and Gaussian convolutions is available. We also decided to give the user the freedom to choose the powder average quality, something that may be inaccessible in other simulation programs. The user can then choose to sacrifice speed for quality or vice-versa. This powder average quality (N) takes a positive integer value which defines the number of triangular edged sections used in the ASG interpolation scheme (see Figure 3.9).[52] This will determine the number of crystallite orientations for which the resonance frequency and intensity is calculated, with the rest of the space being interpolated to generate smooth line shapes. If chemical shift anisotropy is not included or if the principal components of the CS tensor are aligned with those of the EFG tensor (i.e., sets of Euler angles containing only

values of 0°, 90°, 180° and 270°), then a total of (N+2)(N+1)/2 crystallite orientations are considered over an octant of a sphere. This number is quadrupled when the EFG and CS tensors are non-coincident as the powder average must now be done over a hemisphere instead of an octant. Care must be taken to not use too large of a powder average quality as this may lead to memory issues. Potential issues associated with available system memory become more pronounced for the larger spin quantum numbers, as there are more transition frequencies and intensities to store. As a rule of thumb, a powder average quality as small as 50 can often yield sufficiently smooth line shapes. The "sharpness" of the singularities will increase as the value of this parameter is increased. There may however be some issues in accurately modeling very narrow line shapes as the digital precision between the points becomes insufficient. Fortunately, this issue arises only when simulating particularly narrow line shape where an exact solution is not usually needed anyway.

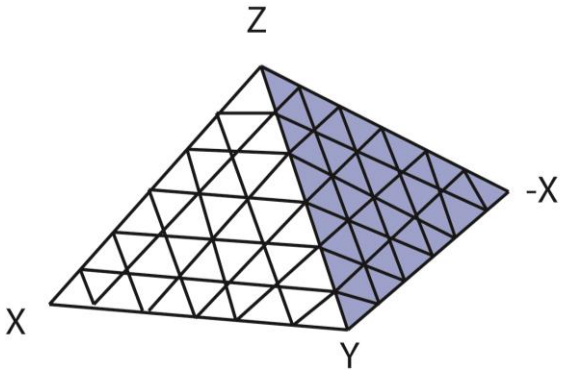

Figure 3.9. A schematic representation of the space tilling in QUEST according to the ASG interpolation procedure. NMR frequency calculations are performed at the vertices of each triangle, and the resonance frequencies for orientations in between the vertices are predicted by linear interpolation. This figure corresponds to a powder average quality of 6 since the pyramid is divided into 6 layers.

QUEST also supports the simulation of multiple sites which are conveniently separated into individual tabs. No restrictions are imposed on the additional sites. As such, these additional sites can take any spin quantum number, Larmor frequency, etc. This is essential for many broad spectra which can have different NMR active isotopes in the same spectral window. This is further supported with the "common spin pairs" tool which calculates the NMR parameters of an additional site automatically for certain elements where different NMR active isotopes can appear in the same window, such as $^{35/37}$Cl, $^{47/49}$Ti, $^{63/65}$Cu, $^{79/81}$Br, $^{113/115}$In, and $^{185/187}$Re. The spectral reference frequency may also be adjusted to any user-defined parameter and is not fixed to the value of the Larmor frequency.

As with many NMR simulation programs, an experimental NMR spectrum (saved in Bruker TOPSPIN format) can be loaded and underlaid beneath the calculated NMR spectrum. In that case, the spectral reference frequency and spectral window may be set automatically to the experimental values.

When a calculation is initiated, a progress bar will appear showing the advancement of the NMR calculation. By default, the frequencies are separated into 500 bins, giving a spectrum with 500 data points, although this can be increased to 2000 by clicking the "calculate high quality spectrum" button. The newest versions of QUEST are parallelized using OpenMP in order to reduce the time necessary to calculate the NMR spectrum.

By default, the transition amplitudes are calculated using the square of the absolute magnitude of the expectation value of the I_x operator (i.e., equation 3.19 when β = 90°). This corresponds to the correct line intensities for a coil perpendicular to the magnetic field.

These intensities are fairly insensitive to the angle the coil makes with the magnetic field for the single quantum NMR transitions, although the classically forbidden "overtone" NMR transitions are highly sensitive to the coil angle.[133] For this reason, it is possible to change the coil angle for spin-1 nuclei such as ^{14}N where significant resolution enhancements can be obtained when observing the overtone (m = 1 to -1) transition.[122,133-135]

Lastly, it is also possible to save the calculated QUEST spectra in Bruker TOPSPIN format. QUEST generates the 1r file which contains a series of binary integers representing the intensity of each data point. As well, QUEST produces the procs, acqu and acqus files which are necessary for representing the horizontal (frequency or chemical shift) axis. It is also possible to save the parameters from simulations into a parameter file for future use.

3.2.4 Experimental Examples

The utility and scope of QUEST is summarized in the Hamiltonian in equation 3.20: the theory is valid and exact for all transitions, and at any applied magnetic field. This is demonstrated in Figure 3.10 for the particular case of a spin-3/2 nucleus with a C_Q of 10 MHz and an axially symmetric EFG (i.e., η = 0) as the Larmor frequency is varied. On the bottom (ν_0 = 100 MHz) we can see a typical NMR spectrum for a spin-3/2 nucleus with the intense central transition (m = 1/2 to -1/2) in the centre which is not affected by the first-order quadrupolar interaction. This transition is flanked by the two satellite transitions (m = 3/2 to 1/2 and -1/2 to -3/2 transitions) which are much broader and largely invariant as a function of the magnetic field as it is decreased in the NMR regime. The central transition breadth, on the other hand, dramatically increases as the magnetic field is decreased. When the value of ν_Q is equivalent to the value of ν_0 (i.e., 5 MHz) the spectrum begins to lose the

features common to quadrupole-perturbed NMR spectra (for example, the "step" in the central transition is no longer present). When ν_0 is 2 MHz, the three overtone transitions (i.e. 3/2 to -1/2, 1/2 to -3/2 and 3/2 to -3/2) now appear in the spectrum and overlap with the "allowed" NMR transitions. These later combine with the NMR transitions when ν_0 is 0 MHz to form the "allowed" NQR transition (i.e., $m = \pm 1/2$ to $\pm 3/2$). We feel that this type of analysis, along with the analysis of the magnetic resonance frequencies done by Bain and Khasawneh,[116] is critical in the understanding of NQR and NMR alike.

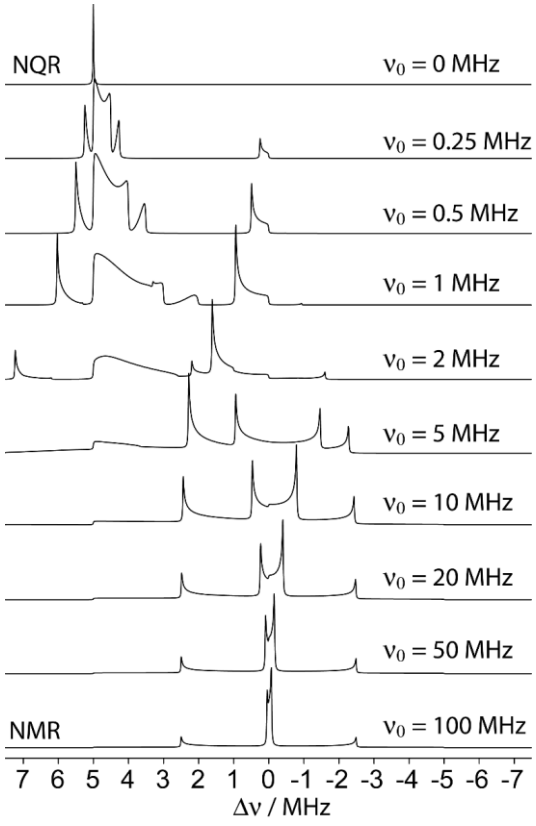

Figure 3.10. QUEST spectral simulations for a spin-3/2 nucleus with an axially symmetric EFG tensor and a C_Q of 10 MHz as the Larmor frequency is incremented from 0 MHz to 100 MHz. A smooth progression is observed from NQR to high-field NMR. The simulation with a ν_0 of 5 MHz corresponds to the situation when $\nu_0 = \nu_Q$.

We have tested the program against experimental data using the following examples: standard-field and low-field bromine NMR spectra of calcium bromide, ^{14}N overtone NMR of glycine, and ^{127}I and $^{185/187}$Re NQR of strontium iodine and dirhenium decacarbonyl. The program is also later used in order to interpret the first SSNMR spectra of covalently-bound organic chlorine sites, which experience very large quadrupolar interactions. The $^{79/81}$Br NMR allows us to test the accuracy of the frequencies calculated by our program in a regime where perturbation theory fails. The ^{14}N overtone NMR spectrum enables us to test the calculated intensities as the overtone line intensities depend strongly on the crystallite and coil orientations. Lastly, we show that QUEST is also valid in the realm of NQR and even predicts the partially allowed "overtone" NQR transition when $\eta \neq 0$.[136] Although overtone NQR transitions have been theoretically discussed for both spin-5/2[137] and spin-7/2,[138,139] and have been detected indirectly using the ^{209}Bi nuclide (spin-9/2),[140] and ^{127}I (spin-5/2),[141] as well as directly using crystals,[142] our example represents the first direct observation of overtone NQR using a powdered sample, to our knowledge. Additionally, it serves to show that QUEST is applicable for the entire continuum of possible quadrupole/Zeeman interactions, from NQR to NMR.

3.2.4.1 $^{79/81}$Br NMR of $CaBr_2$

$^{79/81}$Br NMR experiments on $CaBr_2$ have already been performed at a high magnetic field (21.1 T) and were published previously.[143] The $C_Q(^{81}Br)$ value in this sample is 62.8 MHz and the value of η is 0.445. We have also measured the $^{79/81}$Br NMR spectrum of $CaBr_2$ at 4.7 T ($\nu_0(^{81}Br)$ = 54.0 MHz; $\nu_0(^{79}Br)$ = 50.1 MHz). The spectrum along with exact and second-order perturbation theory simulations is shown in Figure 3.11. At this field, the central- and satellite-transition line shapes for both isotopes overlap with one-another. It

was useful to use QUEST's "common spin pairs" tool for this situation. At this field, the $^{79/81}$Br quadrupolar frequencies ($\nu_Q(^{81}Br)$ = 32.39(1) MHz; $\nu_Q(^{79}Br)$ = 38.69 MHz) nearly match their Larmor frequencies. This may be viewed as the transition point between quadrupole-perturbed NMR and Zeeman-perturbed NQR.

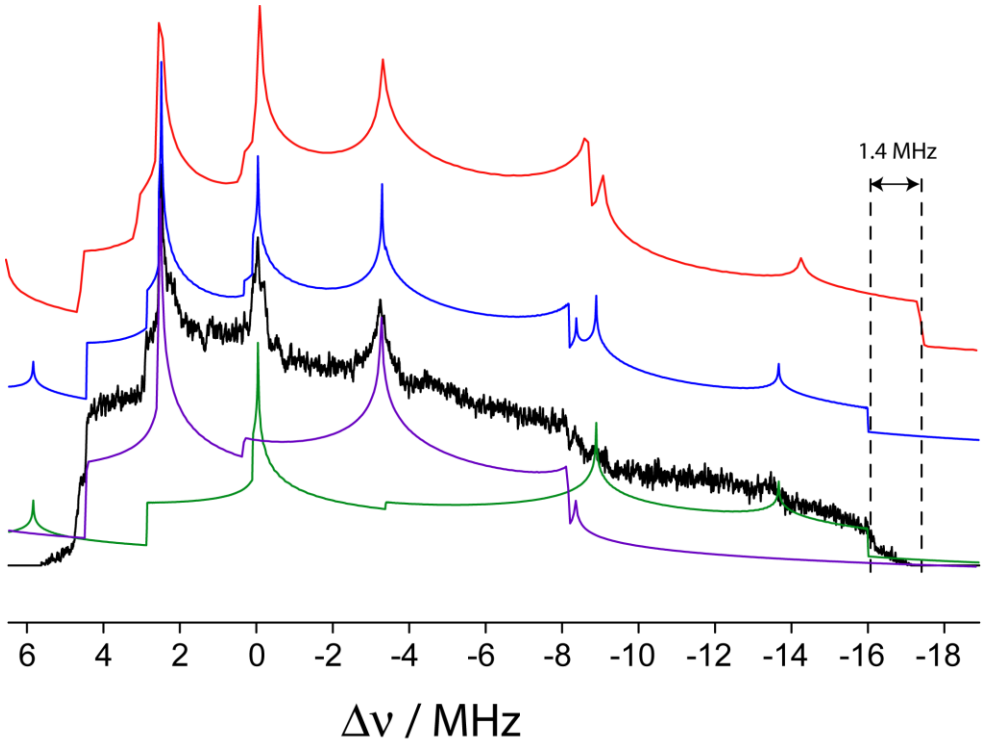

Figure 3.11. $^{79/81}$Br NMR spectrum of $CaBr_2$ acquired at 4.7 T along with its QUEST simulation (blue) and second-order perturbation theory simulation (red). The simulated powder patterns for ^{79}Br and ^{81}Br are shown in green and purple, respectively. At this field, none of the singularities are well reproduced by second-order perturbation theory although the discrepancy is more pronounced at the low-frequency end of the spectrum where there is a difference of 1.4 MHz between the two simulations.

Although none of the singularities are well reproduced by second-order perturbation theory, they are in a somewhat better agreement with experiment at the higher frequency end

of the spectrum than they are at the lower frequency end. For example, the ^{79}Br low-frequency edge predicted by second-order perturbation theory is off by 1.4 MHz from the experiment. The comparison between second-order perturbation theory and QUEST for all singularities is shown in Figure 3.12. All singularities, on the other hand, are well predicted by QUEST, although the intensities for some are degraded at lower frequency. This is associated with complications in the experiment rather than the simulation. As the spectrum spans over 20 MHz and a total of 167 transmitter offsets were necessary to acquire the entire pattern, the Boltzmann populations at each end of the spectrum differ by nearly a factor of two. There may also be significant effects caused by T_2 anisotropy or in the ability of the probe/spectrometer to perform uniformly throughout the large frequency range. Regardless of these issues, this example provides strong evidence that the eigenvalues calculated by QUEST are exact and valid at any currently available magnetic field in the NMR regime.

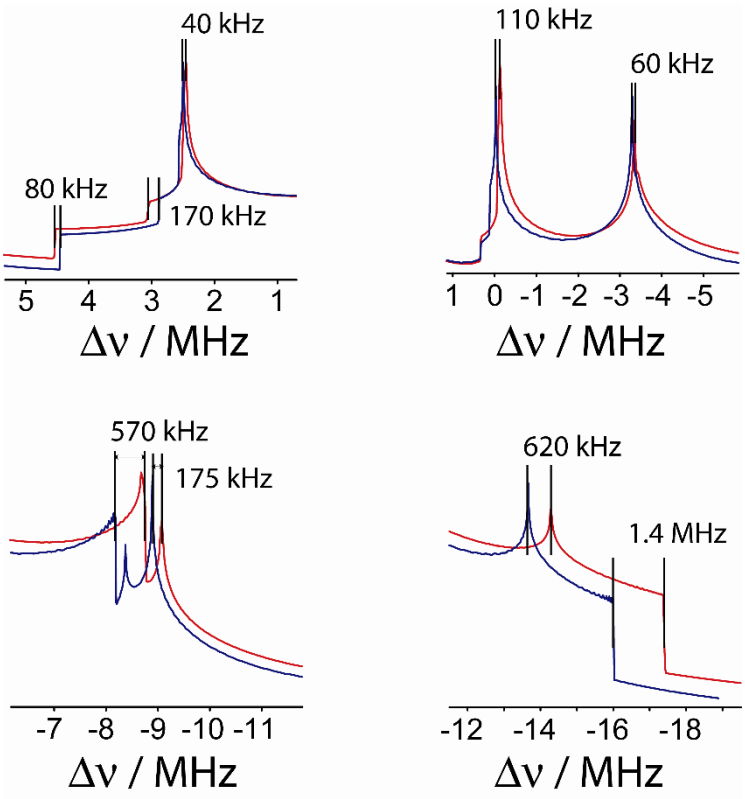

Figure 3.12. Simulated $^{79/81}$Br NMR spectra for $CaBr_2$ at 4.7 T (as in Figure 3.11) using second-order perturbation theory (red) and QUEST (blue) showing the difference in the position of all the singularities, which are marked by black lines. A general feature is that the position of the high frequency edge is much better predicted by second-order perturbation theory than the position of the low frequency edge.

3.2.4.2 ^{14}N overtone NMR of glycine

Overtone NMR spectroscopy involves the direct detection of an NMR signal from typically forbidden transitions which occur at multiples of the Larmor frequency. These transitions involve a change in *m* greater than 1. For example, in the case of a spin-1 nucleus such as ^{14}N, one can directly detect the $m = 1$ to -1 overtone transition.[122,133,134,135] As this transition is symmetric, it is not affected by the first-order quadrupolar interaction and is thus much narrower than the single-quantum transitions. In the case of quadrupolar nuclei, Zeeman eigenstates such as $|1\rangle, |0\rangle$, and $|-1\rangle$ are not appropriate and the true wavefunction for a given ^{14}N spin is a mixture of these three as demonstrated in equation 3.3. The $m = 1$ to -1 overtone NMR transition will contain some character from the allowed $m = 1$ to 0 and $m = 0$ to -1 transitions and will have a finite intensity if the value of C_Q is nonzero. Although in principle these transitions occur for $\Delta m = 2$, in an NMR experiment, only the minute character which is $\Delta m = 1$ is observed; this is possible because of the significant state mixing which is induced by the quadrupolar interaction (see equation 3.3). Since the intensity is a direct product of the mixing of the Zeeman states, this is an ideal case to test the validity of our implementation of equation 3.19 for calculating the line intensities for a coil oriented perpendicular to the magnetic field.

The ^{14}N overtone NMR spectrum of glycine is shown in Figure 3.13 for a coil oriented perpendicular to the magnetic field. The chemical shifts were referenced to the single-quantum NMR transition of nitromethane ($\delta = 0$ ppm).[144] By referencing to the single-quantum NMR transition of nitromethane, we avoid losing the chemical shift information from the overtone NMR spectra. As all EFG and CS tensor parameters are

known from ^{14}N as well as ^{15}N NMR, there are no freely variable parameters (other than the Euler angles which were set to the calculated values reported by O'Dell).[145-147] It can be seen that a single line with a gradual loss in intensity to lower frequency is observed and calculated. This example also demonstrates that the chemical shifts are properly described over a broad frequency range and that the intensities calculated according to equation 3.19 reproduce experiment well.

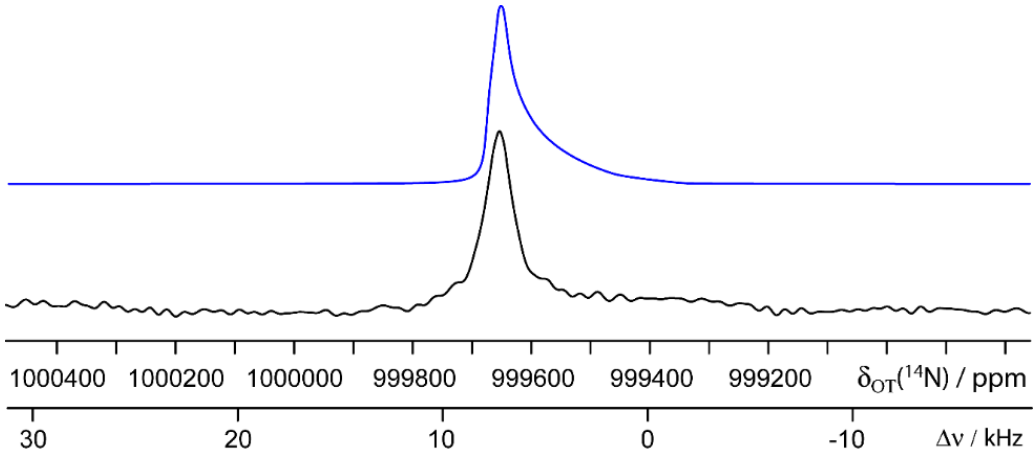

Figure 3.13. ^{14}N overtone NMR spectrum of glycine acquired at 9.4 T (bottom) in a coil perpendicular to the magnetic field along with the QUEST simulation. The overtone shifts (δ_{OT}) are referenced to the single-quantum ^{14}N NMR signal of nitromethane. The simulation is based on the quadrupolar and chemical shift parameters that were previously reported[67,68] and uses the calculated Euler angles of O'Dell et al.[69]

3.2.4.3 NQR and overtone-NQR experiments

^{187}Re and ^{127}I NQR experiments were also performed on dirhenium decacarbonyl (C_Q(^{187}Re) = 134.46(0.06) and η = 0.642(0.001)) and the I(2) site of strontium iodide (C_Q(^{127}I) = 214.0(0.1) MHz and η =0.316(0.002)), respectively.[90] These experiments serve to show that QUEST also performs correctly in the absence of a magnetic field. The calculated resonance frequencies agree with those calculated using the analytical expressions of Semin.[148] Notably, QUEST predicts the presence of the NQR overtone peak for spin-5/2 nuclei (m = ±1/2 to ±5/2) which appears at the sum of the two single-quantum NQR transitions if the value of η is nonzero. This overtone transition is not predicted by QUEST when η is zero and its intensity gradually rises to approximately 10% of the single-quantum transitions when η is 1, as shown in Figure 3.14.

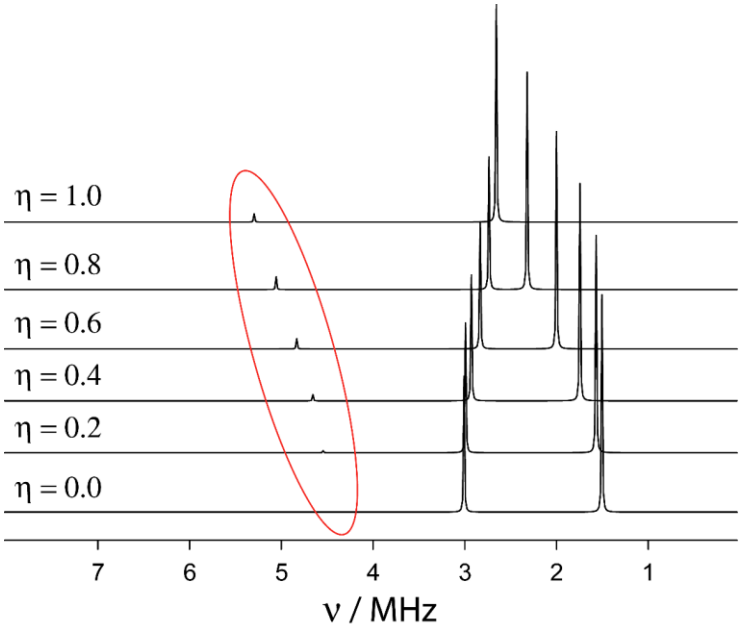

Figure 3.14. QUEST simulations of NQR spectra as a function of η demonstrating the appearance of the partially allowed overtone transition which has been circled. These simulations were performed on an arbitrary spin-5/2 nucleus with a C_Q value of 10 MHz.

The deviation from axial symmetry again, as in the case of overtone NMR transitions, causes state mixing which partially permits the observation of these typically forbidden transitions. Although observation of this transition may not add any new information, it may be helpful in assigning the single-quantum NQR resonances in a sample where multiple sites may be present. As well, we note in passing that these overtone NQR transitions may be used to quantify the effects of the nuclear electric hexadecapole interaction, which to the best of our knowledge has never been conclusively demonstrated using NMR/NQR.[149-151] The ^{127}I overtone NQR spectra of site I(2) in strontium iodide (single-quantum NQR was presented in ref. 90) along with the ^{187}Re NQR spectra for $Re_2(CO)_{10}$ are shown in Figure 3.15. Overall, it can be noted that there is excellent agreement between the experimental and all of the calculated NQR spectra. As well, it is seen that the peak positions calculated using QUEST agree with the positions calculated using the analytical expressions of Semin.[148]

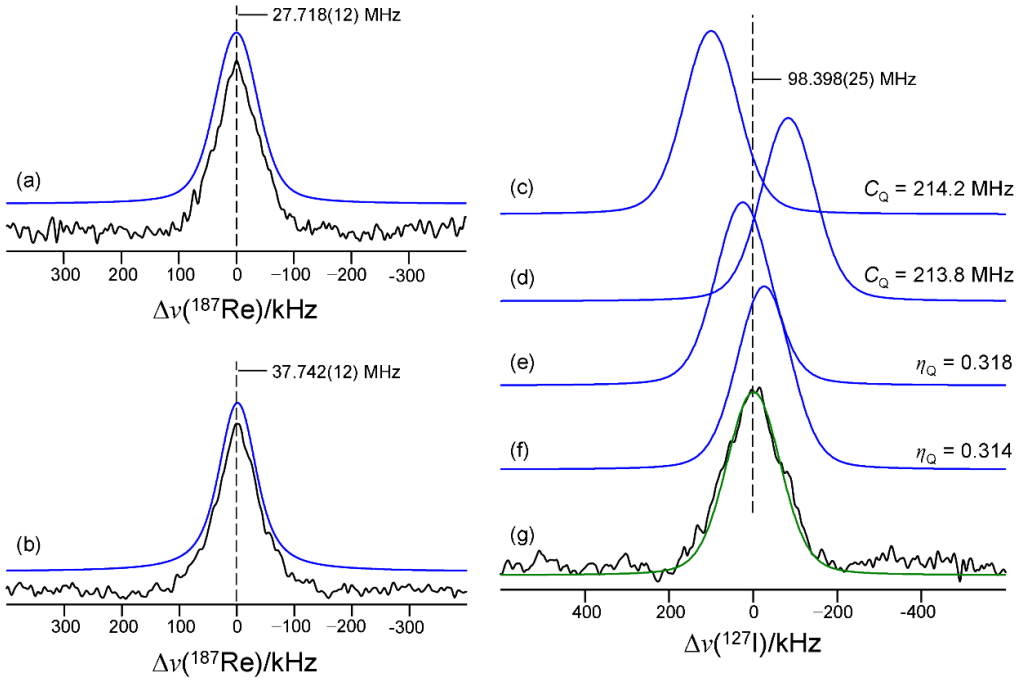

Figure 3.15. ^{187}Re NQR spectra and QUEST simulations for dirhenium decacarbonyl are shown in (a) and (b) for the ±1/2 to ±3/2 and ±3/2 to ±5/2 transitions, respectively. Similarly, the ^{127}I overtone NQR spectrum of the I(2) site of SrI_2 is shown in (g) along with simulations that vary key parameters (c-f) and show the sensitivity of the transition to the NQR parameters. The simulation in (g, green trace) was done with the experimental parameters (C_Q(^{127}I) = 214.0(0.1) MHz and η = 0.316(0.002)) whereas the simulations in (c-f) vary only one of those parameters as indicated in the figure. These spectra were acquired by Dr. Cory M. Widdifield.

3.2.4.4 Covalent Chlorine NMR

A particularly important application of this software is towards the interpretation of the $^{35/37}$Cl NMR spectra of organic chlorine sites. Most of the interesting chlorine chemistry occurs in when Cl is covalently bound to carbon, where chlorine often acts as a leaving

group. Organic chlorine is also present in many pharmaceuticals as well as in crystal design where it can accept a halogen bond.[152] Recent studies show that covalent chlorine is also important in biological chemistry where, for example, the tryptophan 7-halogenase enzyme was found to selectively chlorinate tryptophan moieties.[153] $^{35/37}$Cl NMR spectroscopy of covalently-bound chlorine sites is particularly challenging due to the large EFG that is generated by the carbon-chlorine σ-bond, with only a few examples of neat liquids having been studied where the resolution is limited due to quadrupolar relaxation.[154-156] However, in the solid state, nuclear spin relaxation is typically slower, enabling higher quality ^{35}Cl NMR spectra to be collected, at least in principle. Conventional wisdom is that such chlorine sites cannot be studied in powders by solid-state NMR as the central transition (CT) ($m_I = 1/2 \leftrightarrow -1/2$) can span tens of megahertz in typical commercially available magnetic fields. For this reason, only ionic chlorides[157-162] and inorganic chlorides[163-166] have been studied, as the EFG at these chlorides is often an order of magnitude smaller than for covalently-bound chlorine atoms. A partial ^{35}Cl NMR spectrum has been briefly mentioned in the literature for hexachlorophene.[167]

With the use of the state of the art WURST-QCPMG pulse sequence[55] and an ultrahigh magnetic field strength of 21.1 T it is in fact possible to acquire high quality $^{35/37}$Cl NMR spectra of covalent organic chlorine sites. We have acquired ^{35}Cl WURST-QCPMG NMR spectra of 5-chlorouracil, the pesticide 2-chloroacetamide, sodium chloroacetate, *α,α*'-dichloro-*o*-xylene, chlorothiazide, a diuretic pharmaceutical also known as diuril, 2,4'-dichloroacetophenone, and *p*-chlorophenylalanine, a chlorinated amino acid which is used as an inhibitor of tryptophan hydroxylase. These were chosen as a representative subset of compounds wherein chlorine is bound to sp^2 or sp^3 hybridized carbons. The molecular

structures are shown in Figure 3.16 along with the NMR spectra. The $^{35/37}$Cl CT NMR spectra span on the order of 7 MHz at 21.1 T, necessitating the variable-offset cumulative spectral (VOCS) acquisition approach.[82] Interpretation of the broad spectra of the CT requires exact line shape simulations using the QUEST software since it is known from NQR studies that the values of $C_Q(^{35}Cl)$ for covalently-bound chlorine atoms are on the order of -70 MHz.[168] As the ν_0 for ^{35}Cl at 21.1 T (corresponding to a 900 MHz ^{1}H ν_0) is only 88.2 MHz, the ratio of ν_0/ν_Q is around 2.5, where ν_Q represents the quadrupolar frequency. It is generally assumed that the high-field approximation is only valid if this ratio is higher than 10. This "breakdown" of the high-field approximation has been discussed by Widdifield et al. for the spin-5/2 case in $^{185/187}$Re and ^{127}I NMR.[90] Several of the ^{35}Cl NMR spectra also feature a singularity from the satellite transition of the ^{37}Cl isotope. This can be easily simulated in QUEST with the use of the common spin pair tool. The effect is more pronounced in the ^{37}Cl NMR spectrum of 5-chlorouracil which is shown in Figure 3.16. It is also important to note that since the satellite transitions are affected by third-order quadrupolar effects whereas the central transition is not, the position of the satellite transition singularity could not have been reproduced without the use of an exact treatment of the quadrupolar interaction.

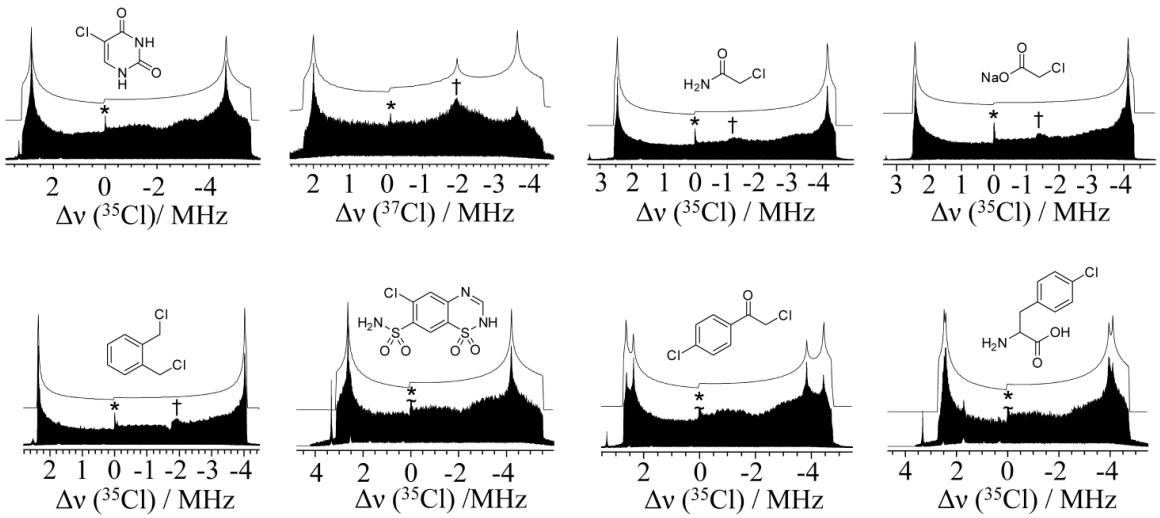

Figure 3.16. $^{35/37}$Cl WURST-QCPMG NMR spectra (bottom traces), exact simulations (top traces), and chemical structures of the chlorine-containing compounds. An asterisk is used to indicate a trace NaCl impurity whereas a cross marks a singularity from the satellite transition of the other chlorine isotope. The sharp lines on the high-frequency ends of the spectra are caused by radio interference.

To demonstrate the critical importance of using the exact Hamiltonian for the interpretation of these NMR spectra, we have compared our simulations with those obtained using second-order perturbation theory. Curiously, the high-frequency singularities are well reproduced with the use of perturbation theory, but the low-frequency part of the spectrum appears stretched, which introduces an error in the chemical shift on the order of 600 ppm and an underestimation of C_Q on the order of 700 kHz. These are, of course, non-trivial errors which would severely alter the interpretation of the NMR spectrum in terms of the chemical environment of the chlorine. Figure 3.17 compares the simulations of the low-frequency edge of the NMR spectrum of 5-chlorouracil using second-order perturbation theory and exact theory. The exact theory reproduces the experimental data whereas

discontinuities in the simulation obtained from second-order perturbation theory are strikingly off by several hundreds of kilohertz from experiment.

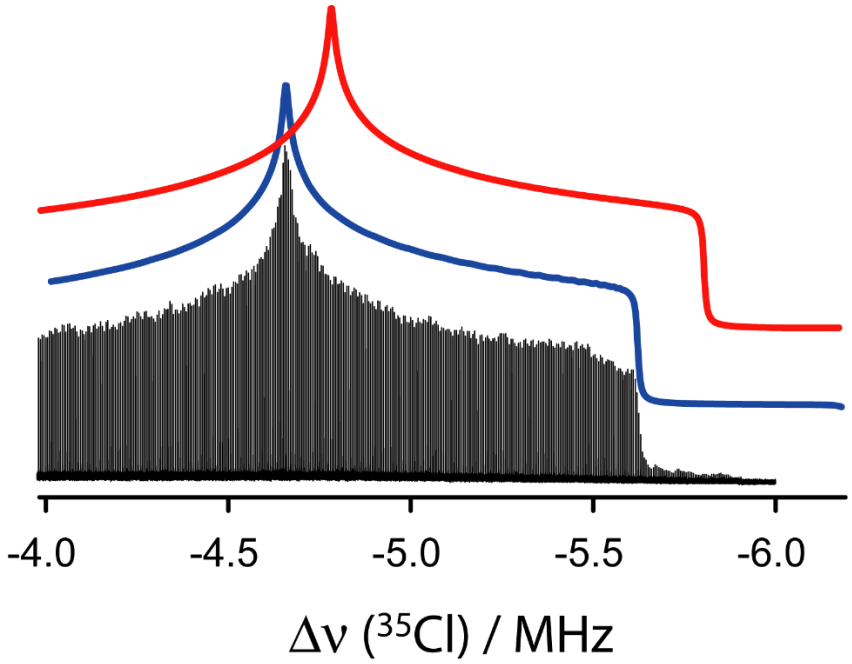

Figure 3.17. Low-frequency edge of the ^{35}Cl NMR spectrum of 5-chlorouracil, showing a comparison between exact theory (blue) and second-order perturbation theory (red) simulations.

Four of the selected samples contain chlorine atoms covalently bound to sp^3-hybridized CH_2 carbons whereas another four contained chlorines which are bound to sp^2 carbons in aromatic rings.

It has been shown by solution NMR that chlorine isotropic chemical shifts (δ_{iso}) are extremely sensitive to the chemical environment. We have also noticed this presently, as all chlorines bound to CH_2 carbons have δ_{iso} values ranging from 150 to 200 ppm whereas those bound to aromatic rings had δ_{iso} values on the order of 300 to 350 ppm. Admittedly, the errors associated with the measurement of this parameter call for additional confirmatory

studies to further substantiate the present findings. Additionally, as has been explained using Townes-Dailey theory,[169,170] the back-donation of π electron density from the chlorine into the π system of the aromatic rings creates a non-zero EFG perpendicular to the plane of the ring which differs from the one parallel to the ring. This leads to a deviation of the EFG from axial symmetry which is evidenced by the value of the quadrupolar asymmetry parameter (η) (which ranges from 0 to 1 and takes a value of 0 in the case of axial symmetry) that deviates from 0. In the compounds we have studied, the asymmetry parameters for the chlorines bound to CH_2 carbons remain nearly axially symmetric (η = 0.008 to 0.032) whereas those bound to aromatic rings are significantly larger (η = 0.073 to 0.139). Figure 3.18 shows a clear separation of the two types of compounds studied here on the basis of their δ_{iso} and η values. It is evident that valuable chemical information can be obtained from ^{35}Cl solid-state NMR which is not available from standard ^{35}Cl NQR experiments.

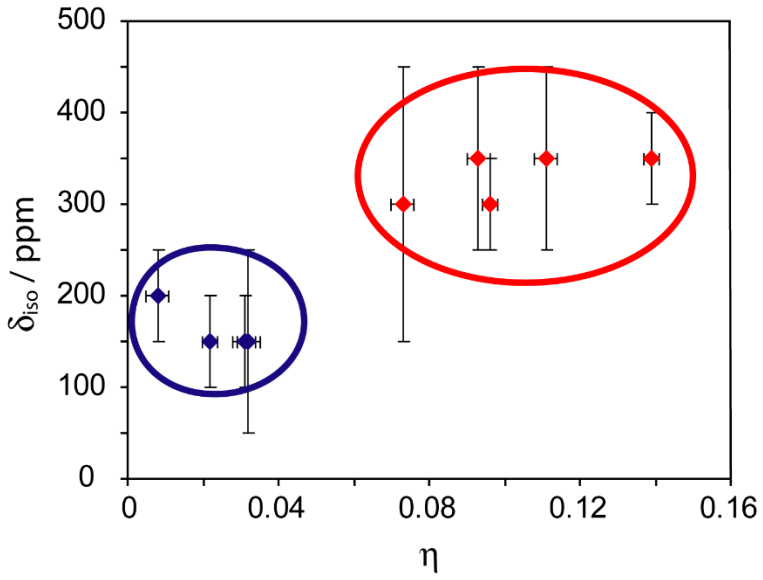

Figure 3.18. Scatter plot of the Cl chemical shifts and quadrupolar asymmetry parameters. Those bound to CH_2 groups are shown in blue whereas those bound to aromatic rings are shown in red.

Table 3.5. Chlorine-35 EFG tensor parameters and isotropic chemical shifts for covalently-bound chlorine atoms

Compound	C_Q / MHz	η	δ_{iso} / ppm
5-chlorouracil	−75.03 ± 0.05	0.096 ± 0.002	300 ± 50
2-chloroacetamide	−68.30 ± 0.05	0.031 ± 0.003	150 ± 50
sodium chloroacetate	−67.75 ± 0.05	0.022 ± 0.002	150 ± 50
α,α'-dichloro-*o*-xylene	−66.43 ± 0.08	0.008 ± 0.003	200 ± 50
chlorothiazide	−73.04 ± 0.08	0.139 ± 0.002	350 ± 50
2,4'-dichloroacetophenone (sp^3 site)	−70.70 ± 0.08	0.032 ± 0.003	150 ± 100
2,4'-dichloroacetophenone (sp^2 site)	−68.65 ± 0.08	0.111 ± 0.003	350 ± 100
p-chlorophenylalanine (site 1)	−69.0 ± 0.2	0.093 ± 0.003	350 ± 100
p-chlorophenylalanine (site 2)	−69.5 ± 0.2	0.073 ± 0.003	300 ± 150

Interestingly, the breadth of the NMR line shapes enhances our ability to distinguish chemically distinct sites relative to solution NMR, as the powder pattern singularities are well separated. 2,4'-dichloroacetophenone was chosen in order to test our ability to distinguish chemically distinct chlorine sites as this compound has a chlorine directly bound to an aromatic ring (i.e., sp^2) and another on a CH_2 group (i.e., sp^3). The singularities for both sites are well separated and these can be simulated and assigned on the basis of their δ_{iso} and η values. It also came as a surprise that two crystallographically distinct chlorine sites were observed for *p*-chlorophenylalanine, as two sets of horn singularities are present in the spectrum. The crystal structure of this compound is not known although we can conclude, based on this NMR data, that there are two non-equivalent molecules in the asymmetric unit. This is supported by our NQR studies as well. This gives us an interesting perspective on the effect that crystal packing has on the NMR parameters. For the two chlorine sites, the value of C_Q varies by only 500 kHz (< 1 % difference) and the η differed by 0.02: these small differences are nevertheless manifested unambiguously in the ^{35}Cl NMR spectrum of *p*-chlorophenylalanine despite its overall breadth.

It is interesting to compare this solid-state NMR method for probing the chlorine chemical environment with those that are already available. To that end, we have acquired ^{35}Cl NQR spectra for all compounds. The NQR resonance is indeed much sharper than the NMR line shapes and all of the compounds in this study have resolved NQR peaks (see Figure 3.19). Unfortunately, only the quadrupolar product ($P_Q = C_Q\sqrt{1+\eta^2/3}$) can be obtained by pure NQR methods with powder samples on I = 3/2 nuclei. Thus, the precise values of δ_{iso}, C_Q, and η cannot be obtained with that method. Importantly, as the respective ranges of C_Q for different chemical species (i.e., Cl bound to sp^2 vs sp^3 carbons) effectively overlap, it is difficult, if not impossible, to obtain unambiguous chemical information from ^{35}Cl NQR of these samples, see Figure 3.19.

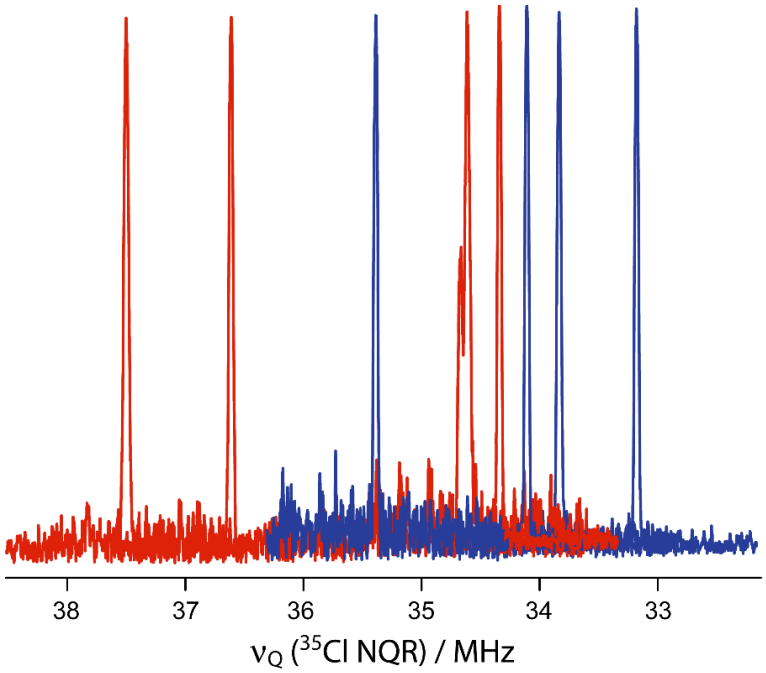

Figure 3.19. ^{35}Cl NQR spectra of the chlorine-containing compounds. The blue spectra correspond to chlorine atoms bound to sp^3 carbons whereas the red spectra correspond to chlorine atoms bound to sp^2 carbons.

Liquid-state ^{35}Cl NMR on the other hand can directly provide only chemical shifts in favourable cases (e.g., neat liquids); however, site resolution is often lost due to the breadth of the resonances relative to the chemical shift range of chlorine. With solid-state ^{35}Cl NMR of powdered samples, we have shown that it is possible to capture the best of both methods while also gaining novel information about η, which appears to be the most distinctive probe of the chlorine chemical environment.

We have lastly investigated the observed trends with the use of gas phase (B3LYP/6-311++G**)[171-173] DFT calculations of the NMR parameters as well as solid-state, periodic, GIPAW DFT calculations[61] with the use of the PBE exchange-correlation functional (see Figure 3.20).[89] Contrary to previous studies on other nuclei, the values of η are much better reproduced with DFT than are the values of C_Q. This is probably due to the fact that C_Q can vary by as much as 2 MHz depending on the temperature whereas the η value remains relatively constant as it depends only on the symmetry along the bond.[174] The chemical shifts are also very well reproduced by DFT, and are in support of the trend we observed (i.e., variation in the chlorine chemical shift may indicate if the adjacent carbon is sp^2 or sp^3). The agreement is significantly greater for GIPAW DFT calculations, which shows that long-range crystal packing effects play a non-negligible role in determining the chlorine magnetic shielding constants.

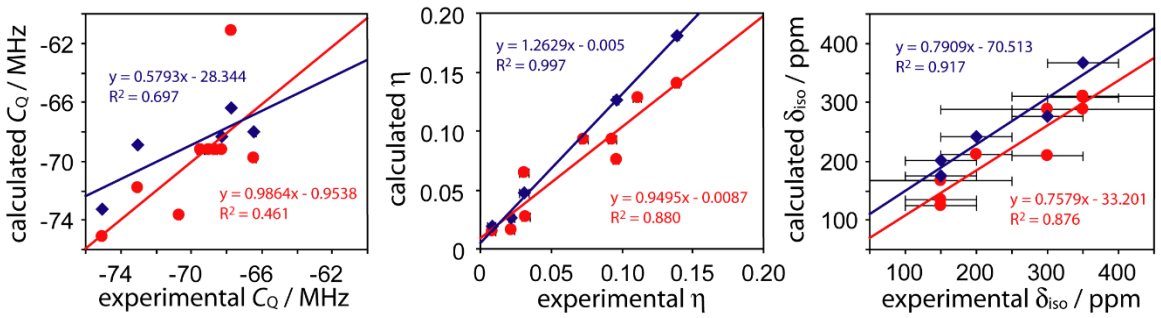

Figure 3.20. Correlation between calculated and experimental C_Q, η, and δ_{iso} values. The red circles correspond to the results from gas phase DFT calculations whereas the blue diamonds correspond to the results from the solid phase GIPAW DFT calculations. Error bars for C_Q are within the size of the symbols.

^{35}Cl solid-state NMR of covalently-bound organic chlorines can then be used as a powerful and sensitive tool for structural investigations. The chemical shifts, and especially the quadrupolar asymmetry parameters, are very sensitive to structure, making it possible to distinguish chemically different and even crystallographically different chlorine sites. In order to properly interpret the data, a program which describes the quadrupolar interaction exactly was necessary.

3.2.5 Conclusions

With the use of the theory developed for the simulation of residual dipolar coupling multiplets (see chapter 3.1), a fast and graphical exact quadrupolar solid-state NMR/NQR line shape simulation program was developed. This program, named QUEST (QUadrupolar Exact SofTware) can be used to simulate the NMR spectra of quadrupolar nuclei is any applied magnetic field strength, from the realm of NQR to NMR. We have validated several aspects pertaining to the applicability of the program with the $^{79/81}$Br NMR spectra of

calcium bromide which exhibited high-order quadrupole-induced effects. Additionally, we have demonstrated that the program can be used to simulate NQR spectra and overtone NMR/NQR spectra, and we have shown the first direct observation of overtone NQR in a powdered sample.

The program was also applied to the interpretation of the NMR spectra of covalently-bound organic chlorine sites which hadn't previously been observed. In that case QUEST enabled the determination of the chemical shift and EFG tensor parameters which proved to be highly sensitive to the nature of the chlorine site. For example, it was demonstrated that chlorine sites that are bound to sp^2 and sp^3 hybridised carbon sites can be unambiguously assigned on the basis of their η and δ_{iso} parameters, both of which cannot be extracted simultaneously by other means. The availability of QUEST to the general public is foreseen to aid in the development of the NMR spectroscopy of nuclei having large quadrupole moments for which no general spectral simulation software was available.

3.2.6 Experimental

3.2.6.1 $^{79/81}$Br NMR

The $^{79/81}$Br NMR spectrum of $CaBr_2$ at 4.7 T ($\nu_0(^{81}Br)$ = 54.0 MHz; $\nu_0(^{79}Br)$ = 50.1 MHz) was acquired using a 7 mm static probe on a Bruker AVANCE III 200 spectrometer. The spectrum was acquired with the Hahn echo pulse sequence with whole echo acquisition using 1.5 μs 90° pulses and an echo delay of 200 μs. The VOCS method was also necessary in this case and 167 pieces were acquired using offsets of 125 kHz. 4000 scans were accumulated for each piece using a recycle delay of 0.5 s.

3.2.6.2 ^{14}N Overtone NMR

The ^{14}N overtone NMR spectrum of glycine was acquired at 9.4 T (ν_0 = 28.9 MHz) using a 7 mm static probe and a Bruker AVANCE III 400 spectrometer. The chemical shifts were referenced to nitromethane ($\delta(CH_3NO_2)$ = 0.0 ppm) using solid NH_4Cl as an external reference (δ = -338.1 ppm).[175] The transmitter frequency was then set to twice that of the single-quantum transition. A simple pulse then acquire method (i.e., a Bloch decay) was used as described by O'Dell[134] and high power 40 μs excitation pulses were applied. A total of 160000 scans were collected with a 0.5 s recycle delay. The spectrum was simulated with the use of the CS and EFG tensor parameters determined from the previous ^{14}N and ^{15}N NMR experiments.[145,146]

3.2.6.3 $^{35/37}$Cl NMR

All ^{35}Cl and ^{37}Cl NMR experiments were performed at 21.1 T using the Bruker AVANCE II spectrometer at the National Ultrahigh-Field NMR Facility for Solids in Ottawa. All samples were purchased from Sigma-Aldrich and used without further purification. For the chlorine NMR experiments, the samples were powdered and packed into 7 mm glass tubes which were then placed into the coil of a home-built 7 mm HX static probe. A WURST-QCPMG pulse sequence[55] was used with proton decoupling using 50 μs WURST pulses that swept over a frequency range of 1 MHz. The VOCS data acquisition method was used,[82] where a series of 33 to 45 spectra were collected, processed and then co-added in the frequency domain. A QCPMG spikelet separation of 5 kHz was used in all cases with a VOCS stepping frequency of 200 kHz to ensure uniformly excited line shapes. 1000 to 2000 scans were used to acquire each piece using a recycle delay of 0.5s. In most

cases 128 echoes were collected for each QCPMG echo train (an acquisition time of 25.7 ms) although for 5-chlorouracil, chlorothiazide, and 2,4'-dichloroacetophenone it was possible to acquire 192 echoes (an acquisition time of 38.4 ms), thus increasing the signal intensity. The ^{37}Cl NMR spectrum of 5-chlorouracil was acquired using the same parameters as those used for ^{35}Cl although 1500 scans were collected. It was necessary to increase the attenuation of the pulses for a certain area in the spectrum (around -2.5 MHz) as the power was not constant throughout the whole range. This varying power leads to "waves" in the line shape around -1.5 and -3.5 MHz.

The ^{35}Cl NQR experiments were performed at 35°C using a 7 mm static NMR probe and an AVANCE III console. A Hahn-echo pulse sequence was used with a 3 μs excitation pulse length and a 6 μs refocusing pulse.

3.2.6.4 DFT Calculations

The ^{35}Cl NMR parameters were calculated at the B3LYP/6-311++G**[171,172,173] level of theory, as implemented in the Gaussian 09 program, using a single molecule as input. These were also calculated using the GIPAW method[61] using the PBE exchange-correlation functional,[89] as implemented in the CASTEP-NMR (version 4.1) program.[61] A 610 eV kinetic energy cut-off was used along with ultrafine k-point grids and on-the-fly generated ultrasoft pseudopotentials.

Chapter 3.3: Homonuclear *J* Coupling Between Quadrupolar Nuclei

3.3.1 Introduction

Since its discovery over 60 years ago,[176] indirect nuclear spin-spin (*J*) coupling has been used to gain insight into chemical structure.[177-181] Unlike direct dipolar coupling, which is a through-space interaction, the *J* coupling interaction is mediated by the electrons that form bonds.[182,183] As *J* coupling is sensitive to bonding interactions, it has been used to probe the nature of hydrogen bonds,[184-186] CH-π interactions,[187] as well as van der Waals' interactions.[188] Although the first direct observation of *J* coupling involved a quadrupolar nucleus (spin $S > 1/2$), ^{121}Sb,[189] the vast majority of the applications of *J* coupling have focussed solely on spin-1/2 nuclei.[190] This is because the quadrupolar interaction leads to rapid relaxation in solution, which often severely broadens the lines and obscures the fine structure of the resonances. In solids, anisotropic line broadening is present which cannot be completely removed by magic angle spinning (MAS) and thus also obscures fine structure in conventional NMR experiments. Double-rotation NMR (DOR) can however be used in order to remove the residual anisotropic quadrupolar broadening in order to observe spin-spin coupling multiplets (see chapter 3.1).

The case for heteronuclear spin-spin coupling has been discussed in chapter 3.1 and can be simulated by assuming Zeeman product states to which small perturbations are applied by the quadrupolar interaction. Additional complications arise in the case of

homonuclear *J* coupled nuclei since the possibilities of similar, or identical, chemical shifts can lead to strong mixing of the Zeeman product states.

In solids, nuclei are said to be chemically equivalent (AA') when they are related by a symmetry operation. The nuclei then have the same tensor magnitudes and give the same powder NMR spectra. If these nuclei are related by an inversion center, or if there is a C_3 rotation axis, or higher, along the internuclear vector, the nuclei additionally share the same tensor orientations and thus resonate at the same frequencies for all crystallite orientations.[191] These spin pairs are termed magnetically equivalent (A_2) and *J* coupling does not affect the NMR spectra of A_2 spin-1/2 spin-pairs.[192] If the coupled spins are not related by any symmetry operation then they are deemed inequivalent (AX). All of these situations are summarized in Table 3.6. Intermediate conditions also exist if the difference in chemical shifts is of the same order of magnitude as the *J* coupling; these are known as AB spin systems. It is unclear what is to be expected in the case of an A_2 spin system of quadrupolar nuclei. In this chapter, theory describing the homonuclear spin-spin coupling involving quadrupolar nuclei will be described. These theoretical predictions are then tested with the use of DOR NMR experiments and numerical simulations using the SIMPSON program.

Table 3.6. Definitions of the various spin systems discussed in the text, typical compounds which would have the appropriate symmetry, and the various equivalencies of the different transitions of quadrupolar nuclei.

Spin system	Label	Notes	Example compound	Equivalence of the different transitions of a quadrupolar nucleus		
				CT : ST	CT : CT	ST : ST
central-satellite magnetic equivalence	CS-A_2	The nuclei have identical tensor magnitudes and orientations and no quadrupolar coupling.	This situation occurs in crystals with cubic symmetry. ex. ^{23}Na nuclei in NaCl(s)	✓	✓	✓
magnetic equivalence	A_2	The nuclei have identical tensor magnitudes and orientations.	The spins need to be related by an inversion center or lie along a C_3 or higher rotation axis. ex. ^{35}Cl nuclei in Cl_2(g)	X	✓	✓
chemical equivalence	AA'	The nuclei have identical tensor magnitudes but differing tensor orientations.	The spins need to be related by a reflection, rotation, translation, or glide symmetry operation. ex. ^{17}O nuclei in H_2O_2	X	✓[a]	X
non-equivalence	AX	The nuclei have generally different tensorial interactions.	The spins are not related by any symmetry operation. ex. ^{17}O nuclei in ROOR'	X	X	X

[a] Note that the central transition resonances are not strictly magnetically equivalent in this case when there is large second-order quadrupolar broadening. This broadening is however removed by DOR.

3.3.2 Theory

The isotropic *J* coupling Hamiltonian is given by:[193]

$$\hat{H}_J = J_{iso}\hat{S}_{1z}\hat{S}_{2z} + \tfrac{1}{2}J_{iso}\left(\hat{S}_{1+}\hat{S}_{2-} + \hat{S}_{1-}\hat{S}_{2+}\right) \quad (3.23)$$

where the first term is secular, does not affect the wavefunctions, and simply returns the product of the magnetic quantum numbers, *m*, of both nuclei and the second term mixes the eigenstates which differ in *m* by 1. The full mixing which is induced by the second part of the *J* coupling Hamiltonian may only occur if the eigenstates in question are degenerate.[194] For a quadrupolar nucleus, due to the presence of the quadrupolar interaction, typically only the eigenstates with the various permutations of the same *m* quantum numbers can be degenerate. For a pair of quadrupolar nuclei, the eigenstates can then be written as:

$$\begin{matrix} \frac{1}{\sqrt{2}}\left(|m_1, m_2\rangle + |m_2, m_1\rangle\right) \\ \frac{1}{\sqrt{2}}\left(|m_1, m_2\rangle - |m_2, m_1\rangle\right) \end{matrix} \quad (3.24)$$

where there are perfectly symmetric and perfectly antisymmetric eigenstates. These, however, only correspond to the eigenstates in situations where the nuclei are magnetically equivalent. The energy levels need to be strictly degenerate at all crystallite orientations for the mixing to consistently occur. The coupled nuclei must then have the same chemical shift and electric field gradient tensor magnitudes and orientations; this is known as an A_2 spin system. If the two spins have identical tensor magnitudes but the tensor orientations differ, both nuclei will resonate at different frequencies and the mixing will not occur; this is an AA' spin system.

The mixing of the eigenstates may also be understood conceptually. In the A_2 case, 'product' eigenstates of the form $|m_S, m_I\rangle$ such as $|\frac{3}{2}, \frac{1}{2}\rangle$ and $|\frac{1}{2}, \frac{3}{2}\rangle$ cannot be distinguished because both nuclei are identical particles. States must then be determined which are symmetric and antisymmetric with respect to the permutation of the spins; for this particular example, the states are rewritten as: $|3,2\rangle = \frac{1}{\sqrt{2}}\left(|\frac{1}{2}, \frac{3}{2}\rangle + |\frac{3}{2}, \frac{1}{2}\rangle\right)$ and $|2,2\rangle = \frac{1}{\sqrt{2}}\left(|\frac{1}{2}, \frac{3}{2}\rangle - |\frac{3}{2}, \frac{1}{2}\rangle\right)$ where the kets are labelled as $|S, M\rangle$ where S is the total spin quantum number and M is the total magnetic quantum number.[192,195] For the A_2 case, m_S and m_I are no longer good quantum numbers; however, S and M are. The eigenstates for these systems are then labelled as $|S, M\rangle$ [196,197] where the allowed transitions involve a ΔM of 1 and ΔS of 0 or ±2.[198] The single-quantum transitions between these can alternatively be identified as those having non-zero transition amplitudes calculated using the $S_+ + I_+$ operator.[195] Similar eigenstates were formulated to explain the fine structure in NQR spectra of homonuclear coupled spins;[199] however, the permutation symmetry is higher for NQR as the Hamiltonian only depends on the absolute value of m.[200] The single quantum NMR transitions are depicted in Figure 3.21 for the homonuclear spin-3/2 case using an energy level diagram, and are compared to the heteronuclear case. It can be seen that, in the latter case, the transitions are well separated as there is no mixing between the I and S states.

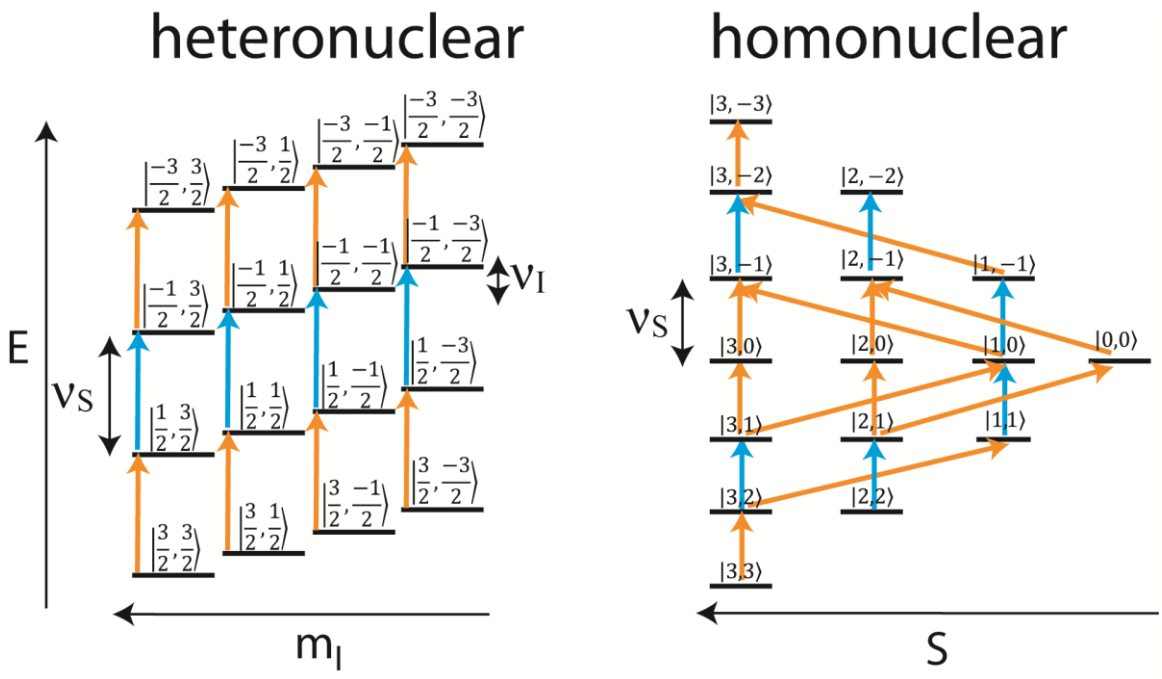

Figure 3.21. Energy level diagrams showing the allowed transitions for both heteronuclear and homonuclear (A_2) spin-3/2 pairs. ν_S corresponds to the Larmor frequency of the observed nucleus and ν_I corresponds to the Larmor frequency of the perturbing nucleus. Blue arrows indicate the transitions associated with the CT (also listed in Table IV) whereas the orange arrows are STs. In the heteronuclear case, the labels take the form $|m_S, m_I\rangle$ whereas in the homonuclear case they are $|S, M\rangle$.

There are four transitions associated with the central transition corresponding to the *S* nucleus coupled to the four states of the *I* nucleus. In the A_2 case, however, because of the large amount of mixing, some eigenstates can undergo single quantum transitions to two different states. There are, in this case, six distinct transitions which can be associated with the CT. For spin-1/2 nuclei, the number of transitions does not change when going from AX to A_2 spin systems since there are no quintet states which can undergo transitions with the

singlet state.[192] The transitions associated with the CT for homonuclear spin-3/2 and spin-5/2 pairs are listed in Table 3.7. Typically, only the CT (m = 1/2 to -1/2 transition) is observed experimentally and only the CT can be easily manipulated using radio-frequency pulses. This is due to its much narrower spectral line shape since it is unaffected by the first-order quadrupolar interaction. We will then only concern ourselves with the CT magnetization.

Table 3.7. List of CT-associated transitions for magnetically equivalent homonuclear A_2 spin pairs involving half-integer spin nuclei ($I < 3$)[a]

transition[a]	operator
1	$\|1,0\rangle\langle 1,1\|$
2	$\|1,-1\rangle\langle 1,0\|$
3	$\|2,-2\rangle\langle 2,-1\|$
4	$\|2,1\rangle\langle 2,2\|$
5	$\|3,-2\rangle\langle 3,-1\|$
6	$\|3,1\rangle\langle 3,2\|$
7	$\|4,-3\rangle\langle 4,-2\|$
8	$\|4,2\rangle\langle 4,3\|$
9	$\|5,-3\rangle\langle 5,-2\|$
10	$\|5,2\rangle\langle 5,3\|$

[a] Only the transitions 1-2 are applicable to spin-1/2 nuclei, 1-6 are applicable to spin-3/2 nuclei and all transitions are present for spin-5/2 nuclei.

For simplicity, the CT multiplets can be thought of as a series of doublets due to the coupling of the central states to each of the pairs of $|m|$ states of the other nucleus. The transitions where both nuclei are in central states (i.e., m = 1/2 or -1/2) are condensed into a single, amplified, doublet with a splitting of $(2S + 3)(2S - 1)J/4$ and originate only from the fully symmetric states. The antisymmetric state does not lead to any central transitions; however, unlike spin-1/2 nuclei,[201] the central antisymmetric state of quadrupolar spin pairs cannot be used to store hyperpolarized magnetization for long periods of time as it can undergo satellite transitions to other antisymmetric states with higher m values.

The doublet originating from the coupling between the central states and states with *m* values of 3/2 and -3/2 is split into two separate doublets with half the intensity each. There are two pairs of resonances in this case instead since the symmetric and antisymmetric states differ in energy because of the second term in the *J* coupling Hamiltonian. The coupling in the symmetric states leads to an amplified splitting of $(S^2+S+9/4)J$ and thus always leads to the doublet of largest splitting within the A_2 multiplets. The splitting of the resonance of the antisymmetric states is of $(2S + 5)(2S - 3)J/4$ and is thus smaller than that of the other doublet.

The raising and lowering operators in the second term of the *J* coupling Hamiltonian do not affect the energy of the states with *m* values greater than 3/2, for the CT. The splittings of the doublets due to coupling to states with higher angular momentum are thus of $2|m|J$, where $|m|$ is the magnetic quantum number of the nucleus which is not in a central state. These splittings correspond to the usual, unamplified, splittings that are observed in AX spin systems, *vide infra.*

The idealized CT multiplets which are expected for pairs of magnetically equivalent quadrupolar nuclei are shown in Figure 3.22 for nuclei with spin of 3/2, 5/2, 7/2, and 9/2. For example, for a pair of magnetically equivalent spin-3/2 nuclei, a 1:2:2:2:1 pentet with equal spacings of 3/2*J* is expected. These are first-order multiplets and do not originate from a *J* recoupling interaction[202-205] or a cross-term interaction.[44] In single crystals, these multiplets will be largely affected by direct dipolar coupling, however, under spinning conditions, the dipolar coupling would be averaged leaving only the effects of the *J* coupling.

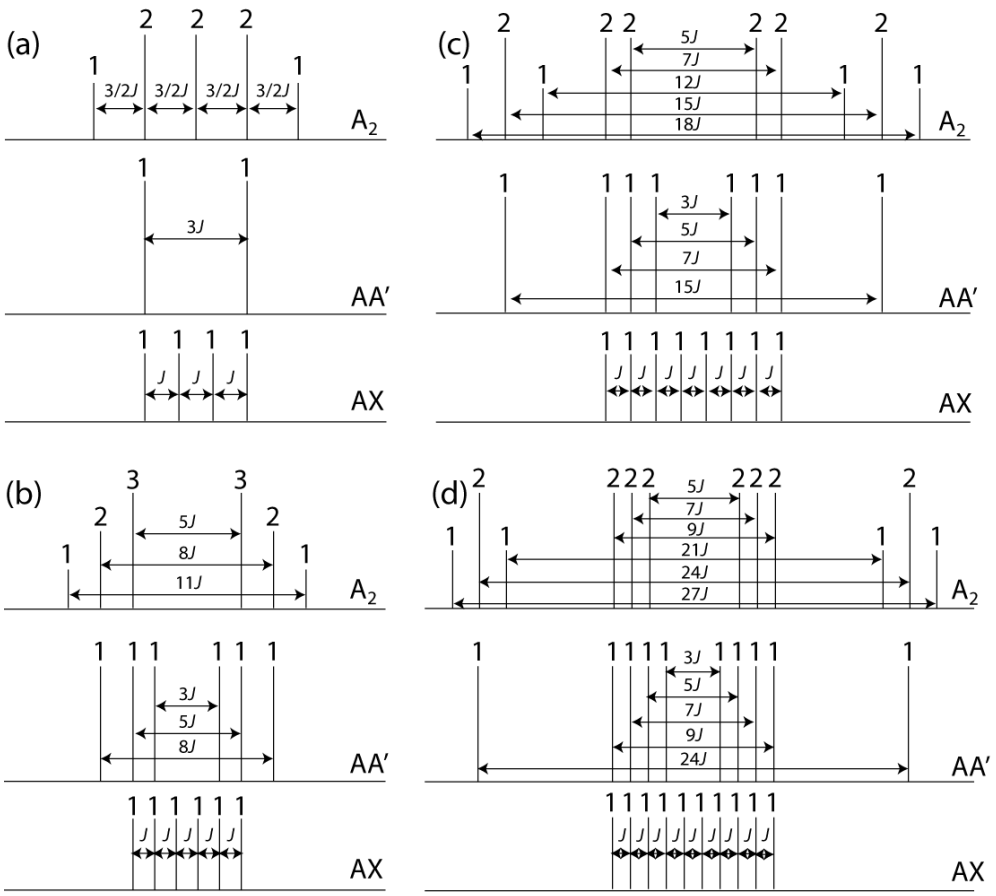

Figure 3.22. Simulated ideal, CT-only, first-order *J* coupling multiplets for the AX, AA', and A_2 spin systems of two homonuclear *J* coupled quadrupolar nuclei with spin quantum numbers of (a) 3/2, (b) 5/2, (c) 7/2, and (d) 9/2 under single-crystal NMR conditions. These multiplets assume a significant quadrupolar interaction such that the CTs are not equivalent with the STs for both nuclei.

In AX spin systems, the eigenstates take the familiar Zeeman product form, $|m_1, m_2\rangle$, and the CT NMR spectra are composed of $2S+1$ uniformly spaced lines of equal intensity separated by the *J* coupling constant, as is usual for heteronuclear *J* coupling. This

corresponds to a superposition of $S + 1/2$ doublets with line splittings of $2|m|J$, where m is the magnetic quantum number of the coupled nucleus.

In the special case where the quadrupolar interaction is zero, or is motionally averaged to zero, as in solution, the satellite transitions are no longer separated from the CT by a first-order quadrupolar splitting and all transitions are degenerate. The eigenstates with the same $\sum m$ value are also degenerate and are, in principle, allowed to mix. In that case, which we will refer to as 'central-satellite magnetic equivalence' (see Table 3.6), the J coupling no longer affects the NMR spectrum and a single resonance is expected. This is what is observed for magnetically equivalent spin-1/2 nuclei. For quadrupolar nuclei in the solid state, this special situation can, however, only occur in cubic structures where the EFG is zero at the nuclei.

3.3.3 Numerical Simulations

In realistic cases, it can be understood that there is a partial breaking of central-satellite magnetic equivalence which is induced by the first-order quadrupolar interaction. The central transition of each nucleus, however, remains equivalent with that of the other nucleus, and so do the satellite transitions of the two nuclei, in spin systems which are magnetically equivalent according to the definition of Waugh.[191] It is important however to understand the thresholds for which the spins can be safely assumed to fall into this regime of magnetic equivalence. We have performed numerical simulations of these multiplets for magnetically equivalent spin pairs as a function of the first-order quadrupolar splitting ($\Delta\nu_Q$) which leads to the partial breaking of central-satellite magnetic equivalence. The

calculations were performed using a single crystal with an axially symmetric EFG tensor whose largest component is oriented along the magnetic field such that $\Delta\nu_Q$ is given by:

$$\Delta\nu_Q = \frac{3C_Q}{2S(2S-1)} \quad (3.25)$$

and represents the frequency separation between the different single-quantum transition resonances.

The simulations for a pair of spin-3/2 nuclei are shown in Figure 3.23 where it can be seen that the singlet obtained under strict conditions of central-satellite magnetic equivalence ($\Delta\nu_Q = 0$) rapidly splits into a multiplet with as many as nine resonances as the $\Delta\nu_Q$:J ratio is increased. Two of these resonances disappear at a $\Delta\nu_Q$:3J ratio of 1 to 2 whereas another two converge to form the resonances of the 1:2:2:2:1 pentet for magnetically equivalent spin-3/2 nuclei (top trace of Figure 3.23). Although five resonances are clearly seen with a $\Delta\nu_Q$/6J ratio as low as 5, a properly spaced first-order multiplet is only observed when this ratio is larger than 10.

These simulations show that the first-order A_2 multiplets should nearly always be observed in experimentally relevant cases since a $\Delta\nu_Q$ as small as 6 kHz is large enough to break the central-satellite magnetic equivalence for a J coupling constant of 100 Hz, which is of the expected size for second- and third-row elements with moderate nuclear magnetogyric ratios. The computational results are largely similar for the higher-spin nuclei. Since the value of the quadrupolar splitting is reduced for higher spin nuclei (see eq. 3.25) and the maximum J splittings are also greater (see Figure 3.22), somewhat larger C_Q values are necessary to ensure that first-order A_2 multiplets (in the absence of central-satellite

equivalence) are observed. Generally, if the $\Delta\nu_Q$ is over 100 times the size of the maximum spectral J splitting, then first-order A_2 multiplets will be observed.

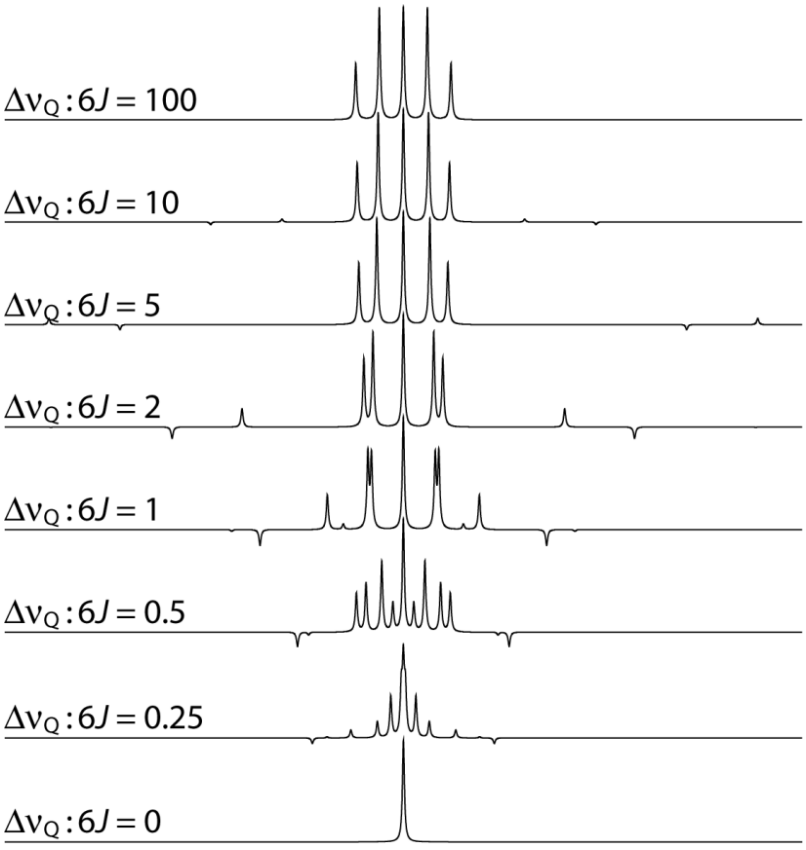

Figure 3.23. Simulated single-crystal CT-only J coupling multiplets for a pair of magnetically equivalent spin-3/2 nuclei are shown as a function of the ratio of the first-order quadrupolar splitting ($\Delta\nu_Q$) to the maximum J splitting ($6J$). For most realistic experimental cases, the ratio will exceed 100 and a simple 1:2:2:2:1 pentet is expected. The bottom trace corresponds to the CS-A_2 case whereas the top trace is the A_2 case. Negative resonances in some of the spectra arise from the ST which are slightly mixed with the CT and thus appear in the spectra calculated with the 'Inc' detection operator.

Some resonances with negative intensities are calculated in some the spectra with small quadrupolar coupling constants. These are ST resonances which aren't completely filtered out by the 'Inc' detection operator due to state mixing. Calculations using the 'Inp' detection operator feature only positive resonances but the multiplets are severely complicated by the overlap of the multiplets from the CT and the STs.

If the spins are chemically equivalent but not magnetically equivalent (i.e., AA'), the satellite transition signals from the two coupled nuclei will appear at different resonance frequencies and thus the satellite transitions behave as if they were non-equivalent. The CT, however, is unaffected by the first-order quadrupolar interaction and will only lose its magnetic equivalence if there are large enough anisotropic second-order quadrupolar effects; note that these are magnetic field dependent and are eliminated by DOR. The splitting for the central states can be expected to remain symmetry-amplified due to the much smaller (or absent) anisotropic second-order quadrupolar effects, whereas the splittings observed for the coupling of a central state to the satellite states will take the form Jm_1m_2. These multiplets for AA' spin systems are also shown in Figure 3.22 along with the multiplets for the A_2 and AX spin systems.

Describing the changeover from the A_2 spin system to the AA' spin system is somewhat more complicated than those from the central-satellite magnetic equivalence spin systems discussed earlier, as it depends on the size of the first-order quadrupolar interaction as well as the *J* coupling and the relative orientation of the EFG tensors. In principle it is the ratio of the difference in quadrupolar splittings ($\Delta\Delta\nu_Q$) between the two nuclei with different tensor orientations to the maximum *J* splitting which dictates the form of the multiplets.

This parameter is calculated as follows in the case of axially symmetric EFG tensors, where β is the angle between the principal component of the EFG tensor and the magnetic field:

$$(3.26)\quad \Delta\Delta\nu_{\mathrm{Q}} = \frac{3C_{\mathrm{Q}}}{4S(2S\text{-}1)} \cdot \Delta(3\cos^2\beta - 1).$$

The changeover from the A_2 to the AA' case is illustrated in Figure 3.24 for a spin-3/2 pair. It is seen that the central and outer resonances of the A_2 pentet, which originate from the coupling to the satellite states, are split and eventually converge to form a doublet with a splitting of 3*J*. This splitting is coincidentally the same splitting as the symmetry-amplified splitting of the central states and thus a doublet is observed. Similar simulations for the larger spin quantum numbers were also performed and, in general, the AA' multiplet is expected when the ratio of $\Delta\Delta\nu_{\mathrm{Q}}$ to the maximum *J* splitting is larger than 100. It is important to note that the second-order quadrupolar interaction was omitted in this case to impose the equivalence of the central states. The simulations are therefore relevant to methods which remove the second-order quadrupolar broadening such as DOR (*vide infra*). Under single-crystal conditions the spectra would typically also be affected with the different chemical shift of the two sites at different crystallite orientations as well as dipolar coupling.

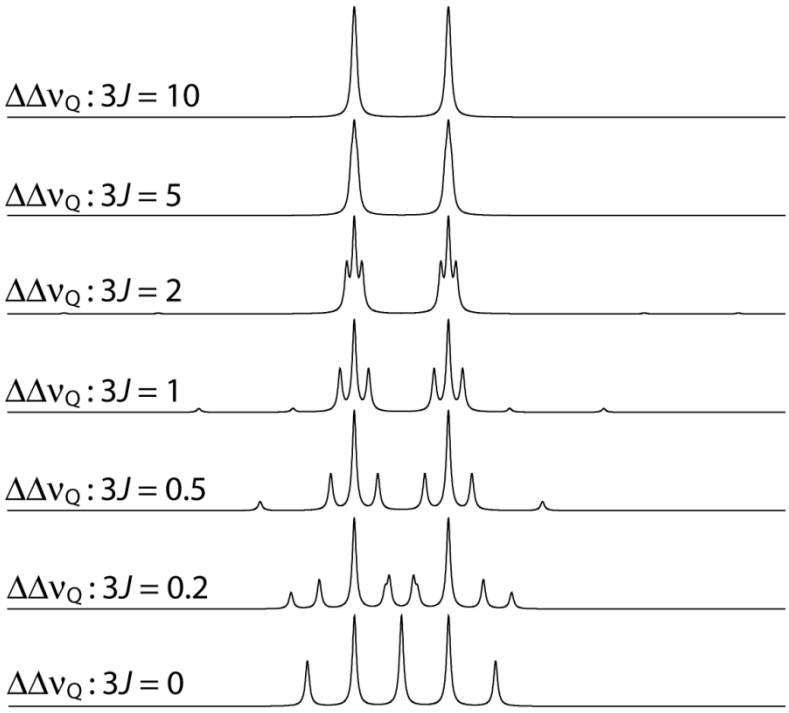

Figure 3.24. Simulated single-crystal CT-only *J* coupling multiplets for a pair of chemically equivalent (AA') spin-3/2 nuclei are shown as a function of the ratio of the difference in quadrupolar splittings ($\Delta\Delta\nu_Q$), induced by different tensor orientations, to the maximum *J* splitting (3*J*). In many realistic experimental cases, the ratio will exceed 10 and a simple splitting of 3*J* is expected. The bottom trace represents the A_2 case.

Using numerical simulations it is also possible to look at the AX to A_2 changeover as was done for spin-1/2 nuclei.[206] Such simulations are shown for spin-3/2 nuclei in Figure 3.25 for limiting cases where the quadrupolar interaction is either zero or non-negligible. It can be seen that for both cases, simple quartets are observed in the AX limit when the ratio of the chemical shift to the maximum *J* splitting is above 100. As the difference in chemical shifts decreases, the familiar 'roofing' effect is observed in each of the doublets; however, the central doublet is much more strongly affected. For the case when C_Q is zero, the

resonances then converge to form a single resonance (Figure 3.25a), as is observed for spin-1/2 nuclei. When the quadrupolar interaction is non-negligible, however, the various doublets are shifted with respect to each other as the chemical shift difference is reduced. The central doublet splitting then becomes amplified to 3*J* at a $\Delta\delta$:3*J* ratio of around 1. As was observed in the AA' case, the peaks attributed to the satellite states converge later than the central states onto the 0 and 6*J* splittings of the A_2 multiplet. Simulations for the higher spin quantum numbers show a similar behavior.

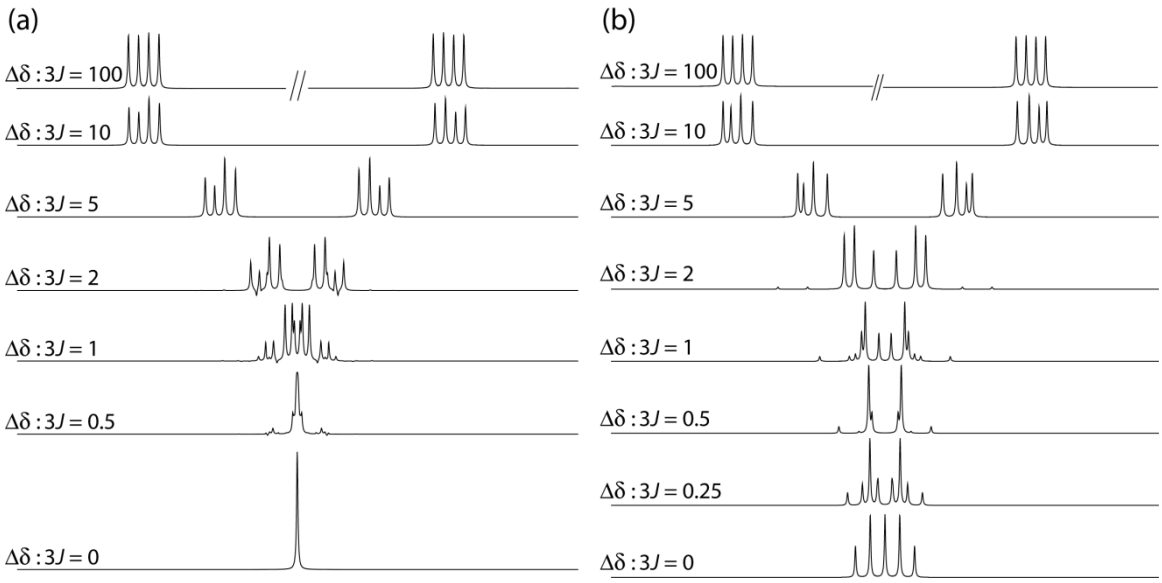

Figure 3.25. Simulated single-crystal CT-only *J* coupling multiplets for a pair of non-equivalent spin-3/2 nuclei (AX) are shown as a function of the ratio of the difference in chemical shifts (Δδ) to the maximum *J* splitting (3*J*). In (a) the case for zero quadrupolar interaction is shown whereas the multiplets in (b) are for nuclei with a non-negligible quadrupolar interaction.

Clearly, the possible forms of the multiplets attributed to *J* coupling in homonuclear spin pairs of quadrupolar nuclei are more diverse than those for their spin-1/2 counterpart

but these ideal multiplets can only be measured in special cases, such as spinning single-crystals, single-crystals with specific orientations, and perhaps in partially aligned media. In powdered solids, the second-order quadrupolar interaction often obscures all fine structure in the NMR spectra under static and MAS conditions. Homonuclear *J* coupling can; however, be observed in DOR NMR experiments. The following section explores the impact of chemical equivalence and other NMR interactions on the spectra obtained from these experiments.

3.3.4 Double-Rotation (DOR) NMR Simulations

In double-rotation NMR, the sample is spun about two angles simultaneously to average the second-order quadrupolar interaction to its isotropic part.[48] The only broadening that remains is that from the spin-spin coupling interactions[207,208] and thus the homonuclear *J* coupling multiplets can be observed in powders.[207]

The individual components of the multiplets however have different dipolar coupling strengths and will be affected differently by the dipolar interaction. Simulations were performed for an idealized spin-3/2 pair, as was mentioned in the computational section, with varying dipolar coupling strength; the typical dipolar coupling constant (R_{DD}) for a diboron spin pair, for example, range from 2.3 to 2.7 kHz. The dipolar coupling tensor was oriented perpendicular to the largest principal components of the EFG tensors, as in B-chlorocatecholborane (see chapter 3.1). It can be seen in Figure 3.26 that dipolar coupling affects the intensities of the various components of the multiplet but does not affect the positions of the resonances. It should then still be possible to accurately measure *J* coupling constants using DOR NMR even when dipolar coupling is present. Additionally, with

proper modelling, it would also be possible to extract the relative orientations of the EFG and dipolar coupling tensors in favourable cases.

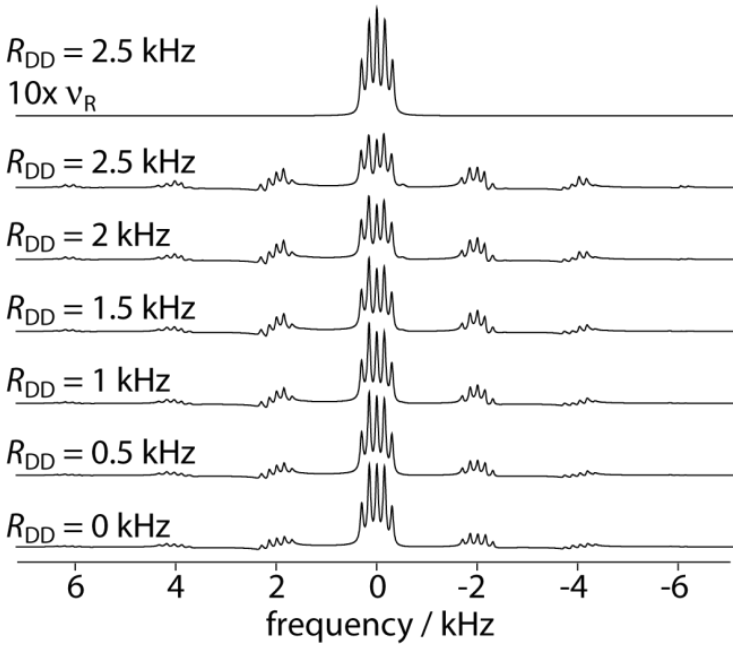

Figure 3.26. Simulated ^{11}B DOR NMR spectra for a pair of magnetically equivalent (A_2) spins are shown as a function of the dipolar coupling constant (R_{DD}). Typical R_{DD} values for a diboron spin pair are of the order of 2.3 to 2.7 kHz. The inner and outer rotor spin rates were of 8 and 2 kHz, respectively, with the exception of the top trace. The rotation frequencies were 10 times larger in the top trace to demonstrate the averaging of the dipolar interaction at higher spinning frequencies.

The DOR multiplets are only visible for A_2 spin pairs if the quadrupolar interaction is non-zero, as the symmetry of the spin states needs to be partially broken. It can be seen in Figure 3.27 that these multiplets are ideal when the quadrupolar interaction is larger than 100 kHz. Numerical simulations may also be used to simulate the DOR NMR spectra in cases when a distorted multiplet is observed because of a small quadrupolar interaction.

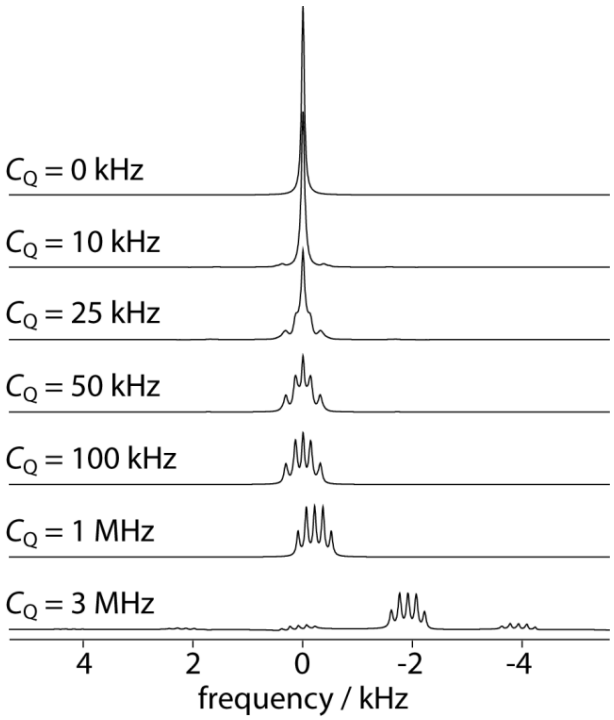

Figure 3.27. Simulated DOR NMR spectra for a pair of magnetically equivalent (A_2) spin-3/2 nuclei are shown as a function of the quadrupolar coupling constant (C_Q). The apparent differences in chemical shift originate from the second-order quadrupole shift. The inner and outer rotor spin rates were of 8 and 2 kHz, respectively.

Simulations were also performed as the orientation between the EFG tensors was modified, to model a pair of chemically equivalent but magnetically inequivalent spin-3/2 nuclei (see Figure 3.28). Clearly, when the angle between the largest principal tensor components (β) is equal to zero, the 1:2:2:2:1 pentet is observed since the spins are magnetically equivalent. This characteristic multiplet is completely lost when the orientation of the EFG tensor orientations differ by as little as 0.25°! With larger deviations, only a single doublet with a splitting of 3J is observed, along with the spinning sidebands. As was mentioned in the previous section, this is caused by the magnetic equivalence of the

CTs but inequivalence of the satellite transitions due to their much larger first-order broadening. Under DOR conditions, all CTs resonate at the same frequencies and can therefore be considered magnetically equivalent. The first-order quadrupolar broadening of the STs is however much larger and the averaging is incomplete at moderate DOR frequencies. This is analogous to the case of chemically-equivalent spin-1/2 nuclei under MAS conditions.[204] Under high-frequency MAS, the spins behave as though they are magnetically equivalent.

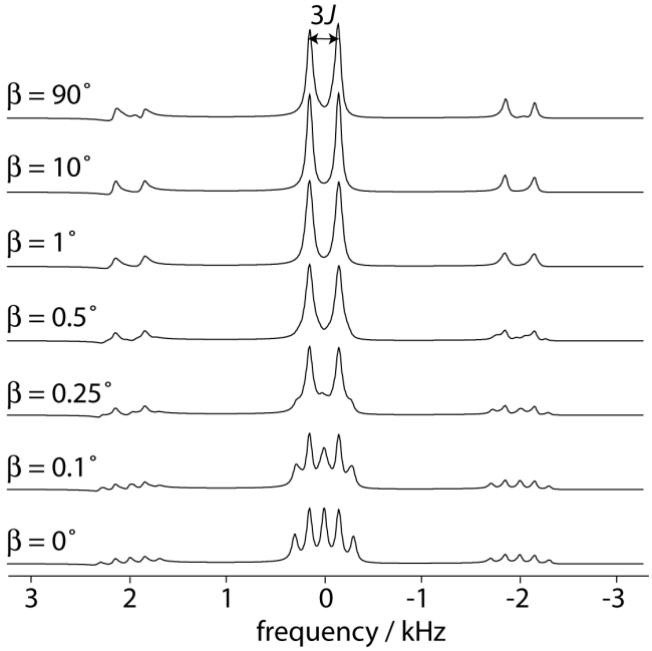

Figure 3.28. Simulated DOR NMR spectra for a pair of chemically equivalent (AA') ^{11}B spins are shown as a function of the relative orientation of the boron EFG tensors. The doublet with a splitting of 3*J* which is expected for an AA' pair is clearly observed when there is even a minute difference in the EFG tensor orientations (~0.5◦). The inner and outer rotor spin rates were of 8 and 2 kHz, respectively. The bottom trace is equivalent to the case of magnetic equivalence (A_2).

The multiplets that are calculated for DOR NMR spectra are identical to those from the single-crystal simulations and thus, DOR NMR spectra can be fit using a simple idealized multiplet. First-order multiplets should be observed using DOR NMR in nearly all cases and the *J* splitting should only disappear for cubic salts where the quadrupolar interaction is exactly zero.

3.3.5 Double-Rotation (DOR) NMR Experiments

3.3.5.1 Bis(catecholato)diboron

Bis(catecholato)diboron (B_2cat_2) is an analogue of BcatCl, BcatBr, and BcatMn which contains a boron-boron bond. It has been previously studied by Brinkmann where no line shape abnormalities were noted.[23] He used ^{11}B-^{11}B double-quantum sidebands in a DQ-SQ correlation experiment to measure the boron bond length with reasonable accuracy. The lack of visible effects of ^{11}B-^{11}B *J* coupling on the MAS NMR spectrum can be understood since the expected 1:2:2:2:1 pentet would have effects comparable to Gaussian or Lorentzian broadening. Similar samples have also been studied using MQMAS NMR where the effects of the *J* coupling are also hardly visible.[42] The DOR NMR spectrum of B_2cat_2 is shown in Figures 3.29a. It can be seen that the DOR centreband is composed of a series of five lines whose intensities, when the sideband intensities are summed, amounts to the expected 1:2:2:2:1 ratios. By fitting this DOR spectrum with a simple multiplet (while also including the effects of heteronuclear RDC to ^{10}B), we were able to extract the value of $|J_{iso}(^{11}B,^{11}B)|$ of 130 ± 20 Hz. The sidebands were not co-added into the centerband as this leads to a loss in resolution, perhaps because of the instability of the double-rotor. As a result, however, the line intensities cannot be perfectly reproduced by our simulation. The ^{11}B MAS NMR

spectrum was then fit while including both the *J* coupling and the quadrupolar broadening; the parameters are summarized in Table 3.8.

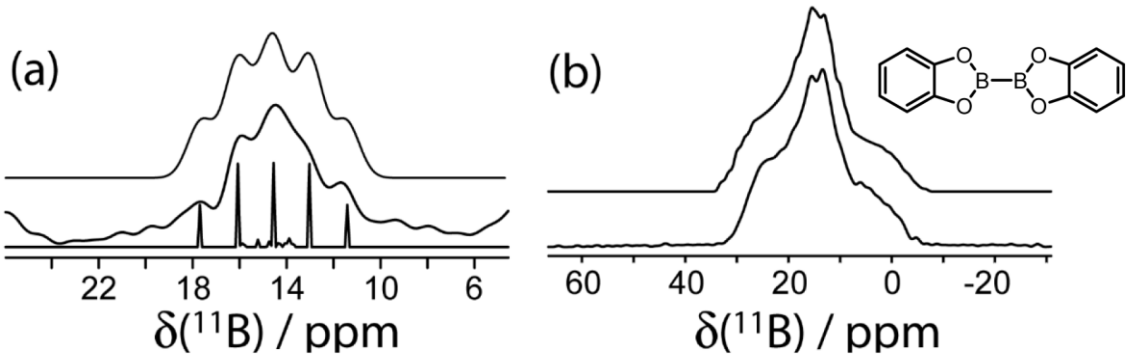

Figure 3.29. ^{11}B NMR spectra of B_2cat_2. In (a) the centerband of the DOR NMR spectrum is shown along with simulations including (top) and excluding (bottom) line broadening. In (b) the MAS spectrum is shown along with its simulation.

Table 3.8. Experimental and computed ^{11}B NMR parameters for B_2cat_2

parameter	experiment	(GI)PAW DFT	TPSS/QZ4P
δ_{iso} / ppm[a]	30.5 ± 1.0	43.8	37.5
$\|C_Q\|$ / MHz	2.85 ± 0.05	3.17	2.83
η	0.85 ± 0.05	0.78	0.78
$\|J_{iso}(^{11}B, ^{11}B)\|$ / Hz	130 ± 20	--	108

[a] The calculated ^{11}B shielding was converted to chemical shift using the absolute shielding scale (σ_{iso} = 110.9 ppm).[59]

The magnetic shielding and EFG tensor parameters were also calculated using cluster based DFT as well as GIPAW DFT. Both methods reproduce the EFG tensor parameters fairly well and they are in better agreement with our experimentally determined values than those previously reported.[23] The value of J_{iso} calculated using cluster-based DFT is found to be positive and of the same order of magnitude as that determined using DOR NMR spectroscopy. These data are also reported in Table 3.8.

3.3.5.2 Dimanganese decacarbonyl

Dimanganese decacarbonyl ($Mn_2(CO)_{10}$) contains two directly bonded manganese atoms with octahedral coordination environments completed by carbonyl ligands, similar to BcatMn. $Mn_2(CO)_{10}$ has previously been studied by NMR under stationary conditions, where the EFG tensor parameters were determined with a high precision.[80] Wi and co-workers have also used MQMAS in order to estimate the value of J_{iso}.[42] As previously mentioned, however, the spectral analysis and interpretation is much simpler in the case of DOR since isotropic *J* coupling multiplets are expected (i.e., no density matrix propagation, no diagonalization, and no powder averaging required). The DOR spectrum is shown in Figures 3.30a where a broadened 'doublet' is observed having a splitting of approximately $5J_{iso}$. A value of $|J_{iso}|$ of 100 ± 20 Hz could be measured, which is within the experimental error of that determined using MQMAS. The MAS NMR spectrum, acquired at 9.4 T, is also shown in Figure 3.30b where the main features of the unusual line shape are reproduced. The simulation parameters are given in Table 3.8.

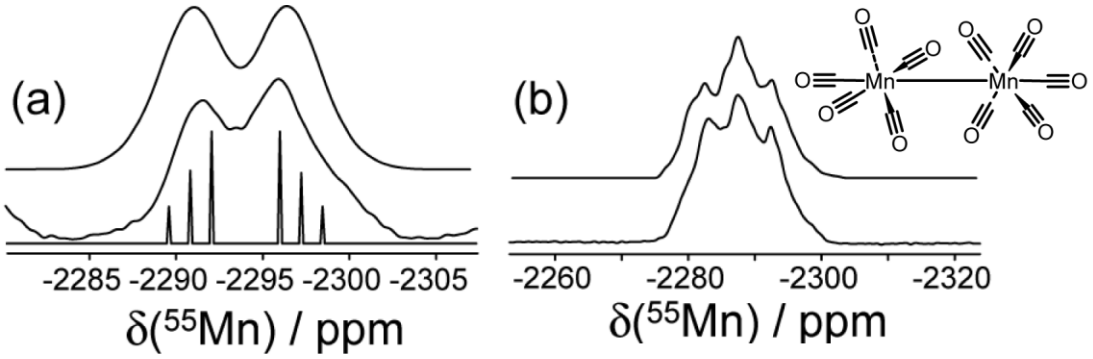

Figure 3.30. ^{55}Mn NMR spectra of $Mn_2(CO)_{10}$. In (a) the centerband of the DOR NMR spectrum is shown along with simulations including (top) and excluding (bottom) line broadening. In (c) the MAS spectrum is shown along with its simulation.

TPSS/QZ4P DFT calculations were also performed on a model of a molecule of $Mn_2(CO)_{10}$. The calculated EFG tensor parameters are in reasonable agreement with those determined experimentally. The J_{iso} value which is calculated is also within the experimental error of the experimentally determined value. All DFT calculated values are listed in Table 3.9 along with the experimental ones.

Table 3.9. Experimental and computed ^{55}Mn NMR parameters for $Mn_2(CO)_{10}$

parameter	experiment	TPSS/QZ4P
δ_{iso} / ppm	-2288 ± 2	--[a]
$\|C_Q\|$ / MHz	3.28 ± 0.05	5.95
η	0.35 ± 0.05	0.66
$\|J_{iso}(^{55}Mn, ^{55}Mn)\|$ / Hz	100 ± 20	90

[a] The ^{55}Mn absolute shielding scale has not been determined.

It is interesting to comment on the potential effects of spin rate-dependent quadrupolar-driven homonuclear dipolar recoupling, also known as n = 0 rotational resonance, in these samples. As discussed by Edén and Frydman,[209] and later by Barrow et al.,[28] the effects of quadrupolar driven recoupling are largest when the spin rate is of the order of the quadrupolar frequency. For the analogous CSA-driven recoupling this criterion is nearly always satisfied;[202,203,204,205] however, for B_2cat_2, the quadrupolar frequency is on the order of several MHz and so quadrupolar-driven dipolar recoupling is expected to be unimportant. It is also known that homonuclear dipolar broadening is much more efficiently suppressed by DOR than MAS and the remaining broadening should then be fairly minor.[210] Additionally, multiple DOR NMR spectra were acquired with variable spinning speeds and the positions of the centerbands remained constant. Finally, in the case of $Mn_2(CO)_{10}$, since the EFG tensors and the dipolar tensor share the same principal axis frame, no quadrupolar-driven dipolar recoupling is expected.[209]

3.3.6 Conclusions

We have outlined the theory for the homonuclear *J* coupling interactions between quadrupolar nuclei. The *J* coupling multiplets that are expected under various conditions for the cases of inequivalent, chemically equivalent, and magnetically equivalent spin pairs have been described. Surprisingly, *J* coupling still affects the NMR spectra in A_2 spin pairs of quadrupolar nuclei, unlike spin-1/2 pairs. The first-order multiplets that are observed for magnetically equivalent quadrupolar spin pairs originate from a partial symmetry breaking caused by the first-order quadrupolar interaction. Using numerical simulations, we have explored the changeovers between each of the four possible first-order situations (AX, AA', A_2, and CS-A_2) and provide thresholds for each of the situations. Generally, the ideal first-order multiplet is observed when the difference in frequency caused by first-order quadrupolar splittings or chemical shifts is 100 times greater than the maximum spectral splitting due to *J*.

We have also used numerical calculations to simulate DOR NMR spectra of homonuclear *J* coupled spin pairs. We found that the DOR NMR spectra closely match those which were calculated for single crystals and that dipolar and quadrupolar interactions have little effect on the resulting spectra under realistic experimental conditions. Experimental DOR NMR spectra from A_2 spin pairs of spin-3/2 and 5/2 nuclei have also been obtained and show the expected multiplet structures. It is then possible to not only measure heteronuclear but also homonuclear *J* coupling between pairs of quadrupolar nuclei if DOR NMR is used to enhance the resolution.

3.3.7 Experimental

3.3.7.1 Solid-State NMR

Samples of B_2cat_2 and $Mn_2(CO)_{10}$ were purchased from Aldrich and were used without further purification. All DOR NMR experiments were performed at 9.4 T using outer-rotor synchronization to remove the odd-ordered sidebands.[57] The ^{11}B DOR NMR experiments were performed using 20 μs CT selective excitation pulses, either 1 or 2 s recycle delays, and either 128 or 256 scans. The ^{55}Mn NMR experiments were performed using a 12.5 μs CT selective excitation pulse, 256 scans, and a 2 s recycle delay.

3.3.7.2 DFT Calculations

The DFT calculations of the NMR parameters were performed using the CASTEP[61] and ADF[64,65] software suites for the (GI)PAW and cluster model DFT calculations, respectively. The PBE exchange-correlation functional[89] was used for the CASTEP calculations along with ultrafine k-point grids, on-the-fly generated ultrasoft pseudopotentials and a 610 eV kinetic energy cutoff. The TPSS/QZ4P[74,203] method was used for the cluster model DFT calculations. In all cases the crystal structures were used as input for the calculations without further optimization.[211,212]

3.3.7.3 Numerical Simulations

All spectral simulations were performed using the SIMPSON program, version 3.1.0, with the exception of the DOR simulations which used version 1.1.2.[126] Calculations of the idealized multiplets were performed using a single crystallite orientation and the quadrupolar interaction was treated using first-order perturbation theory. By using only first-order

quadrupolar effects, the second-order quadrupole broadening is eliminated and the equivalence of the central transition is imposed; this is relevant for fast-spinning DOR NMR experiments. Second-order quadrupole shifts could, in principle, lift the magnetic equivalence of the CT signals for both nuclei in an orientation-dependent way for single crystals, but removing these effects better represents spinning experiments. With this approach it is possible to isolate each individual effect of the multiplets that are, in principle, simultaneously present in an NMR experiment. All calculations were set to detect only the central transition.

Simulations of the DOR experiments were performed for a pair of ^{11}B nuclei at 9.4 T. Typically the quadrupolar coupling constant (C_Q) was set to 3 MHz and the asymmetry parameter (η) to 0.5. Unlike the single-crystal simulations, the second-order quadrupolar interaction was included in these simulations. The DOR simulations were typically performed unsynchronized using a 2 kHz outer rotor spinning frequency and an 8 kHz inner rotor spinning frequency. A 20 kHz spectral window was used and 1024 data points were acquired and apodized using 60 Hz of Lorentzian broadening. All DOR simulations used 66 crystallite orientations and the REPULSION scheme;[213] simulations using a greater number of orientations showed only negligible differences.

Chapter 3.4: Homonuclear *J*-Resolved Experiments for Quadrupolar Nuclei

3.4.1 Introduction

In the previous chapters it has been shown that the *J* coupling between directly bonded quadrupolar nuclei in heteronuclear or homonuclear spin pairs can be measured with the use of high-resolution DOR experiments. In order to perform these experiments it is unfortunately necessary to have highly specialised, non-commercially available, probe hardware. There is then a need to develop techniques to measure spin-spin coupling between quadrupolar nuclei that can be applied using conventional solid-state NMR hardware.

J coupling multiplets are hardly ever resolved in the MAS NMR spectra of spin-1/2 nuclei. These are much more reliably, and accurately, measured with the use of two-dimensional *J*-resolved NMR experiments[214], or spin echo modulation.[215,216] Heteronuclear *J*-resolved experiments have been performed for spin pairs involving a spin-1/2 nucleus and a quadrupolar nucleus;[190] however, attempts to perform such experiments on pairs of quadrupolar nuclei have been met with limited success.[27,28] In a *J*-resolved experiment, chemical shifts (and second-order quadrupolar coupling) are refocused with a 180° radiofrequency pulse. However, if both of the coupled spins are inverted by this pulse, the evolution of the *J* coupling is not perturbed and the spin echo intensity is modulated.[217] For quadrupolar nuclei with significant quadrupole couplings, typically only the central transition (CT, m = 1/2 to -1/2 transition) can be inverted and thus only the *J* coupling

involving two spins in the central states would modulate the spin echo intensity, whereas most of the signal would be perfectly refocused.

3.4.2 Theory

All CTs in an A_2 spin pair, for example, are characterized by $\Delta I = 0$ (I being the total spin of the system). We can then treat a spin system of two homonuclear coupled quadrupolar nuclei of spin S as an ensemble of isolated 'nuclei' with spins of $2S$, $2S$-1…0. The triplet states ($I = 1$) may be represented as a nucleus with a spin of 1. Both transitions involving the triplet states can be associated with the central transitions, and thus all of the transitions are manipulated when using central transition selective pulses. A 90° pulse excites single quantum transitions and the scaled density matrix takes the following form:

$$(3.27)\quad \boldsymbol{\rho}(0) = \begin{bmatrix} 0 & -1 & 0 \\ 1 & 0 & -1 \\ 0 & 1 & 0 \end{bmatrix}.$$

The propagator for evolution under the homonuclear J coupling (assuming that the transmitter is on resonance) is the following:

$$(3.28)\quad \mathbf{U}_J(t) = \exp\begin{bmatrix} \frac{-iJt}{4} & 0 & 0 \\ 0 & \frac{-iJt(4S(S+1)-1)}{8} & 0 \\ 0 & 0 & \frac{-iJt}{4} \end{bmatrix}$$

and the propagator for a 180° pulse is given by

$$(3.29)\quad \mathbf{U}_{180} = \begin{bmatrix} 0 & 0 & -1 \\ 0 & -1 & 0 \\ -1 & 0 & 0 \end{bmatrix}.$$

The density matrix after a spin echo sequence (t/2-180°-t/2) is calculated as:

$$(3.30)\quad \boldsymbol{\rho}(t) = \mathbf{U}_{\mathrm{J}}(t/2)\mathbf{U}_{180}\mathbf{U}_{\mathrm{J}}(t/2)\boldsymbol{\rho}(0)\mathbf{U}_{\mathrm{J}}^{\dagger}(t/2)\mathbf{U}_{180}^{\dagger}\mathbf{U}_{\mathrm{J}}^{\dagger}(t/2)$$

$$(3.31)\quad \boldsymbol{\rho}(t) = \begin{bmatrix} 0 & \exp\left(\frac{iJt(2S+3)(2S-1)}{8}\right) & 0 \\ -\exp\left(\frac{-iJt(2S+3)(2S-1)}{8}\right) & 0 & \exp\left(\frac{-iJt(2S+3)(2S-1)}{8}\right) \\ 0 & -\exp\left(\frac{iJt(2S+3)(2S-1)}{8}\right) & 0 \end{bmatrix}$$

The two single quantum transitions are then modulated as a function of t as

$$(3.32)\quad \cos\left(\frac{Jt(2S+3)(2S-1)}{8}\right) + i\sin\left(\frac{Jt(2S+3)(2S-1)}{8}\right)$$

and

$$(3.33)\quad \cos\left(\frac{Jt(2S+3)(2S-1)}{8}\right) - i\sin\left(\frac{Jt(2S+3)(2S-1)}{8}\right)$$

so that the total signal amplitude is proportional to:

$$(3.34)\quad \cos\left(\frac{Jt(2S+3)(2S-1)}{8}\right).$$

If we now consider the states with total spin I = 2, the initial density matrix, following a CT-selective 90°, pulse is the following, (see Figure 3.31 in chapter 3.3):

$$(3.35)\quad \boldsymbol{\rho}(0) = \begin{bmatrix} 1.5 & -0.5 & 0 & 0 & 0 \\ -0.5 & 1.5 & 0 & 0 & 0 \\ 0 & 0 & 0 & 0 & 0 \\ 0 & 0 & 0 & -1.5 & -0.5 \\ 0 & 0 & 0 & -0.5 & -1.5 \end{bmatrix}.$$

The propagator during free evolution under the J coupling is:

$$(3.36)\quad \mathbf{U}_J(t) = \exp\begin{bmatrix} \frac{iJt(S(S+1)-9/4)}{2} & 0 & 0 & 0 & 0 \\ 0 & \frac{3iJt}{4} & 0 & 0 & 0 \\ 0 & 0 & \frac{9iJt}{4} & 0 & 0 \\ 0 & 0 & 0 & \frac{3iJt}{4} & 0 \\ 0 & 0 & 0 & 0 & \frac{iJt(S(S+1)-9/4)}{2} \end{bmatrix}$$

and that for the CT-selective 180° pulse is:

$$(3.37)\quad \mathbf{U}_{180} = \begin{bmatrix} 0 & -1 & 0 & 0 & 0 \\ 1 & 0 & 0 & 0 & 0 \\ 0 & 0 & 1 & 0 & 0 \\ 0 & 0 & 0 & 0 & -1 \\ 0 & 0 & 0 & 1 & 0 \end{bmatrix}.$$

If we then calculate the signal after a spin-echo sequence,

$$(3.38)\quad \boldsymbol{\rho}(t) = \mathbf{U}_J(t/2)\mathbf{U}_{180}\mathbf{U}_J(t/2)\boldsymbol{\rho}(0)\mathbf{U}_J^{\dagger}(t/2)\mathbf{U}_{180}^{\dagger}\mathbf{U}_J^{\dagger}(t/2),$$

we obtain

$$(3.39)\quad \boldsymbol{\rho}(t) = \begin{bmatrix} 1.5 & -0.5 & 0 & 0 & 0 \\ -0.5 & 1.5 & 0 & 0 & 0 \\ 0 & 0 & 0 & 0 & 0 \\ 0 & 0 & 0 & -1.5 & -0.5 \\ 0 & 0 & 0 & -0.5 & -1.5 \end{bmatrix},$$

which is identical to the density matrix at the start of the experiment. The *J* coupling in these pentet states is then refocused with a CT-selective spin-echo. As the total spin of the states increases, the CT coherences are more greatly isolated. The *J* coupling is refocused for all states with the exception of the triplet states.

The observed spin can be coupled to the 2*S*+1 different states of the other nucleus and only two of these correspond to the central states. As mentioned, only those can become

J modulated when central transition selective pulses are applied. It then follows that only $1/(S+1/2)$ of the central transition signal is *J* modulated, and similarly, only this same fraction can be excited in central transition-selective DQ-SQ correlation experiments. This corresponds to theoretical maximum excitation efficiencies of 50%, 33%, 25%, and 20% for DQ-SQ correlation experiments involving nuclei of spin 3/2, 5/2, 7/2, and 9/2, respectively. In the case of AX spin systems, the effect of the central transition selective spin echo can be described analogously to the spin-1/2 case.[217]

For magnetically equivalent or non-equivalent spin pairs, only a simple doublet is expected in a *J*-resolved experiment involving quadrupolar nuclei since the inversion pulse is CT-selective. For non-equivalent pairs, the splitting would simply equal the *J* coupling constant, as is familiar from NMR experiments on spin-1/2 nuclei. However, if the spins are magnetically equivalent, the splitting would be $(2S + 3)(2S - 1)J/4$, as noted earlier. For spin-1/2 nuclei, this term evaluates to zero and explains the lack of *J* splittings for pairs of magnetically equivalent spins;[218] conversely, we notice that the splitting is amplified for quadrupolar nuclei by factors of 3, 8, 15, and 24 for nuclei of spin 3/2, 5/2, 7/2, and 9/2, respectively. These large scaling factors suggest that very precise *J* coupling constants may be measured with this method and that smaller multiple-bond *J* coupling constants may also be accessible.

3.4.3 DQF-J-Resolved NMR Experiments

3.4.3.1 Pulse Sequences

An experimental demonstration using a ^{55}Mn (S = 5/2) J-resolved experiment on dimanganese decacarbonyl, which contains a Mn-Mn metal-metal bond, is presented in Figure 3.31. The most basic J-resolved experiment (Fig. 3.31a) shows that most of the signal is not J modulated since only 1/(S+1/2) of spins in the triplet states can be used to measure J coupling. The other transitions lead to a strong peak at zero frequency that can completely dominate the weaker J doublet (Fig. 3.31g). The time domain signal shows a strong exponential decay and only a very weak modulation (Fig. 3.31d). This lack of modulation is consistent with previous attempts to perform this experiment in the literature. We have then employed two double-quantum filtered (DQF) J-resolved experiments which use either the J coupling (Fig. 3.31b) or the dipolar coupling (Fig. 3.31c) in order to select the triplet states which are J modulated. DQF J-resolved experiments have also been performed to overcome the low natural abundances of certain isotopes.[219,220] In the first experiment, an INADEQUATE[221,222] block is used to excite the DQ transitions prior to performing the spin echo. In the latter, the recently described $\mathrm{BR2}_2^1\mathrm{BR2}_2^1$ symmetry-based DQ recoupling scheme is used to excite double quantum transitions[223] with COG72(4, 13, 4, 1, 0; 35) phase cycling.[224,225] The use of dipolar coupling, as opposed to J coupling, may be helpful for samples with small J coupling constants as the dipolar coupling may be larger and require shorter DQ excitation times.

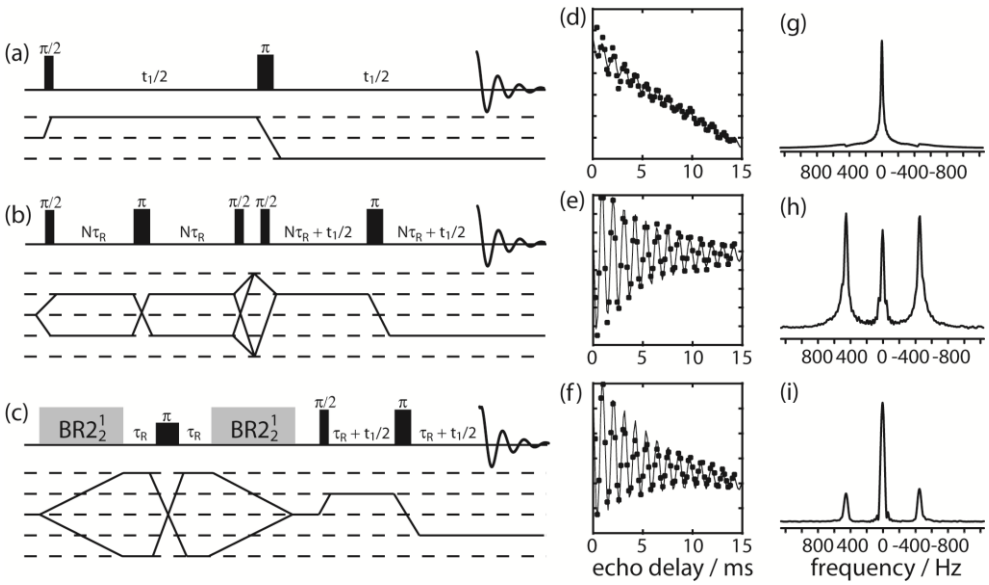

Figure 3.31. *J*-resolved NMR experiments for half-integer spin quadrupolar nuclei. Radiofrequency pulse sequences for the regular, *J*-DQF, and dipolar-DQF *J*-resolved experiments are shown in (a), (b), and (c), respectively; the coherence transfer pathways describing these experiments are shown below the pulse schemes. The modulations of the echo intensities as a function of the echo delay for ^{55}Mn in $Mn_2(CO)_{10}$ subjected to each of the three experiments are shown in (d), (e), and (f), and the Fourier transforms of these signals are shown in (g), (h), and (i).

Both DQF experiments perform well in suppressing the central peak to reveal a well-resolved doublet in the frequency domain and strong cosinusoidal oscillations in the time domain. The intensity of the central peak in Figure 3.31i is larger when compared to that in Figure 3.31h due to intermolecular DQ dipolar recoupling. Importantly, the splitting which we measure is eight times larger than the *J* coupling constant measured using 1D double-rotation (DOR) NMR (see chapter 3.3); this is the expected *J* coupling amplification factor for magnetically equivalent spin-5/2 nuclei. The much sharper lines measured presently,

along with the amplification of the *J* coupling, make it possible to obtain sub-hertz precision ($J(^{55}Mn,^{55}Mn)$ = 113.0 ± 0.5 Hz), nearly two orders of magnitude higher precision than is possible with DOR NMR.

3.4.3.2 Symmetry-Breaking Reaction

The dependence of the observed spectral splitting on the criterion of magnetic equivalence provides a stringent test for the symmetry of molecules, with large, amplified, splittings expected for symmetric molecules imparting magnetic equivalence. To test this hypothesis, we have chemically broken the symmetry of B_2cat_2 using the popular N-heterocyclic carbene (NHC) IMes (see Figure 3.32). This reaction forms an sp^2-sp^3 diboron compound, which are important sources of nucleophilic boron for *β*-boration reactions (see chapter 3.5). In B_2cat_2, the two boron nuclei are magnetically equivalent under conditions of high-power ^1H decoupling. As ^{11}B has a spin of 3/2, we expect to observe a spectral splitting that is approximately three times larger in B_2cat_2 than in B_2cat_2·Imes (where magnetic equivalence is absent) even though the bonding should remain fairly similar. The results of ^{11}B DQF-*J*-resolved experiments on bis(pinacolato)diboron (B_2pin_2), B_2cat_2, and its NHC-complexed analogue, B_2cat_2·Imes, are shown in Figure 3.33. No ^{11}B-^{11}B *J* coupling can be observed in solution for these compounds due to rapid quadrupolar relaxation. Interestingly, the *J* coupling constant is notably smaller in B_2pin_2 ($J(^{11}B,^{11}B)$ = 120 ± 2 Hz) than in B_2cat_2 ($J(^{11}B,^{11}B)$ = 136 ± 1 Hz). This is consistent with the longer B-B bond in B_2pin_2 (1.704 Å)[172] when compared to B_2cat_2 (1.678 Å),[211] and demonstrates the utility of this method in studying molecular structure in diboron complexes as these experiments are rapid, easy to implement, and can be performed on any powdered sample. The *J* coupling constant obtained for B_2cat_2 using the DQF-*J*-resolved experiment is an order of magnitude

more precise than that obtained using DOR NMR, and does not require specialized hardware.

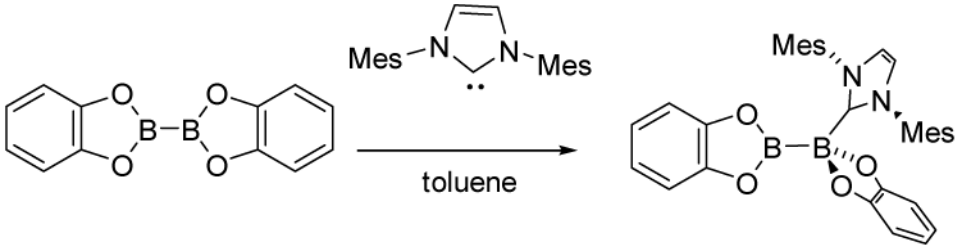

Figure 3.32. Reaction of a diboron compound (B_2cat_2) with an NHC (IMes) to break the molecular and magnetic symmetry.

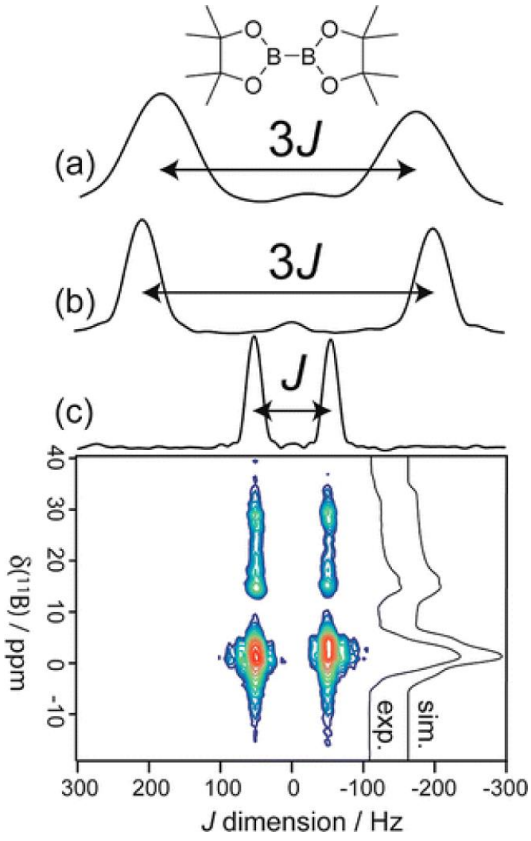

Figure 3.33. *J*-DQF *J*-resolved NMR spectra for B_2pin_2 (a), B_2cat_2 (b), and B_2cat_2·Imes (c) are shown. In (c), the three- and four-coordinate boron peaks are resolved and split by *J*.

In the case of B_2cat_2·Imes, the three- and four-coordinate boron sites are clearly resolved (Fig. 3.33c) and are both split by a common *J* coupling constant of 106.8 ± 0.4 Hz. This unequivocally indicates the presence of a bond between the two boron sites. The observed splitting is notably smaller than that of 408 ± 3Hz in B_2cat_2 and 360 ± 6 Hz in B_2pin_2. This is easily understood, as the *J* splitting is only amplified in the case of magnetically equivalent spin pairs. Upon breaking the symmetry of B_2cat_2 by coordinating it to an NHC, the doublet splitting is equal to *J* as opposed to 3*J*. Since the *J* coupling was found to be smaller in B_2cat_2·Imes when compared to B_2cat_2, weakening of the B-B bond when it is complexed to an NHC has been demonstrated, a feature that is important to the reactivity of such compounds.[226] In the X-ray crystal structure of an analogous B_2pin_2 that is coordinated to an NHC,[227] it is also clear that the B-B bond is weakened (B-B distance of 1.743 Å); however, *J* couplings provide a more rapid approach to characterizing the boron-boron bond, and directly probe the electronic structure of the bond, as opposed to an internuclear distance.

3.4.4 Numerical Simulations of DQF-J-Resolved NMR Experiments

The sensitivity of the splittings measured using DQF-*J*-resolved experiments to the symmetry of the compounds should be determined. An open question concerns whether chemical equivalence will give an amplified splitting, as in DOR, or if a splitting of *J* will be observed. It is also important to investigate the effects of similar chemical shifts and dipolar coupling on the observed multiplets. These situations can be evaluated computationally with the use of numerical simulations of the DQF-*J*-resolved NMR experiments.

In Figure 3.34, simulations of the indirect dimension of a double-quantum filtered *J*-resolved experiment are shown as the chemical shift difference is increased. It can be seen that a simple doublet with a splitting of 3*J* is observed in the magnetically equivalent case, which then increases as the chemical shift difference increases while a doublet with a splitting of *J* begins to appear. In these intermediate cases, the splitting of the outer doublet may be unreliable but the inner doublet would yield the correct *J* coupling constant. These simulations show that fairly large chemical shift differences are necessary in order to observe only a simple doublet with a splitting of *J*. In realistic cases, however, the differences in quadrupolar coupling and tensor orientations between the two coupled nuclei would further break the magnetic equivalence and a single doublet with a splitting if *J* should be observed.

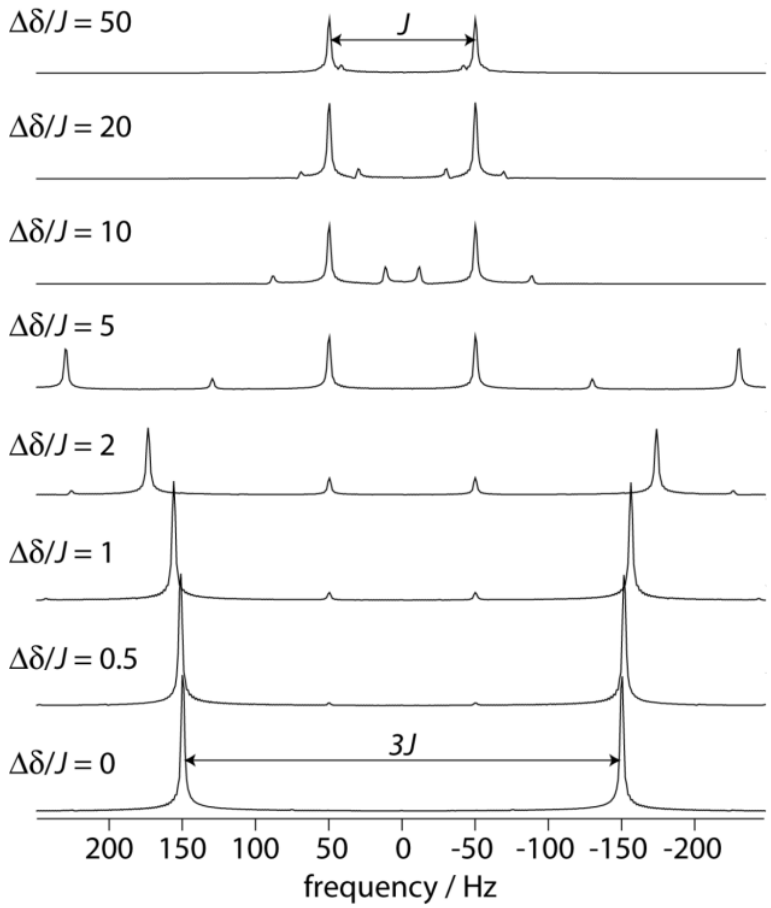

Figure 3.34. The indirect dimension of a 2D DQF-*J*-resolved experiment is shown as a function of the difference in chemical shifts between two spin-3/2 nuclei. C_Q is the same for both nuclei. In the bottom spectrum, the spins are magnetically equivalent (A_2) and the observed splitting is 3*J* whereas when the chemical shift difference is large, the splitting is of *J*, as is expected for an AX spin pair. Experimentally, most realistic cases will correspond to the top or bottom traces.

The effect of including dipolar coupling simply reduces the intensity of the doublet whereas the splitting remains the same. The intensity loss can be regained by increasing the spinning frequency in order to better average the dipolar coupling. Similarly, if the

quadrupolar coupling constant is smaller than 500 times the *J* coupling constant, a significant decrease in the intensity of the doublet is observed (see Figure 3.35).

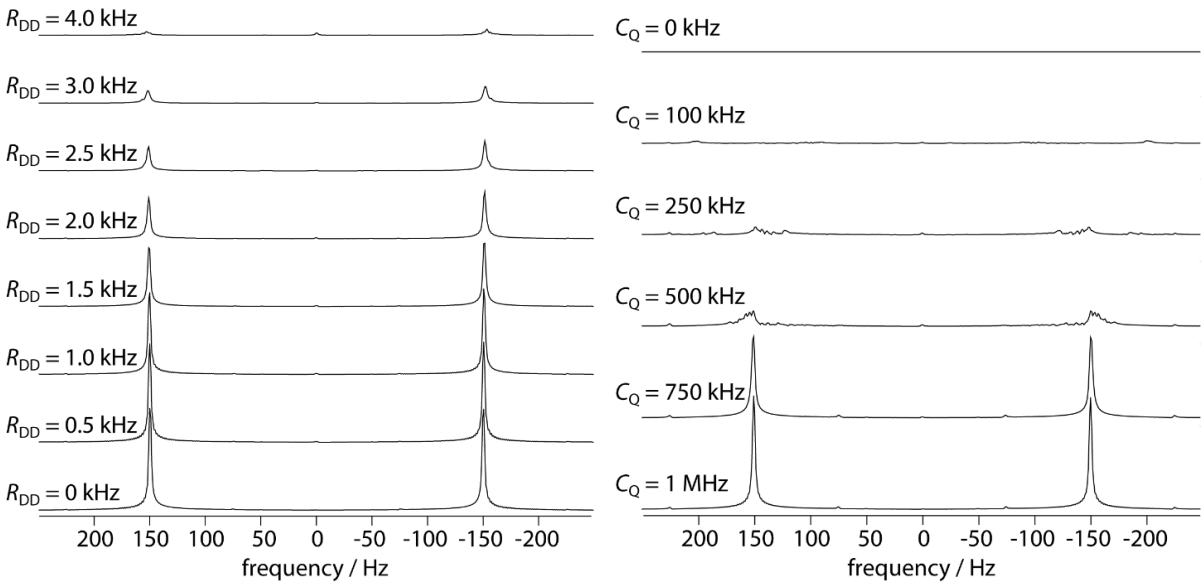

Figure 3.35. The DQF *J*-resolved doublets for a pair of magnetically equivalent ^{11}B nuclei are shown as a function of the dipolar coupling strength (left) and the quadrupolar coupling constant (right). The spinning frequency used for the simulations was 10 kHz. Faster spinning reduces the effects of dipolar coupling.

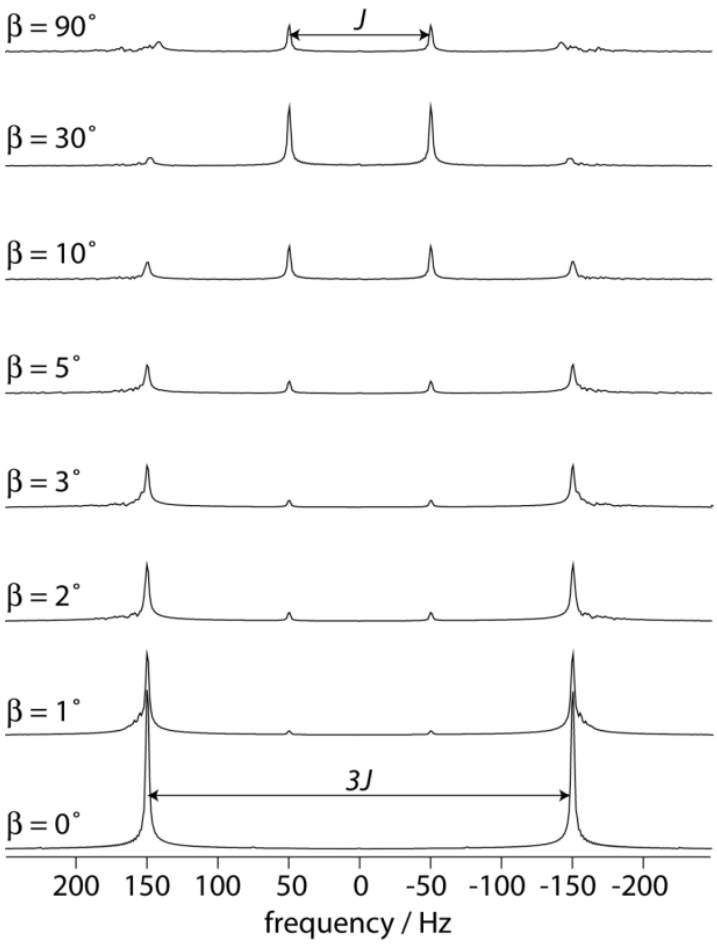

Figure 3.36. The indirect dimension of a 2D DQF-*J*-resolved experiment is shown as a function of the difference in EFG tensor orientations between two chemically equivalent (AA') spin-3/2 nuclei. In the bottom spectrum, the spins are magnetically equivalent (A_2) and the observed splitting is 3*J* whereas when the difference in tensor orientations is large, the splitting is *J*.

If the relative orientation of the EFG tensors is altered to generate a chemically equivalent yet magnetically inequivalent spin pair (Figure 3.36), the outer doublet with a splitting of 3*J* decreases in intensity whereas the doublet with a splitting of *J* increases in intensity. The inner doublet is dominant when the difference between the tensor orientations

is greater than 5° for a typical diboron spin pair. Interestingly, unlike what was seen for DOR NMR (see chapter 3.3), the splitting of the central states does not remain amplified for a chemically equivalent spin pair under *J*-resolved MAS conditions. This difference originates from the second-order quadrupolar broadening which separates the CT signals of the two nuclei to different portions of the MAS powder patterns. Under infinitely fast MAS conditions, the resonance frequencies for the two spins would still differ and they would remain inequivalent. If a *J*-resolved experiment were performed under DOR conditions, or at a higher magnetic field strength so that the second-order quadrupolar interaction is absent, a splitting of 3*J* would be observed.

3.4.5 Impact of Residual Dipolar Coupling

Residual dipolar coupling, which was extensively described in chapter 3.1, can have a profound effect on *J* coupling multiplets when a quadrupolar nucleus is involved. In the heteronuclear case, which also applies to AX homonuclear spin systems, the second-order quadrupolar-dipolar cross-term shifts the resonances according to the spin state of the coupled nucleus as follows:[202,42]

$$\nu_{DD}^{(2)S}(m_{\mathrm{I}}) = \left(\frac{3R_{\mathrm{DD}}C_{\mathrm{Q}}^{\mathrm{I}}}{20\nu_0^{\mathrm{I}}}\right)\left(\frac{I(I+1)-3m_{\mathrm{I}}^2}{I(2I-1)}\right)\left(3\cos^2\beta - 1 + \eta^{\mathrm{I}}\sin^2\beta\cos 2\alpha\right). \quad (3.40)$$

In the expression above, R_{DD} is the dipolar coupling constant, $C_{\mathrm{Q}}^{\mathrm{I}}$ and ν_0^{I} are the quadrupolar coupling constant and Larmor frequency of the coupled nucleus, I is the spin quantum number of that nucleus, m_{I} is the magnetic quantum number of its spin state, η^{I} is its quadrupolar asymmetry parameter and β and α and polar angles relating the orientations of the EFG tensor of I to the dipolar vector.

It can be seen from expression 3.40 that the frequency shifts caused by the second-order quadrupolar-dipolar cross-term (ν_S) only depend on the square of the magnetic quantum number of the coupled nucleus. This is due to the second-order nature of this interaction which will always depend on the absolute magnitude of *m* but not its sign, much like the second-order quadrupolar interaction which is identical for both of the central states. Both components of the *J*-resolved multiplet (which correspond to the 1/2 and -1/2 states of the coupled spin) would then be affected in the same way, to second-order. The effects of the second-order quadrupolar-dipolar cross-term can be further shown to cancel in a *J*-resolved experiment using the density matrix formalism. Since only the CT is manipulated, we can simplify the system by considering only fictitious spin-1/2 nuclei. After a central-transition selective 90° excitation pulse, the density matrix of a two-spin system (considering only the central transition) is proportional to the following:

$$(3.41)\quad \boldsymbol{\rho}(0) = \begin{bmatrix} 0 & -1 & -1 & 0 \\ 1 & 0 & 0 & -1 \\ 1 & 0 & 0 & -1 \\ 0 & 1 & 1 & 0 \end{bmatrix}$$

The propagator for the evolution of the *J* coupling and RDC during a period *t*/2 for a Hahn echo experiment is as follows. Since second-order quadrupolar-dipolar cross-term would affect both components of the doublet equally, due to its second-order nature, the propagator including both *J* coupling and the cross-term (*D*) would have the following form:

$$(3.42)\quad \mathbf{U}_{\mathrm{J+D}}(t/2) = \exp\begin{bmatrix} -i(Jt/8 + D) & 0 & 0 & 0 \\ 0 & iJt/8 & 0 & 0 \\ 0 & 0 & iJt/8 & 0 \\ 0 & 0 & 0 & -(iJt/8 - D) \end{bmatrix}.$$

The propagator for an ideal 180° pulse, calculated as the product of the pulses acting on both nuclei, is as follows.

$$(3.43)\quad \mathbf{U}_{180} = \begin{bmatrix} 0 & 0 & 0 & 1 \\ 0 & 0 & -1 & 0 \\ 0 & -1 & 0 & 0 \\ 1 & 0 & 0 & 0 \end{bmatrix}$$

The density matrix after a spin echo can be calculated using equation 3.30 which gives the following:

$$(3.44)\quad \boldsymbol{\rho}(t) = \begin{bmatrix} 0 & -\exp(-iJt/2) & -\exp(-iJt/2) & 0 \\ \exp(iJt/2) & 0 & 0 & -\exp(iJt/2) \\ \exp(iJt/2) & 0 & 0 & -\exp(iJt/2) \\ 0 & \exp(-iJt/2) & \exp(-iJt/2) & 0 \end{bmatrix}.$$

It is clear from equation 3.44 that there are two components modulated at $\pm J/2$ and a splitting of J would be observed in the frequency domain. The second-order quadrupolar-dipolar cross-term interaction is then fully refocused and would not affect the *J*-resolved spectra of homonuclear *J* coupled quadrupolar nuclei. In a *J*-resolved experiment, the splitting would then always be equal to the *J* coupling constant, or the amplified splitting, even in the presence of a strong quadrupolar interaction.

Interestingly, this conclusion also applies to heteronuclear *J*-resolved experiments[228,229] for which the effects of RDC would be eliminated in the indirect dimension. The effects of isotropic *J* coupling and dipolar coupling can be separated conveniently using either a heteronuclear or homonuclear *J*-resolved experiment. In this respect, the *J*-resolved experiment does have another advantage over DOR NMR, since the

DOR multiplets may become distorted by RDC when the quadrupolar interaction is sufficiently large, but the *J*-resolved splittings remain unaffected. The resolution in a *J*-resolved experiment is also superior since simpler multiplets are measured and the distribution of chemical shifts, the magnetic field inhomogeneity, and the RDC are refocused, thus leading to much sharper resonances.

3.4.6 Static J/D-Resolved Experiments

In many cases, unfortunately, it is not possible to perform MAS experiments on quadrupolar nuclei due to their excessively broad spectral line shapes. In most cases, it is in fact impossible to acquire the whole spectral line shape with a single radiofrequency transmitter offset.[230] This is unfortunately the case for many systems exhibiting metal-metal bonds,[231] for which *J*-resolved experiments would provide an unprecedented experimental insight into the nature of the metal-metal bond, since most metals are quadrupolar.

3.4.6.1 Digallium Compounds

Ga-Ga bonded compounds comprise a particularly interesting class.[232,233] Gallium metal-metal bonded systems have notably demonstrated that the bonding which is observed for the lighter main group elements is not necessarily representative of the heavier elements. For example, compounds featuring non-linear Ga-Ga triple bonds that are weaker than the corresponding double bonds have been prepared.[234-236] Ga-Ga bonded systems also provided the first example of all-metal aromaticity[237,238] and many systems exhibit σ-aromaticity have been prepared.[239,240] The simplest Ga-Ga bonded systems are formed by dissolving gallium dichloride in a coordinating solvent such as dioxane.[241-243] Unlike $GaCl_2$, which has mixed

monovalent and trivalent gallium sites,[244,163] the coordinated gallium dichloride compounds feature divalent Ga-Ga bonded sites; the dioxane salt is often used as a source of Ga(II).

Three Ga-Ga bonded compounds have been prepared, $Ga_2Cl_4(dioxane)_2$, $Ga_2Cl_4(THP)_2$, and $Ga_2Cl_4(THF)_2$; see Figure 3.37. Two polymorphs are known for $Ga_2Cl_4(dioxane)_2$; when it is crystallized at 0°C, it forms dimeric, ethane-like molecules,[241] whereas when it is crystallized at room temperature it forms a polymeric series of 5-coordinate gallium dimers interconnected by dioxane ligands.[243] The crystal structures for the other two compounds are unknown; however, the presence of a Ga-Ga bond has been inferred from Raman spectroscopy for both (ν(Ga-Ga) = 213-258 cm^{-1}).[242] The purity of the compounds was confirmed by Ga and Cl ICP-MS elemental analysis and ^{13}C MAS NMR.

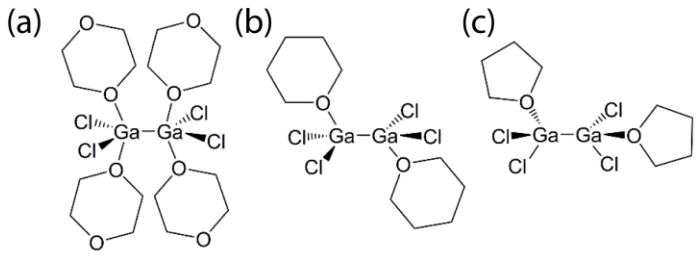

Figure 3.37. Structures of $Ga_2Cl_4(dioxane)_2$ (a), $Ga_2Cl_4(THP)_2$ (b), and $Ga_2Cl_4(THF)_2$ (c).

The ultra-wideline $^{69/71}Ga$ and ^{35}Cl (all are spin-3/2 nuclides) NMR spectra were acquired using the WURST-QCPMG pulse sequence[55] in a magnetic field of 21.1 T (see Figure 3.38). Even at such a high magnetic field strength, the CT NMR spectra span over a megahertz and it was necessary to acquire the full spectra in multiple pieces. The line shapes were simulated exactly using QUEST software (see chapter 3.2) and the simulation parameters are given in Table 3.10.

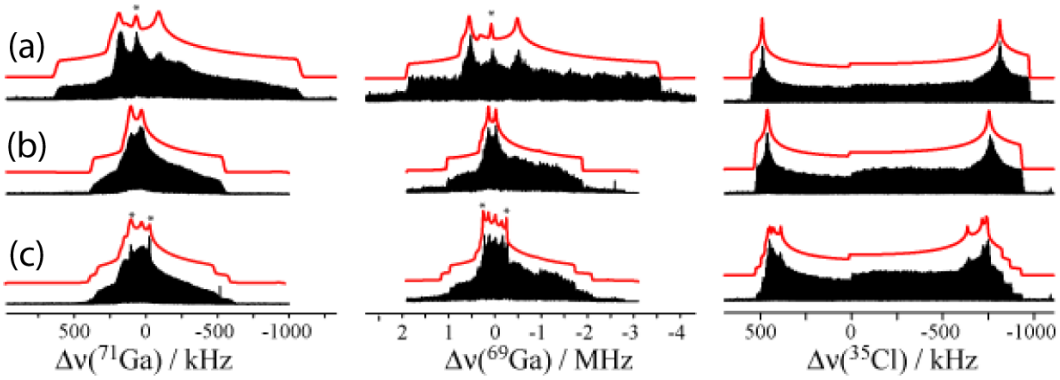

Figure 3.38. ^{71}Ga (left), ^{69}Ga (middle), and ^{35}Cl (right) ultra-wideline WURST-QCPMG NMR spectra (21.1 T) for stationary powdered samples of $Ga_2Cl_4(dioxane)_2$, (a), $Ga_2Cl_4(THP)_2$, (b), and $Ga_2Cl_4(THF)_2$, (c). The experimental spectra are shown in black and the QUEST simulations are overlaid in red. Asterisks denote small impurity resonances.

Table 3.10. ^{71}Ga and ^{35}Cl Chemical Shifts and Quadrupolar Parameters

compound	site	δ_{iso} / ppm	$\lvert C_Q \rvert$ / MHz	η
$Ga_2Cl_4(dioxane)$	Ga	200 ± 50	46.0 ± 0.5	0.75 ± 0.02
	Cl	100 ± 50	31.0 ± 0.1	0.09 ± 0.01
$Ga_2Cl_4(THP)_2$,	Ga	250 ± 50	32.8 ± 0.5	0.90 ± 0.02
	Cl	100 ± 50	30.2 ± 0.1	0.11 ± 0.01
$Ga_2Cl_4(THF)_2$,	Ga1	250 ± 50	35.5 ± 0.5	0.80 ± 0.02
	Ga2	250 ± 50	31.4 ± 0.5	0.90 ± 0.02
	Cl1	100 ± 50	27.4 ± 0.2	0.08 ± 0.02
	Cl2	100 ± 50	28.9 ± 0.2	0.07 ± 0.02
	Cl3	100 ± 50	29.5 ± 0.2	0.08 ± 0.02
	Cl4	100 ± 50	30.1 ± 0.2	0.11 ± 0.02

The gallium chemical shifts for these Ga(II) compounds (200 to 250 ppm) fall between the known ranges for Ga(III) (700 to 0 ppm) and Ga(I) sites (0 to -700 ppm).[163,245-248] We are unaware of any previous reports of $^{69/71}$Ga NMR spectra for diamagnetic Ga(II) compounds. It can also be observed that the quadrupolar interaction at these gallium sites is much larger than what is typically found for Ga(I) or Ga(III) sites.[163,245,249] The C_Q(^{71}Ga) value for $Ga_2Cl_4(dioxane)_2$ is also noticeably larger than the values obtained for

$Ga_2Cl_4(THP)_2$ and $Ga_2Cl_4(THF)_2$, as is also evident qualitatively from the breadth of the powder patterns in Figure 3.38. This is a clear indication that 5-coordinate gallium sites are present in $Ga_2Cl_4(dioxane)_2$, rather than more symmetrical tetrahedrally-coordinated gallium sites. This observation is consistent only with the polymeric polymorph of $Ga_2Cl_4(dioxane)_2$, since the dimeric polymorph features only four-coordinate gallium sites.[241] $Ga_2Cl_4(THP)_2$ and $Ga_2Cl_4(THF)_2$ cannot form such polymeric structures since THP and THF are monodentate ligands; these possess monomeric ethane-like structures and four-coordinate gallium sites.[241] The lower $C_Q(^{71}Ga)$ values for $Ga_2Cl_4(THP)_2$ and $Ga_2Cl_4(THF)_2$ are consistent with such structures.

The $C_Q(^{35}Cl)$ values of 27.4 to 31.0 MHz and near-axial symmetry of the ^{35}Cl EFG tensor ($\eta \approx 0$) are consistent with those of terminal chlorine sites, and are in agreement with the molecular structures drawn in Figure 3.37.[163] It was also possible to resolve four separate low-frequency edges in the ^{35}Cl NMR spectrum of $Ga_2Cl_4(THF)_2$, indicating that the four chlorine sites in the molecule are crystallographically inequivalent. This compound also has two inequivalent gallium sites, as seen in the $^{69/71}Ga$ NMR spectra. Due to the symmetry of $Ga_2Cl_4(dioxane)_2$, only a single gallium and chlorine site are expected; however, it is surprising that there is only a single gallium and chlorine site observed for $Ga_2Cl_4(THP)_2$ since its dioxane analogue, whose crystal structure is known,[241] does not have any particular symmetry.

3.4.6.2 Shifted Echo J/D-Resolved Experiment

While the above spectral analyses provide useful coordination information, they do not provide any direct insight into the Ga-Ga bond. It is however known that valuable,

unambiguous information about the crystallographic symmetry of a molecule can be obtained from homonuclear *J*-resolved MAS NMR experiments on quadrupolar spin pairs (*vide supra*). However, such MAS experiments cannot be performed in cases when the quadrupolar interaction results in CT powder patterns spanning more than the available MAS rate (MHz vs tens of kHz). Unfortunately, those are precisely the cases encountered for the vast majority of quadrupolar metal isotopes of interest. In those general cases, one is limited to performing NMR experiments on stationary powder samples[230] for which 2D NMR experiments are impractical or atypical. We have designed a shifted-echo 2-pulse *J/D*-resolved NMR experiment which can be used to obtain 2D NMR spectra for samples which yield ultra-wideline one-dimensional NMR spectra (see Figure 3.39). Since there is no double-quantum filter, the *J/D*-resolved spectra will always feature a large peak at zero frequency which originates from ^{71}Ga sites coupled to ^{69}Ga, a satellite transition of ^{71}Ga, or a crystallite in a part of the powder pattern that is outside the bandwidth pulses. The use of a simple two-pulse experiment, however, has a greater sensitivity, a wider excitation bandwidth, and greater resolution since the shifted echo ensures that purely absorptive line shapes are obtained.

Both the *J* and dipolar coupling interactions affect the *J/D*-resolved NMR spectra. The modulation frequency in the indirect dimension is given by $\pm(J/2 + d/2)$ when the sites are magnetically inequivalent (AX or AA' spin system) and $\pm(3J/2 - 3d/2)$ when the sites are magnetically equivalent (A_2 spin system). The dipolar modulation strength ($d = -R_{eff}(3\cos^2\theta - 1)$) depends on the angle between the Ga-Ga bond and the applied magnetic field (θ) and the effective dipolar coupling constant ($R_{eff} = R_{DD} - \Delta J/3$, where R_{DD} is the dipolar coupling constant and ΔJ is the anisotropy of the *J* coupling tensor). Simulated *J*/*D*-resolved NMR

spectra are shown in Figure 3.39 for the AX and A_2 cases. In addition to showing clear spectral splittings of *J* or 3*J*, respectively, it can also be seen that the sense of the Pake-like powder patterns comprising each component of the doublet are reversed in A_2 spin systems, providing an additional handle on the symmetry of the system. With this simple 2D NMR approach, evidence for metal-metal bonding, information regarding the crystal symmetry, and insight into the electronic structure of the bond can be obtained simultaneously. This approach is also more sensitive, general, and easier to implement and interpret than other methods designed to measure dipolar coupling between quadrupolar nuclei such as symmetry-based recoupling[23,24] and R^3.[22,250]

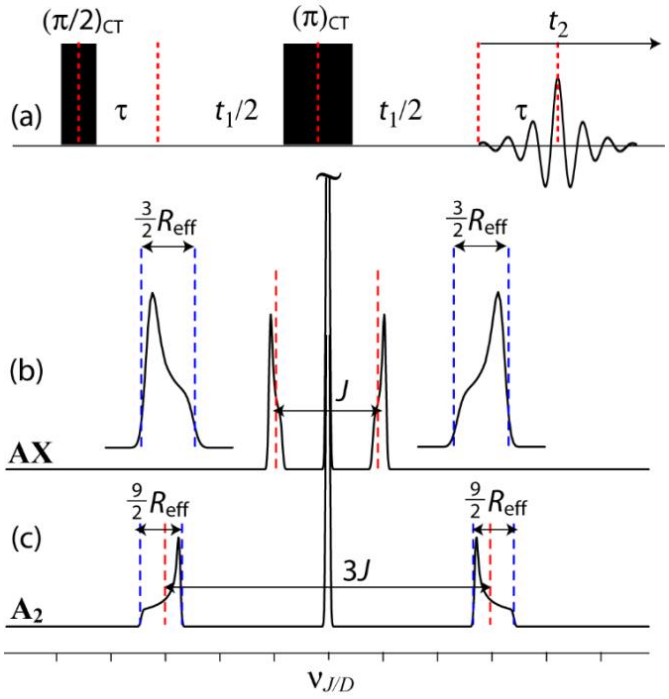

Figure 3.39. Shifted-echo *J*/*D*-resolved NMR pulse sequence (a) and the resulting theoretical spectra for the AX (b) and A_2 (c) cases. Note the inversion of the sense of the line shapes in the AX compared to the A_2 case. Insets in (b) are enlarged to clearly show the line shapes.

We have performed ^{71}Ga *J/D*-resolved NMR experiments on the digallium compounds, and the resulting spectra are shown in Figure 3.40. Due to the limited bandwidth of the square rf pulses, the 2D experiments are performed on only a single piece of the powder pattern (i.e., a single transmitter offset); the fact that the experiments can be done in this way opens the door to examining *J* couplings involving nuclei with enormous quadrupolar interactions. In all cases, the central part of the powder pattern with the highest intensity was used. Some spectra at various offsets were also acquired for $Ga_2Cl_4(THF)_2$ and were found to be consistent with the one displayed in Figure 3.40. It can be seen that for $Ga_2Cl_4(THP)_2$, the splitting is greatly amplified when compared to the other two samples. It is unreasonable to conclude that the larger splitting is caused by a much larger *J* coupling in this sample due to the structural similarity of the compounds. The key evidence which proves that the larger splitting observed for $Ga_2Cl_4(THP)_2$ must be 3*J* and not *J* is that the powder patterns are oriented as required for the A_2 case. The sense of the powder patterns for $Ga_2Cl_4(dioxane)_2$ and $Ga_2Cl_4(THF)_2$ are as expected for an AX or AA' spin system. It can then be concluded that the gallium sites in $Ga_2Cl_4(THP)_2$ are magnetically equivalent and that the molecule must have an inversion center. Although the Ga sites in $Ga_2Cl_4(dioxane)_2$ are related by two C_2 axes,[241] they do not share the same tensor orientations and they comprise an AA' spin system for which the splitting is not amplified.

The *J/D*-resolved NMR experiment therefore not only establishes the ethane-like structure of $Ga_2Cl_4(THP)_2$, whose crystal structure is unknown, but also makes it possible to determine that the molecule must adopt a staggered conformation with an inversion center, as depicted in Figure 3.37. This conclusion is also in agreement with the single ^{35}Cl, $^{69/71}$Ga, and ^{13}C resonances that were observed, consistent with high symmetry. We can also

conclude that the molecular conformation of $Ga_2Cl_4(THF)_2$ is eclipsed, as in the $Ga_2Cl_4(dioxane)_2$ dimer polymorph,[241] since there is no inversion symmetry and there are two distinct gallium sites and four distinct chlorine sites.

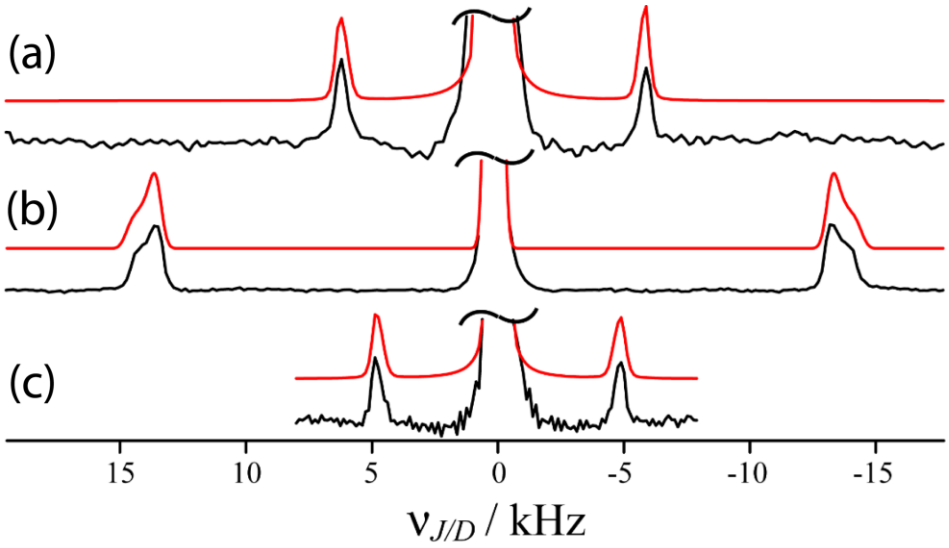

Figure 3.40. *J/D*-resolved ^{71}Ga NMR spectra for $Ga_2Cl_4(dioxane)_2$, (a), $Ga_2Cl_4(THP)_2$, (b), and $Ga_2Cl_4(THF)_2$, (c) (stationary powdered samples; B_0 = 21.1 T). The experimental spectra are in black and the simulations are shown in red. The peak at zero frequency is truncated for clarity

The measured *J* coupling constants (listed in Table 3.11) are significantly larger than the direct dipolar coupling constants (~800 Hz) for digallium compounds.[241] The magnitude of $J(^{71}Ga,^{71}Ga)$ is also well reproduced by hybrid DFT calculations (Table 3.11). It is interesting to also note that the *J* coupling for $Ga_2Cl_4(dioxane)_2$ is significantly larger than for $Ga_2Cl_4(THP)_2$ and $Ga_2Cl_4(THF)_2$, indicating that $J(^{71}Ga,^{71}Ga)$ is very sensitive to the geometry and electronic structure of the Ga-Ga bond.

Table 3.11. $J(^{71}Ga,^{71}Ga)$ Coupling Constants

compound	J_{iso}^{expt} / kHz	J_{iso}^{B3LYP} / kHz	ΔJ^{expt} / kHz[a]	ΔJ^{B3LYP} / kHz
$Ga_2Cl_4(dioxane)_2$	12.0 ± 0.3	10.42	1.5 ± 0.7	1.21
$Ga_2Cl_4(THP)_2$	9.2 ± 0.1	8.10	1.5 ± 0.2	1.18
$Ga_2Cl_4(THF)_2$	9.6 ± 0.3	8.13	1.5 ± 0.7	1.18

[a] These values assume a R_{DD} value of 800 Hz.

The DFT calculations also showed that the *J*(Ga,Ga) coupling mostly originates from the Ga-Ga σ-bonding natural localized molecular orbital (NLMO)[251]. The measured *J* coupling can then be taken as a direct probe of this particular orbital. The DFT calculations also predict a lower NBO orbital energy (by 0.036 a.u.) for the Ga-Ga bond in $Ga_2Cl_4(dioxane)_2$ when compared to the other samples. This method could be used to characterize a wide range of different bonding modes since the $J(^{71}Ga,^{71}Ga)$ values can be related to the DFT energy of the Ga-Ga bond.

By fitting the fine structure of the *J/D*-resolved spectra, which is most evident for $Ga_2Cl_4(THP)_2$, it is possible to extract an effective dipolar coupling constant of 300 Hz, which is significantly smaller than the expected dipolar coupling constant of 800 ± 50 Hz (from diffraction studies).[241] The difference is attributed to an anisotropic *J* coupling of 1.5 kHz. This is only the third Δ*J* value to be determined for a pair of quadrupolar nuclei using NMR, and the first for a homonuclear spin pair.[71] The value is well reproduced using DFT calculations (see Table 3.11). In the case of lighter coupled nuclei, where Δ*J* is much smaller than R_{DD}, the R_{eff} values measured would provide internuclear distance information.

3.4.7 Conclusions

In this chapter it has been shown that homonuclear *J* coupling between quadrupolar nuclei can be measured with the use of *J*-resolved experiments. Several specially tailored pulse sequences have been developed to measure *J* coupling between half-integer

quadrupolar nuclei. The importance of using either a *J*-based or a dipolar-based double-quantum filter to remove non-modulated signals from spins coupled to the satellite transitions of the other nucleus is demonstrated. These DQF-*J*-resolved experiments provide hardware advantages over the use of 1D DOR experiments and also enable a much simpler spectral analysis since only a single doublet is expected for every spin pair. Additionally, the splitting is amplified in the case of magnetic equivalence, providing a direct experimental probe of the symmetry of the molecule. The amplification of the *J*-splittings also enables the measurement of smaller *J* coupling values, and possibly probe *J* coupling between quadrupolar nuclei across multiple intervening bonds. These experiments hold promise for studying dimetallic and dimetalloid coordination environments, a common motif in inorganic complexes. More generally, the method provides a rapid and direct approach to probe homonuclear bonding interactions in powdered solids.

It has also been demonstrated that *J/D*-resolved experiments can also be performed on nuclei exhibiting very large quadrupolar interactions, for which the spectra qualify as 'ultra-wideline', if the 2D experiment is performed using only a single piece of the powder pattern. This has been applied to studying compounds with gallium-gallium metal-metal bonding interactions exhibiting *J* and dipolar coupling interactions which are four and five orders of magnitude smaller than the quadrupolar interaction, respectively. The value of $J(^{71}\mathrm{Ga},^{71}\mathrm{Ga})$ is also shown to be a direct probe of the metal-metal bond strength with the use of a NLMO analysis. This method is expected to be quite general and can be applied to study a wide array of metal-metal bonded systems for which the *J* coupling was believed to be inaccessible due to the sheer magnitude of the quadrupolar interaction. This work also shows that samples yielding ultra-wide one-dimensional NMR spectra are amenable to two-

dimensional experiments that could yield valuable heteronuclear and homonuclear proximity information in, for example, metal-organic frameworks and heterogeneous catalysts.

3.4.8 Experimental

3.4.8.1 Sample Preparation

All procedures used standard Schlenk and glovebox techniques. $GaCl_2$ and B_2cat_2 were purchased from Aldrich and IMes and B_2pin_2 were purchased from Strem Chemicals; all were used without further purification. B_2cat_2·Imes was prepared by dissolving 78.1 mg of B_2cat_2 and 100.0 mg of Imes in 5 mL of dry toluene and mixing it for two hours under an inert atmosphere. B_2cat_2·Imes was isolated as a fine precipitate which was decanted, washed with a small amount of cold toluene, and dried under vacuum. The purity of the compound was determined using ^{13}C CPMAS NMR and ^{11}B MAS NMR, where no traces of the starting materials were observed. To prepare the digallium compounds, 400 mg of $GaCl_2$ was placed in a Schlenk flask that was cooled with liquid nitrogen, and an excess of the desired ligand was then added to the flask using a cannula. The solvent was then allowed to slowly thaw while stirring until a clear, colourless, solution was obtained. The excess ligand was then removed *in vacuo* to yield the desired compound, of the form $Ga_2Cl_4L_2$, where L is THF, THP, or dioxane, as a white powder. The sample purity was confirmed with the use of gallium and chlorine ICP-MS elemental analysis.

All powdered samples were tightly packed into 4 mm o.d. ZrO_2 rotors under inert conditions. NMR experiments were performed at an applied magnetic field of 9.4 T or 21.1 T using Bruker AVANCE III 400 and AVANCE II 900 NMR spectrometers equipped with a

triple resonance 4 mm MAS probe. SPINAL-64 decoupling[88] was used during both the acquisition and evolution periods in all protonated samples.

3.4.8.2 ^{55}Mn NMR

The ^{55}Mn NMR experiments were all performed under 10 kHz MAS with the use of 25 μs central transition selective 90° pulses and 50 μs central transition selective 180° pulses (i.e., rf power of 3.3 kHz).

The regular *J*-resolved experiment was performed using 72 t_1 increments of 400 μs (2.5 kHz spectral window). 64 transients were acquired for each slice with a recycle delay of 1 s.

The *J*-based DQF *J*-resolved spectrum was acquired using a total double-quantum excitation and reconversion period of eight rotor cycles. 2048 transients were acquired for each of the 72 t_1 increments and a 0.5 s recycle delay was used.

The dipolar-based DQF *J*-resolved spectrum was acquired using two $\mathrm{BR2}_2^1$ recoupling cycles (eight rotor cycles for both the excitation and reconversion periods) and thus the total DQF period lasted ten rotor cycles. 1440 scans were acquired for each of the 72 t_1 increments and a 0.5 s recycle delay was used. A second spectrum was acquired using four $\mathrm{BR2}_2^1$ cycles as opposed to two. Since the peak at zero frequency grew in this spectrum, it is likely that it originates from intermolecular dipolar recoupling.

The *J*-resolved spectra are processed in magnitude mode. Apparent distortions are caused by the tail of the non-modulated signal.

3.4.8.3 ^{11}B NMR

The ^{11}B *J*-based DQF *J*-resolved experiments were all performed using 20 μs central transition selective 90° pulses and 40 μs central transition selective 180° pulses (i.e. rf power of 6.25 kHz) and a 2 s recycle delay. For B_2cat_2, 15 kHz MAS was used and the total double quantum excitation and reconversion time was 36 rotor cycles. 768 transients were acquired for each of the 24 t_1 increments of 1.33 ms. For B_2pin_2, 13.5 kHz MAS was used and the total double quantum excitation and reconversion time was 24 rotor cycles. In this case, the sample was cooled to 0°C to increase the T_2. 384 transients were acquired for each of the 16 t_1 increments of 740 μs. For B_2cat_2·Imes, 12.5 kHz MAS was used and the total double quantum excitation and reconversion time was 88 rotor cycles. 320 transients were acquired for each of the 40 t_1 increments of 1.6 ms.

3.4.8.4 ^{35}Cl NMR

All ^{35}Cl solid-state NMR experiments were performed using the 21.1 T magnet at the National Ultra-High Field NMR Facility for Solids in Ottawa ($\nu_0(^{35}Cl)$ = 88.2 MHz) using a Bruker AVANCE II spectrometer and a 4 mm double-resonance static probe. The WURST-QCPMG pulse sequence[55] was used with ^{1}H decoupling using 50 μs WURST-80 pulses sweeping 2 MHz. 24 echoes were acquired with a spikelet separation of 5 kHz. Typically 3 pieces, each acquired with 1024 scans and a recycle delay of 0.5 s, were necessary to record the entire powder pattern.

3.4.8.5 $^{69/71}$Ga NMR

All $^{69/71}$Ga solid-state NMR experiments were performed using the 21.1 T magnet at the National Ultra-High Field NMR Facility for Solids in Ottawa ($\nu_0(^{69}Ga)$ = 216.0 MHz and

$\nu_0(^{71}Ga)$ = 274.5 MHz) using a Bruker AVANCE II spectrometer and a 4 mm double-resonance static probe. The WURST-QCPMG pulse sequence was used with ^{1}H decoupling using 50 μs WURST-80 pulses sweeping 2 MHz. Typically, for ^{71}Ga, 3 pieces, each acquired with 1024 scans and a recycle delay of 0.5 s, were necessary to record the entire powder pattern. In the case of ^{69}Ga, 2048 scans were acquired for each of the 6 subspectra with a recycle delay of 0.5 s.

The *J/D*-resolved spectra were acquired using the pulse sequence described in the main text using 1 and 2 μs CT-selective 90° and 180° pulses, respectively. 36 to 128 t_1 increments of either 12.5 or 31.25 μs were used to acquire the *J/D* spectra. 512 to 1024 scans were acquired for each of the t_1 increments using a recycle delay of 0.5 s. In all cases the echo was shifted by 15 μs for the phase-sensitive acquisition.

3.4.8.6 Density Functional Theory

All DFT calculations were performed using the Amsterdam Density Functional program[64] (ver. 2009) with the B3LYP hybrid DFT functional[171,172] and the TZP basis set.[203] The revPBE GGA functional[252] was used in the case of the NLMO analysis due to the lower computational cost. The molecular structure of $Ga_2Cl_4(dioxane)_2$ from its single-crystal X-ray diffraction structure was used as input whereas DFT-optimized structures were used in the case of $Ga_2Cl_4(THP)_2$ and $Ga_2Cl_4(THF)_2$. The NLMO decomposition[251] of the *J* coupling calculations was performed using the NBO 5.0 program[253] that is implemented within ADF.

3.4.8.7 Numerical Simulations of J-Resolved Experiments

All spectral simulations were performed using the SIMPSON program, version 3.1.0.[126] Simulations of double-quantum filtered *J*-resolved experiments were performed for a pair of ^{11}B nuclei at 9.4 T. Typically the quadrupolar coupling constant (C_Q) was set to 3 MHz and the asymmetry parameter (η) to 0.5.

Simulations of the *J*-resolved experiments were performed using 10 kHz MAS spinning, 30 and 60 μs CT-selective 90° and 180° pulses, respectively, and 232 crystallite orientations according to the ZCW scheme.[254-256] The *J*-DQF pulse sequence previously published was employed with a total double-quantum filtration time of 40 rotor cycles. 256 data points were acquired with a 1 ms t_1 increment. The data were apodized using 15 Hz of Gaussian broadening and processed in magnitude mode.

Chapter 3.5: *J*-Resolved NMR Spectroscopy of Diboron Compounds

3.5.1 Introduction

Much work is currently being done on the development of novel diboron reagents for use in *β*-boration reactions. [226,257-268] The *β*-boration reaction involves the attack of a nucleophilic boron site, from a diboron compound, onto an electron deficient alkene to form a C-B bond (see Figure 3.41). The organoboron compounds that can then be formed are of tremendous synthetic use since the C-B bond can be easily converted to C-X, C-O, C-N, and even C-C bonds (using Suzuki-type cross-coupling reactions).[269]

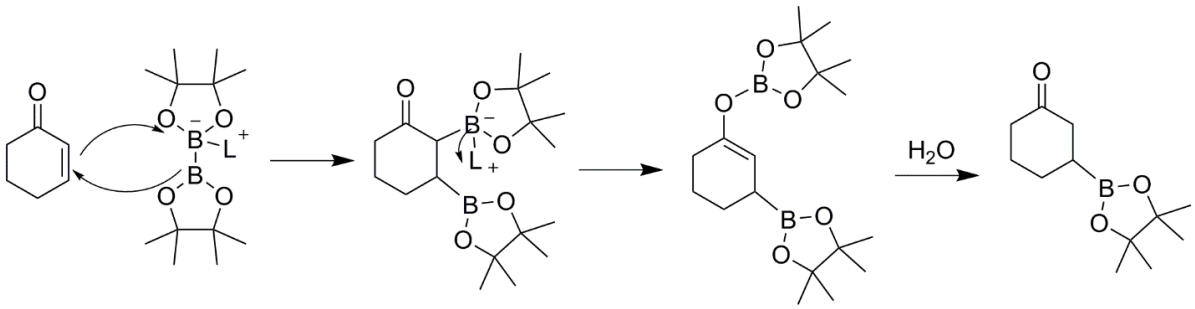

Figure 3.41. A schematic representation of the mechanism for the *β*-boration reaction involving an sp^2-sp^3 hybridized diboron compound and an *α,β*-unsaturated ketone.

These reactions are typically performed using a metal catalyst, however strategies are being developed in order to form these valuable species in a metal-free way. For example, several groups have shown that the formation of a mixed sp^2-sp^3 diboron species substantially increases the reactivity.[226,258,259] This is attributed to the electron donation of the additional group on the sp^3-hybridised boron site which weakens the B-B bond and also

induces a polarization of the bond that increases the nucleophilicity of the reactive sp^2-hybridised boron site.[226,258] Recent studies also show that there is also much to learn concerning the reactivity of diboron systems whose chemistry is fairly unexplored.[270-272]

Much of the reactivity of the diboron reagents is attributed to the nature of the boron-boron bond; namely its strength and polarization. The recently-developed solid-state NMR experiments that were described in chapter 3.4 may well be of use for gaining experimental insight into the nature of the boron-boron bond in these species in order to better understand their reactivity.

In this chapter, we report on DQF *J*-resolved solid-state NMR measurements of the $J(^{11}B,^{11}B)$ coupling constants in a series of diboron compounds in order to provide direct information on the B-B bond. Via density functional theory (DFT) calculations we decompose the *J* coupling into various natural bond orbital (NBO) and natural localised molecular orbital (NLMO) contributions[251] and determine which structural and electronic factors contribute to the $J(^{11}B,^{11}B)$ values. The sensitivity of $J(^{11}B,^{11}B)$ to structure and symmetry is then leveraged as a screening technique to probe the nature of the B-B bond in a mixture of diboron reagents. Several ^{11}B-^{11}B *J* coupling constants ranging from 9 to 151 Hz have been measured either directly, or through its effects on the ^{1}H NMR spectra, for various boranes in solution. These splittings are, however, rarely resolved for diboron compounds due to rapid quadrupolar relaxation.[273,274]

The compounds investigated in this chapter, B_2cat_2, B_2pin_2, B_2cat_2·IMes, tetrahydroxy diboron ($B_2(OH)_4$), pinacolato bis(2-hydroxypropyl)amino diboron (LB_2pin), tetrakis(pyrrolidino) diborane (B_2pyr_4), [bis(catecholato)diboron]·picoline (B_2cat_2·pic), and

[bis(catecholato)diboron]·dipicoline ($B_2cat_2{\cdot}pic_2$), are shown in Figure 3.42. Some proof-of-principle experiments on three of these samples have been reported in the previous chapter. B_2cat_2,[211] B_2pin_2,[260] and $B_2(OH)_4$[275] are sp^2-sp^2 diboron compounds with oxygen ligands. $B_2cat_2{\cdot}$IMes represents an intermediate in an NHC-catalysed β-boration reaction.[226] LB_2pin is a mixed sp^2-sp^3 diboron reagent designed for copper-catalysed β-boration reactions.[258,261] B_2pyr_4 features nitrogen ligands[276] as opposed to oxygen ligands, and compounds $B_2cat_2{\cdot}pic$ and $B_2cat_2{\cdot}pic_2$, along with B_2cat_2, form a series of compounds produced by a sequential addition of 4-picoline ligands.[277] Finally, 9-BBN, a popular hydroboration reagent, was also investigated due to its dimer structure[278] in order to determine whether it is possible to measure $J(^{11}B,^{11}B)$ across multiple intervening bonds.

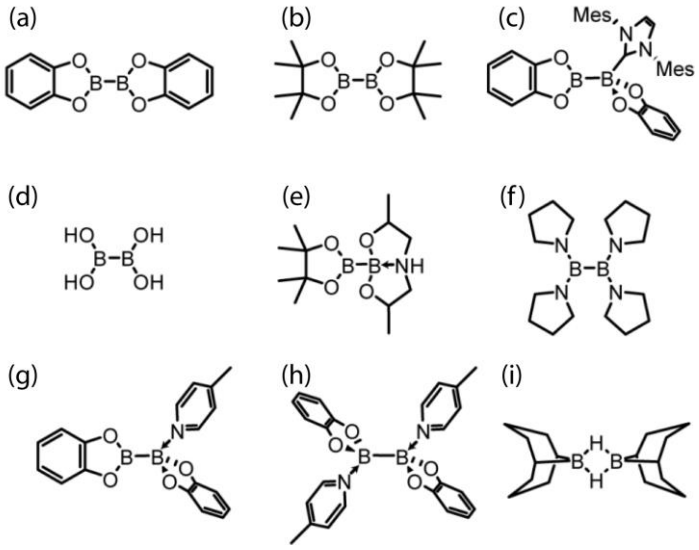

Figure 3.42. Scheme depicting the molecular structures of B_2cat_2 (a), B_2pin_2 (b), $B_2cat_2{\cdot}$IMes (c), $B_2(OH)_4$ (d), LB_2pin (e), B_2pyr_4 (f), $B_2cat_2{\cdot}pic$ (g), $B_2cat_2{\cdot}pic_2$ (h), and 9-BBN (i).

3.5.2 Boron-11 Quadrupolar Interactions and Chemical Shifts

The ^{11}B MAS NMR spectra of $B_2(OH)_4$, LB_2pin, B_2pyr_4, $B_2cat_2 \cdot pic$, and 9-BBN are shown in Figure 3.43. A ^{11}B multiple-quantum magic-angle spinning (MQMAS) NMR spectrum[279] of B_2pyr_4 is also shown, in which the two distinct boron sites are spectrally resolved. This is in agreement with the single-crystal X-ray structure that features two crystallographically distinct boron sites.[276] The parameters used for the simulations are given in Table 3.12. Generally, as can be expected, the three- and four-coordinate boron sites can be easily distinguished on the basis of their NMR parameters.[280] The spectra are affected by the electric quadrupolar interaction between the electric field gradient (EFG) tensor at the nucleus and the electric quadrupole moment of the nucleus (Q) as well as the isotropic chemical shift (δ_{iso}). The quadrupolar interaction is typically parameterised using the quadrupolar coupling constant (C_Q) and the asymmetry parameter (η) which describe the magnitude and axial asymmetry of the EFG tensor, respectively. The four-coordinate boron sites are more shielded, having isotropic chemical shifts ranging from 1 to 11.0 ppm whereas the three-coordinate boron sites have chemical shifts of 29.5 to 35.2 ppm. As can be also expected, the C_Q values are much smaller for the four-coordinate boron sites (< 2.2 MHz) than for the three-coordinate boron sites (2.7 to 3.2 MHz) due to the higher tetrahedral symmetry of the former.

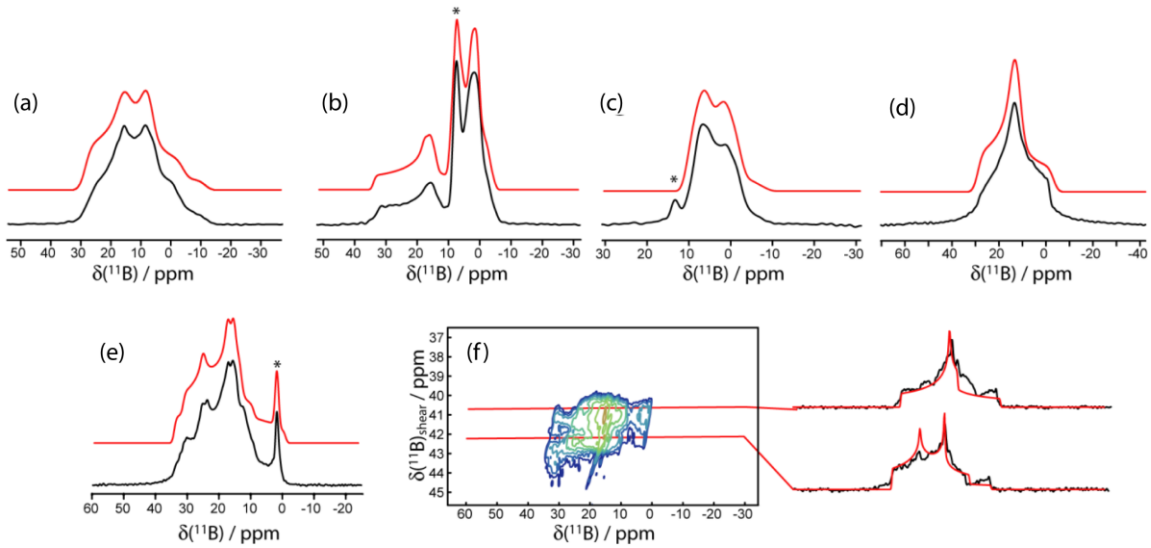

Figure 3.43. ^{11}B MAS NMR spectra of $B_2(OH)_4$ (a), LB_2pin (b), B_2pyr_4 (c), B_2cat_2·pic (d), and 9-BBN (e) acquired at 9.4 T using a Hahn echo sequence. The MQMAS NMR spectrum of B_2pyr_4, including slices along the isotropic dimension, is also shown in (f). In all cases the experimental spectra are in black and the simulations are in red. An asterisk denotes an impurity. A slight upwards tilt in the MQMAS spectrum of B_2pyr_4 is observed which is caused by the second-order quadrupolar-dipolar cross term interaction between ^{11}B nuclei and the ^{14}N and ^{11}B nuclei.[42]

It can also be observed that upon the formation of a sp^3-boron site by the coordination of a ligand to compounds B_2cat_2 and B_2pin_2 (i.e. B_2cat_2·IMes and LB_2pin) there is a noticeable increase in the quadrupolar coupling constant and asymmetry parameter of the remaining three-coordinate boron site (i.e., the chemically active site in β-boration reactions). This site has maintained all of the same direct bonding interactions with its neighbouring atoms; however, a non-negligible change in C_Q of 200 kHz is observed. This change is in agreement with the model of Hoveyda, whereby the binding of an additional

ligand on one of the boron atoms polarises the B-B bond and induces a larger positive charge on the resulting four-coordinate boron center.[226] The increase in the asymmetry parameter originates from the increase in the intermediate V_{22} EFG tensor component which is calculated to be aligned along the B-B bond vector (*vide infra*). Since the sum of the EFG tensor components is always zero, the increase in $|V_{22}|$ is seen here to also increase $|V_{33}|$, which is manifested in an increase in the magnitude of the quadrupolar coupling constant.

Table 3.12. ^{11}B NMR parameters for the diboron compounds studied in this work

compound	δ_{iso} / ppm	C_Q / MHz	η
B_2cat_2	30.5 ± 0.5	2.85 ± 0.05	0.85 ± 0.05
B_2pin_2	31.5 ± 0.5	2.70 ± 0.05	0.85 ± 0.1
B_2cat_2·Imes (site 1)	1 ± 1[a]	N/A[a]	N/A[a]
B_2cat_2·Imes (site 2)	34 ± 1	2.9 ± 0.1	0.90 ± 0.05
$B_2(OH)_4$	29.5 ± 1.0	3.2 ± 0.1	0.58 ± 0.05
LB_2pin (site 1)	7.0 ± 0.5	(-)1.7 ± 0.1	0.7 ± 0.1
LB_2pin (site 2)	34 ± 1	2.9 ± 0.1	0.90 ± 0.05
B_2pyr_4 (site 1)	31.2 ± 0.5	2.7 ± 0.1	1.00 ± 0.05
B_2pyr_4 (site 2)	35.2 ± 0.5	2.9 ± 0.1	0.50 ± 0.08
B_2cat_2·pic_2	11.0 ± 0.5	(-)2.2 ± 0.05	0.15 ± 0.10
9-BBN	29 ± 1	(-)2.7 ± 0.1	1.00 ± 0.15

[a] No anisotropic line shape was observed.

The impact of an additional ligand (see the structures of B_2cat_2·Imes and LB_2pin in Figure 3.42) is also evident from the deshielding of the three-coordinate ^{11}B resonances (by 3 to 4 ppm). The mechanism explaining this deshielding of the three-coordinate boron site has been well described for boronic acids and originates from a decrease of the smallest magnetic shielding tensor component caused by the interaction of ligand MOs with the unoccupied boron *p* orbital.[281]

DFT calculations of the magnetic shielding and EFG tensors have been performed for these samples. Both cluster-based calculations, using a single molecule of the substance as input, and gauge-including projector-augmented wave (GIPAW) calculations,[61,63,282,283]

using the published crystal structures as input,[211,260,261,275,276,277,278] have been performed. The chemical shifts and the EFG tensor components are both well-reproduced using both methods (see Figure 3.44). The cluster-based calculations reproduce the experimental EFG tensor components better (slope of 1.02) than the PAW calculations, which systematically overestimate the EFG tensor components, as was previously mentioned in chapter 2.1 (slope of 1.13). This overestimation has been hypothesized to originate from molecular motions that would decrease the experimental C_Q values;[284] however, since the cluster-based calculations reproduce the EFG tensor components quantitatively, the overestimation likely originates from the use of a frozen core approximation within PAW. Conversely, the chemical shifts are better reproduced by the GIPAW DFT calculations than by the cluster-based calculations (see Figure 3.44). The plot correlating the calculated magnetic shielding with the experimental chemical shifts has a slope of -0.94 with GIPAW and -0.82 with cluster-based calculations; perfect agreement would give a slope of -1. Since not all compounds could be included in the GIPAW DFT calculations, due to the lack of a crystal structure, it may be premature to state that GIPAW DFT calculations better reproduce the ^{11}B chemical shifts.

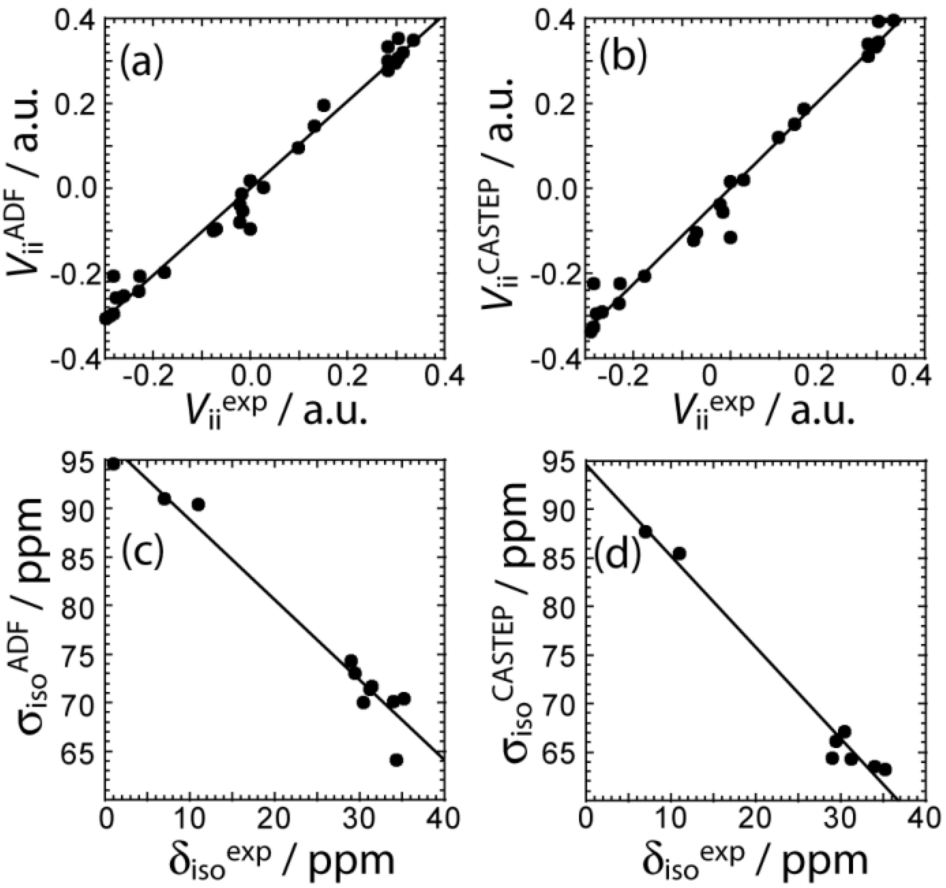

Figure 3.44. Correlations between the experimental EFG tensor components and the calculated ones using (a) cluster model DFT ($V_{ii}^{ADF} = 1.02V_{ii}^{exp}$, $R = 0.990$) and (c) PAW DFT ($V_{ii}^{CASTEP} = 1.13V_{ii}^{exp}$, $R = 0.989$) are shown. The correlations between the experimental chemical shifts and the calculated magnetic shielding constants using (c) cluster model DFT ($\sigma_{iso}^{ADF} = -0.825\delta_{iso}^{exp} + 97.0$ ppm, $R = 0.980$) or (d) GIPAW DFT ($\sigma_{iso}^{CASTEP} = -0.941\delta_{iso}^{exp} + 94.6$ ppm, $R = 0.988$) are shown.

3.5.3 Boron-Boron J Coupling Constants

^{11}B *J*-resolved NMR experiments using a *J*-based double-quantum filter have been performed on all of the samples in Figure 3.42. The *J*-resolved spectra are shown in Figure 3.45 and the $J(^{11}B,^{11}B)$ values are listed in Table 3.13. The *J*-resolved spectra for compounds B_2cat_2, B_2pin_2, $B_2(OH)_4$, and $B_2cat_2 \cdot pico_2$ have noticeably larger splittings than the other compounds (see Figure 3.45). This originates from a symmetry-amplified *J* splitting effect which is present when the two nuclei are magnetically equivalent; for spin-3/2 nuclei such as ^{11}B, the amplification factor is 3 (see Figure 3.45). The spin states associated with the quadrupolar central transition in these compounds are mixed which leads to a larger splitting in a *J*-resolved experiment. This splitting is amplified whereas the actual *J* coupling constant is not. Once this effect is taken into consideration, it can be seen that all diboron systems have similar *J* coupling constants ranging from 136 to 98 Hz. Knowledge about either the molecular structure or the expected magnitude of the coupling constant is, unfortunately, necessary in order to determine whether or not the *J* splitting is amplified. We note that amplifications of the *J* splittings are also observed in MQMAS NMR spectra, however; this is due to the detection of mixed single and triple quantum coherences.[285]

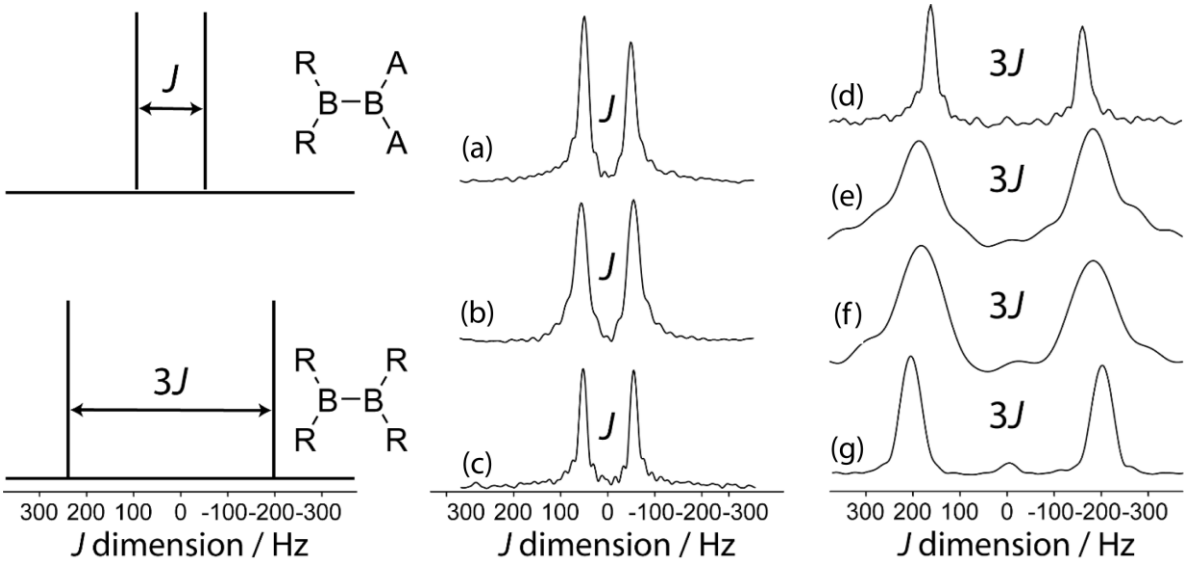

Figure 3.45. On the left a schematic representation of the result of a ^{11}B DQF-*J*-resolved NMR experiment on a molecule wherein the boron atoms are not related by a crystallographic inversion centre (top) and a molecule wherein the boron atoms are related by crystallographic inversion symmetry (bottom) is shown. The symmetry in the bottom diboron system leads to an amplification of the *J* splitting (but not the coupling constant itself) by a factor of 3. Slices of the indirect dimension of the ^{11}B DQF-*J*-resolved NMR experiments carried out on the diboron compounds B_2pyr_4 (a), LB_2pin (b), $B_2cat_2{\cdot}IMes$ (c), $B_2cat_2{\cdot}pic_2$ (d), $B_2(OH)_4$ (e), B_2pin_2 (f), and B_2cat_2 (g) are shown. The spectra for the species that do not exhibit magnetic equivalence are shown in the middle and those corresponding to molecules with a center of inversion are shown on the right.

Table 3.13. $J(^{11}B,^{11}B)$ coupling constants for the compounds in Figure 3.42 extracted using ^{11}B DQF-*J*-resolved NMR

compound	$J(^{11}B,^{11}B)$ / Hz
B_2cat_2	136 ± 1
B_2pin_2	120 ± 2
B_2cat_2·Imes	106.8 ± 0.6
$B_2(OH)_4$	121 ± 3
LB_2pin	111 ± 3
B_2pyr_4	98 ± 2
B_2cat_2·pic	115 ± 4
B_2cat_2·pic_2	108 ± 1
9-BBN	(-)10 ± 7

When the reaction of B_2cat_2 with 4-picoline, intended to form B_2cat_2·pic_2, is halted prematurely,[277] some of the B_2cat_2 will not have reacted and some will have ligated to one 4-picoline molecule as opposed to two, giving B_2cat_2·pic. Spectra of the resulting mixture provides a striking example of the excellent resolution which can be obtained in *J*-resolved experiments since the linewidth is governed by the spin-spin relaxation time constant (see chapter 3.4). A *J*-resolved spectrum of the reaction mixture extracted before the reaction was completed is shown in Figure 3.46. It can be clearly seen that the symmetry-amplified doublet signals from B_2cat_2 and B_2cat_2·pic_2 are present along with a smaller, unamplified doublet. The latter doublet can be attributed to B_2cat_2·pic where only a single 4-picoline molecule has complexed to B_2cat_2. The doublet splitting is smaller due to the absence of an inversion center relating the two boron sites in the crystal structure.

It is interesting to comment on the tremendous spectral resolution which can be obtained for quadrupolar nuclei in powders using DQF-*J*-resolved spectroscopy. In some cases, the resolution that can be achieved surpasses that which could be obtained using DOR NMR (see chapter 3.3) or MQMAS NMR, for which the line widths are about an order of

magnitude larger for these compounds.[42] This is in part due to the fact that the DQF *J*-resolved NMR experiment is insensitive to residual dipolar interaction (to ^{11}B and ^{14}N, for example),[42] unlike DOR (see chapter 3.1) and MQMAS[40,41,42] and thus leads to narrower resonances. It is also interesting to notice that the *J* coupling constant steadily decreases from B_2cat_2 to $B_2cat_2 \cdot pic$ and $B_2cat_2 \cdot pic_2$ with the addition of each 4-picoline ligand, which correlates with a lengthening of the B-B bond.[277] However, the spectral splitting greatly decreases when a single 4-picoline molecule is added, and then greatly increases when the second is added, since the inversion symmetry of the crystal is reinstated (see Figure 3.42).[277] Thus, the NMR method not only provides excellent resolution of the mixture of compounds, but also gives direct evidence for the presence or absence of crystallographic inversion symmetry. Since the optimal double-quantum filter time depends on the *J* splitting and the samples have differing spin-spin relaxation time, this experiment is not quantitative. If the DQF efficiency was modeled numerically (as done in chapter 3.4 for example), or determined using pure forms of the different compounds, the various components of the mixture could be quantified.

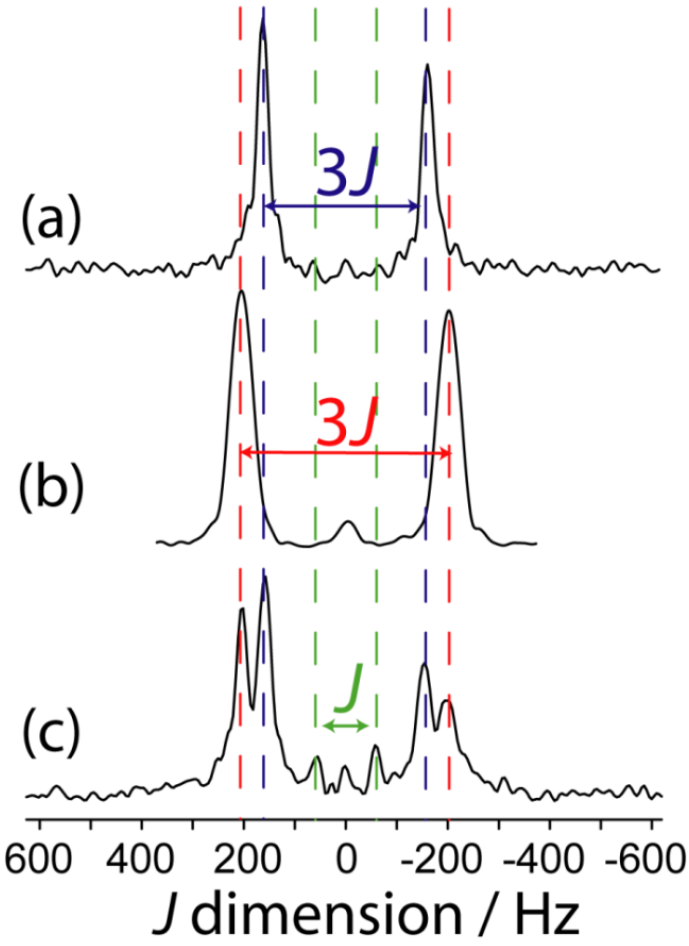

Figure 3.46. Slices of the indirect dimension of ^{11}B DQF-*J*-resolved NMR spectra for (a) $B_2cat_2 \cdot pic_2$, (b) B_2cat_2, and a reactive mixture containing B_2cat_2, $B_2cat_2 \cdot pic$, and $B_2cat_2 \cdot pic_2$, as marked by the colour-coded dashed lines.

The *J*-resolved spectrum for the symmetric compound B_2pyr_4 may be puzzling at first since the *J*-splitting is not amplified (splitting of $J = 98 \pm 2$ Hz). Diboron compounds with oxygen ligands prefer planar structures due to the stabilising effect of π delocalisation.[286] Diboron compounds with nitrogen ligands, however, have much weaker π delocalisation stabilisation energies and stronger hyperconjugation interactions.[286] That, combined with steric repulsion, means a staggered structure is often preferred in these

systems.[287,288] The crystalline structure of B_2pyr_4 shows that it has a N-B-B-N dihedral angle of 76.4°. The two boron nuclei are not related by an inversion center and the splitting in the DQF-*J*-resolved spectrum therefore is given by *J* rather than 3*J*.

3.5.3.1 NBO/NLMO Analysis of J Coupling

To gain a greater understanding of the factors that contribute to the $J(^{11}B,^{11}B)$ values we have analysed the *J* coupling in terms of natural bond orbitals (NBO)[289] and natural localised molecular orbitals (NLMO)[251,290] using the NBO 5.0 code[253] implemented in the Amsterdam Density Functional (ADF) software.[64] NBOs are a set of very localized (strictly 1- to 3-centered) high-occupancy orbitals whereas the NLMOs are expansions of the NBOs that include the longer range effects. The boron-boron σ-bonding NLMOs for the diboron compounds are shown in Figure 3.47. It can be seen that in the cases of the sp^2-sp^3 hybridized diboron compounds as well as with B_2pyr_4 the NLMO is skewed towards the sp^2 hybridized center. This effect is caused by a hyperconjugation interaction between the B-L bonding orbitals and the empty *p* orbital of the boron center. Such a hyperconjugation interaction would affect the strength of the boron-boron bond, however, it is unclear whether this can be detected using NMR spectroscopy.

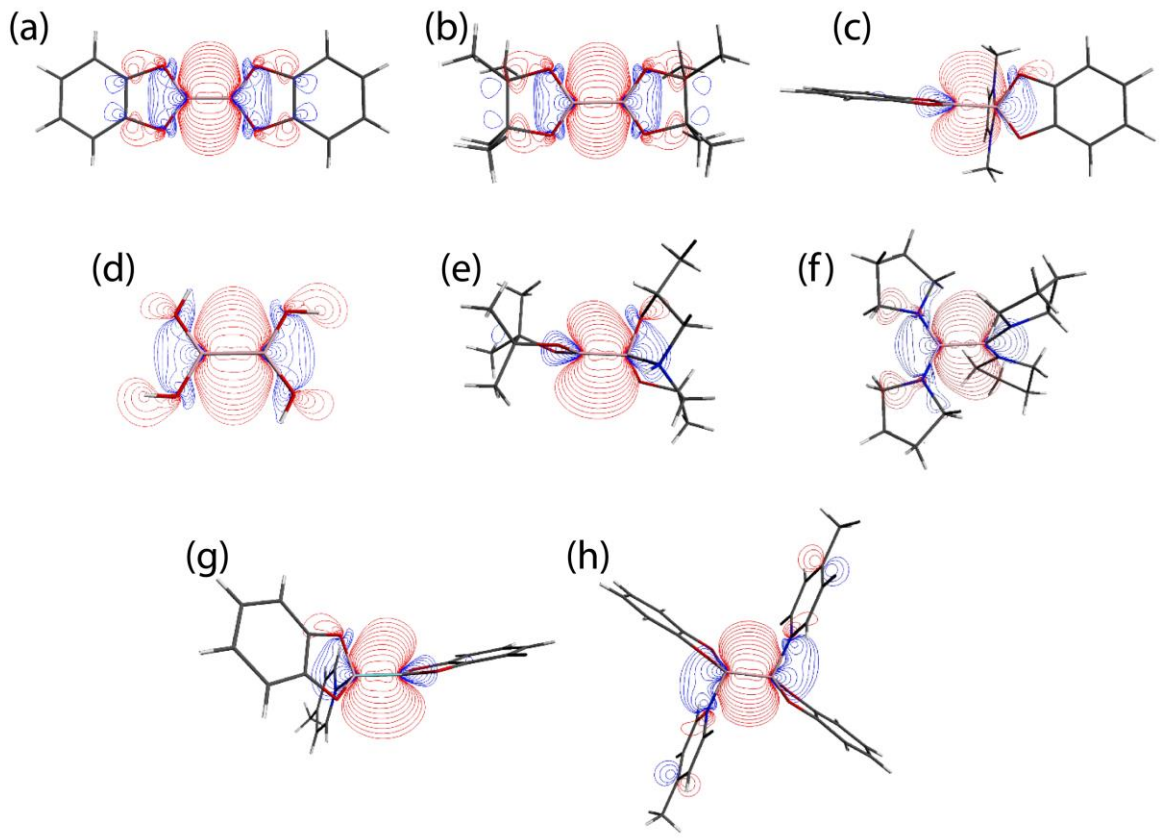

Figure 3.47. Cross sections of the B-B σ-bonding NLMOs for B_2cat_2 (a), B_2pin_2 (b), B_2cat_2·IMes (c), $B_2(OH)_4$ (d), LB_2pin (e), B_2pyr_4 (f), B_2cat_2·pic (g), and B_2cat_2·pic_2 (h). It can be seen that there is a significant impact of hyperconjugation on the NLMOs in (c), (e), (f), and (g).

As can be seen in Figure 3.48, the experimental $J(^{11}B, ^{11}B)$ values are very well reproduced with DFT which serves to validate our theoretical approach. For all the diboron compounds, nearly 100% of the *J* coupling originates from the Fermi contact (FC) mechanism. This mechanism involves the interaction of a nucleus with an electron situated at the nucleus. Since only *s* orbitals have a non-zero electron density at the nucleus, only orbitals with significant *s* character can contribute to *J* via the FC mechanism. This is clear

when one examines the main NLMOs which contribute to the *J* coupling. For all diboron compounds, approximately 50% of the *J* coupling originates from the boron core orbitals and another 50% originates from the B-B σ-bonding orbital, shown in Figure 3.47 (see Table 3.14). Example NLMOs are depicted in Figure 3.48. The percentage contribution from the B-B σ-bonding orbital alone does not correlate with the *J* coupling or the bond length. Hyperconjugation also, surprisingly, doesn't seem to have an effect on the experimental *J* coupling constants. This is perhaps the case since a pure boron *p* orbital cannot contribute to the $J(^{11}B, ^{11}B)$ coupling via the FC mechanism. Similarly, the π-delocalisation which is present in the planar diboron compounds does not affect the $J(^{11}B, ^{11}B)$ coupling. However, the $J(^{11}B, ^{11}B)$ values are well correlated to the B-B σ-bonding NBO energy (see Table 3.14 and Figure 3.48). The $J(^{11}B, ^{11}B)$ values can then be used to directly report on the strength of the B-B σ bond, as the δ_{iso} and C_Q values can be used to report on the polarization of the bond, as described earlier.[226]

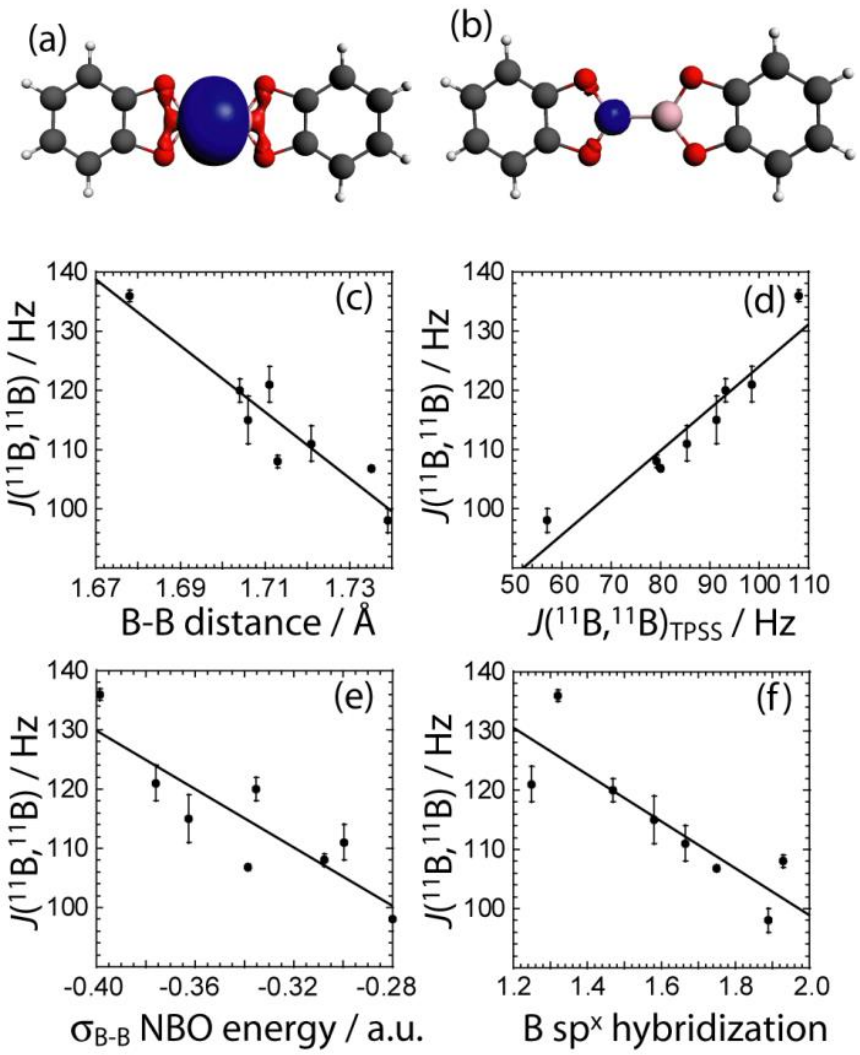

Figure 3.48. The $\sigma_{B\text{-}B}$ NLMO and the boron core NLMO are depicted in (a) and (b), respectively (blue). The boron atoms are coloured pink, the carbon atoms are grey, the oxygen atoms are red, and the hydrogen atoms are white. The correlations between the experimental $J(^{11}B,^{11}B)$ coupling constants and the (c) B-B bond length (J = 1072.2 Hz – $d_{B\text{-}B}$ · 559.0 Hz/Å, R = 0.94), (d) TPSS/QZ4P computed $J(^{11}B,^{11}B)$ values (J = 52.8 Hz – J^{TPSS} · 0.713, R = 0.95), (e) $\sigma_{B\text{-}B}$ NBO energy (J = 31.38 Hz – E_{NBO} · 246.3 Hz/a.u., R = 0.87), and (f) the hybridisation state of the boron orbitals in the $\sigma_{B\text{-}B}$ NLMO (J = 178.12 Hz – x ·39.6 Hz, R = 0.86) are also shown.

Table 3.14. Results from an NBO/NLMO analysis of the boron-boron bonds in the diboron compounds

compound	B-B bond NLMO / %[a]	B core NLMO / %[a]	B-B bonding NBO energy/ a.u.	B-B bond sp^x hybridisation[b]
B_2cat_2	51.8	58.0	-0.399	1.32
B_2pin_2	50.5	62.0	-0.335	1.47
B_2cat_2·Imes	54.9	56.2	-0.339	1.17 and 2.33
$B_2(OH)_4$	59.0	56.0	-0.376	1.25
LB_2pin	53.8	58.8	-0.300	1.38 and 1.67
B_2pyr_4	47.0	65.1	-0.280	1.89
B_2cat_2·pic	51.4	58.2	-0.363	1.21 and 1.95
B_2cat_2·pic_2	46.0	52.4	-0.308	1.93

[a] These numbers correspond to the percentage of the *J* coupling which originates from those particular NLMOs.

[b] The number indicated corresponds to the *p* character of the bond (x).

We can also analyze the hybridisation of the NLMOs and how they relate to the value of *J*. As can be seen in Table 3.14 and Figure 3.48, the degree of hybridisation of the boron orbitals participating in the B-B bond also correlates strongly with the value of $J(^{11}B, ^{11}B)$. Compounds in which the boron *s* orbitals contribute more strongly to the B-B bond have a larger *J* coupling constant since the FC mechanism dominates the *J* coupling in this case. This larger *s* character is also consistent with a shorter B-B bond since *s* orbitals have a shorter radial distribution. This is fully consistent with the observed inverse correlation of the bond length with the value of *J* (see Figure 3.48).

DFT calculations of the *J* coupling constants in a series of model, planar, diboron systems with various ligands were also performed and analysed within the NBO/NLMO framework. For these calculations, the B-B bond length was purposely fixed at 1.74 Å to eliminate the effects of bond length variations. This bond length was chosen as it is representative for these systems whose MP2 optimised bond lengths range from 1.758 Å to 1.714 Å.[286] As can be seen in Figure 3.49, there is a dramatic increase in the calculated

$J(^{11}B, ^{11}B)$ value as the ligand atom is changed from H to C, N, O, and finally F. This is consistent with our experimental observation that a diboron system with nitrogen ligands has a smaller *J* coupling constant than one with oxygen ligands. This increase in *J* coupling constant is also consistent with the increase in the strength of the B-B bond as the electronegativity of the ligands increases, and the increase in the boron *s* character of the bonding NLMO. These calculations then show that the differences in *J* coupling constants which are observed are caused by the differences in the *s* character of the bond and not directly by differences in bond length. The correlation between the $J(^{11}B, ^{11}B)$ values and the *s* character of the bond had been hypothesised nearly 40 years ago.[291]

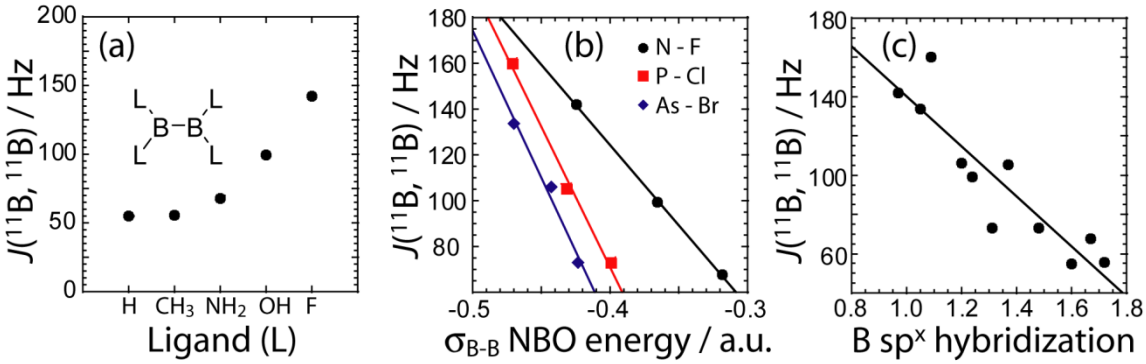

Figure 3.49. In (a) the DFT calculated $J(^{11}B,^{11}B)$ values are plotted as a function of the ligand (L). (b) DFT calculated $J(^{11}B,^{11}B)$ values as a function of the NBO energy. (c) $J(^{11}B,^{11}B)$ values versus the hybridisation state of the boron orbitals comprised in the $\sigma_{B\text{-}B}$ NLMO.

3.5.3.2 Bent's Rule

Within the framework of the hybridisation concept, according to Bent's rule,[292] electron withdrawing groups will reduce the *p* character of the boron atomic orbitals and thus increase the relative *s* character of the boron orbitals participating in the boron-boron

bond. This increase in *s* character decreases the orbital bond energy and shortens the boron-boron bond. Increased *s* character enables an increased contribution to $J(^{11}B, ^{11}B)$ via the FC mechanism. This is consistent with the smaller ^{11}B-^{11}B *J* coupling constant measured in tertrakis(dimethylamino)diborane[293] and the calculated ^{11}B-^{11}B *J* coupling constant in B_2H_4.[294] A similar effect dominates the $J(^{13}C, ^{1}H)$ values of organic molecules.[295-297]

3.5.3.3 Measuring J Coupling across multiple intervening bonds

A potentially exciting application of ^{11}B DQF-*J*-resolved spectroscopy is the structural study of borate glasses.[28] For example, ^{29}Si *J*-resolved spectroscopy is similarly used to probe the connectivities in silicate glasses where the number of nearest neighbours can unambiguously be determined even in a disordered structure.[298] We have then explored the possibility of measuring ^{11}B-^{11}B *J* coupling across multiple intervening bonds in 9-BBN. 9-BBN is a common organic reagent used in hydroboration reactions but it exists as a dimer connected by two 3-centered B-H-B bonds in the liquid and solid states.[278] The boron nuclei are also related by an inversion center and thus the *J* splitting will be amplified by a factor of 3, aiding in the detection of a small *J* coupling constant. The ^{11}B *J*-resolved spectrum is shown in Figure 3.50. Due to the small magnitude of the coupling and the short relaxation times of this sample, it was not possible to resolve a doublet; however, the mere presence of a *J*-DQF signal shows that there is a *J* coupling interaction between the two nuclei. From the spectrum it is possible to estimate the *J* coupling as 10 ± 7 Hz. This is consistent with the magnitude of the ^{11}B-^{10}B *J* coupling measured in diborane ($|J(^{11}B,^{10}B)|$ = 1.3 Hz; $|J(^{11}B,^{11}B)| = 3.8 \pm 0.5$ Hz).[299] A two-bond *J* coupling constant would likely be even smaller than a *J* coupling across a 3-centered 2-electron bond. Therefore, in order to measure $J(^{11}B,$

^{11}B) in borate glasses it may be advantageous to perform MAS NMR experiments at cryogenic temperatures to increase the spin-spin relaxation time constants.[300]

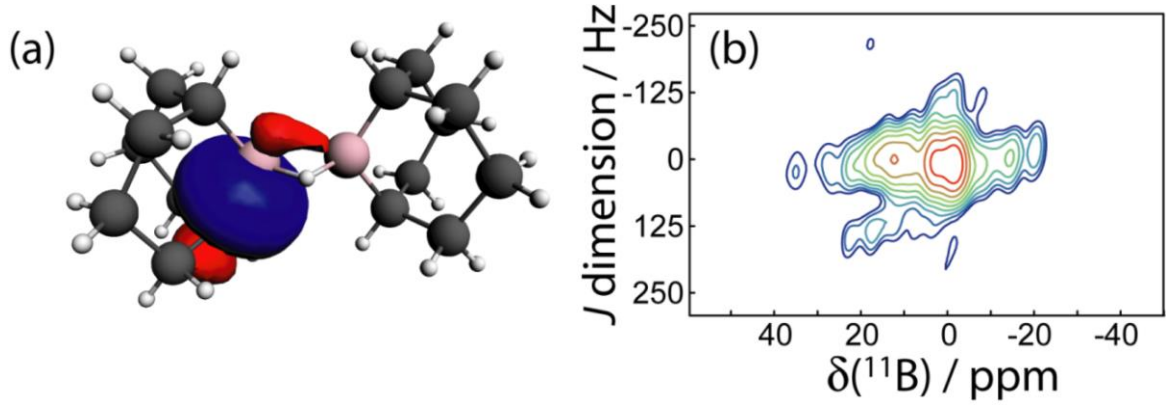

Figure 3.50. In (a), one of the four the $\sigma_{C\text{-}B}$ NLMOs is shown which is responsible for the $J(^{11}B,^{11}B)$ coupling in 9-BBN. In (b), the ^{11}B DQF-*J*-resolved NMR spectrum of 9-BBN is shown; the presence of a signal is indicative of a non-negligible *J* coupling.

Interestingly, DFT calculations indicate that the two-bond *J* coupling constant is negative in 9-BBN ($J(^{11}B, ^{11}B)_{TPSS}$ = -10.0 Hz), in contrast to the positive one-bond values for the diboron compounds. An NLMO analysis shows that this is because the two 3-centered bonds contribute negligible amounts to the *J* coupling whereas the B-C σ-bonding orbitals instead contribute most of the *J* coupling. These have a tail which connects to the other boron site (see Figure 3.50). Since these orbitals have a node in between the two boron nuclei, the sign of the FC contribution to *J* coupling is inverted and the *J* coupling is negative.[295]

3.5.4 Conclusions

It has been demonstrated that ^{11}B DQF-*J*-resolved spectroscopy is a robust tool for studying a variety of diboron compounds. The $J(^{11}B, ^{11}B)$ values which are measured with

this method were shown to be rich in useful electronic information. The $J(^{11}B, ^{11}B)$ values are shown to be correlated with the energy of the B-B σ-bonding NBO. Within a related series of compounds, a larger *J* coupling constant then directly correlates with a stronger B-B bond. The *J* coupling constants also directly report on the hybridisation of the boron orbitals which contribute to the B-B bond. Along with the EFG tensor data and ^{11}B chemical shifts it is then possible to gain experimental insight into the B-B bonding orbital as well as the polarization of the bond. This makes ^{11}B NMR a very powerful technique for screening potentially useful *β*-boration reagents. For example, diboron compounds with nitrogen ligands have noticeably weaker B-B bonds and may then have a higher reactivity towards electron deficient alkenes than diboron compounds with oxygen ligands.[301]

It was also demonstrated that ^{11}B DQF-*J*-resolved spectroscopy can be used as a high-resolution analysis technique for separating the signals from a mixture of diboron systems and identifying stable reaction intermediates. For the systems studies here, the resolution of this technique surpasses that of MQMAS and DOR NMR, which are some of the leading techniques used to obtain high-resolution NMR spectra of quadrupolar nuclei in solids. Additionally, the splittings observed in the *J*-resolved spectra indicate the presence or absence of crystallographic inversion symmetry.

Using the symmetry amplification of the *J* splitting in 9-BBN it was possible to measure a rare example of a *J* coupling between two quadrupolar nuclei across multiple intervening bonds. This is an exciting advance towards studying amorphous systems such as borate glasses where measuring *J* coupling could yield unprecedented structural information.

3.5.5 Experimental

B_2cat_2, B_2pin_2, $B_2(OH)_4$, B_2pyr_4, 9-BBN, 4-picoline, and bis(2-hydroxypropyl)amine were obtained from Aldrich and used without further purification. All reactions were performed using standard Schlenk and glove box techniques using anhydrous solvents. B_2cat_2·IMes (see chapter 3.4), LB_2pin,[258] B_2cat_2·pic, and B_2cat_2·pic_2[277] were prepared using published literature procedures.

3.5.5.1 NMR experiments

All ^{11}B NMR experiments were performed at an applied external magnetic field of 9.4 T using a Bruker Avance III NMR spectrometer equipped with a Bruker 4 mm triple resonance MAS probe. The ^{11}B MAS NMR spectra were acquired using a spin-echo sequence to remove the probe background signal. The ^{11}B central-transition selective 90° pulse length was 20 μs and the echo delay was 80 μs for rotor synchronisation (ν_{rot} = 12.5 kHz). Between 8 and 192 transients were acquired for each sample using a relaxation delay of 4 s. The chemical shifts were referenced to $F_3B{\cdot}O(C_2H_5)_2$ using $NaBH_4$ as a secondary reference (-42.06 ppm).[302] Spectral line shapes were simulated using WSolids1.[53]

The ^{11}B DQF *J*-resolved MAS NMR experiments were performed using 25 μs central-transition selective 90° pulses, and high-power ^1H decoupling. The MAS frequency was typically 12.5 kHz and the t_1 increments were set to either 40 μs or 80 μs for rotor synchronization. 36 t_1 slices of 64 to 540 transients were acquired and the spectra were processed in magnitude mode. 9-BBN was cooled to 0°C in order to increase its spin-spin relaxation time constant and obtain sharper *J*-resolved signals. The DQF *J*-resolved MAS NMR experiments are straightforward to run, since only the double-quantum filter delay

needs to be optimised, and are quite sensitive; a high quality *J*-resolved spectrum can be obtained in 2 h in a moderate applied magnetic field strength.

The ^{11}B MQMAS NMR spectrum of B_2pyr_4 was acquired using the 3-pulse z-filtered sequence with proton decoupling.[303] The excitation, conversion, and detection pulses lasted 4.5, 2.0, and 20 μs, respectively. 80 t_1 slices of 1560 scans were acquired with a t_1 increment of 80 μs and the spectrum was processed using the States method.[304]

3.5.5.2 DFT calculations

GIPAW DFT calculations of the ^{11}B magnetic shielding and EFG tensors were performed using the CASTEP-NMR program (version 4.4).[282] The published crystal structures were used as input.[211,260,261,275,276,277,278] The data were analysed using the EFGShield program (version 4.1).[124] Standard, on-the-fly generated ultrasoft pseudopotentials available within CASTEP were used for all atoms. A 610 eV kinetic energy cutoff and "fine" quality *k*-point grids were used in all cases. The generalised gradient approximation (GGA) DFT functional of Perdew, Burke, and Ernzerhof (PBE)[89] was used for all the calculations.

Cluster-model DFT calculations were performed using the ADF program (ver. 2009)[64] and the data were analysed using EFGShield.[124] The models consisted of a single molecular unit, with the exception of $B_2(OH)_4$ for which the four neighbouring molecules, which form hydrogen bonds, were also included. The shielding and EFG tensor calculations used the revised PBE GGA functional of Zhang and Yang[252] whereas the *J* coupling calculations used the meta-GGA functional of Tao, Perdew, Staroverov, and Scuseria (TPSS).[74] All calculations used the quadruple-zeta quadruple-polarised (QZ4P) basis set.[203]

The NBO/NLMO analysis of the *J* coupling constants was performed using the NBO program (version 5.0)[253] which is incorporated into ADF.

References

[1] Wasylishen, R. A. *Dipolar & Indirect Coupling Basics*, in: Harris, R. K.; Wasylishen, R. E., Eds. *eMagRes*, John Wiley & Sons, 2009.

[2] Kumar, A.; Ernst, R. R.; Wüthrich, K. *Biochem. Biphys. Res. Commun.* **1980**, *95*, 1-6

[3] Guillion, T.; Schaefer, J. *J. Magn. Reson.* **1989**, *81*, 196-200.

[4] Jaroniec, C. P.; Filip, C.; Griffin, R. G. *J. Am. Chem. Soc.* **2002**, *124*, 10728-10742.

[5] Brouwer, D. H.; Darton, R. J.; Morris, R. E.; Levitt, M. H. *J. Am. Chem. Soc.* **2005**, *127*, 10365-10370.

[6] Brouwer, D. H.; Cadars, S.; Eckert, J.; Liu, Z.; Terasaki, O.; Chmelka, B. F. *J. Am. Chem. Soc.* **2013**, *135*, 5641-5655.

[7] Bouchevreau, B.; Martineau, C.; Mellot-Draznieks, C.; Tuel, A.; Suchomel, M. R.; Trébosc, J.; Lafon, O.; Amoureux, J.-P.; Taulelle, F. *Chem. Mater.* **2013**, *25*, 2227-2242.

[8] Bouchevreau, B.; Martineau, C; Mellot-Draznieks, C.; Tuel, A.; Suchomel, M. R.; Trébosc, J.; Lafon, O.; Amoureux, J.-P.; Taulelle, F. *Chem. Eur. J.* **2013**, *19*, 5009-5013.

[9] Elena, B.; Emsley, L. *J. Am. Chem. Soc.* **2005**, *127*, 9140-9146.

[10] Elena, E.; Pintacuda, G.; Mifsud, N.; Emsley, L. *J. Am. Cehm. Soc.* **2006**, *128*, 9555-9560.

[11] Brouwer, D. H.; Langendoen, K. P. *CrystEngComm* **2013**, *15*, 8748-8762.

[12] Grey, C. P.; Veeman, W. S. *Chem. Phys. Lett.* **1992**, *192*, 379-385.

[13] Gullion, T. *Chem. Phys. Lett.* **1995**, *246*, 325-330.

[14] Nijman, M.; Ernst, M.; Kentgens, A. P. M.; Meier, B. H. *Mol. Phys.* **2000**, *98*, 161-178.

[15] Lu, X.; Lafon, O.; Trébosc, J.; Tricot, G.; Delevoye, L.; Méar, F.; Montagne, L.; Amoureux, J.-P. *J. Chem. Phys.* **2012**, *137*, 144201.

[16] Lu, X.; Lafon, O.; Trébosc, J.; Amoureux, J.-P. *J. Magn. Reson.* **2012**, *215*, 34-49.

[17] Pourpoint, F.; Trébosc, J.; Gauvin, R. M.; Wang, Q.; Lafon, O.; Deng, F.; Amoureux, J.-P. *ChemPhysChem* **2012**, *13*, 3605-3615.

[18] Fernandez, C.; Pruski, M. *Top. Curr. Chem.* **2012**, *306*, 119-188.

[19] Dowell, N. G.; Ashbrook, S. E.; Wimperis, S. *J. Phys. Chem. A* **2002**, *106*, 9470-9478.

[20] Edén, M.; Frydman, L. *J. Phys. Chem. B* **2003**, *107*, 14598-14611.

[21] Ajithkumar, T. G.; van Eck, E. R. H.; Kentgens, A. P. M.; *Solid State Nucl. Magn. Reson.* **2004**, *26*, 180-186.

[22] Wi, S.; Logan, J. W.; Sakellariou, D.; Walls, J. D.; Pines, A. *J. Chem. Phys.* **2002**, *117*, 7024-7033.

[23] Brinkmann, A.; Edén, M. *Can. J. Chem.* **2011**, *89*, 892-899.

[24] Brinkmann, A.; Edén, M. *Phys. Chem. Chem. Phys.* **2014**, *16*, 7037-7050.

[25] Ashbrook, S. E.; Wimperis, S. *J. Chem. Phys.* **2009**, *131*, 194509.

[26] Iuga, D. *J. Magn. Reson.* 2011, *208*, 225-234.

[27] Hung, I.; Uldry, A.-C.; Becker-Baldus, J.; Webber, A. L.; Wong, A.; Smith, M. E.; Joyce, S. A.; Yates, J. R.; Pickard, C. J.; Dupree, R.; Brown, S. P. *J. Am. Chem. Soc.* **2009**, *131*, 1820-1834.

[28] Barrow, N. S.; Yates, J. R.; Feller, S. A.; Holland, D.; Ashbrook, S. E.; Hodgkinson, P.; Brown, S. P. *Phys. Chem. Chem. Phys.* **2011**, *13*, 5778-5789.

[29] Wu, G.; Wasylishen, R. E. *Mol. Phys.* **1998**, *95*, 1177-1183.

[30] Kundla, E.; Alla, M. *Proceedings of the 20th Congress AMPERE, Tallinn, 1978*, Kundla, E.; Lippmaa, E.; Saluvere, T., Eds., Spring-Verlag: Berlin, 1979, p. 92.

[31] Naito, A.; Ganapathy, S.; McDowell, C. A. *J. Chem. Phys.* **1981**, *74*, 5393-5397.

[32] Hexem, J. G.; Frey, M. H.; Opella, S. J. *J. Chem. Phys.* **1982**, *77*, 3847-3856.

[33] Zumbulyadis, N.; Henrichs, P. M.; Young, R. H. *J. Chem. Phys.* **1981**, *75*, 1603-1611.

[34] Menger, E. M.; Veeman, W. S.; *J. Magn. Reson.* **1982**, *46*, 257-268.

[35] Böhm, J.; Fenzke, D.; Pfeifer, H. *J. Magn. Reson.* **1983**, *55*, 197-204.

[36] Olivieri, A. C.; Frydman, L.; Diaz, L. E. *J. Magn. Reson.* **1987**, *75*, 50-62.

[37] Olivieri, A. C. *J. Magn. Reson.* **1989**, *81*, 201-205.

[38] Harris, R. K.; Olivieri, A. C. *Prog. Nucl. Magn. Reson. Spectrosc.* **1992**, *24*, 435-456.

[39] Wi, S.; Sun, H.; Oldfield, E.; Hong, M. *J. Am. Chem. Soc.* **2005**, *127*, 6451-6458.

[40] Wu, G.; Yamada, K. *Chem. Phys. Lett.* **1999**, *313*, 519-524.

[41] McManus, J.; Kemp-Harper, R.; Wimperis, S. *Chem. Phys. Lett.* **1999**, *311*, 292-298.

[42] Wi, S.; Frydman, L. *J. Chem. Phys.* **2000**, *112*, 3248-3261.

[43] Wi, S.; Frydman, V.; Frydman, L.; *J. Chem. Phys.* **2001**, *114*, 8511-8519.

[44] Ashbrook, S. E.; McManus, J.; Thrippleton, M. J.; Wimperis, S. *Prog. Nucl. Magn. Reson. Spectrosc.* **2009**, *55*, 160-181.

[45] Ashbrook, S. E.; Wimperis, S. *Prog. Nucl. Magn. Reson. Spectrosc.* **2004**, *45*, 53-108.

[46] Wi, S.; Ashbrook, S. E.; Wimperis, S.; Frydman, L. *J. Chem. Phys.* **2003**, *118*, 3131.

[47] Man, P. P. *Quadrupolar Interactions*, in: Harris, R. K.; Wasylishen, R. E., Eds. *eMagRes*, John Wiley & Sons, 2009.

[48] Samoson, A.; Lippmaa, E.; Pines, A. *Mol. Phys.* **1988**, *65*, 1013-1018.

[49] Chmelka, B. F.; Mueller, K. T.; Pines, A.; Stebbins, J.; Wu, Y.; Zwanziger, J. W. *Nature* **1989**, *339*, 42-43.

[50] Samoson, A.; Pines, A. *Rev. Sci. Instrum.* **1989**, *60*, 3239-3241.

[51] Dupree, R. *Double Rotation NMR*, in: Harris, R. K.; Wasylishen, R. E., Eds. *eMagRes*, John Wiley & Sons, 2009.

[52] Alderman, D. W.; Solum, M. S.; Grant, D. M. *J. Chem. Phys.* **1986**, *84*, 3717-3725.

[53] Eichele, K.; Wasylishen, R. E. WSolids1: Solid-State NMR Spectrum Simulation Package v. 1.20.15, University of Tübingen, Tübingen, Germany, 2011.

[54] Coapes, R. B.; Souza, F. E. S.; Fox, M. A.; Batsanov, A. S.; Goeta, A. E.; Yufit, D. S.; Leech, M. A.; Howard, J. A. K.; Scott, A. J.; Clegg, W.; Marder, T. B. *J. Chem. Soc., Dalton Trans.* **2001**, 1201-1209.

[55] O'Dell, L. A.; Schurko, R. W. *Chem. Phys. Lett.* **2008**, *464*, 97-102.

[56] Chapman, R. P.; Widdifield, C. M.; Bryce, D. L. *Prog. Nucl. Magn. Reson. Spectrosc.* **2009**, *55*, 215-237.

[57] Samoson, A.; Lippmaa, E. *J. Magn. Reson.* **1989**, *84*, 410-416.

[58] Casabella, P. A. *J. Chem. Phys.* **1964**, *41*, 3793-3798.

[59] Jackowski, K.; Makulski, W.; Szyprowska, A.; Antušek, A.; Jaszuński, M.; Jusélius, J. *J. Chem. Phys.* **2009**, *130*, 044309.

[60] Gee, M.; Wasylishen, R. E.; Laaksonen, A. *J. Phys. Chem. A* **1999**, *103*, 10805-10812.

[61] Segall, M. D.; Lindan, P. J. D.; Probert, M. J.; Pickard, C. J.; Hasnip, P. J.; Clark, S. J.; Payne, M. C. *J. Phys.: Condens. Matter* **2002**, *14*, 2717-2744.

[62] Pickard, C. J.; Mauri, F. *Phys. Rev. B* **2001**, *63*, 245101.

[63] Profeta, M.; Mauri, F.; Pickard, C. J. *J. Am. Chem. Soc.* **2003**, *125*, 541-548.

[64] te Velde, G.; Bickelhaupt, F. M.; Baerends, E. J.; Fonseca Guerra, C.; van Gisbergen, S. J. A.; Snijders, J. G.; Ziegler, T. *J. Comput. Chem.* **2001**, *22*, 931-967.

[65] Fonseca Guerra, C.; Snijders, J. G.; te Velde, G.; Baerends, E. J. *Theor. Chem. Acc.* **1998**, *99*, 391-403.

[66] Amsterdam Density Functional Software ADF2009.01. SCM; Theoretical Chemistry, Vrije Universiteit: Amsterdam, The Netherlands. http://www.scm.com/, 2010.

[67] Pyykkö, P. *Chem. Phys.* **1977**, *22*, 289-296.

[68] Autschbach, J. *J. Chem. Phys.* **2008**, *129*, 094105.

[69] Pyykkö, P. *Mol. Phys.* **2008**, *106*, 1965-1974.

[70] Harbison, G. S.; Slokenbergs, A.; Barbara, T. M. *J. Chem. Phys.* **1989**, *90*, 5292-5298.

[71] Jakobsen, H. J.; Bildøe, H.; Brorson, M.; Gan, Z.; Hung, I. *J. Magn. Reson.* **2013**, *230*, 98-110.

[72] Bryce, D. L.; Wasylishen, R. E. *Acc. Chem. Res.* **2003**, *36*, 327-334.

[73] Bryce, D. L.; Autschbach, J. *Can. J. Chem.* **2009**, *87*, 927-941.

[74] Tao, J.; Perdew, J. P.; Staroverov, V. N.; Scuseria, G. E. *Phys. Rev. Lett.* **2003**, *91*, 146401.

[75] van Lenthe, E.; Baerends, E. J. *J. Comput. Chem.* **2003**, *24*, 1142-1156.

[76] Perera, A. *Mol. Phys.* **2010**, *108*, 3017-3025.

[77] Thomas, B.; Paasch, S.; Steuernagel, S.; Eichele, K. *Solid State Nucl. Magn. Reson.* **2001**, *20*, 108-117.

[78] Forgeron, M. A. M.; Bryce, D. L.; Wasylishen, R. E.; Rösler, R. *J. Phys. Chem. A* **2003**, *107*, 726-735.

[79] Coursen, D. L.; Hoard, J. L.; *J. Am. Chem. Soc.* **1952**, *74*, 1742-1750.

[80] Ooms, K. J.; Feindel, K. W.; Terskikh, V. V.; Wasylishen, R. E. *Inorg. Chem.* **2006**, *45*, 8492-8499.

[81] Feindel, K. W.; Ooms, K. J.; Wasylishen, R. E. *Phys. Chem. Chem. Phys.* **2007**, *9*, 1226-1238.

[82] Massiot, D.; Farnan, I.; Gautier, N.; Trumeau, D.; Trokiner, A.; Coutures, J. P. *Solid State Nucl. Magn. Reson.* **1995**, *4*, 241-248.

[83] Das, T. P.; Hahn, E. L. *Nuclear Quadrupole Resonance Spectroscopy, supplement 1* in Seitz, F.; Turnbull, D., Eds. *Solid State Physics*, Academic Press, New York, 1958.

[84] Ireland, P. S.; Brown, T. L. *J. Magn. Reson.* **1975**, *20*, 300-312.

[85] Kraihanzel, C. S.; Herman, L. G. *J. Organomet. Chem.* **1968**, *15*, 397-407.

[86] Waltz, K. M.; He, X.; Muhoro, C. Hartwig, J. F. *J. Am. Chem. Soc.* **1995**, *117*, 11357-11358.

[87] Waltz, K. M.; Muhoro, C. N.; Hartwig, J. F. *Organometallics* **1999**, *18*, 3383-3393.

[88] Fung, B. M.; Khitrin, A. K.; Ermolaev, K. *J. Magn. Reson.* **2000**, *142*, 97-101.

[89] Perdew, J. P.; Burke, K.; Ernzerhof, M. *Phys. Rev. Lett.* **1996**, 77, 3865-3868.

[90] Widdifield, C. M.; Bryce, D. L.; *J. Phys. Chem. A* **2010**, *114*, 10810-10823.

[91] Widdifield, C. M.; Bain, A. D.; Bryce, D. L.; *Phys. Chem. Chem. Phys.* **2011**, *13*, 12413-12420.

[92] Hamaed, H.; Laschuk, M. W.; Terskikh, V. V.; Schurko, R. W. *J. Am. Chem. Soc.* **2009**, *131*, 8271-8279.

[93] Michaelis, V. K.; Aguiar, P. M.; Terskikh, V. V.; Kroeker, S. *Chem. Commun.* **2009**, 4660-4662.

[94] Michaelis, V. K.; Kroeker, S. *J. Phys. Chem. C* **2010**, *114*, 21736-21744.

[95] Chen, F.; Ma, G.; Cavell, R. G.; Terskikh, V. V.; Wasylishen, R. E. *Chem. Commun.*, **2008**, 5933-5935.

[96] Lo, A, Y. H.; Jurca, T.; Richeson, D. S.; Bryce, D. L. *J. Phys. Chem. Lett.* **2010**, *1*, 3078-3084.

[97] Bryce, D. L. *Dalton Trans.* **2010**, *39*, 8593-8602.

[98] Sutrisno, A.; Lu, C.; Lipson, R. H.; Huang, Y. *J. Phys. Chem. C* **2009**, *113*, 21196-21201.

[99] Larsen, F. H.; Skibsted, J.; Jakobsen, H. J.; Nielsen, N. C. *J. Am. Chem. Soc.* **2000**, *122*, 7080-7086.

[100] Lipton, A. S.; Heck, R. W.; de Jong, W. A.; Gao, A. R.; Wu, X.; Roehrich, A.; Harbison, G. S.; Ellis, P. D. *J. Am. Chem. Soc.* **2009**, *131*, 13992-13999.

[101] Griffin, J. M.; Berry, A. J.; Ashbrook, S. E.; *Solid State Nucl. Magn. Reson.* **2011**, *40*, 91-99.

[102] Pound, R. V. *Phys. Rev.* **1950**, *79*, 685-702.

[103] Creel, R. B.; von Meerwall, E.; Griffin, C. F.; Barnes, R. G. *J. Chem. Phys.* **1973**, *58*, 4930-4935.

[104] Vega, A. J., *Quadrupolar Nuclei in Solids*, in: Harris, R. K.; Wasylishen, R. E., Eds. *eMagRes*, John Wiley & Sons, 2009.

[105] Jerschow, A. *Prog. Nucl. Magn. Reson. Spectrosc.* **2005**, *46*, 63-78.

[106] Power, W. P.; Wasylishen, R. E.; Mooibroek, S.; Pettitt, B. A.; Danchura, W. *J. Phys. Chem.* **1990**, *94*, 591-598.

[107] Chu, P. J.; Gerstein, B. C. *J. Chem. Phys.* **1989**, *91*, 2081-2101.

[108] Attrell, R. J.; Widdifield, C. M.; Korobkov, I.; Bryce, D. L. *Cryst. Growth. Des.* **2012**, *12*, 1641-1653.

[109] Gan, Z.; Srinivasan, P.; Quine, J. R.; Steuernagel, S.; Knott, B. *Chem. Phys. Lett.* **2003**, *367*, 163-169.

[110] Muha, G. M. *J. Magn. Reson.* **1983**, *53*, 85-102.

[111] Creel, R. B.; Drabold, D. A. *J. Molec. Struct.* **1983**, *111*, 85-90.

[112] Sanctuary, B. C.; Halstead, T. K.; Osment, P. A. *Mol. Phys.* **1983**, *49*, 753-784.

[113] Bain, A. D. *Mol. Phys.* **2003**, *101*, 3163-3175.

[114] Khasawneh, M.; Hartman, J. S.; Bain, A. D. *Mol. Phys.* **2004**, *102*, 975-983.

[115] Possa, D.; Gaudio, A. C.; Freitas, J. C. C. *J. Magn. Reson.* **2011**, *209*, 250-260.

[116] Bain, A. D.; Khasawneh, M. *Concepts Magn. Reson. Part A* **2004**, *22*, 69-78.

[117] Bain, A. D. *Chem. Phys. Lett.* **2012**, *531*, 267-271.

[118] Bain, A. D.; Berno, B. *Prog. Nucl. Magn. Reson. Spectrosc.* **2011**, *59*, 223-244.

[119] Donley, E. A.; Long, J. L.; Liebisch, T. C.; Hodby, E. R.; Fisher, T. A.; Kitching, J. *Phys. Rev. A* **2009**, *79*, 013420.

[120] Comment, A.; Mayaffre, H.; Mitrović, V.; Horvatić, M.; Berthier, C.; Grenier, B.; Millet, P. *Phys. Rev. B* **2010**, *82*, 214416.

[121] Bulutay, C. *Phys. Rev. B* **2012**, *85*, 115313.

[122] Tycko, R.; Opella, S. J. *J. Chem. Phys.* **1987**, *86*, 1761-1774.

[123] Arfken, G. *Mathematical methods for physicists, 3rd ed.*, Academic Press, New York, 1985.

[124] Adiga, S.; Aebi, D.; Bryce, D. L. *Can. J. Chem.* **2007**, *85*, 496-505.

[125] Smith, S. A.; Levante, T. O.; Meier, B. H.; Ernst, R. R. *J. Magn. Reson. Ser. A* **1994**, *106*, 75-105.

[126] Bak, M.; Rasmussen, J. T.; Nielsen, N. C. *J. Magn. Reson.* **2000**, *147*, 296-330.

[127] Veshtort, M.; Griffin, R. G. *J. Magn. Reson.* **2006**, *178*, 248-282.

[128] Massiot, D.; Fayon, F.; Capron, M.; King, I.; Le Calvé, S.; Alonso, B.; Durand, J.-O.; Bujoli, B.; Gan, Z.; Hoatson, G. *Magn. Reson. Chem.* **2002**, *40*, 70-76.

[129] Kemp, T. F.; Smith, M. E. *Solid State Nucl. Magn. Reson.* **2009**, *35*, 243-252.

[130] Bain, A. D.; *J. Magn. Reson.* **2006**, *179*, 308-310.

[131] Galassi, M.; Davies, J.; Theiler, J.; Gough, B.; Jungman, G.; Alken, P.; Booth, M.; Rossi, F. *GNU Scientific Library Reference Manual, Third Edition, for version 1.12*, Network Theory Ltd., United Kingdom, 2009.

[132] Edén, M. *Concepts Magn. Reson. Part A* **2003**, *18*, 24-55.

[133] Tycko, R.; Opella, S. J.; *J. Am. Chem. Soc.* **1986**, *108*, 3531-3532.

[134] O'Dell, L. A.; Ratcliffe, C. I. *Chem. Phys. Lett.* **2011**, *514*, 168-173.

[135] O'Dell, L. A.; Ratcliffe, C. I.; Kong, X.; Wu, G. *J. Phys. Chem. A* **2012**, *116*, 1008-1014.

[136] Segel, S. L.; Anderson, L. A. *J. Chem. Phys.* **1968**, *49*, 1407-1410.

[137] Reddy, R.; Narasimhan, P. T. *J. Molec. Struct.* **1989**, *192*, 309-319.

[138] Ramamoorthy, A.; *Mol. Phys.* **1991**, *72*, 1425-1429.

[139] Ageev, S. Z.; Sanctuary, B. C. *Mol. Phys.* **1996**, *87*, 1423-1438.

[140] Liao, M.-Y.; Harbison, G. S.; *J. Chem. Phys.* **1999**, *111*, 3077-3082.

[141] Grechishkin, V. S.; Sinyavskii, N. Y.; *Izv. Vyssh. Uchebn. Zaved., Fiz.* **1991**, *34*, 708-711.

[142] Suits, B. H.; Slichter, C. P. *Phys. Rev. B* **1984**, *29*, 41-51.

[143] Widdifield, C. M.; Bryce, D. L. *J. Phys. Chem. A* **2010**, *114*, 2102-2116.

[144] Harris, R. K.; Becker, E. D.; Cabral de Menezes, S. M.; Goodfellow, R.; Granger, P. *Pure Appl. Chem.* **2001**, *73*, 1795-1818.

[145] Strohmeier, M.; Stueber, D.; Grant, D. M. *J. Phys. Chem. A* **2003**, *107*, 7629-7642.

[146] O'Dell, L. A.; Schurko, R. W. *Phys. Chem. Chem. Phys.* **2009**, *11*, 7069-7077.

[147] O'Dell, L. A.; Schurko, R. W.; Harris, K. J.; Autschbach, J.; Ratcliffe, C. I. *J. Am. Chem. Soc.* **2011**, *133*, 527-546.

[148] Semin, G. K. *Russ. J. Phys. Chem. A* **2007**, *81*, 38-46.

[149] Segel, S. L. *J. Chem. Phys.* **1978**, *69*, 2434-2438.

[150] Doering, E. B.; Waugh, J. S. *J. Chem. Phys.* **1986**, *85*, 1753-1756.

[151] Tracey, A. S.; Radley, K. *Liq. Cryst.* **1989**, *6*, 319-323.

[152] Metrangolo, P.; Resnati, G. *Halogen Bonding – Fundamentals and Applications*, Springer-Verlag, Berlin, 2008.

[153] Dong, C.; Flecks, S.; Unversucht, S.; Haupt, C.; van Pée, K.-H.; Naismith, J. H. *Science* **2005**, *309*, 2216-2219.

[154] Barlos, K.; Kroner, J.; Nöth, H.; Wrackmeyer, B. *Chem. Ber.* **1978**, *111*, 1833-1838.

[155] Barlos, K.; Kroner, J.; Nöth, H.; Wrackmeyer, B. *Chem. Ber.* **1980**, *113*, 3716-3723.

[156] Fedotov, M. A.; Malkina, O. L.; Malkin, V. G. *Chem. Phys. Lett*. **1996**, *258*, 330-335.

[157] Bryce, D. L.; Sward, G. D.; Adiga, S. *J. Am. Chem. Soc*. **2006**, *128*, 2121-2134.

[158] Chapman, R. P.; Bryce, D. L. *Phys. Chem. Chem. Phys.* **2007**, *9*, 6219-6230.

[159] Bryce, D. L.; Bultz, E. B. *Chem. Eur. J*. **2007**, *13*, 4786-4796.

[160] Hamaed, H.; Pawlowski, J. M.; Cooper, B. F. T.; Fu, R.; Eichhorn, S. H.; Schurko, R. W. *J. Am. Chem. Soc*. **2008**, *130*, 11056-11065.

[161] Gordon, P. G.; Brouwer, D. H.; Ripmeester, J. A. *J. Phys Chem A* **2008**, *112*, 12527-12529.

[162] Gordon, P. G.; Brouwer, D. H.; Ripmeester, J. A. *ChemPhysChem* **2010**, *11*, 260-268.

[163] Chapman, R. P.; Bryce, D. L. *Phys. Chem. Chem. Phys*. **2009**, *11*, 6987-6998.

[164] Rossini, A. J.; Mills, R. W.; Briscoe, G. A.; Norton, E. L.; Geier, S. J.; Hung, I.; Zheng, S.; Autschbach, J.; Schurko, J. W. *J. Am. Chem. Soc*. **2009**, *131*, 3317-3330.

[165] Hung, I.; Shetty, K.; Ellis, P. D.; Brey, W. W.; Gan, Z. *Solid State Nucl. Magn. Reson*. **2009**, *36*, 159-163.

[166] Lucier, B. E. G.; Reidel, A. R.; Schurko, R. W. *Can. J. Chem*. **2011**, *89*, 919-937.

[167] Terskikh, V. V.; Lang, S. J.; Gordon, P. G.; Enright, G. D.; Ripmeester, J. A. *Magn. Reson. Chem*. **2008**, *47*, 398-406.

[168] Semin, G. K.; Babushking, T. A.; Yakobson, G. G. *Nuclear Quadrupole Resonance in Chemistry*, John Wiley and Sons, New York, 1975.

[169] Townes, C. H.; Dailey, B. P. *J. Chem. Phys*. **1949**, *17*, 782-796.

[170] Townes, C. H.; Dailey, B. P. *J. Chem. Phys*. **1952**, *20*, 35-40.

[171] Becke, A. D. *J. Chem. Phys*. **1993**, *98*, 5648-5652.

[172] Lee, C.; Yang, W.; Parr, R. G. *Phys. Rev. B* **1988**, *37*, 785-789.

[173] Krishnan, R.; Binkley, J. S.; Seeger, R.; Pople, J. A. *J. Chem. Phys*. **1980**, *72*, 650-654.

[174] Chandramani, R.; Devaraj, N.; Sastry, V. S. S.; Ramakrishna, J. *Aust. J. Chem*. **1976**, *29*, 2363-2367.

[175] Claramunt, R. M.; Sanz, D.; López, C.; Jiménez, J. A.; Jimeno, M. L.; Elguero, J.; Fruchier, A. *Magn. Reson. Chem.* **1997**, *35*, 35-75.

[176] Hahn, E. L. *Phys. Rev.* **1950**, *80*, 580-594.

[177] Lesage, A. *Indirect coupling and connectivity*, eMagRes, John Wiley & Sons, 2009.

[178] Karplus, M. *J. Chem. Phys.* **1959**, *30*, 11-15.

[179] Karplus, M. *J. Am. Chem. Soc.* **1963**, *85*, 2870-2871.

[180] Sternhell, S. *Q. Rev.* **1969**, *23*, 236-270.

[181] Kessler, H.; Gehrke, M.; Griesinger, C. *Angew. Chem. Int. Ed.* **1988**, *27*, 490-536.

[182] Ramsey, N. F. *Phys. Rev.* **1953**, *91*, 303-307.

[183] Wasylishen, R. E. *Indirect nuclear spin-spin coupling tensors*, eMagRes, John Wiley & Sons, 2009.

[184] Shenderovich, I. G.; Smirnov, S. N.; Denisov, G. S.; Gindin, V. A.; Golubev, N. S.; Dunger, A.; Reibke, R.; Kirpekar, S.; Malkina, O. L.; Limbach, H.-H. *Ber. Bunsenges. Phys. Chem.* **1998**, *102*, 422-428.

[185] Dingley, A. J.; Grzesiek, S. *J. Am. Chem. Soc.* **1998**, *120*, 8293-8297.

[186] Brown, S. P.; Pérez-Torralba, M.; Sanz, D.; Claramunt, R. M.; Emsley, L. *Chem. Commun.* **2002**, 1852-1853.

[187] Plevin, M. J.; Bryce, D. L.; Boisbouvier, J. *Nature Chem.* **2010**, *2*, 466-471.

[188] Ledbetter, M. P.; Saielli, G.; Bagno, A.; Tran, N.; Romalis, M. V. *Proc. Natl. Acad. Sci. U.S.A.* **2012**, *109*, 12393-12397.

[189] Proctor, W. G.; Yu, F. C. *Phys. Rev.* **1951**, *81*, 20-30.

[190] Massiot, D.; Fayon, F.; Deschamps, M.; Cadars, S.; Florian, P.; Montouillout, V.; Pellerin, N.; Hiet, J.; Rakhmatullin, A.; Bessada, C. *C. R. Chimie* **2010**, *13*, 117-129.

[191] Waugh, J. S. *Selective averaging*, Academic Press, New York, 1976, pp. 18.

[192] Pople, J. A.; Schneider, W. G.; Bernstein, H. J. *High-Resolution Nuclear Magnetic Resonance*, McGraw-Hill, New York, 1959, p. 110-119.

[193] Levitt, M. H. *Spin Dynamics*, John Wiley & Sons, Chichester, 2009, pp.358.

[194] Pake, G. E. *J. Chem. Phys.* **1948**, *16*, 327-336.

[195] Facey, G.; Gusev, D.; Morris, R. A.; Macholl, S.; Buntkowsky, G. *Phys. Chem. Chem. Phys.* **2000**, *2*, 935-941.

[196] Szymański, S.; *J. Magn. Reson.* **1997**, *127*, 199-205.

[197] Bernatowicz, P.; Szymański, S. *J. Magn. Reson.* **2001**, *148*, 455-458.

[198] Yokozeki, A.; Muenter, J. S. *J. Chem. Phys.* **1980**, *72*, 3796-3804.

[199] Poplett, I. J. F. *Dipolar Structure in Nuclear Quadrupole Resonance: A Survey*, in: Smith, J. A., Ed., *Advances in Nuclear Quadrupole Resonance, Vol. 4*, Heyden and Son, London, 1980.

[200] Itoh, K.; Kambe, K. *J. Phys Soc. Jpn.* **1957**, *12*, 763-769.

[201] Carravetta, M.; Johannessen, O. G.; Levitt, M. H. *Phys. Rev. Lett.* **2004**, *92*, 153003.

[202] Maricq, M. M.; Waugh, J. S. *J. Chem. Phys.* **1979**, *70*, 3300-3316.

[203] Kubo, A.; McDowell, C. A. *J. Chem. Phys.* **1990**, *92*, 7156-7170.

[204] Wu, G.; Wasylishen, R. E. *J. Chem. Phys.* **1993**, *98*, 6138-6149.

[205] Wu, G.; Wasylishen, R. E. *J. Chem. Phys.* **1994**, *100*, 4828-4834.

[206] Hahn, E. L.; Maxwell, D. E. *Phys. Rev.* **1952**, *88*, 1070-1084.

[207] Hung, I.; Wong, A.; Howes, A. P.; Anupõld, T.; Past, J.; Samoson, A.; Mo, X.; Wu, G.; Smith, M. E.; Brown, S. P.; Dupree, R. *J. Magn. Reson.* **2007**, *188*, 246-259.

[208] Alderman, O. L. G.; Iuga, D.; Howes, A. P.; Pike, K. J.; Holland, D.; Dupree, R. *Phys. Chem. Chem. Phys.* **2013**, *15*, 8208-8221.

[209] Edén, M.; Frydman, L. *J. Chem. Phys.* **2001**, *114*, 4116-4123.

[210] Wu, Y.; Peng, Z.-Y.; Olejniczak, Z.; Sun, B. Q.; Pines, A. *J. Magn. Reson. Ser. A* **1993**, *102*, 29-33.

[211] Clegg, W.; Elsegood, M. R. J.; Lawlor, F. J.; Norman, N. C.; Pickett, N. L.; Robins, E. G.; Scott, A. J.; Nguyen, P.; Taylor, N. J.; Marder, T. B. *Inorg. Chem.* **1998**, *37*, 5289-5293.

[212] Churchill, M. R.; Amoh, K. N.; Wasserman, H. J. *Inorg. Chem.* **1981**, *20*, 1609-1611.

[213] Bak, M.; Nielsen, N. C. *J. Magn. Reson.* **1997**, *125*, 132-139.

[214] Aue, W. P.; Karhan, J.; Ernst, R. R. *J. Chem. Phys.* **1976**, *64*, 4226-4227.

[215] Hahn, E. L. *Phys. Rev.* **1950**, *15*, 580-594.

[216] Hahn, E. L.; Maxwell, D. E. *Phys. Rev.* **1951**, *84*, 1246-1247.

[217] Duma, L.; Lai, W. C.; Carravetta, M.; Emsley, L.; Brown, S. P.; Levitt, M. H. *ChemPhysChem* **2004**, *5*, 815-833.

[218] Musher, J. I. *J. Chem. Phys.* **1967**, *46*, 1537-1538.

[219] Lai, W. C.; McLean, N.; Gansmüller, A.; Verhoeven, M. A.; Antonioli, G. C.; Carravetta, M.; Duma, L.; Bovee-Geurts, P. H. M.; Johannessen, O. G.; de Groot, H. J. M.; Lugtenburg, J.; Emsley, L.; Brown, S. P.; Brown, R. C. D.; DeGrip, W. J.; Levitt, M. H. *J. Am. Chem. Soc.* **2006**, *128*, 3878-3879.

[220] Martineau, C.; Fayon, F.; Legein, C.; Buzaré, J.-Y.; Silly, G.; Massiot, D. *Chem. Commun.* **2007**, 2720-2722.

[221] Bax, A.; Freeman, R.; Frenkiel, T. A. *J. Am. Chem. Soc.* **1981**, *103*, 2102-2104.

[222] Lesage, A.; Bardet, M.; Emsley, L. *J. Am. Chem. Soc.* **1999**, *121*, 10987-10993.

[223] Wang, Q.; Hu, B.; Lafon, O.; Trébosc, J.; Deng, F.; Amoureux, J. P. *J. Magn. Reson.* **2009**, *200*, 251-260.

[224] Levitt, M. H.; Madhu, P. K.; Hughes, C. E. *J. Magn. Reson.* **2002**, *155*, 300-306.

[225] Jerschow, A.; Kumar, R. *J. Magn. Reson.* **2003**, *160*, 59-64.

[226] Lee, K.-s.; Zhugralin, A. R.; Hoveyda, A. H. *J. Am. Chem. Soc.* **2009**, 131, 7253-7255.

[227] Kleeberg,C.; Crawford, A. G.; Batsanov, A. S.; Hodgkinson, P.; Apperley, D. C.; Cheung, M. S.; Lin,Z.; Marder, T. B. *J. Org. Chem.* **2012**, 77, 785-789.

[228] Massiot, D.; Fayon, F.; Alonso, B.; Trebosc, J.; Amoureux, J.-P. *J. Magn. Reson.* **2003**, *164*, 160-164.

[229] Amoureux, J.-P.; Trebosc, J.; Wiench, J. W.; Massiot, D.; Pruski, M. *Solid State Nucl. Magn. Reson.* **2005**, *27*, 228-232.

[230] Schurko, R. W. *Acc. Chem. Res.* **2013**, *46*, 1985-1995.

[231] Spiess, H. W.; Sheline, R. K. *J. Chem. Phys.* **1970**, *53*, 3036-3041.

[232] Robinson, G. H. *Acc. Chem. Res.* **1999**, *32*, 773-782.

[233] Robinson, G. H. *Chem. Commun.* **2000**, 2175-2181.

[234] Su, J.; Li, X.-W.; Crittendon, R. C.; Robinson, G. H. *J. Am. Chem. Soc.* **1997**, *119*, 5471-5472.

[235] Xie, Y.; Grev, R. S.; Gu, J.; Schaefer III, H. F.; Schleyer, P. v. R.; Su, J.; Li, X.-W.; Robinson, G. H. *J. Am. Chem. Soc.* **1998**, *120*, 3773-3780.

[236] Hardman, N. J.; Wright, R. J.; Phillips, A. D.; Power, P. P. *J. Am. Chem. Soc.* **2003**, *125*, 2667-2679.

[237] Li, X.-W.; Pennington, W. T.; Robinson, G. H. *J. Am. Chem. Soc.* **1995**, *117*, 7578-7579.

[238] Boldyrev, A. I.; Wang, L.-S. *Chem. Rev.* **2005**, *105*, 3716-3757.

[239] Twamley, B.; Power, P. P. *Angew. Chem. Int. Ed.* **2000**, *39*, 3500-3503.

[240] Kuznetsov, A. E.; Boldyrev, A. I.; Li, X.; Wang, L.-S. *J. Am. Chem. Soc.* **2001**, *123*, 8825-8831.

[241] Beamish, J. C.; Small, R. W. H.; Worrall, I. J. *Inorg. Chem.* **1979**, *18*, 220-223.

[242] Beamish, J. C.; Boardman, A.; Small, R. W. H.; Worrall, I. J. *Polyhedron*, **1985**, *4*, 983-987.

[243] Wei, P.; Li, X.-W.; Robinson, G. H. *Chem. Commun.* **1999**, 1287-1288.

[244] Wilkinson, A. P.; Cheetham, A. K.; Cox, D. E. *Acta Cryst B* **1991**, *47*, 155-161.

[245] B. R. McGarvey, M. J. Taylor, D. G. Tuck, *Inorg. Chem.* **1981**, *20*, 2010-2013.

[246] Černy, Z.; Macháček, J.; Fusek, J.; Kříž, O.; Čásensky, B.; Tuck, D. G. *J. Organomet. Chem.* **1993**, *456*, 25-30.

[247] Massiot, D.; Vosegaard, T.; Magneron, N.; Trumeau, D.; Montouillout, V.; Berthet, P.; Loiseau, T.; Bujoli, B. *Solid State Nucl. Magn. Reson.* **1999**, *15*, 159-169.

[248] Ash, J. T.; Grandinetti, P. J. *Magn. Reson. Chem.* **2006**, *44*, 823-831.

[249] Okuda, T.; Sato, M.; Hamamoto, H.; Ishihara, H.; Yamada, K.; Ichiba, S. *Inorg. Chem.* **1988**, *27*, 3656-3660.

[250] Wi, S.; Heise, H.; Pines, A. *J. Am. Chem. Soc.* **2002**, *124*, 10652-10653.

[251] Autschbach, J. *J. Chem. Phys.* **2007**, *127*, 124106.

[252] Zhang, Y.; Yang, W. Phys. Rev. Lett., **1998**, *80*, 890.

[253] Glendening, E. D.; Badenhoop, J. K.; Reed, A. E.; Carpenter, J. E.; Bohmann, J. A.; Morales, C. M.; Weinhold, F. NBO 5.0., Theoretical Chemistry Institute, University of Wisconsin, Madison, WI, 2001.

[254] Zaremba, S. K., *Ann. Mat. Pura Appl.* **1966**, *73*, 293-317.

[255] Conroy, H. *J. Chem. Phys.* **1967**, *47*, 5307-5318.

[256] Cheng, V. B.; Suzukawa Jr., H. H.; Wolfsberg, M. *J. Chem. Phys.* **1973**, *59*, 3992-3999.

[257] Mun, S.; Lee, J.-E.; Yun, J. *Org. Lett.*, **2006**, *8*, 4887-4889.

[258] Gao, M.; Thorpe, S. B.; Santos, W. L. *Org. Lett.*, **2009**, *11*, 3478-3481.

[259] Bonet, A.; Pubill-Ulldemolins, C.; Bo, C.; Gulyás, H.; Fernández, E. *Angew. Chem. Int. Ed.* **2011**, *50*, 7158-7161.

[260] Kleeberg, C.; Crawford, A. G.; Batsanov, A. S.; Hodgkinson, P.; Apperley, D. C.; Cheung, M. S.; Lin, Z.; Marder, T. B. *J. Org. Chem.* **2012**, *77*, 785-789.

[261] Gao, M.; Thorpe, S. B.; Kleeberg, C.; Slebodnick, C.; Marder, T. B.; Santos, W. L. *J. Org. Chem.* **2011**, *76*, 3997-4007.

[262] Pubill-Ulldemolins, C.; Bonet, A.; Bo, C.; Gulyás, H.; Fernández, E. *Chem. Eur. J.* **2012**, *18*, 1121-1126.

[263] Cid, J.; Gulyás, H.; Carbó, J. J.; Fernández, E. *Chem. Soc. Rev.* **2012**, *41*, 3558-3570.

[264] Gulyás, H.; Bonet, A.; Pubill-Ulldemolins, C.; Solé, C.; Cid, J.; Fernández, E. *Pure Appl. Chem.* **2012**, *84*, 2219-2231.

[265] Pubill-Ulldemolins, C.; Bonet, A.; Gulyás, H.; Bo, C.; Fernández, E. *Org. Biomol. Chem.* **2012**, *10*, 9677-9682.

[266] Bonet, A.; Sole, C.; Gulyás, H.; Fernández, E. *Org. Biomol. Chem.* **2012**, *10*, 6621-6623.

[267] *JP. Pat.*, WO 2013133203 A1, 2013.

[268] Cid, J.; Carbó, J. J.; Fernández, E. *Chem. Eur. J.* **2012**, *18*, 12794-12802.

[269] Smith, K. *Organoboron Chemistry*, in: Schlosser, M., Ed. *Organometallics in Synthesis: A Manual, Volume 1*, John Wiley & Sons, ltd., Chichester, 2002.

[270] Braunschweig, H.; Damme, A.; Dewhurst, R. D.; Kramer, T.; Kupfer, T.; Radacki, K.; Siedler, E.; Trumpp, A.; Wagner, K.; Werner, C. *J. Am. Chem. Soc.* **2013**, *135*, 8702-8707.

[271] Litters, S.; Kaifer, E.; Enders, M.; Himmel, H.-J. *Nature Chem.* **2013**, *5*, 1029-1034.

[272] Braunschweig, H.; Dewhurst, R. D.; Hörl, C.; Phukan, A. K.; Pinzner, F.; Ullrich, S. *Angew. Chem.* **2014**, *53*, 3241-3244.

[273] Siedle, A. R. *Annu. Rep. NMR Spectrosc.* **1988**, *20*, 205-314.

[274] Greiwe, P.; Bethäuser, A.; Pritzkow, H.; Kühler, T.; Jutzi, P.; Siebert, W. *Eur. J. Inorg. Chem.* **2000**, 1927-1929.

[275] Baber, R. A.; Norman, N. C.; Orpen, A. G.; Rossi, J. *New J. Chem.* **2003**, *27*, 773-775.

[276] Ali, H. A.; Goldberg, I.; Srebnik, M. *Eur. J. Inorg. Chem.* **2002**, 73-78.

[277] Nguyen, P.; Dai, C.; Taylor, N. J.; Power, W. P.; Marder, T. B.; Pickett, N. L.; Norman, N. C. *Inorg. Chem.* **1995**, *34*, 4290-4291.

[278] Brauer, D. J.; Krüger, C. *Acta Cryst. B*, **1973**, *29*, 1684-1690

[279] Frydman, L.; Harwood, J. S. *J. Am. Chem. Soc.*, **1995**, *117*, 5367-5368.

[280] Kriz, H. M.; Bray, P. J. *J. Magn. Reson.* **1971**, *4*, 76-84.

[281] Weiss, J. W. E.; Bryce, D. L. *J. Phys. Chem. A*, **2010**, *114*, 5119-5131.

[282] Charpentier, T. *Solid State Nucl. Magn. Reson.* **2011**, *40*, 1-20.

[283] Bonhomme, C.; Gervais, C.; Babonneau, F.; Coelho, C.; Pourpoint, F.; Azaïs, T.; Ashbrook, S. E.; Griffin, J. M.; Yates, J. R.; Mauri, F.; Pickard, C. J. *Chem. Rev.*, **2012**, *112*, 5733-5779.

[284] Dračínský, M.; Hodgkinson, P. *CrystEngComm*, **2013**, *15*, 8705-8712.

[285] Wu, G.; Kroeker, S.; Wasylishen, R. E.; Griffin, R. G.; *J. Magn. Reson.* **1997**, *124*, 237-239.

[286] Demachy, I.; Volatron, F.; *J. Phys. Chem.*, **1994**, *98*, 10728-10734.

[287] Mo, Y.; Lin, Z. *J. Chem. Phys.* **1996**, *105*, 1046-1051.

[288] Watts, C. R.; Badenhoop, J. K. *J. Chem. Phys.*, **2008**, *129*, 104307.

[289] Foster, J. P.; Weinhold, F. *J. Am. Chem. Soc.*, **1980**, *102*, 7211-7218.

[290] Reed, A. E.; Weinhold, F. *J. Chem. Phys.*, **1985**, *83*, 1736-1740.

[291] Kroner, J.; Wrackmeyer, B.; *J. Chem. Soc., Faraday Trans. 2* **1976**, *72*, 2283-2290.

[292] Bent, H. A. *Chem. Rev.* **1961**, *61*, 275-311.

[293] Bachmann, F.; Nöth, H.; Pommerening, H.; Wrackmeyer, B.; Wirthlin, T. *J. Magn. Reson.* **1979**, *34*, 237-239.

[294] Wrackmeyer, B.; *Z. Naturforsch B*, **2004**, *59*, 1192-1199.

[295] Autschbach, J.; Le Guennic, B. *J. Chem. Ed.*, **2007**, *84*, 156-171.

[296] Muller, N.; Pritchard, D. E. *J. Chem. Phys.*, **1959**, *31*, 1471-1476.

[297] Muller, N.; Pritchard, D. E. *J. Chem. Phys.*, **1959**, *31*, 768-771.

[298] Florian, P.; Fayon, F.; Massiot, D. *J. Phys. Chem. C*, **2009**, *113*, 2562-2572.

[299] Farrar, T. C.; Quinting, G. R. *Inorg. Chem.* **1985**, *24*, 1941-1943.

[300] Concistrè, M.; Carignani, E.; Borsacchi, S.; Johannessen, O. G.; Mennucci, B.; Yang, Y.; Geppi, M.; Levitt, M. H. *J. Phys. Chem. Lett.*, **2014**, *5*, 512-516.

[301] Cid, J.; Carbó, J. J.; Fernández, E. *Chem. Eur. J.* **2014**, *20*, 3616-3620.

[302] Hayashi, S.; Hayamizu, K. *Bull. Chem. Soc. Jpn.* **1989**, *62*, 2429-2430.

[303] Amoureux, J.-P.; Fernandez, C.; Steuernagel, S. *J. Magn. Reson. Ser. A*, **1996**, *123*, 116-118.

[304] States, D. J.; Haberkorn, R. A.; Ruben, D. J. *J. Magn. Reson.* **1982**, *48*, 286-292.

Part IV: General Conclusions

As has been highlighted in the individual chapters of this thesis, various approaches can be taken in order to obtain quantitative structural information with the use of the NMR spectroscopy of quadrupolar nuclei. Although many of the applications discussed in this thesis were for simple systems, it is foreseen that the applications of NMR spectroscopy of quadrupolar nuclei to structural chemistry will continue its rapid growth. In recent years, new techniques such as isotropic spin-1/2-quadrupolar correlation experiments, the WURST-QCPMG pulse sequence, and dynamic nuclear polarization have greatly extended the structural information that can be extracted from quadrupolar nuclei and extended the range of systems that can be studied; many of these techniques are still also in their infancy. The continuous advent of ever higher field magnets will, of course, continue to have the largest impact on the NMR spectroscopy of quadrupolar nuclei.

In the first part of this thesis it was shown that the simplest of the NMR interactions to extract in the case of quadrupolar nuclei, namely the quadrupolar interaction, can be used directly in order to refine crystalline structures in a systematic way. A least-squares refinement procedure was used in order to optimise the fractional coordinates of a crystal structure so to improve the agreement between experimentally determined EFG tensor components and those that are predicted with the use of PAW DFT calculations. This approach was shown to improve on the DFT-refined crystal structures of various materials and, in principle, does not significantly increase the computational time due to the EFG tensor's low computational cost.

This NMR crystallographic approach was applied to sodium aluminoborate ($Na_2B_2Al_2O_7$), a non-linear optical material. In this case, diffraction techniques were limited due to the system's propensity to form stacking faults, however, NMR crystallographic techniques are particularly apposite. The importance of cross-validating the refined structure is, however, important in order to ensure that the data is not over fitted. The incorporation of dipolar information, through the use of spin diffusion DOR data, was also shown to be beneficial, using sodium pyrophosphates as an example, since the sites need to be correctly assigned for this approach to be successful. With these samples, it was also shown that the EFG tensor at ionic sites, such as Na cations, is particularly well suited to crystal structure refinements due to the lack of overpowering covalent interactions, and the long range sensitivity of the EFG tensor.

Lastly, it was shown that the site information from the NMR spectroscopy of quadrupolar nuclei can be used for the application of NMR-driven crystallography and the structure of $ZrMgMo_3O_{12}$, a near-zero thermal expansion material, was solved *ab initio*. The EFG-based crystal structure refinement strategy could then be used in order to obtain chemically-reasonable structural parameters that can be related to the thermal expansion properties of the compound.

The second part of the thesis focussed on the theory and measurements of spin-spin coupling between pairs of quadrupolar nuclei. *J* and dipolar coupling provide the clearest structural information from NMR spectroscopy and can, in principle, give a complete picture of the bonding connectivities and internuclear distances in a system, if all the spin-spin coupling pairs are evaluated. The most direct measurement of the spin-spin coupling interactions between quadrupolar spins can be obtained by evaluating the fine structure of

the NMR resonances; unfortunately, the dominant quadrupolar interaction often completely obscures the fine structure. It was shown that these multiplets can nonetheless be easily detected with the use of double-rotation techniques in order to remove the second-order quadrupolar broadening. These residual dipolar coupling multiplets provide information relating to the effective dipolar coupling and *J* coupling constants between the quadrupolar nuclei involved. The theory developed to describe these multiplets could additionally be applied to simulating the NMR spectra of quadrupolar nuclei exactly at any applied magnetic field strength. This QUadrupolar Exact SofTware (QUEST) could then be used to analyse the first NMR spectra of covalently-bound organic chlorine sites and show that the spectra can unambiguously distinguish the chemical environments of the chlorine.

It was also noticed that the *J* coupling interaction surprisingly still affects the NMR spectra for pairs of magnetically equivalent quadrupolar nuclei. The unusual multiplets that are predicted can be observed directly if double-rotation is used in order to remove the second-order quadrupolar broadening. These multiplets can, in theory, be used to easily distinguish between non-equivalent, chemically equivalent, and magnetically equivalent spin pairs of quadrupolar nuclei.

The measurement of *J* coupling between quadrupolar nuclei is however much more easily achieved by using specially-tailored 2D *J*-resolved NMR experiments that can be performed with the use of conventional magic angle spinning hardware. The precision in the determination of the *J* coupling constants is an order of magnitude higher with these experiments than is achievable using 1D DOR experiments since the resolution is only limited by T_2. Interestingly, the splitting observed in the indirect dimension of a *J*-resolved experiment is amplified in the A_2 case, aiding the measurement of small *J* coupling constants

in symmetric molecules and directly providing information regarding the symmetry of the molecule. These experiments have been applied to studying important diboron species for which it was shown that information regarding the nature and strength of the boron-boron bond can be easily extracted. Static experiments can also be performed in ultra-wideline cases where the *J* and dipolar coupling can be simultaneously extracted. This has, for example, been applied to studying metal-metal bonding in digallium compounds. Valuable metal-metal bonding information can in principle be obtained for numerous other challenging systems.

I foresee that the NMR spectroscopy of quadrupolar nuclei will continue to grow in order to gain unprecedented insights into the structure of materials and molecular crystals that weren't accessible in the past. The advent of DNP will likely make it possible to routinely observe low-sensitivity quadrupolar nuclei such as ^{17}O, and ^{43}Ca, whose developments have been limited by their low natural abundances, as well as quadrupolar nuclei involved in heterogeneous catalysis. In the future, solid-state NMR of quadrupolar nuclei may well be used as a routine technique alongside diffraction in order to solve the structures of materials.

Appendix

List of Publications

19. Perras, F. A.; Bryce, D. L. *J. Phys. Chem. Lett.* **2014**, *5*, 4049-4054.

18. Perras, F. A.; Bryce, D. L. *Chem Sci.* **2014**, *5*, 2428-2437.

17. Perras, F. A.; Bryce, D. L. *J. Magn. Reson.* **2014**, *242*, 23-32.

16. Dicaire, N. M.; Perras, F. A.; Bryce, D. L. *Can. J. Chem.* **2014**, *92*, 9-15.

15. Perras, F. A.; Bryce, D. L. *J. Am. Chem. Soc.* **2013**, *135*, 12596-12599.

14. Perras, F. A.; Korobkov, I.; Bryce, D. L. *CrystEngComm* **2013**, *15*, 8727-8738.

13. Perras, F. A.; Bryce D. L. *J. Chem. Phys.* **2013**, *138*, 174202.

12. Perras, F. A.; Viger-Gravel, J.; Burgess, K. M. N.; Bryce, D. L. *Solid State Nucl. Magn. Reson.* **2013**, *51-52*, 1-15.

11. Perras, F. A.; Bryce, D. L. *J. Phys. Chem. C* **2012**, *116*, 19472-19482.

10. Perras, F. A.; Widdifield, C. M.; Bryce, D. L. *Solid State Nucl. Magn. Reson.* **2012**, *45-46*, 36-44.

9. Burgess, K. M. N.; Perras, F. A.; Lebrun, A.; Messner-Henning, E.; Korobkov, I.; Bryce, D. L. *J. Pharm. Sci.* **2012**, *101*, 2930-294.

8. Perras, F. A.; Bryce, D. L. *Angew. Chem. Int. Ed.* **2012**, *51*, 4227-4230.

7. Jeletic, M.; Perras, F. A.; Gorelski, S. I.; Le Roy, J. J.; Korobkov, I.; Bryce, D. L.; Murugesu, M. *Dalton Trans.* **2012**, *41*, 8060-8066.

6. Capicciotti, C. J.; Leclere, M.; Perras, F. A.; Bryce, D. L.; Paulin, H.; Harden, J.; Ben, R. N. *Chem. Sci.* **2012**, *3*, 1408-1416.

5. Perras, F. A.; Korobkov, I.; Bryce, D. L. *Phys. Chem. Chem. Phys.* **2012**, *14*, 4677-4681.

4. Perras, F. A.; Bryce, D. L. *J. Magn. Reson.* **2011**, *213*, 82-89.

3. Perras, F. A.; Bryce, D. L. *J. Magn. Reson.* **2011**, *211*, 234-239.

2. Perras, F. A.; Bryce, D. L. *Can. J. Chem.* **2011**, *89*, 789-802.

1. Bryce, D. L.; Dorval Courchesne, N. M.; Perras, F. A. *Solid State Nucl. Magn. Reson.* **2010**, *36*, 182-191.

List of Conference Presentations

22. **Perras, F. A.**; Bryce, D. L. *Homonuclear J Coupling Between Quadrupolar Nuclei Measured Using an Ultra-Wideline 2D J-Resolved Experiment. A Direct Probe of Metal-Metal Bonding*. Oral Presentation at the Rocky Mountain Conference on Magnetic Resonance, Copper Mountain, CO, July 17, 2014.

21. **Perras, F. A.**; Lummiss, J. A. M.; Reckling, A. M.; Fogg, D. E.; Bryce, D. L. *Analysing the Metal-Ligand Orbital Interactions in Ruthenium Metathesis Catalysts Using a Combined Solid-State NMR and NLMO Approach*. Poster presentation at the ISHC conference, Ottawa, ON, July 8, 2014

20. **Perras, F. A.**; Romao, C. P.; Werner-Zwansiger, U.; Lussier, J. A.; Bieringer, M.; Miller, K. J.; Marinkovic, B. A.; Zwansiger, J. W.; White, M. A.; Bryce, D. L. *NMR Crystallographic Structure Determination and Refinement of the Near-Zero Thermal Expansion Material* $ZrMgMo_3O_{12}$. Poster presentation at the Euromar 2014 conference, Zurich, CH, July 2, 2014.

19. **Perras, F. A.**; Bryce, D. L. *Symmetry-Amplified J Splittings for Quadrupolar Spin Pairs: Cases of Magnetic Equivalence, Chemical Equivalence, and Non-Equivalence.* Oral presentation at the ENC, Boston, MA, Marche 27 2014

18. **Perras, F. A.**; Bryce, D. L. *The Peculiarities of Homonuclear Spin-Spin Coupling Between Quadrupoles*. Oral presentation at the MOOT mini-NMR symposium, Kingston, On. October 26 2013. (**winner of a talk prize**)

17. **Perras, F. A.**; Burgess, K. M. N.; Dicaire, N.; Bryce, D.L. *Structure and Polymorphism in Small Molecules and Drugs: Insights from Solid-State NMR of Quadrupolar Nuclei*. Oral presentation at the SMASH conference, Santiago de Copostela, Spain, September 23 2013.

16. **Perras, F. A.**; Bryce, D. L. *J Coupling Between Magnetically Equivalent Spins and Other Secrets Revealed by DOR NMR*. Oral presentation at the 8th alpine conference on solid-state NMR, Chamonix, France, September 12 2013.

15. **Perras, F. A.**; Bryce, D. L. *Measurement of Dipolar and J coupling in Pairs of Quadrupolar Nuclei Using DOR NMR*. Oral presentation at the Canadian Chemistry Conference and Exhibition, Québec, Qc. May 28 2013. (**winner of the best physical/theoretical talk prize**)

14. **Perras, F. A.**; Bryce, D. L. *J Coupling Between Magnetically Equivalent Spins*. Oral presentation at the Ottawa-Carleton chemistry institute meeting, Ottawa, On. May 16 2013. (**winner of a talk prize**)

13. **Perras, F. A.**; Bryce, D.L. *Direct Measurement of Dipolar and* J *Coupling in Homonuclear and Heteronuclear Coupled Quadrupolar Spin Pairs using Double-Rotation NMR*. Poster presentation at the ENC, Asilomar, CA, April 14 2013.

12. **Perras, F. A.**; Bryce, D. L. *EFG-Based NMR Crystallographic Structure Refinement and Cross-Validation of* $Na_2Al_2B_2O_7$. Oral presentation at the MOOT mini-NMR symposium, Québec, Qc. October 20 2012.

11. Bryce, D. L.; **Perras, F. A.**, Widdifield, C. M.; Viger-Gravel, J.; Leclerc, S.; Burgess, K. M. N.; Chapman, R. P.; Attrell, R. J. *Development and Applications of Quadrupolar Halogen Solid State NMR Spectroscopy*. Plenary lecture at the Conference on Nuclear Magnetic Resonance in Chemistry, Physics, and Biological Sciences, Institute for Organic Chemistry, Warsaw, Poland, September 28 2012.

10. **Perras, F. A.**; Bryce, D. L. *Obtaining Distance Information from High-Resolution Double-Rotation NMR of Quadrupolar Nuclei in Solids.* Poster presentation at the Canadian Chemistry Conference and Exhibition, Calgary, Ab. May 29 2012.

9. **Perras, F. A.**; Widdifield, C. M.; Bryce, D. L. *The QUEST for Chlorine*. Oral presentation at the Canadian Chemistry Conference and Exhibition, Calgary, Ab. May 27 2012.

8. **Perras, F. A.**; Bryce, D. L. *^{35}Cl Solid-State NMR of Covalently-Bound, Organic, Chlorine at 21.1 T and the use of the QUEST (QUadrupolar Exact SofTware).* Oral presentation at the Solid-State NMR workshop at the CSC conference, Calgary, Ab. May 26 2012.

7. **Perras, F. A.**; Bryce, D. L. *Obtaining Distance Information from High-Resolution Double-Rotation NMR of Quadrupolar Nuclei in Solids.* Poster presentation at the Ottawa-Carleton chemistry institute meeting, Ottawa, On. May 18 2012.

6. **Perras, F. A.**; Bryce, D. L. *A Double-Rotation NMR Study of a new Hydrate of Deoxycytidine Monophosphate and Other Sodium Nucleotide Salts.* Poster presentation at the MOOT mini-NMR symposium, Toronto, On. October 22 2011.

5. **Perras, F. A.**; Bryce, D. L. Removal of Sidebands in Double-Roation NMR Using Inversion Pulses. Oral presentation at the Canadian Chemistry Conference and Exhibition, Montreal, Qc. June 6 2011.

4. **Perras, F. A.**; Bryce, D. L. *Removal of Sidebands in Double-Rotation NMR*. Oral presentation at the Ottawa-Carleton chemistry institute meeting, Ottawa, On. May 27 2011.

3. **Perras, F. A.**; Bryce, D. L. *A ZORA-DFT and NLMO Study of the One-Bond Fluorine-X Indirect Nuclear Spin-Spin Coupling Tensors for Various VSEPR Geometries*. Oral presentation at the MOOT mini-NMR symposium, Halifax, NS. October 16 2010.

2. **Perras, F. A.**; Bryce, D. L.; Dorval Courchesne, N. M. *Exploring the Validity of Common Assumptions Made in the Characterization of J Coupling Tensor Anisotropies.* Poster presentation at the Ottawa-Carleton chemistry institute meeting, Ottawa, On. May 21 2010. (**winner of a poster prize**)

1. Bryce, D. L.; **Perras, F. A.**; Dorval Courchesne, N. M. *Measurement of $\Delta^1J(^{199}Hg,^{31}P)$ in $[HgPCy_3(OAc)_2]_2$ and relativistic ZORA DFT Investigations of Mercury-Phosphorus Coupling Tensors.* Oral presentation at the MOOT mini-NMR symposium, Ottawa, On. October 17, 2009.

Example Input Files

ADF J Coupling Calculation

```
$ADFBIN/adf << eor
Title B2cat2 - scf

Basis
 Type QZ4P
 Core None
End

Symmetry NOSYM

Atoms
    1.O         0.276184    0.378582    1.697755
    2.O         0.887113    1.406364    3.658016
    3.C         1.279814    1.293240    1.434547
    4.C         1.875240    1.602487    0.224408
    5.C         2.874728    2.581793    0.257190
    6.C         3.246976    3.208873    1.452378
    7.C         2.636733    2.885847    2.669896
    8.C         1.651072    1.915974    2.623232
    9.B         0.044164    0.460100    3.072721
   10.H         1.577514    1.112987   -0.695279
   11.H         3.371504    2.860434   -0.665913
   12.H         4.025854    3.963633    1.435983
   13.H         2.916545    3.366287    3.600106
   14.B        -1.096396   -0.457648    3.905616
   15.O        -1.345929   -0.361757    5.276644
   16.C        -2.343895   -1.282885    5.538815
   17.C        -2.952556   -1.581766    6.745023
   18.C        -3.940758   -2.572413    6.712390
   19.C        -4.289531   -3.220339    5.521247
   20.C        -3.666838   -2.906891    4.307531
   21.C        -2.693310   -1.924812    4.353737
   22.O        -1.922418   -1.419593    3.321933
   23.H        -3.928624   -3.403163    3.380414
   24.H        -5.059834   -3.983744    5.537770
   25.H        -4.446583   -2.844232    7.632564
   26.H        -2.671768   -1.077359    7.661978
End

Integration 6.0

XC
   metaGGA TPSS
```

```
End

End Input
eor

$ADFBIN/cpl<< eor
maxmemoryusage 40
nmrcoupling
atompert {9}
atomresp {14}
dso
pso
sd
fc
scf {convergence=1e-7}
END
END INPUT
eor
```

ADF Shielding and EFG Calculation

```
$ADFBIN/adf << eor
Title BMncat - scf

Basis
 Type ZORA/TZ2P
 Core None
End

Symmetry NOSYM

relativistic spinorbit zora

Atoms
 Mn                11.30410000    1.11880000    2.19010000
 O                 11.54540000    1.09920000    5.27760000
 O                 13.60610000    1.18550000    4.30450000
 O                  9.09130000   -0.37970000    3.56900000
 O                  9.96730000    1.18410000   -0.47670000
 O                 13.72260000    2.55910000    1.22760000
 O                 10.16490000    3.66460000    3.24280000
 O                 12.77230000   -1.44940000    1.92090000
 C                 12.51850000    1.12580000    6.27460000
 C                 12.35250000    1.11600000    7.62740000
 C                 13.52210000    1.16520000    8.37830000
 C                 14.76100000    1.22130000    7.78910000
 C                 14.91590000    1.22830000    6.42930000
 C                 13.75930000    1.19460000    5.68680000
```

```
 C                   9.91630000    0.18950000    3.03320000
 C                  10.48110000    1.14410000    0.54420000
 C                  12.79300000    2.01450000    1.59610000
 C                  10.58980000    2.70230000    2.81530000
 C                  12.20420000   -0.46330000    2.00390000
 B                  12.22690000    1.12300000    4.08510000
 H                  11.49270000    1.08230000    8.03090000
 H                  13.46070000    1.15390000    9.32750000
 H                  15.53310000    1.25640000    8.34170000
 H                  15.77360000    1.26270000    6.02150000
End

Integration 6.0

qtens

XC
   metaGGA TPSS
End

End Input
eor

$ADFBIN/nmr << eor
NMR
  U1K BEST
  Out TENS
  Atoms 1 20
  SCF 1.d-4
END
eor
```

ADF NLMO Decomposition of the J coupling

```
$ADFBIN/adf << eor

ATOMS
 O    0.28100    0.35614    1.71209
 O    0.87548    1.40221    3.66129
 C    1.28883    1.28673    1.44080
 C    1.86010    1.59030    0.23781
 C    2.84960    2.56787    0.26640
 C    3.20391    3.21345    1.44917
 C    2.59689    2.89690    2.66193
 C    1.63123    1.91769    2.62009
 B    0.03992    0.45618    3.06921
 H    1.62699    1.14496   -0.56279
 H    3.32680    2.81066   -0.54884
 H    3.94855    3.85542    1.44290
```

```
 H    2.84515    3.31168    3.52251
 B   -1.09338   -0.45618    3.90468
 O   -1.33445   -0.35614    5.26179
 C   -2.34229   -1.28673    5.53308
 C   -2.91356   -1.59030    6.73607
 C   -3.90305   -2.56787    6.70748
 C   -4.25736   -3.21345    5.52471
 C   -3.65035   -2.89690    4.31195
 C   -2.68469   -1.91769    4.35380
 O   -1.92894   -1.40221    3.31259
 H   -3.89861   -3.31168    3.45137
 H   -5.00201   -3.85542    5.53099
 H   -4.38025   -2.81066    7.52273
 H   -2.68044   -1.14496    7.53668
END

save TAPE15
FULLFOCK
AOMAT2FILE

BASIS
 type QZ4P
 core None
END

XC
  metaGGA TPSS
End

SCF
 converge 1.0e-8
END

SYMMETRY nosym

INTEGRATION
 accint 4.5
 accsph 5.5
end

relativistic scalar zora

end input
eor

$ADFBIN/adfnbo << eor
write
spherical
fock
TESTJOB
end input
```

```
eor

rm adfnbo.37 adfnbo.39 adfnbo.49 adfnbo.48
cp TAPE21 NLMO.t21
$ADFBIN/gennbo < FILE47

$ADFBIN/adfnbo << eor
 copy
 spherical
 fock
end input
eor

$ADFBIN/adfnbo << eor
 spherical
 fock
 read
end input
eor

rm adfnbo.37 adfnbo.39 adfnbo.49 adfnbo.48

rm TAPE15 TAPE21 TAPE13 logfile

$ADFBIN/cpl << eor
maxmemoryusage 40
nmrcoupling
atompert {9}
atomresp {14}
 dso
 pso
 sd
 fc
 scf {convergence=1e-7}
 contributions 1e19 nbo
end
endinput
eor

rm TAPE15 TAPE21 TAPE13 logfile

$ADFBIN/adf << eor
ATOMS
 O    0.28100    0.35614    1.71209
 O    0.87548    1.40221    3.66129
 C    1.28883    1.28673    1.44080
 C    1.86010    1.59030    0.23781
 C    2.84960    2.56787    0.26640
 C    3.20391    3.21345    1.44917
 C    2.59689    2.89690    2.66193
 C    1.63123    1.91769    2.62009
```

```
 B    0.03992    0.45618    3.06921
 H    1.62699    1.14496   -0.56279
 H    3.32680    2.81066   -0.54884
 H    3.94855    3.85542    1.44290
 H    2.84515    3.31168    3.52251
 B   -1.09338   -0.45618    3.90468
 O   -1.33445   -0.35614    5.26179
 C   -2.34229   -1.28673    5.53308
 C   -2.91356   -1.59030    6.73607
 C   -3.90305   -2.56787    6.70748
 C   -4.25736   -3.21345    5.52471
 C   -3.65035   -2.89690    4.31195
 C   -2.68469   -1.91769    4.35380
 O   -1.92894   -1.40221    3.31259
 H   -3.89861   -3.31168    3.45137
 H   -5.00201   -3.85542    5.53099
 H   -4.38025   -2.81066    7.52273
 H   -2.68044   -1.14496    7.53668
END

BASIS
 type QZ4P
 core None
END

XC
  metaGGA TPSS
End

SYMMETRY nosym

SCF
 converge 1.0e-8
END

INTEGRATION
 accint 4.5
 accsph 5.5
end

relativistic spinorbit zora

end input
eor

rm TAPE15

$ADFBIN/cpl << eor
maxmemoryusage 40
nmrcoupling
atompert {9}
```

```
atomresp {14}
 dso
 pso
 sd
 fc
 scf {convergence=1e-7}
 contributions 1e19 nbo
end
endinput
eor
```

SIMPSON DOR Simulation

```
spinsys {
      channels 11B
      nuclei   11B 11B

       quadrupole 1 2 3e6 0.5 0 0 0
       quadrupole 2 2 3e6 0.5 0 0 0
       jcoupling 1 2 100 0 0 0 0 0
       dipole 1 2 0 0 15 0
}

par {
      proton_frequency              400e6

      dor                           1
      outer_rotor_angle             54.735610
      inner_rotor_angle             30.555592
      outer_spin_rate               2000
      inner_spin_rate               8000

      crystal_file                  rep66
      gamma_angles                  8
      method                        direct
      verbose                       1101

      start_operator                Inx
      detect_operator               Inc

      np                            1024

      variable sw                   20000
      variable dw                   1.0e6/sw


}

proc pulseq {} {
      global par
```

```
      for {set k 0} {$k < $par(np)} {incr k} {
            acq
            delay $par(dw)
      }
}

proc main {} {
      global par

      set f [fsimpson]

      fsave $f $par(name).fid
      faddlb $f 60 0
      fzerofill $f [expr 4*$par(np)]
      fft $f
      fsave $f $par(name).spe
}
```

SIMPSON DQF-J-Resolved Simulation

```
spinsys {
      channels 11B
      nuclei   11B 11B

       quadrupole 1 2 3e6 0.5 0 0 0
       quadrupole 2 2 3e6 0.5 0 0 0
       jcoupling 1 2 100 0 0 0 0 0
       dipole 1 2 0 0 0 0
}



par {
spin_rate 10000
sw spin_rate/20
np 256
proton_frequency 400e6
crystal_file zcw232
gamma_angles 20
start_operator Inz
detect_operator Inc
variable rf 4166.6
variable p90 30
variable p180 60
}


proc pulseq {} {
```

```
global par

maxdt 1.0

matrix set 1 totalcoherence {1}
matrix set 2 totalcoherence {-1}
matrix set 4 totalcoherence {1 -1}
matrix set 5 totalcoherence {-1 1}
matrix set 7 totalcoherence {2 -2}


reset
delay [expr 10.0e6/($par(spin_rate))]
store 6
reset

reset
delay [expr 4.0e6/($par(spin_rate))]
store 8
reset

for {set n 1} {$n<$par(np)} {incr n 1} {
  reset

  pulse $par(p90) $par(rf) 0
  delay [expr 1.0e6/($par(spin_rate))-30]
  prop 8
  filter 4
  pulse $par(p180) $par(rf) 90
  delay [expr 1.0e6/($par(spin_rate))-60]
  prop 8
  filter 5
  pulse $par(p90) $par(rf) 0
  filter 7

  pulse $par(p90) $par(rf) 0
  delay [expr 1.0e6/($par(spin_rate))-60]
  prop 8
  filter 1

  for {set i 1} {$i<$n} {incr i 1} {
    prop 6
    }

  pulse $par(p180) $par(rf) 90
  delay [expr 1.0e6/($par(spin_rate))-60]
  prop 8
  filter 2
  for {set i 1} {$i<$n} {incr i 1} {
    prop 6
```

```
      }
    acq
  }
}


proc main {} {
global par

set f [fsimpson]

      fsave $f $par(name).fid
      faddlb $f 1.5 0
       fzerofill $f [expr 4*$par(np)]
       fft $f
      fsave $f $par(name).spe


}
```